Vibrational Spectroscopy on the Silicon Hydride Mode: Probing Ultrafast Dynamics in Small Molecules to Macromolecular Polymer Systems

A DISSERTATION
SUBMITTED TO THE FACULTY OF THE GRADUATE SCHOOL
OF THE UNIVERSITY OF MINNESOTA
BY

Courtney Marie Olson

IN PARTIAL FULFILLMENT OF THE REQUIREMENTS
FOR THE DEGREE OF
DOCTOR OF PHILOSOPHY

Professor Aaron M. Massari, Advisor

June 2019

Acknowledgements

I want to start off by thanking all the people who have helped me reach my goal of receiving my doctorate. First, the most important people in my life who have always been there for me and always will: my family. I want to thank my parents. Mom and Dad, without your unwavering support, I don't think I could have reached this point. Knowing how much you love me and how proud you are of my accomplishments helps push me every day. You listen to all my concerns even though you don't fully understand the context, and I appreciate that. Thank you to my brother, Nick. Even though we don't talk much or communicate well, I know you are always there for me. You are the rock. I want to thank the rest of my family as well. You are the greatest support system, and I hope to make you all proud.

Thank you to all my friends, of course! I do need to point a few of them out though. Thank you to my two best friends that I am still glad to call my best friends even though we are miles and miles apart. Kim Loughlin and Hannah Stewart, you have been there for me through many of my life changes. You still wanted to be my friend, even though I thought I was a strange one to be around. You two know how to make me laugh and we can always get right back into our conversations even though it has been weeks. Thank you for sticking with me. Thank you to my graduate school friends. There are so many of you to name, so I won't list all of you. You know who you are and know that I appreciate every single one of you. And know, I will miss all of you and will try to stay in touch.

Thank you to all my professors at my undergraduate institution, Ohio Northern University. Thank you to Dr. Nicole Karn, now at The Ohio State University. You are the one that made me excited to do research and then ultimately pursue graduate school.

Without your foundational efforts, I don't know where I would have ended up today. I also want to thank all of the other professors that helped me reach to this point: Dr. Trilisa Perrine, Dr. Tevye Celius, Dr. Bradley Wile, Dr. Amelia Anderson-Wile, Dr. Kimberly Broekemeier, Dr. Jeffrey Gray, and Dr. Chris Spiese. All of you shaped me to be the great scientist that I am today, and I am eternally grateful.

Of course, I need to thank the professors at the University of Minnesota, who have mentored me throughout my graduate career. More specifically, thank you to Dr. David Blank and Dr. Renee Frontiera for the insight and guidance throughout my career.

Thank you to the Massarians, past and present, of course. Thank you to Ivan Spector and Chris Huber for showing me the intricacies of the laser and the 2D-IR set-up. Thank you to Brynna, Zahra, and Patrick for showing me the other nuances of the laser and the delightful conversations. I thank all of you for being able to handle my questions and helping me when I made a mistake. Without your guidance, I don't know where I would be today. Thank you to Theresa Leibig, my first undergraduate researcher. You taught me to become a great mentor and showed me what hard work truly was. Sometimes I think you taught me more than what I taught you. Thank you to Thorn Dramstad. I hope I was able to teach you some things about the laser, and I believe the future of the SFG side is in great hands. Even though we haven't known each other for long, I am glad to call you a great friend. Thank you to Grace Gretz. You an aspiring undergraduate who will go far. I am proud to have been your mentor, and I am excited to see where you go. Thank you to the newest member of the lab, Joel Patrow. Even though you haven't been here long, I have appreciated our talks and the helpful nuggets of information. And last but not least, thank you to Cynthia Pyles. The first graduate student I mentored and the member of the group I

have known the longest. I am so thankful you joined the lab and let me train you. You have been a wonderful lab mate and a great friend. You have been there for so many events, and I appreciate that. I can't wait to see what you will do in the future. But know this, even though I will be far and not the best communicator, you will always be one of my true best friends.

Last and not the least, thank you Dr. Aaron Massari. Without you coming to my poster on that fateful day at the 2009 ACS conference in Indianapolis and telling me about the University of Minnesota, I would not have gone here and experienced all the opportunities this institution has to offer. I appreciate that you kept pushing me and believing in me, so I could strive for my lofty goals. You are the best adviser, and I hope I can pay it forward one day.

Dedication

To my parents, Mark and Kim Olson.

Abstract

This thesis describes Fourier transform infrared (FTIR) and two-dimensional infrared (2D-IR) spectroscopy applied to small molecule silanes (trimethoxysilane and triphenylsilane) and polydimethylsiloxane (PDMS). 2D-IR spectroscopy gives information about the dynamics that the vibrational probe is sensitive to and the heterogeneous and homogeneous contributions to the linear FTIR lineshape. The vibrational probe used for all the studies in this thesis is the silicon hydride stretch due to being present in the small molecule silanes and in PDMS. The studies presented show how the silicon hydride mode was first characterized in small molecules to understand the probe more. Then, the probe was utilized in polymer systems to study more complex motions to make the connection between the ultrafast dynamics of polymers to the macroscopic properties.

The first study involved studying the solvation dynamics of two small molecule silanes in three neat solvents using FTIR and 2D-IR spectroscopies along with molecular dynamics simulations. The two different molecules exhibited different degrees of vibrational solvatochromism, and the differences was found to be a result of higher mode polarization with more electron withdrawing ligands using density functional theory calculations. The solvent dynamics were found to be dominated by their interactions with neighboring solvent molecules rather than with the solute.

Next, FTIR and 2D-IR spectroscopies were used to study PDMS cross-linked films and siloxane oligomers without solvent and swollen or dissolved in various solvents. There is an absence of vibrational solvatochromism in these systems, which was shown by 2D-IR spectroscopy to be due to the heterogeneity. The silicon hydride mode in the cross-linked, solvent-free PDMS film exhibited spectral diffusion, which must be due to the

polymer structural motions. However, once the solvent penetrates the network, the dynamics become a convolution of the solvent and polymer motions due to the motions being of similar timescale.

In the last study discussed, FTIR and 2D-IR spectroscopies were used to study the ultrafast structural dynamics of PDMS thin films with various physical and chemical changes done to the polymer, which included elevated curing temperature, increased cross-linker agent concentration, compression, and cooling near the glass transition temperature. The FTIR spectra were found to be relatively insensitive to all of these perturbations, which 2D-IR spectroscopy revealed was caused by the overwhelming heterogeneity. There is clearly a disconnect between the microscopic and macroscopic behavior in this polymer due to having only slight differences in the heterogeneous and homogeneous dynamics.

Table of Contents

List of Abbreviations

$AgGaS_2$	silver gallium sulfide
AM1	Austin model 1
CHARMM	Chemistry at HARvard Macromolecular Mechanics
CHELPG	charges from electrostatic potentials using a grid based method
$CHCl_3$	chloroform
CLS	center line slope
CW	continuous wave
DAF	dipole autocorrelation functions
DFT	density functional theory
FFCF	frequency-frequency correlation function
FID	free induction decay
FTIR	Fourier transform infrared
FWHM	full width at half maximum
IEFPCM	polarizable continuum model using the integral equation formalism variant
IPP	infrared pump probe
IR	infrared
IVR	intramolecular vibrational redistribution
LO	local oscillator
MCT	mercury cadmium telluride (HgCdTe) detector
MBH	mobile block Hessian
MD	molecular dynamics
MM	molecular mechanical
MW	molecular weight
NBO	natural bonding orbital
NMR	nuclear magnetic resonance

NPT	isothermal-isobaric
OAP	off-axis parabolic mirror
OPA	optical parametric amplifier
OKE	optical Kerr effect spectroscopy
PCM	polarizable continuum model
PDMS	polydimethylsiloxane
PO-DVR	potential-optimized discrete variable representation
PZA	piezo-electric actuator
QM	quantum mechanical
QM/MM	quantum mechanical and molecular mechanical
QVP	quantum-mechanical perturbation theory
QVP4	fourth order quantum-mechanical perturbation theory
SMD	Minnesota solvation model
SVD	singular value decomposition
TriMOS	trimethoxysilane
TriPS	triphenylsilane
VER	vibrational energy relaxation
VES	vibrational echo spectroscopy
VSE	vibrational stark effect
ZnSe	zinc selenide
2D-IR	two-dimensional infrared

List of Figures

List of Tables

Chapter 1. Introduction

1.1. Motivation

Understanding the interaction between solute and solvent is fundamental for science. Such interactions influence the properties of the solute particles. For example, the environment around a molecule in the condensed phase can affect the spectral position, intensity, and lineshapes of molecular vibrational absorption bands.[1] These are the long time averaged properties of the solute-solvent interactions found using linear infrared spectroscopy. This can also be said of polymer systems as well, which can be considered to be solvent-like. Polymers can be exposed to solvents, but the polymer matrix itself could be considered a more viscous solvent bath.

Molecules are not static, but are in fact continuously vibrating, rotating, and translating throughout the microscopic environment. These motions constitute the dynamics of the system, which are generally not captured with linear spectroscopy. The linear line width contains information about the dynamics, since the line width is a combination of inhomogeneous and homogeneous broadening phenomena. However, the convolution of inhomogeneous and homogeneous broadening means that the dynamic specific interactions beneath the linear lineshape are not discernable. These dynamics can be recovered through the use of nonlinear infrared spectroscopy, so the origins of spectral broadening can be determined. In combination with dynamics simulations, the measured dynamics will illuminate the specific interactions that are occurring in the condensed phase.

Two-dimensional infrared (2D-IR) spectroscopy has been a developing technique, since the first 2D-IR experiment was published in 1998.[2] Many 2D-IR studies have made use of the metal carbonyl vibrational mode, which gives a strong signal due to its strong transition dipole.[3-5] The silane vibrational mode, $\nu_{Si\text{-}H}$, has proven itself to be a promising

new avenue of study for 2D-IR spectroscopy, existing as it does in many contexts that are of interest to the materials community. Recently, there has been research on the sensitivity of the ν_{Si-H} to solvents in materials such as silica sol-gel glasses[6] and porous silica nanoparticles,[7] but this mode has not yet been extensively studied. Once this mode's sensitivity to solvents has been studied in simple systems, more complex systems where the silane is part of a cross-linked network can be studied more fruitfully. The silane vibrational mode is intrinsic to materials based on their synthesis, so there would be no altering of the material, an improvement over previous materials studies where a metal carbonyl was added.[8-10] The dynamics of the material in its natural form could be studied using the silane vibrational mode, which opens the door for a whole new class of systems to study with 2D-IR spectroscopy without altering the material.

In this work, 2D-IR spectroscopy was first used to investigate the effect of the local solvent environment on the dephasing dynamics of ν_{Si-H} in small molecule silanes to elucidate sensitivity of this vibrational mode to various solvents and to lay a foundation for future 2D-IR silane experiments. From there, polydimethylsiloxane became the research focus. The polymer was exposed to solvents first to have a better comparison to the small molecule silanes. Polymer swelling is a widely used metric to measure the amount of cross-linking in elastomer networks, so 2D-IR spectroscopy was used to probe the reliability of these measurements. The polymer was then altered to change its macroscopic properties to see if there is a connection from the microscopic structural dynamics and the macroscopic properties. This will help to further the understanding of the role of the ultrafast dynamics have on the macroscopic properties of polymers and to test the elasticity theories.

1.2. Solvation

Before going to the more complicated systems that are going to be studied, the small molecule must be fully understood. Solvation is the process of solvent molecules responding to the presence of solute molecules. More specifically, solvation is a microscopic molecular process by which the potential energy of a solute is minimized by favorable interactions with the solvent.[1] Solvation can have many system dependent effects on the solute molecules. An example of this is catalysis,[11-13] where the solvent can influence the rate, rate order, mechanism, and the products of reactions.[1,14-17] The energies of the initial and transition states of a reaction are also influenced by the solvent.[1] Charge transfer reactions are extremely sensitive to the type of solvent environment, since the charge transfer can be either facilitated or hindered depending on the polarity of the surrounding medium.[18]

The intermolecular interactions between the solute and solvent include nonspecific forces such as the electrostatic forces arising from Coulomb forces (i.e. dipole/dipole), polarization forces arising from induced dipole moments (i.e. dipole/nonpolar), as well as specific forces such as hydrogen-bonding.[19] Understanding solvation requires understanding the balance between the long- and short-range interactions for every molecule.[20] With only this brief discussion, the description of solvation has already become complex.

1.2.1. Static Solvent Effects

The solute spectroscopic observables, such as the position, intensity, and shape/width of a peak, can be influenced by the various solute-solvent interactions.[21-24]

This phenomenon is called solvatochromism.[19] The impact of the solvent on these observables has been well-documented for various spectroscopies.[1,19,25-26] The focus of this section will be the effect of the solvent on infrared (IR) absorption.

Fourier transform infrared (FTIR) spectroscopy can measure the frequency, peak width, and intensity of the absorption of IR light by a particular bond. The frequency is dictated by the type of bond, while the shift of the frequency (direction and magnitude) gives insight into the type of solvent interactions when the molecule is introduced to solvent. The peak width is related to the range of solvent interactions. The peak intensity is usually not affected much by the solvent, so it doesn't provide much information about the solvent interactions.[19,27] However, the peak intensity can provide information about the system when specific interactions are occurring with the vibrational mode, such as hydrogen bonding: the intensity of a vibrational stretch increases when involved in a hydrogen bond with the solvent.[28-29]

The solvent effects on the IR frequency depend strongly on the vibrational mode of interest. The direction of the peak shift can either be red (lower frequency, bathochromic) or blue (higher frequency, hypsochromic).[19] During the process of a mode's vibration, either the magnitude or the direction of the transition dipole will change or both. The solvent interacts with the molecule by affecting the potential of the vibration. For a single normal mode, the frequency shift of the mode, $\Delta\nu$, due to the presence of the solvent can be described by:

$$\Delta\nu \propto -\left[\left(\frac{\delta\theta}{\delta q}\right)^2 - \frac{1}{\mu}\frac{\delta^2\mu}{\delta q^2}\right]V \tag{1.1}$$

where V is the potential for a specific vibration from the solvent, μ is the magnitude of the transition dipole of the solute, θ is the angle between the solvent electric field and the transition dipole, and q is the normal internal coordinate of the bond. Inside the brackets in Eq. 1.1, the bond bending is described by $\left(\frac{\delta\theta}{\delta q}\right)^2$, while the bond stretch is described by $\frac{1}{\mu}\frac{\delta^2\mu}{\delta q^2}$. Assumptions made in Eq. 1.1 are that a time-independent local electric field is applied by the solvent to the solute and that the perturbing force is small compared to that of the vibrational mode of interest. If the solvation lowers the potential by stabilizing the energy levels, then V in Eq. 1.1 will be negative making the frequency shift positive before considering the type of vibration. Therefore, the sign of the shift will be dictated by the bond either bending or stretching. In the case of a stretching vibration, a red shift will occur due to the magnitude of the dipole changing but not the direction. In the case of a bending vibration, a blue shift will occur due to the direction of the dipole changing but not the magnitude.[27] The frequency shift has also been correlated to other solvent properties such as the acceptor number, acid dissociation constants, and hydrogen bond capabilities.[25-26] For example, hydrogen bonding tends to red shift stretching vibrations.[27-29] Another specific interaction that can occur is halogen bonding, where the halogen in the solvent interacts with the vibrational probe.[30-31] However, there may not always be a correlation between the frequency shift and one solvent parameter due to the various interactions available.

Solvation, in physical terms, is the interaction of the surrounding electric field with the solute. The solution can be considered as a collection of dipoles and point charges combining to form a net electric field. The net electric field due to the solvent

instantaneously interacts with the electric dipole of the vibrating bond, which influences the frequency of the vibrational mode. This phenomenon is referred to as the vibrational Stark effect (VSE), which can quantify the change in frequency, $\Delta\bar{\nu}$, as

$$hc\Delta\bar{\nu} = -\Delta\vec{\mu} \cdot \vec{F}_{\text{ext}} \tag{1.2}$$

where h is Planck's constant, c is the speed of light, $\Delta\vec{\mu}$ is the change in the dipole moment of the vibration, and $\vec{F}_{\text{ext}}$ is the applied field, which in this case is the solvent. $\Delta\bar{\nu}$ is in units of cm^{-1} and $\Delta\vec{\mu}$ can be expressed as debeyes or cm^{-1}/(MV/cm), which is the frequency shift per unit of applied field. VSE can show how sensitive or insensitive a probe is to the local electric fields [32-34]

Another effect of VSE is peak broadening due to the variety of chemical environments in solutions that will vibrate with different frequencies.[32-34] The peak width involves the variation in the number and type of chemical environments, so the peak width is solvent-sensitive. The peak becomes broader as more different chemical environments are introduced. Usually, the peak is wider when there are stronger solute-solvent interactions.[1] The usual trend is that the stronger the solute-solvent interactions involving the vibrational mode, the wider the peak. Both polar and nonpolar solvents have a wide variety of possible solute-solvent configurations. However, the polar solvents exert a stronger perturbation on the vibration due to the electric field produced by the dipole. This trend also holds true for specific interactions as well. For example, the stretching vibration for a hydrogen bond-donating species broadens significantly.[1,28-29,35]

1.2.2. Solvent Dynamics

Solvation is not a static process. In fact, solvation is a dynamic process that involves the solute and solvent molecules constantly moving, vibrating, and rotating. The net electric field of the solvent is continuously changing due to the constant motion in the system, which changes the interaction with the vibrational mode of interest. The solvent and solute molecules can have different motions, so the solvent dynamics are the time-dependent motions of solvent molecules independent of a solute molecule.

The peak width is affected by homogeneous broadening and inhomogeneous broadening. Homogeneous broadening is due to fast frequency fluctuations where all the molecules are affected the same way causing the peak shape to be Lorentzian. Inhomogeneous broadening is due to slower fluctuations where the molecules are affected differently causing the peak shape to be Gaussian. Therefore, the different solvents will have different effects on the different types of broadening.[36]

Static inhomogeneous broadening arises when the frequency fluctuations become so slow that they are considered static. The different chemical environments give different frequencies. However, the frequency fluctuations are not always very fast or very slow. They can also occur at the intermediate timescales, which complicates the peak shape further. These intermediate fluctuations are called spectral diffusion, which can be considered to be the timescales of diffusion of the homogeneous lineshapes between different frequencies.[36] Spectral diffusion will be discussed later (see Section 2.3.1), but what should be mentioned here is that spectral diffusion is very sensitive to the solvent.[37-38]

Solution dynamics have been studied through the use of theoretical modelling such as molecular dynamic simulations.[39-42] The different aspects of solvent dynamics can be measured experimentally using ultrafast spectroscopies such as Optical Kerr Effect spectroscopy,[43-45] transient absorption spectroscopy,[46-47] and vibrational echo spectroscopy (VES),[48-50] and 2D-IR spectroscopy, which is the focus of this thesis.

1.3. Polydimethylsiloxane Background

The main focus of this thesis is on elastomer polymer networks, more specifically polydimethylsiloxane (PDMS). PDMS is one of the simplest nonhydrocarbon polymers, with its structure shown in Figure 1.1. Figure 1.1 shows the Si-O-Si backbone where the R group can either be a methyl or a hydrogen. Therefore, the Si-H vibrational probe can be utilized for ultrafast spectroscopies as was done with the small molecule silanes. It should be noted that pure PDMS is when the R group is always a methyl group. PDMS was chosen not only due to the intrinsic vibrational probe, but also due to its unique properties and various applications. Siloxanes have a wide range of industrial applications such as adhesives, coatings, and encapsulants.[51-53] PDMS has a high degree of backbone flexibility due to having a low rotational energy of Si-O, large interatomic distance, and open Si-O-Si bond angle, allowing it to have a low glass transition temperature, T_g.[51,53-56] T_g is the transition of a polymer from a hard and brittle state into a viscous or rubbery state.[57] Other great properties of PDMS are being optically transparent in the UV-vis regions, easy fabrication, biocompatibility, thermal and oxidative stability, and low cost.[58-63] As mentioned earlier though, the form of PDMS I am interested in is its cross-linked elastomer form and not its singular chain form.

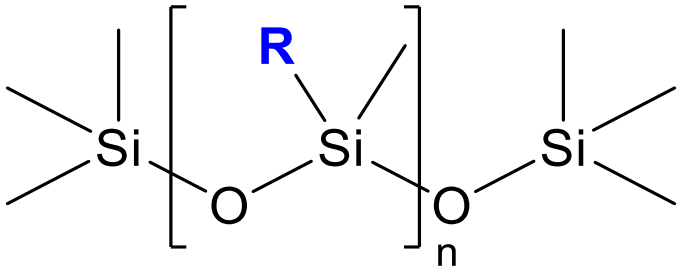

Figure 1.1. Structure of polydimethylsiloxane (PDMS) where the R can be either a methyl group or a hydrogen. The repeating unit of the polymer is the central unit.

1.3.1. Cross-Linking via Platinum-Catalyzed Hydrosilylation Reaction

To make an elastomer polymer network, the polymer chains are covalently linked together via cross-links.[64] The elastomer synthesis is simple and inexpensive,[58-60,65] and in this case a kit was used for ease of synthesis. A Sylgard® 184 silicon elastomer kit from Dow Corning was used to fabricate the cross-linked thin films. The kit consists of an elastomer base (Sylgard-184A) and a curing agent (Sylgard-184B).[66-68] The elastomer base contains >60 wt% dimethylvinyl-terminated poly(dimethylsiloxane) oligomers, 30-60 wt% dimethylvinylated and trimethylated silica, 1-5 wt% tetra(trimethoxysiloxy)silane, and a Pt-based catalyst. The curing agent contains 40-70 wt% poly(dimethyl, methylhydrogen siloxane), 15-40 wt% dimethylvinyl-terminated poly(dimethylsiloxane) oligomers, 10-30 wt% dimethylvinylated and trimethylated silica, and 1-5 wt% tetramethyl tetravinyl cyclotetrasiloxane.[60-62,69]

The silicon hydride bond is a polar, long, and weak bond that is very reactive and is used for the cross-linking reaction.[70] The reactive species will be considered the cross-linker. The curing agent contains the cross-linker, which is poly(dimethyl, methylhydrogen siloxane due to the silicon hydride as shown in Figure 1.1. The cross-linking reaction

proceeds via a platinum-catalyzed hydrosilylation reaction, which involves the addition of a Si-H bond to a vinyl group.[61,71]

The Chalk-Harrod mechanism is the most widely accepted mechanism for the platinum-catalyzed hydrosilylation reaction. Figure 1.2 shows the catalytic cycle for a generic platinum catalyst. The first step is the oxidative addition of the silicon hydride group containing molecule onto the platinum catalyst which activates the catalyst. The platinum center goes from an oxidative state of 0 to II. The vinyl group (or in this case, a simple ethylene) is coordinated onto the platinum complex.[72-73] Before moving on in the catalytic cycle, there are actually two versions of the mechanism: the original Chalk-Harrod mechanism[74] and the Modified Chalk-Harrod mechanism.[75-77] In the original mechanism, the ethylene inserts into the metal-hydride bond to generate an intermediate, which then undergoes reductive elimination to release the product with the newly formed Si-C bond.[72-74] In the modified mechanism, the ethylene inserts into the metal-silyl bond, which then undergoes reductive elimination to form the same Si-C bond. An example set of the hydrosilylation reactions with the Sylgard® 184 kit is shown in Figure 1.3. The groups utilized in the reactions are bolded in different colors to emphasize their locations. The silicon hydride groups are blue, the vinyl groups are red, and the newly formed bonds are red. One of the Si-H groups is purple at the end to show that the Si-H group could continue to react, or the reaction could stop there and have unreacted Si-H groups.

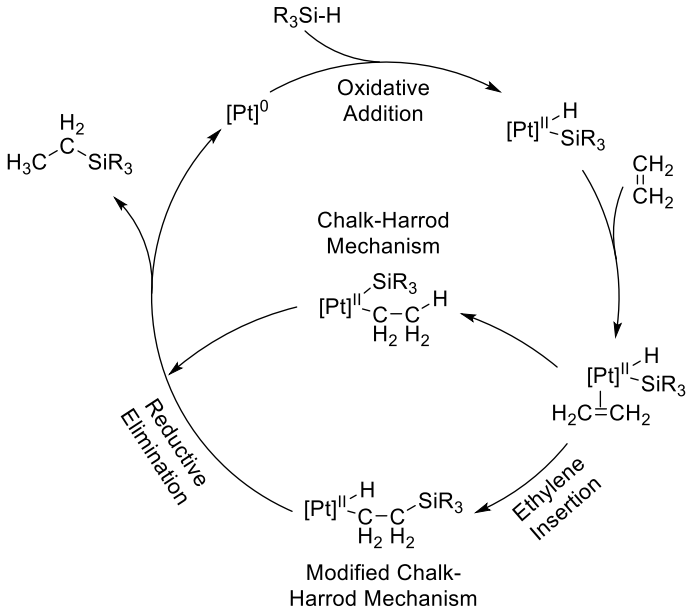

Figure 1.2. The catalytic cycle for the original Chuck-Harrod and Modified Chalk-Harrod Mechanisms for the platinum-catalyzed hydrosilylation reaction. Both mechanisms proceed similarly until the ethylene insertion step, but they both reach the desired product.

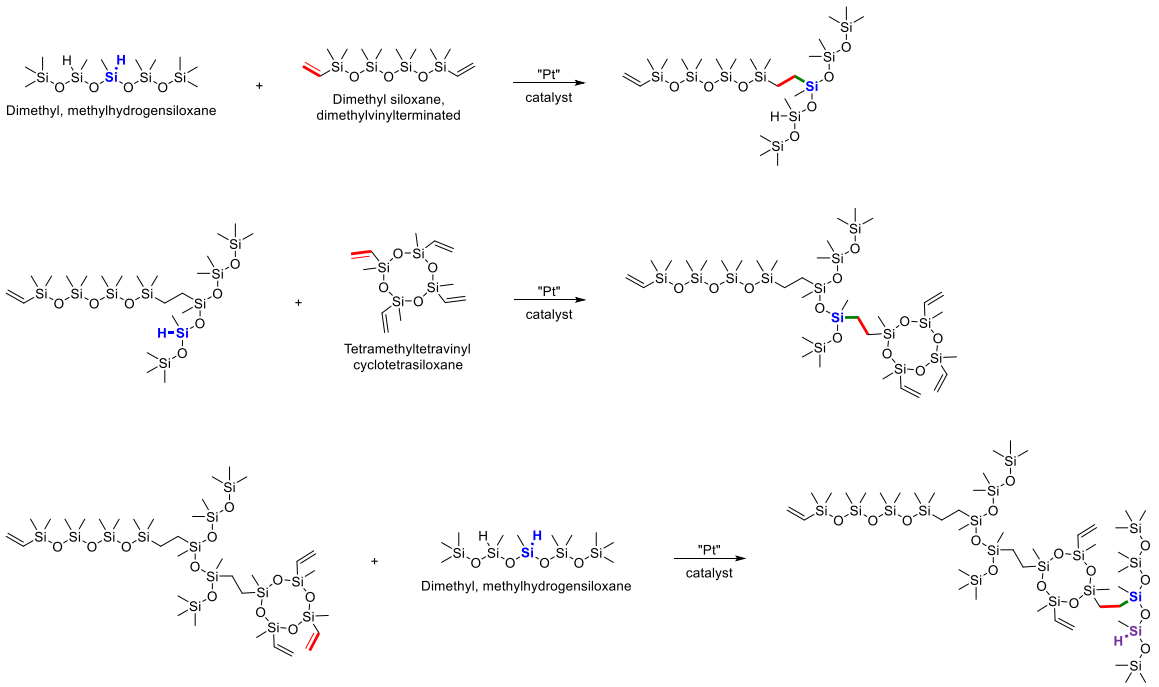

Figure 1.3. One set of reactions that could occur during the cross-linking process of PDMS. The product from the previous reaction becomes one of the reactants in the next reaction. The groups that are involved in that step in the reaction are bolded in different colors. The Si-H groups are blue, the vinyl groups are red, and the newly formed bonds are green. At the end, the Si-H group is shown as purple to show that it could keep reacting if there are still vinyl groups present.

The hydrosilylation reaction is not the only reaction that can occur during this process. Over a longer time, the residual vinyl and silicon hydrogen groups can further react. There is always a possibility that there are silanols when working with silicon, which could react with the silicon hydrogen bonds. The silicon hydrogen groups could also decompose. These secondary reactions are favored when an excess of Si-H groups over vinyl groups is used and mainly occur after the primary hydrosilylation reaction is completed.[52,72,78]

As mentioned earlier, multifunctional silicon vinyl polymers are used to make the three-dimensional elastomer networks. Pure PDMS elastomer networks usually exhibit poor mechanical properties, so these other components are added to make composite elastomers with more desirable properties for industrial applications.[79] Changing the polymer chain lengths and adding fillers helps promote the desirable mechanical properties of the elastomer. Adding different ratios of reactants and increasing the reaction temperature can also affect the mechanical properties as well.[61-63,80] Due to these tunable properties, PDMS has many key materials applications such as microfluidics,[81] coatings,[53] contact lens materials,[53] and much more. However, synthesizing elastomer films in this manner means there is a lack of understanding of the microscopic structure, which dictates many macroscopic properties.

1.4. Elasticity Theories

Elasticity is a unique property to some polymers, but especially elastomers. Elasticity is defined as recoverability of the polymer network from a deformation. To exhibit elasticity, the material must: be able to be stretched and regain its shape after the

deformation, be above its T_g to exhibit high local segment mobility, and contain cross-links to restrain some of the mobility (otherwise, the material would become a liquid). Due to these unique properties, a thermodynamic background of what is occurring when an elastomer is being stretched is needed.[82-83]

The first law of thermodynamics states the change in the internal energy of a system is the sum of all the energy changes: heat absorbed by the system and the work done on the system

$$\mathrm{d}U = \mathrm{d}q + \mathrm{d}w \tag{1.3}$$

where d represents change, U is the internal energy, q is the heat, and w is the work. The work component is usually written as $-p\mathrm{d}V$, where p is an external pressure and V is the volume. However, the elastomer network has another contribution to the work due to the stretching process, which is defined as the elastic work, w_E,

$$\mathrm{d}w_E = f\mathrm{d}L \tag{1.4}$$

where f is the retractive force and L is the length of the elastomer. The final substitution needed for Eq. 1.3 is given in the second law of thermodynamics where the change in entropy ($\mathrm{d}S$), associated with the isothermal, reversible absorption is

$$\mathrm{d}S = \frac{\mathrm{d}q}{T} \tag{1.5}$$

By substituting Eqs. 1.4 and 1.5 into Eq. 1.3, the following equation can be derived

$$\mathrm{d}U = T\mathrm{d}S - p\mathrm{d}V + f\mathrm{d}L \tag{1.6}$$

The Helmholtz free energy, F, is useful to use from here, since the system will be held at constant volume and temperature. The Helmholtz energy is defined as

$$F = U - TS \tag{1.7}$$

which can be written in differential form as

$$\mathrm{d}F = \mathrm{d}U - \mathrm{d}(TS) = \mathrm{d}U - T\mathrm{d}S - S\mathrm{d}T \tag{1.8}$$

Substituting Eq. 1.6 into Eq. 1.8, gives

$$\mathrm{d}F = -S\mathrm{d}T - p\mathrm{d}V + f\mathrm{d}L \tag{1.9}$$

Eq. 1.9 shows that the Helmholtz free energy is a thermodynamic state function of temperature, volume, and length, meaning $\mathrm{d}F$ can be written as a complete differential

$$\mathrm{d}F = \left(\frac{\partial F}{\partial T}\right)_{V,L} \mathrm{d}T + \left(\frac{\partial F}{\partial V}\right)_{T,L} \mathrm{d}V + \left(\frac{\partial F}{\partial L}\right)_{T,V} \mathrm{d}L \tag{1.10}$$

where the subscripts denote what is held constant with each partial derivative. Comparing Eqs. 1.9 and 1.10, the partial derivatives of the Helmholtz free energy can be defined

$$\left(\frac{\partial F}{\partial T}\right)_{V,L} = -S \tag{1.11}$$

$$\left(\frac{\partial F}{\partial V}\right)_{T,L} = -p \tag{1.12}$$

$$\left(\frac{\partial F}{\partial L}\right)_{T,V} = f \tag{1.13}$$

The second derivative of the Helmholtz free energy does not depend on the order of differentiation

$$\frac{\partial^2 F}{\partial T \partial L} = \frac{\partial^2 F}{\partial L \partial T} \tag{1.14}$$

So, using Eqs. 1.11 and 1.13, Eq. 1.14 can be rewritten as one of Maxwell's relations

$$-\left(\frac{\partial S}{\partial L}\right)_{T,V} = \left(\frac{\partial f}{\partial T}\right)_{V,L} \tag{1.15}$$

Using Eq. 1.13 with Eq. 1.7, the retractive force applied to stretch the elastomer becomes

$$f = \left(\frac{\partial F}{\partial L}\right)_{T,V} = \left[\frac{\partial (U - TS)}{\partial L}\right]_{T,V} = \left(\frac{\partial U}{\partial L}\right)_{T,V} - T\left(\frac{\partial S}{\partial L}\right)_{T,V} \tag{1.16}$$

There are two contributions to the retractive force: internal energy and entropy. The first term describes how the internal energy changes with the sample length, and the second

term describes how entropy of the system changes with the sample length but is multiplied by the absolute temperature. The second term in Eq. 1.16 can be rewritten using Eq. 1.15 to have the second term in terms of the retractive force instead

$$f = \left(\frac{\partial U}{\partial L}\right)_{T,V} + T\left(\frac{\partial f}{\partial T}\right)_{V,L} = f_E + f_S \tag{1.17}$$

The two contributions to the retractive force are the energetic contributions, f_E, and the entropic contributions, f_S. The definitions for f_E and f_S are

$$f_E = \left(\frac{\partial U}{\partial L}\right)_{T,V} \tag{1.18}$$

$$f_S = T\left(\frac{\partial f}{\partial T}\right)_{V,L} = -T\left(\frac{\partial S}{\partial L}\right)_{T,V} \tag{1.19}$$

An assumption is made that the network is 'ideal.' f_E has no contribution to the retractive force due to the entropic contribution being much more dominant. This holds mostly true, since it does not require too much energy to stretch the polymer, except at large stretching lengths. Therefore, the entropic contribution to the retractive force is more important than the energetic one. In Eq. 1.17, there is a temperature dependence on the retractive force, where there is an increase in the force with increasing temperature.[82-85]

1.4.1. Affine Network Model

The simplest model to describe the elasticity is the affine network model.[83,86-88] The microscopic deformation of the elastomer network is assumed to be proportional to the macroscopic deformation of the sample when the elastomer network is stretched. Hence, the deformation changes in an affine manner. There are many other assumptions made when using this model to describe the deformation. The cross-links in the network do not fluctuate due to being suppressed by the local intermolecular entanglements. The

strands and cross-links do not interact with each other, so the network is ideal in this case. An ideal polymer network is monodisperse, neglects both the excluded volume of chains and entanglement effects, homogeneous, and has no defects.[83,86-93]

Before any deformation of the sample, the unperturbed dimensions of the sample are defined as $L_{x,0}$, $L_{xy,0}$, and $L_{z,0}$. Factors (λ_x, λ_y, and λ_z) are applied to the original dimensions to obtain the new dimensions of the deformed network

$$L_x = \lambda_x L_{x,0} \tag{1.20}$$

$$L_y = \lambda_y L_{y,0} \tag{1.21}$$

$$L_z = \lambda_z L_{z,0} \tag{1.22}$$

Based on the assumptions described earlier, the elastic energy, ΔF_{el}, can be defined as

$$\Delta F_{el} = \frac{1}{2} vkT\left(\lambda_x^2 + \lambda_y^2 + \lambda_z^2 - 3\right) \tag{1.23}$$

where v is the number of freely-joined Gaussian chains, k is the Boltzmann constant, and T is the absolute temperature. The retractive force will be considered with deformation in one direction, the z direction. Eq. 1.13 is manipulated with these new variables to redefine f as

$$f = \left(\frac{\partial \Delta F_{el}}{\partial L}\right)_{T,V} = L_{z,0}^{-1}\left(\frac{\partial \Delta F_{el}}{\partial \lambda_z}\right)_{T,V} \tag{1.24}$$

where $\lambda = \lambda_z = L_z/L_{z,0}$ based on Eq. 1.22. The volume of the sample is constant during deformation, since the chemical identity of the sample does not change. Therefore, the x and y deformation components are defined as $\lambda_x = \lambda_y = \lambda^{-1/2}$. Inserting Eq. 1.23 into Eq. 1.24 results in[57,84,92-93]

$$f = \left(\frac{\upsilon kT}{L_{z,0}}\right)[\lambda - 1/\lambda^2] \tag{1.25}$$

To obtain a quantity that is measurable, both sides of Eq. 1.25 can be divided by the initial cross section area ($L_{x,0}L_{y,0}$) that is normal to the stretching direction to get the tensile stress

$$\sigma_t = \frac{f}{area} = \frac{\upsilon kT}{L_{x,0}L_{y,0}L_{z,0}}[\lambda - 1/\lambda^2] = \frac{\upsilon kT}{V}[\lambda - 1/\lambda^2] \tag{1.26}$$

where V is the original volume of the elastomer network. Young's Modulus, E, is related to the tensile stress as long as the strain is small

$$E = \lim_{\lambda \to 1} \frac{\partial \sigma_t}{\partial \lambda} = 3kT\frac{\upsilon}{V} = \frac{3\rho RT}{M_x} \tag{1.27}$$

where substitution occurred for υ/V in terms of the molecular weight between the cross-links, M_x, and ρ, which is the network density that has units of mass per unit volume. The other variable in Eq 1.27 is R, which is the universal gas constant.[57,84,92-93] The elastic modulus is one way to quantify the elasticity of the elastomer by measuring the resistance to deformation in one dimension.[94-95] Like was shown earlier in Section 1.4, the modulus again increases with temperature based on its entropic origins.

Eq. 1.27 is modified a bit further due to real networks. The term ρ/M_x can be defined into a quantity υ, which is the number of network strands per unit volume. The final definition of Young's modulus for the affine network model is

$$E = 3\upsilon RT \tag{1.28}$$

which can be seen is a simple equation to describe a complicated process. Eq. 1.28 also shows no contribution of the cross-links junctions due to the cross-links being static.[57,84,89,92-93,96-97]

1.4.2. Phantom Network Model

The phantom network model was then developed, since the cross-link should have the capability of movement.[83,98] However, many assumptions, some of which are the same as the affine network model, are made here as well. The cross-links in the polymer network should be able to fluctuate inside the polymer network around their mean positions due to thermal fluctuations. The fluctuations are also Gaussian in nature. The microscopic deformation of the mean positions of the cross-links is affine to the macroscopic deformation, while the fluctuations are independent of this strain. As with the affine network model, this model applies to ideal homogeneous networks.[83,89-93,98]

To start off, the fluctuations need to be defined in this model. The fluctuations of the mean-square end-to-end vector, $\langle(\Delta r)^2\rangle$, are defined as

$$\langle(\Delta r)^2\rangle = \frac{2}{\phi}\langle r^2\rangle_0 \tag{1.29}$$

where ϕ is the functionality (the number of chains originating from a cross-link junction) that is a value between 1 and 4. This is for a network with a tree-like topology. The fluctuations of a cross-link around its mean position, $\langle(\Delta R)^2\rangle$, are defined as

$$\langle(\Delta R)^2\rangle = \frac{(\phi-1)}{\phi(\phi-2)}\langle r^2\rangle_0 \tag{1.30}$$

A vector, $\boldsymbol{r}_{ij}$, between points i and j in the elastomer network can be defined by the instantaneous and time averaged fluctuations

$$\boldsymbol{r}_{ij} = \bar{\boldsymbol{r}}_{ij} + \boldsymbol{\Delta r}_{ij} \tag{1.31}$$

where $\Delta\boldsymbol{r}_{ij}$ is the instantaneous fluctuations of $\boldsymbol{r}_{ij}$ and $\bar{\boldsymbol{r}}_{ij}$ is the time average of those same fluctuations. If both sides of Eq. 1.31 are squared and the ensemble average is taken, the following equation is obtained

$$\langle r_{ij}^2 \rangle = \langle \bar{r}_{ij}^2 \rangle + \langle r_{ij}^2 \rangle \tag{1.32}$$

due to the instantaneous fluctuations and the mean values being uncorrelated. If points i and j are two ends of a polymer chain and by inserting Eq. 1.29 into Eq. 1.32, Eq. 1.32 can be simplified to

$$\langle \bar{r}^2 \rangle = \left(1 - \frac{2}{\phi}\right) \langle r^2 \rangle_0 \tag{1.33}$$

Based on the assumptions that the mean positions of the cross-links are proportional with the macroscopic strain and the fluctuations are strain independent, the factor, λ, for the deformation of the polymer network from Section 1.4.1 can be added to Eq. 1.31 to obtain

$$\boldsymbol{r}_{ij} = \boldsymbol{\lambda}\bar{\boldsymbol{r}}_{ij} + \Delta\boldsymbol{r}_{ij} \tag{1.34}$$

where

$$\langle \bar{r}^2 \rangle = \left[\left(1 - \frac{2}{\phi}\right)\frac{\lambda_x^2 + \lambda_y^2 + \lambda_z^2}{3} + \frac{2}{\phi}\right] \langle r^2 \rangle_0 \tag{1.35}$$

ΔF_{el} can then be defined for the phantom network model as

$$\Delta F_{el} = \frac{1}{2}\left(1 - \frac{2}{\phi}\right) \upsilon kT\left(\lambda_x^2 + \lambda_y^2 + \lambda_z^2 - 3\right) \tag{1.36}$$

which is similar to the affine network model except for the extra term, containing the functionality of the cross-links.[92-93,99]

Young's modulus for the phantom model network is

$$E = \frac{3\rho RT}{M_x}\left(1 - \frac{2}{\phi}\right) \tag{1.37}$$

where this can also be modified for real networks to become

$$E = 3(\upsilon - \mu)RT \tag{1.38}$$

where μ is the number of moles of junctions per unit volume of the network to account for the cross-links in the elastomer network. Eq. 1.38 shows that the phantom network model

modulus would be lower than the affine network model modulus due to allowing the cross-links to fluctuate. The fluctuation of the cross-links causes the network to become softer.[84,89,92-93,96-97]

1.4.3. Modeling Real Networks

The affine network model and the phantom network model are at the two extremes: no fluctuations to fully fluctuating. Previous experiments have shown that the elastic modulus is not well-modeled using these two extremes and needs to include other factors.[89,96,100] In real networks, there may be physical restrictions on the cross-links to cause less fluctuations. In response to this, many other models were developed to account for the many possibilities. However, only a few are going to be discussed, since there are a plethora of models trying to describe the elastic modulus.

To allow for partial fluctuations of the cross-links, Flory and Erman developed the constrained junction model.[101-103] This model assumes that the cross-links fluctuate like the phantom network model but can be hindered somewhat by the entanglements like the affine network model. In other terms, the elastomer acts more affine-like at small deformations and more phantom-like at larger deformations. Therefore, the modulus is found to be intermediate between the affine network and phantom network models. Dossin and Graessley[104] proposed the following equation to account for the intermediate behavior

$$E = 3(\upsilon - h\mu)RT \tag{1.39}$$

where h is an empirical parameter that can vary between 0 and 1. The affine network model limit is when $h = 0$, and the phantom network model limit is when $h = 1$.

In real networks, physical entanglements are most likely formed during the cross-linking process and become trapped, immobile. Therefore, Langley and Graessley[104-105] included a contribution from the entanglements as an additional term to the modulus

$$E = 3(\upsilon - h\mu)RT + 3E_eT_e \tag{1.40}$$

where E_e is the maximum contribution to the modulus due to the trapped entanglements and T_e is the fraction of trapped entanglements in the network. Eq. 1.40 is useful, since this allows for the separation of the contributions from the chain entanglements due to chemical cross-links and the permanently trapped physical entanglements. It can also be seen that the modulus could be higher than the phantom network model modulus based on the contribution from the trapped physical entanglements.

Due to the type of entanglements not being defined, the behavior of the entanglements is not considered. The slip-link model[106-107] modeled the entanglements as slip-links (rings) joining the polymer chains together to act as additional cross-links. The ring junction has the ability to slide with the loop size changing without the polymer chains detaching from one another. The elasticity changes based on the behavior of the entanglement and not just the quantity. DeGennes[108] also proposed that the linear chains should be free to "reptate", wriggle around in space, but the entanglements that are present must have restrictions on their movements. The differences in these movements causes the different properties of the elastomers.

This small description of some of the theories highlights the challenges to describing how polymer structure and cross-links contribute to the elastic modulus. Some believe that the entanglements affect the properties by restricting the fluctuations,[109] while others argue that they contribute more to the cross-link contribution by acting like pseudo-

cross-links.[110-112] However, heterogeneity of the polymer is not considered. The heterogeneity could also affect the elasticity of the polymer. Most models agree that the elastic modulus of an elastomer network is governed somewhat by the dynamics of the cross-links.[93,113] Polymer structural dynamics span many orders of magnitude in time from milliseconds[114-115] to picoseconds.[115-116] The faster motions that are available are the skeletal and lattice vibrations, which have typical periods of 0.1 ps to 1 ps.[115] The rotations of the internal segments like methyl group reorientations have been measured on the few-ps timescale.[113,117] The slower motions are the drifting of chains or slow changes in conformation. These motions occur on the timescale of 1 μs to 10 μs.[115] The focus of this work is to see if the ultrafast structural dynamics that polymers exhibit contribute to the macroscopic elasticity.

1.5. Elastomer Swelling

Another unique property of elastomers is the ability to swell in a solvent, instead of dissolving. Swelling is when the dimensions of the elastomer increase to allow the solvent to penetrate the polymer matrix. The swelling will continue until equilibrium is reached.[84,118-119] The expansion of the network equilibrates with the retractive forces imposed by the cross-links, which is driven by thermodynamics.[118,120-122] The free energy of mixing promotes expansion through the enthalpic contributions from solvent-polymer interactions that stabilize the extended chain conformations and the entropic contributions due to chain extension.[87,91,121,123] For the hydrophobic polymer PDMS, nonpolar solvents are the most favorable and contribute to the enthalpy of mixing through dispersion interactions.[124-126]

The theory of swelling is based on the elasticity as well due to the elastomer stretching in multiple dimensions during the swelling process. The simpler theories are based on the affine network and phantom network models. The Flory-Rehner expression for swelling for an affine network model is

$$\ln(1 - v_2) + v_2 + \chi v_2^2 = v_1 n \left[\frac{v_2}{2} - v_2^{1/3}\right] \tag{1.41}$$

and for the phantom network model is

$$\ln(1 - v_2) + v_2 + \chi v_2^2 = -v_1(n - \mu)v_2^{1/3} \tag{1.42}$$

where v_2 is the polymer volume fraction at equilibrium swelling, χ is the polymer-solvent interaction parameter, v_1 is the molar volume of the solvent, μ is the number of moles of junctions per unit volume of the network, and n is the number density of precursor chains that was used to prepare the network. These equations show a balance between the thermodynamic forces and the elastic forces. The left side shows the thermodynamic forces due to the solvent swelling of the polymer network, while the right side shows the elastic forces that are resisting the stretching of the network. The interaction parameter is dependent both on the solvent and the polymer. Eqs. 1.41 and 1.42 are used to obtain the interaction parameter, which depends both on the solvent and the polymer.[89,119] If the interaction parameter is known, Eq. 1.42 can be used to find the number of cross-links in the polymer system, since the amount of cross-links can be difficult to calculate in an elastomer network.[89,119]

Thermodynamics determine the average polymeric structures before and after swelling. However, the kinetics of reaching those states and many of their final properties are dictated by structural dynamics.[127] Polymer dynamics span many orders of magnitude

in time from milliseconds[114-115] to picoseconds.[115-116] Swelling requires the diffusion of the solvent through the polymer matrix, which is facilitated by local backbone and side chain motions of the elastomer network.[128-135] These same motions serve to increase the permeability of the polymer to other small molecules once the polymer is in its swollen state.[129,133] Therefore, it is important not to only characterize the average structure, but also the structural motions of the elastomer network along with the solvent penetrants.

The remainder of this thesis is organized as follows. Chapter 2 provides a comprehensive background on linear and nonlinear spectroscopy, which includes FTIR, 2D-IR, and infrared pump-probe spectroscopies. It also explains the data treatment and the extraction of the frequency-frequency correlation function to obtain information about the heterogeneous and homogeneous contributions to the linear lineshape. Chapter 3 presents a 2D-IR study on small molecule silanes in three solvents to explain the enhanced solvatochromism and spectral diffusion. Chapter 4 moves onto the studies of PDMS by starting with studying the influence of solvent swelling on the structural dynamics of the polymer by using 2D-IR spectroscopy. Chapter 5 presents a 2D-IR study of PDMS that undergoes physical and chemical changes to see if the structural dynamics contribute to the macroscopic properties.

Chapter 2. Linear and Nonlinear Infrared Spectroscopy

2.1. Macroscopic Polarization

To understand the information that can be gained from infrared (IR) spectroscopy, the quantum mechanical processes involved must be discussed. The first place to start is with ideal gas molecules possessing a vibrational mode oriented along the z-axis. The electric field of light, $\vec{E}(t)$, that interacts with the molecule is

$$\vec{E}(t) = \vec{E}'(t)\cos\left(\vec{k}\cdot\vec{r} - \omega t + \phi\right) \tag{2.1}$$

where t is time, $\vec{r}$ is the position vector, $\vec{k}$ is a wavevector that describes the direction of the light propagation, ω is the frequency of the light, ϕ is the phase, and $\vec{E}'(t)$ is the pulse envelope that is a vectorial property of the light. $\vec{E}'(t)$ is the parameter that includes the polarization of the light. For now, the electric field of a laser pulse will be considered simply as

$$E(t) = E'(t)\cos(\omega t) \tag{2.2}$$

where the light is polarized along the z-axis to match the orientation of the vibrational mode.[36,136-137]

The energy of interaction between the vibrational mode (the dipole of the molecule) and a laser pulse is

$$\widehat{W}(t) = -\hat{\mu}E(t) \tag{2.3}$$

where $\widehat{W}(t)$ is the operator for the interaction energy and $\hat{\mu}$ is the dipole operator. The hats above these variables identifies them as operators and future variables as well. The total Hamiltonian, $\widehat{H}$, then is

$$\widehat{H} = \widehat{H}_0 + \widehat{W}(t) \tag{2.4}$$

where $\widehat{H}_0$ is the Hamiltonian for the isolated molecule. Due to having time involved in the Hamiltonian, the time-dependent Schrödinger equation must be used to solve for the wave function, $|\Psi\rangle$, of the molecule.

$$i\hbar\frac{\partial}{\partial t}|\Psi\rangle = \widehat{H}|\Psi\rangle \tag{2.5}$$

In the absence of a laser pulse, $\widehat{H}_0$ is time-independent, so the solution becomes

$$|\Psi\rangle = \sum_n c_n e^{-\frac{iE_n t}{\hbar}}|n\rangle \tag{2.6}$$

where $|n\rangle$ is an eigenstate for the Hamiltonian, c_n is a weighting coefficient or population of state n, and E_n is the energy of state n. Once the laser pulse starts to interact with the molecule, the coefficients couple with the electric field and become time-dependent. The time-dependent coefficients can be solved by substituting Eq. 2.6 into Eq. 2.5 to obtain

$$\frac{\partial}{\partial t}c_m(t) = -\frac{i}{\hbar}\sum_n c_n(t)e^{\frac{-i(E_n E_m)t}{\hbar}}\langle m|\widehat{W}(t)|n\rangle \tag{2.7}$$

where m and n are the states of the system and E_m and E_n are the energies of states m and n, respectively. Eq. 2.7 can be altered slightly by using Eq. 2.3 to obtain

$$\frac{\partial}{\partial t}c_m(t) = \frac{i}{\hbar}\sum_n c_n(t)e^{-i\omega_{mn}t}\langle m|\hat{\mu}|n\rangle E(t) \tag{2.8}$$

where ω_{mn} is the frequency of the transition defined as $\omega_{mn} = (E_n - E_m)/\hbar$. The transition dipole moment can be found in Eq. 2.8 and is defined as $\langle m|\hat{\mu}|n\rangle$. The transition dipole is the change in the charge distribution of a molecule when it is vibrationally excited.[36,136-137]

The transition dipole moment can be further defined

$$\langle m|\hat{\mu}|n\rangle = \frac{d\mu}{dx}\langle m|\hat{x}|n\rangle \tag{2.9}$$

where x is the coordinate of the vibrating bond and $\frac{d\mu}{dx}$ is the change of the static dipole of the molecule as it changes, or the transition dipole strength. The transition dipole strength scales with the intensity of the corresponding IR peak. The term $\langle m|\hat{x}|n\rangle$ is what gives rise to the vibrational selection rules: $\Delta v = \pm 1$.[36,137]

After the laser pulse is done interacting with the system, the coefficient becomes time-independent again, which leaves the system in a superposition between states. For simplicity, a two-level system will be considered, where $|0\rangle$ and $|1\rangle$ represent the ground and first excited vibrational states, respectively. Defining $\omega_{mn} = \omega_{01} = (E_1 - E_0)/\hbar$, the two coupled equations obtained from Eq. 2.8 are

$$\frac{\partial}{\partial t} c_1(t) = \frac{i}{\hbar}\, c_0(t) e^{-i\omega_{01}t} \langle 1|\hat{\mu}|0\rangle E(t)$$

$$\frac{\partial}{\partial t} c_0(t) = \frac{i}{\hbar}\, c_1(t) e^{i\omega_{01}t} \langle 0|\hat{\mu}|1\rangle E(t). \tag{2.10}$$

The superposition between states $|0\rangle$ and $|1\rangle$ can be described as

$$|\Psi\rangle = c_0 e^{-\frac{iE_0 t}{\hbar}}|0\rangle + i c_1 e^{-\frac{iE_1 t}{\hbar}}|1\rangle \tag{2.11}$$

where c_n includes the transition dipole moment and other factors as seen from Eqs. 2.8 and 2.10. The time dependence in Eq. 2.11 is found in the term $\frac{iE_n t}{\hbar}$ for each state. The coefficients c_0 and c_1 are real, positive numbers and are no longer time-dependent due to the laser pulse not interacting with the system. There is an i for c_1 to determine the phase of the rotating wavefunction. However, $c_1 \ll c_0$, so $c_0 \approx 1$ meaning the imaginary part of c_0 can be ignored. The light created a coherent linear superposition of states, also denoted a wavepacket. The time evolution of the wavepacket in Eq. 2.11 can be described by a molecular response function, $R(t)$. For a single molecule, the molecular response function

is proportional to the electric field of the laser pulse interacting with the charges to make the molecule vibrate. Since there are many molecules in a real system, the pulse has created a non-equilibrium charge distribution in the sample that is referred to as the macroscopic polarization, $P(t)$, which evolves according to $R(t)$.[36,137]

The macroscopic polarization is the expectation value of the transition dipole, which is defined as

$$\begin{aligned} P(t) &= \langle\hat{\mu}\rangle = \langle\Psi|\hat{\mu}|\Psi\rangle \\ &= \left(c_0 e^{\frac{iE_0 t}{\hbar}}\langle 0| - ic_1 e^{\frac{iE_1 t}{\hbar}}\langle 1|\right)\hat{\mu}\left(c_0 e^{-\frac{iE_0 t}{\hbar}}|0\rangle + ic_1 e^{-\frac{iE_1 t}{\hbar}}|1\rangle\right) \\ &= c_0 c_1 \langle 0|\hat{\mu}|1\rangle \sin(\omega_{01} t) + c_0^2\langle 0|\hat{\mu}|0\rangle + c_1^2\langle 1|\hat{\mu}|1\rangle. \end{aligned} \tag{2.12}$$

This equation was further simplified due to $\langle 0|\hat{\mu}|0\rangle$ and $\langle 1|\hat{\mu}|1\rangle$ being related to the static dipoles of the ground or first excited states, respectively. The first term in Eq. 2.12 describes the time-dependent coherence (superposition of states) of the molecular response functions and the other two terms describe the static electric dipoles for the ground and first excited states. However, Eq. 2.12 assumes pure states, which are characterized by a single wavefunction. Real systems are imperfect which requires mixed states.[36,137]

To describe mixed states, the density matrix is needed. The density matrix, ρ, is defined as the outer product of the wavefunction and its conjugate.

$$\rho(t) = |\Psi\rangle\langle\Psi| \tag{2.13}$$

The elements of the density matrix, ρ_{nm}, can be obtained.

$$\rho(t) = \sum_{n,m} c_m^*(t) c_n(t) |n\rangle\langle m| = \sum_{n,m} \rho_{nm} |n\rangle\langle m| \tag{2.14}$$

Eq. 2.14 shows that the density matrix is a square matrix. The diagonal terms are when $n = m$ ($|c_n(t)|^2$), which describes the populations of the states. The off-diagonal terms

are when $n \neq m$ $(c_m(t)^* c_n(t))$, which describe the time-dependent coherences between the states due to containing a time-dependent factor, $e^{-i\omega_{nm}t}$. Some additional terms that can be added are the vibrational relaxation and dynamics. However, for simplicity, the additional terms are ignored.[36,137]

The macroscopic polarization was defined earlier as the expectation value of the transition dipole. With density matrix formalism, $P(t)$ becomes

$$P(t) = \langle\hat{\mu}\rangle = \sum_{n,m}\langle c_n c_m^*\rangle\mu_{nm} = \sum_{n,m}\rho_{nm}\mu_{mn} \tag{2.15}$$

where this expression is called the trace of $\rho\,\mu$. The expectation value of the transition dipole can be defined as

$$\langle\hat{\mu}\rangle \equiv \mathrm{Tr}(\hat{\mu}\rho(t)) \equiv \langle\hat{\mu}\rho(t)\rangle. \tag{2.16}$$

When light interacts with the system, the density matrix is multiplied by a transition dipole matrix, $\hat{\mu}$. The transition dipole matrix is made up of only off-diagonal terms to force the system to be either in a coherence state or a population state depending on the density matrix prior to the interaction with the laser pulse.[36,137]

2.2. Linear Infrared Spectroscopy

For linear IR spectroscopy, a few assumptions can be made. First, no nonlinear processes will occur, since the laser pulse that interacts with the system is weak. Second, only two vibrational levels (the ground state and the first excited state) need to be considered, since all the molecules are in their ground vibrational state before the interaction with the laser pulse. Therefore, the response function can be defined as

$$R^{(1)}(t_1) \propto i\langle\hat{\mu}(t_1)[\mu_0, \rho(-\infty)]\rangle \tag{2.17}$$

where $R^{(1)}(t_1)$ is the linear response function and $\rho(-\infty)$ is the equilibrium density matrix that does not evolve in time under the Hamiltonian used. The response function in Eq. 2.17 leaves some ambiguity in how density matrix interacts with the laser pulse. Therefore, double sided Feynman diagrams are used to pictorially represent the different combinations possible, where Figure 2.1 shows the double-sided diagram for the linear response.[36,137]

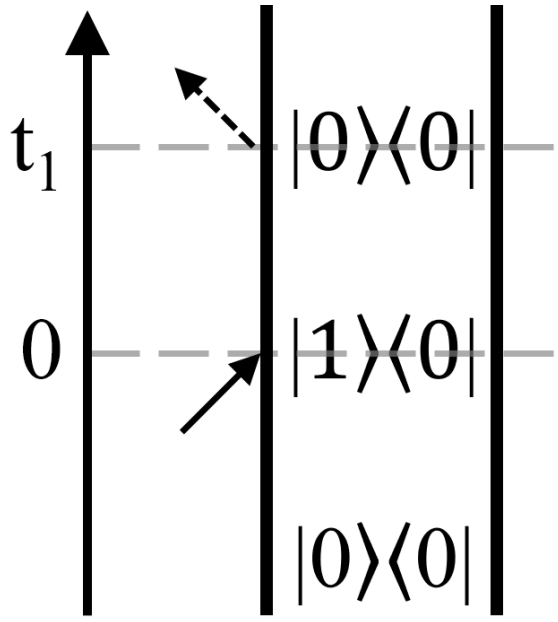

Figure 2.1. Double-sided Feynman diagram of the linear response.

Time begins at the bottom of a Feynman diagram and progresses upwards as indicated by the time axis on the left side of the diagram. The middle of the diagram represents a density matrix in the $|n\rangle\langle m|$ state. The left side represents the ket vector and the right side represents the bra vector. The molecule is in a population state when $n = m$, while the molecule is in a coherence state when $n \neq m$. The two vertical lines in each diagram represent the time evolution of the ket and the bra of the density matrix. The solid arrows represent wave vectors of incident light, while dashed arrows represent the emitted

signal. Arrows that point up and to the right represent positive wave vectors, which implies a positive frequency. This causes a transition to a higher energy state with a ket vector or a transition to a lower energy state with a bra vector. Arrows that point up and to the left represent negative wave vectors, which implies a negative frequency. This causes a transition to a lower energy state with a ket vector or a transition to a higher energy state with a bra vector. Stimulated absorption is shown with arrows that point towards the density matrix whereas stimulated emission is shown with arrows pointed away from the density matrix. Only a negative or a positive wavevector can interact, but not both when the rotating wave approximation is applied. The complex conjugate of the pathway shown in Figure 2.1 can also produce an appropriate signal. For simplicity, only the diagrams with the emitted signal proceeding from the ket will be shown.[36,137-138]

The linear molecular response function has been shown to be

$$R^{(1)}(t) = |\mu_{10}|^2 e^{-i\omega_{01}t} e^{-g(t)} \tag{2.18}$$

where μ_{10} is the transition dipole moment of the 0-1 vibrational transition, ω_{01} is the frequency of the 0-1 transition, and $g(t)$ is the lineshape function. The lineshape function is given by

$$g(t) = \int_0^t \int_0^{t_1} dt'' \, dt' \, \langle \delta\omega_{01}(t)\delta\omega_{01}(0)\rangle = \int_0^t \int_0^{t_1} dt'' \, dt' \, C_{FFCF}(t) \tag{2.19}$$

where $\delta\omega_{01}(t)$ is the frequency fluctuations in the time of the vibrational transition of interest, $\delta\omega_{01}(0)$ is the initial frequency of the vibrational transition, and $C_{FFCF}(t)$ is called the frequency-frequency correlation function (FFCF). The FFCF contains the dynamic information about the chemical system under study. The specifics of what the FFCF entails will be described later in Section 2.3.6. In brief, the FFCF describes the time dependency

of the frequency of a vibrational mode. The linear lineshape on its own will not reveal the dynamics but are hidden within the lineshape due to the FFCF.[36,137,139]

The emitted signal arising from the macroscopic polarization inherently has its phase shifted by 90º. The linear macroscopic polarization, $P^{(1)}(t)$, is a convolution of the incident electric field $E(t)$ with the linear molecular response function, $R^{(1)}(t)$. A system of interest is also not one molecule, but an ensemble of molecules. When there is a distribution of molecules with each having its own $R(t)$, the originally coherent oscillators will lose their phase relationship with one another over time resulting in a free induction decay (FID) of $P(t)$. In the case of solvent and structural dynamics, the dephasing (phase loss) of the molecular response functions is much larger when the intermolecular interactions are allowed to change over time.[36,137] Two-dimensional infrared (2D-IR) spectroscopy provides insight regarding these dephasing processes.

2.3. Two-Dimensional Infrared Spectroscopy

One of the first techniques that used infrared light to investigate the ultrafast dynamics was vibrational echo spectroscopy (VES).[48-49] To explore the dynamics even further, 2D-IR spectroscopy was developed from VES. The first 2D-IR experiment was performed by Hamm, Lim, and Hochstrasser in 1998 where protein dynamics were measured by observing the amide vibrational modes.[2] 2D-IR spectroscopy has expanded since then by exploring organic semiconductor thin films,[8-10] catalysis,[12-13,140-141] ionic liquids,[142] and studying the solvent dynamics with different vibrational modes.[5,13,37,141]

2.3.1. Environmental Dynamics

The molecular environment is dynamic. All the molecules in a system constantly move, vibrate, and rotate at room temperature. This constant motion means that the net electric field of the environment is continuously changing, which then changes the interaction with the vibrational oscillator. The environmental dynamics are composed of solvent and structural dynamics that are time-dependent motions.

Fourier transform infrared (FTIR) spectroscopy is a common linear spectroscopy technique for studying chemical systems. Typically, only the average peak frequency is reported. However, there is much more information contained in the spectral lineshape that is lost to linear spectroscopy. A normal FTIR spectrum is approximated as a Gaussian peak, but there are many components that make-up the linear lineshape as shown in Figure 2.2.

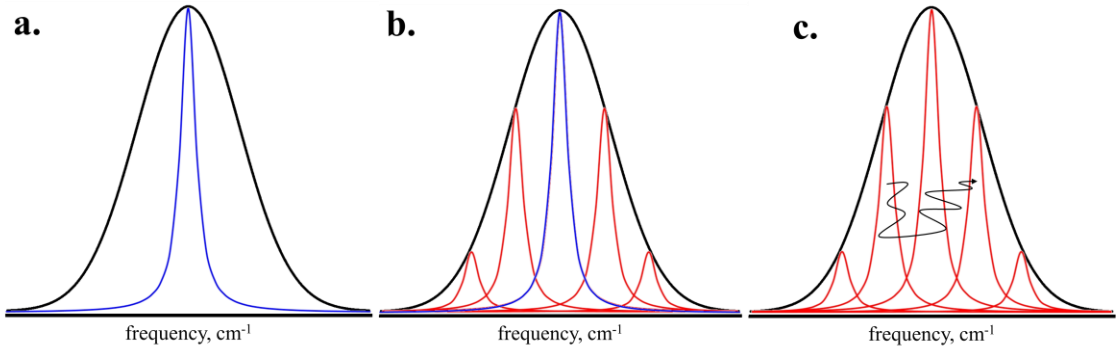

Figure 2.2. Illustrations of a) homogeneous broadening, b) static inhomogeneous broadening, and c) spectral diffusion. The black curve represents the total lineshape which is predominantly Gaussian. The blue curve represents the Lorentzian lineshape and the homogeneous component. The red curves also represent the homogeneous component, but each one of the curves represents a subensemble of oscillators that give rise to a certain frequency.

The lineshape is affected by the homogeneous and inhomogeneous broadening of the system. Homogeneous broadening is due to fast frequency fluctuations, and all the

vibrating oscillators are affected the same way. This causes the same way causing the lineshape to be Lorentzian as shown in Figure 2.2a with the blue curve. Inhomogeneous broadening is due to slower, random fluctuations, which affect each oscillator differently and causes the lineshape to be Gaussian as shown as the black curve in Figure 2.2a-c. Therefore, depending on the environment of the system, the homogeneous and inhomogeneous contributions will be different.[36,141]

In IR spectroscopy, homogeneous broadening is composed of three processes: vibrational relaxation, orientational relaxation, and phase relaxation. All of these processes contribute to the dephasing time of the system, which is related to the homogeneous linewidth (Γ).

$$\Gamma = \frac{1}{\pi T_2} = \frac{1}{\pi T_2^*} + \frac{1}{2\pi T_1} + \frac{1}{3\pi T_{or}} \tag{2.20}$$

where T_2 is the total dephasing time, T_1 is the vibrational lifetime associated with the vibrational relaxation, T_2^* is the pure phasing time associated with the phase relaxation, and T_{or} is the reorientation time associated with the orientational relaxation. Homogeneous broadening arises from the fact that the oscillators can interact with their surroundings which can affect each of these processes in different ways, so it becomes system dependent.[36,138]

The dephasing time represents the time for the phase relationship between the different oscillators in the ensemble to be lost. A classical description of dephasing will be helpful to visualize this concept. Start with an ensemble of oscillators in which all the vibrations start with the same phase. In the absence of external interactions, the vibrations will remain in phase with each other forever. In real systems, the surroundings (the solvent or other oscillators) can perturb each oscillator in the ensemble differently. The vibrations

will lose their phase relationship with each other due to the perturbations. The time for this loss is quantified as T_2. Vibrational dephasing of the system can help to discern the interactions between the oscillator and the environment.[138]

The pure dephasing time is the time it takes for the oscillators that comprise the macroscopic polarization to lose their phase relationship without the loss of vibrational excitation. Pure dephasing arises from fast intramolecular dynamics and intermolecular interactions that cause random, fast fluctuations in the vibrational frequency of the mode. These interactions are generally the low-frequency modes of the system of interest.[143] In liquids, the pure dephasing time is the fastest process, meaning the majority of the homogeneous linewidth is due to the pure dephasing according to Eq. 2.20.[144] The environment may not have much of an effect if the primary method of relaxation is intramolecular dynamics versus intermolecular interactions.[145]

The vibrational lifetime, T_1, is the time it takes for the energy of the vibrational excitation to relax into the surroundings, including the molecular environment and other portions of the same molecule. One possible relaxation pathway is intramolecular vibrational redistribution (IVR), where the energy moves to other modes on the same molecule.[146] The energy can be transferred back to the original mode depending on the energy levels of the other modes in the molecule. In such a case, there is a large IVR contribution to the peak width due to the process occurring quite rapidly.[3,146] The environment can influence IVR by changing the relative positions of the vibrational probe's vibrational energy levels. IVR can be hindered by intermolecular interactions as shown by King and colleagues.[3] If there are no other intramolecular vibrational modes close in energy to the excited vibrational mode but vibrational modes in the molecular

environment are available and similar in energy, the system undergoes intermolecular vibrational energy relaxation (VER), where the energy can be transferred to the environment modes through strong intermolecular interactions or collision between the environment and probe molecules. This is usually significantly slower than IVR.[147]

The reorientation time is the timescale of rotations available to the molecule of interest. The orientational relaxation can be strongly affected by the environment depending on the size of the probe to the environment molecular environment. A smaller probe will have a faster T_{or} due to the freedom to rotate freely with the amount of space available.[27] A larger molecule, such as a polymer, will have a slower orientational relaxation, since the molecule will lack the space to rotate freely. The reorientation time, in instances with larger molecules, will not contribute much to the line width and can be ignored.[3,148] The viscosity of the environment can also have an influence on the rotation of the molecules, where a high viscosity leads to slower orientational relaxation.[148-150] Usually, the reorientation time has little contribution to the peak width, since the solute molecules usually take much longer to reorient themselves than other processes.[148]

However, the oscillators can experience different environments causing a shift in the peak frequency via the Vibrational Stark Effect (VSE) as discussed in Section 1.2.1.[32-34] Every oscillator can experience a different environment, but oscillators with similar environments are grouped into a subensemble with an associated frequency and homogeneous lineshape. If the oscillators are unable to move, the distribution of the subensembles is the static inhomogeneous broadening as shown in Figure 2.2b. The combination of the subensembles becomes the overall Gaussian lineshape. However, in many condensed phase systems, the oscillators and the environment are constantly moving

around and are not frozen in a specific configuration over time. Due to fluctuations in the system, the oscillators can experience different frequencies over time as shown in Figure 2.2c. Spectral diffusion is the time-dependent vibrational frequency due to the molecular fluctuations. The FTIR peak width reflects the range of the chemical environments around the oscillator as well as the spectral diffusion and homogeneous broadening.[13,36,141]

The ability to distinguish between the different sources of broadening is beyond the scope of FTIR spectroscopy and IR pump-probe spectroscopy. For instance, FTIR spectroscopy is not able to distinguish between a system with a broad homogeneous linewidth and a small inhomogeneity versus a system with a narrow homogeneous linewidth and a large inhomogeneity. Both FTIR peak widths could have the same lineshape. A sample that experienced a large amount of spectral diffusion appears the same as one with a huge static inhomogeneity in an FTIR spectrum. Overall, the dynamics of a particular environment (homogeneous broadening) are indistinguishable from those arising from changes in environments (spectral diffusion) or even from a static distribution of environments (static inhomogeneous broadening). In order to obtain the information about the underlying processes that constitute the total peak width, a nonlinear technique must be used. 2D-IR spectroscopy will be able to expand on the information provided by FTIR spectroscopy by determining the dynamics of the system, which leads to an increased understanding of the interactions between a vibrating mode and its surroundings.

2.3.2. Theory

Once the laser pulses increase in power (like with ultrafast laser systems), nonlinear processes can occur. The macroscopic polarization is then often fit to a Taylor series expansion

$$P = P^{(1)}(E) + P^{(2)}(E^2) + P^{(3)}(E^3) \tag{2.21}$$

where $P^{(n)}$ is the n^{th} order polarization and is a function of E, which is the electric field of the laser pulse, raised to the n^{th} power to show the number of electric fields interacting with the system. The macroscopic polarization is a n+1 level tensor. The vibrational echo signal, which is the signal of interest for 2D-IR spectroscopy, comes from the third-order polarization, $P^{(3)}$, which involves interaction with three laser pulses. The echo signal is often described as a four-wave mixing process due to having four waves involved: the emitted field as well as three incident laser pulses. Since there are three pulses, the timing between the pulses needs to be defined: t_1 is the time between the first and second pulses, t_2 is the time between the second and third pulses, and t_3 is the time between the third pulse and the emission of the echo signal.[36] The timing of these pulses can be seen visually in Figure 2.3.

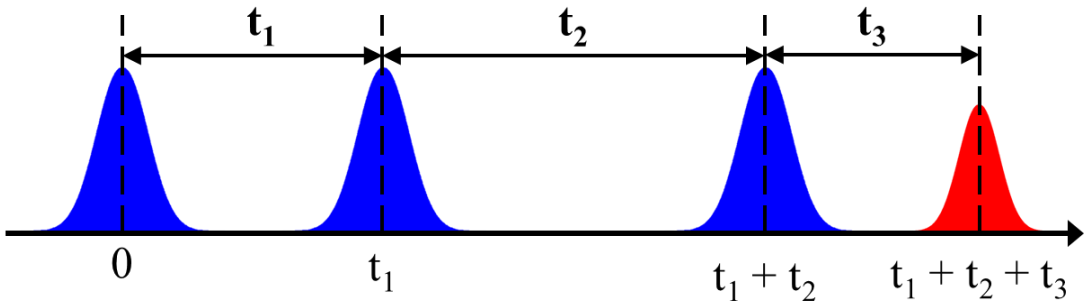

Figure 2.3. The visual representation of the labeling of the timing between the pulses along with the time at which the pulses interact with the system. The blue Gaussians represent the pulses that interact with the sample and the red Gaussian represents the echo signal that is emitted.

Initially (before any laser pulse interacts with the system), the system is in a population state. A population state is indicated by having non-zero terms only along the diagonal in the density matrix, which represents a system with populations of both the ground and first excited states. However, an assumption will be made that the system starts in the ground state. The first laser pulse, at t = 0, puts the system into a coherent state, which is indicated by having non-zero terms in both the diagonal and off-diagonal in the density matrix. The coherent state is the superposition of the v = 0 (ground vibrational state) and v = 1 (first excited vibrational state) energy levels. Therefore, the first pulse causes the molecules to "oscillate" in phase at their initial frequencies, which can be described as labeling the oscillators with their initial frequencies. The time elapsed between the first and second pulse is denoted the first coherence period, t_1. During this period, the oscillators undergo free induction decay (FID) due to dephasing of the macroscopic polarization. The dephasing will occur more rapidly if there is inhomogeneous broadening occurring.[36,137]

The second laser pulse, at $t = t_1$, causes a population state. Upon the interaction with the second pulse, the system has two possible pathways: (1) stimulated absorption to the

first excited state or (2) stimulated emission to the ground state. Either pathway results in the system no longer oscillating in a superposition, so not a coherence. Hence, the time between the second and third pulse is considered the population period, t_2. Due to no longer being in a coherence state, the only dephasing mechanisms allowed during this period are population relaxation (vibrational lifetime) and spectral diffusion. Spectral diffusion is the process where the oscillators evolve to different frequencies due to experiencing the different configurations of the system during a population period.[36,137]

The final interaction occurs at $t = t_1 + t_2$, which pushes the system back into a coherence state. The time between the third pulse and echo is considered the final coherence period, t_3. For a two-level system, there are two coherent states of interest. If the coherent state is the same as the original coherent state, then the FID continues until all the phase relationships are lost. If the coherent state is the phase conjugate of the original coherent state, the dephasing that occurred in the first coherent state is reversed. The various coherent states will evolve in the "opposite direction," rebuilding the phase relationship lost due to the inhomogeneity, and then proceeding to lose them by FID. Thus, this pathway is called the rephasing pathway due to rebuilding the phase relationships, while the earlier pathway is called the non-rephasing pathway due to the continued loss of the phase relationships.[36,137]

At $t = t_1 + t_2 + t_3$, the system emits an electric field, which is referred to as the vibrational echo signal. The interaction of the three incoming electric fields and the emitted echo signal can be defined by the third order response function, $R^{(3)}(t_3, t_2, t_1)$,

$$R^{(3)}(t_3, t_2, t_1) \propto i \langle \hat{\mu}(t_3) \left[\hat{\mu}(t_2) \left[\hat{\mu}(t_1) [\mu_0, \rho(-\infty)] \right] \right] \rangle \tag{2.22}$$

Again, double-sided Feynman diagrams will be useful to show how the laser pulses are interacting with the system. There are six different response function pathway diagrams that emit in the direction of interest as shown in Figure 2.4. The interpretation of the Feynman diagrams can be found in Section 2.2. Each diagram represents a unique sequence of light interactions and has a unique third order molecular response functions represented as R_n. The explicit expressions for each R_n will not be shown or discussed here, but can be found in various references.[36,137-138]

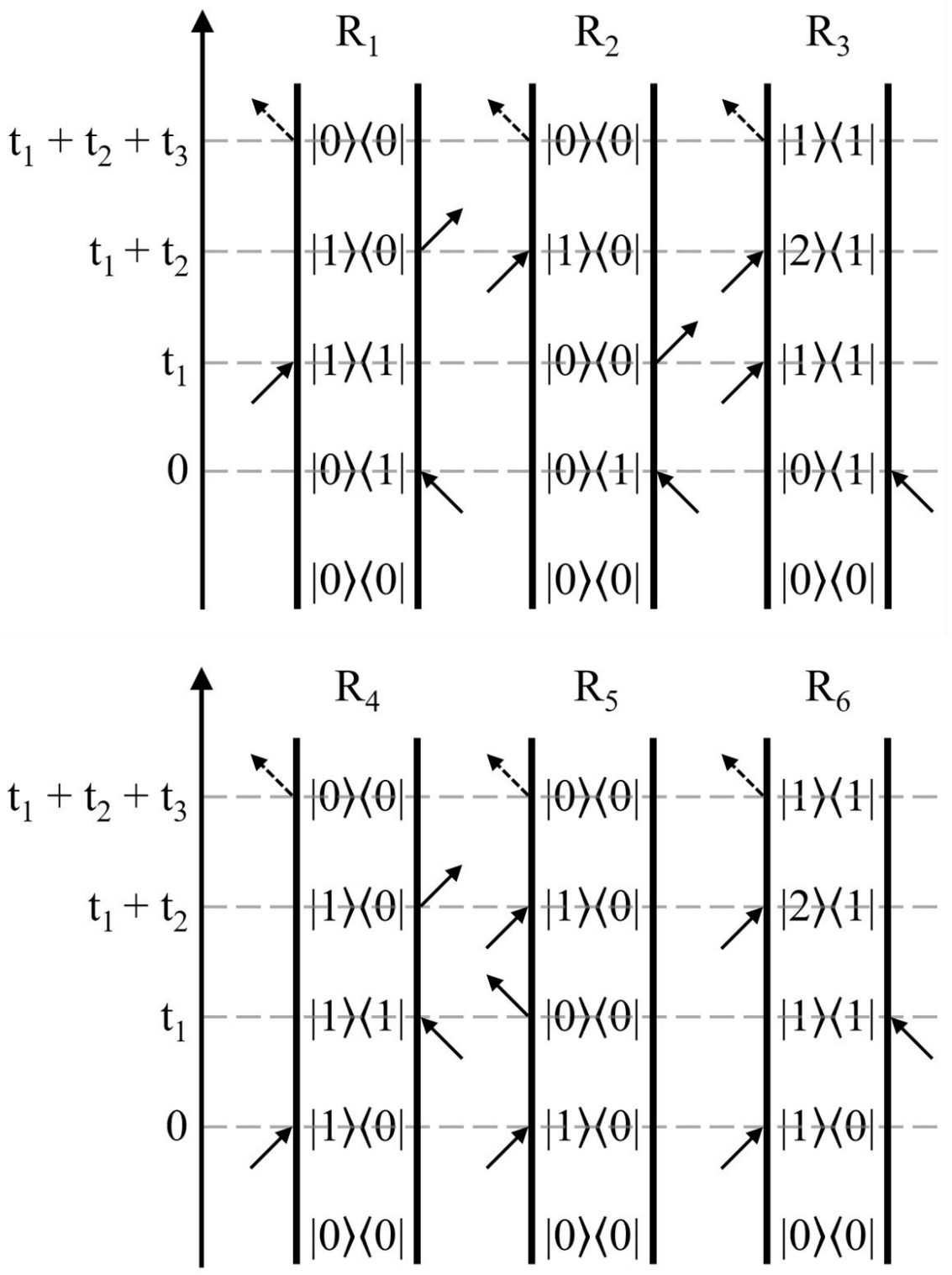

Figure 2.4. Double-sided Feynman diagram for producing echo signal. Each diagram represents a different response function pathway labeled R_1-R_6, where R_1-R_3 are the rephasing pathways and R_4-R_6 are the non-rephasing pathways.

The Feynman diagrams in Figure 2.4 are organized by the sequence of positive and negative incident wavevectors. The rephasing pathways, R_1 – R_3, use the ordering of negative, positive, and positive wavevectors. On the other hand, the non-rephasing pathways, R_4 – R_6, use the ordering of positive, negative, and positive wave vectors. The sign of the response function associated with a particular pathway is dictated by the type of interactions with the wavevectors. For a more realistic three level system, the system can be excited into a coherence between the first and the second excited states as seen in R_3 and R_6. It should be noted that the Feynman diagrams illustrate the possible response function pathways that lead to the rephasing or non-rephasing of the macroscopic polarization but not of the molecular response functions.[36,137-138]

To understand the Feynman diagram more, the R_1 pathway will be described. The system starts in the ground state, $|0\rangle\langle 0|$. The first pulse at $t = 0$ puts the system into a coherence state of $|0\rangle\langle 1|$ from the ground state via stimulated absorption. This occurs due to an interaction with a negative wavevector on the bra of the ground state. The second pulse at $t = t_1$ puts the system into a population state of $|1\rangle\langle 1|$ via stimulated absorption with an interaction with a positive wavevector on the ket of the previous state. The third pulse at $t = t_1 + t_2$ puts the system into a second coherence state of $|1\rangle\langle 0|$ via stimulated emission with an interaction with a positive wavevector on the bra of the previous state. Finally, the echo emits at $t = t_1 + t_2 + t_3$ via stimulated emission to put the system back into its ground state. Based on this description, the 0-1 vibrational transition (via stimulated emission or ground state bleach) is described by R_1, R_2, R_4, and R_5; while the 1-2 vibrational transition (via excited state absorption) is described by R_3 and R_6.[36,137-138] 2D-IR spectroscopy does not directly measure the various response functions. The objective

of 2D-IR spectroscopy is to measure the macroscopic polarization and extract the molecular response function to find the underlying dynamics of the system.

2.3.3. Experimental Setup

A 4 W continuous wave (CW) neodymium vanadate laser (Spectra-Physics, Millenia), which is frequency doubled to 532 nm, pumps a titanium sapphire (Ti:Sapph) crystal inside a prebuilt oscillator (KMLabs, Model MTS). A mode-locked seed pulse is generated centered at 800 nm with a FWHM of ~50 nm and pulse duration of ~25 fs at a repetition rate of 93 MHz.[8,13] The seed pulse is aligned into a regeneratively amplified Ti:Sapph crystal (Spectra-Physics, Spitfire-Pro). The pulse is stretched in time by diffraction gratings before entering the amplifier cavity to prevent damage to the optics. Inside the cavity, the 800 nm seed pulse is overlapped in a Ti:Sapph crystal with 8 W of 527 nm pulsed light from a diode-pumped, intracavity doubled, Q-switched neodymium yttrium lithium fluoride (Nd:YLF) pump laser (Spectra-Physics, Empower). Within the cavity, the pulse injection and release are controlled by two transiently birefringent Pockels cells. Once the buildup occurs in the cavity, a 1.6 W, 800 nm pulse is generated. After compression, the new generated pulses have a temporal width of ~40 fs centered around 800 nm with a full width at half maximum (FWHM) of 30 nm and at a repetition rate of 1 kHz. The output power is 1.1 W, which was split between the two experiments, where the 2D-IR experiment receives ~51% of the total power.[8,13]

The 560 mW beam is sent into an optical parametric amplifier (OPA, Spectra-Physics, OPA-800C), where it is immediately split into three different beams. Approximately 96% of the energy is transmitted and used for pumping the OPA. The

remaining 4% of the energy is reflected by a beam splitter to produce a white light continuum using a sapphire crystal that provides the seed pulse for the OPA. The white light is then directed towards a 3 mm thick β-barium borate (BBO) crystal. The major portion of the beam from earlier is split into two pump beams. About 15% of the beam is used to pump the pre-amplification stage, while the remainder of the beam is used to pump the power amplifier stage. Through the first pass of the white light through the BBO crystal, the pre-amplifier beam is temporally and spatially overlapped with the white light to generate the signal and idler beams. The signal and idler beams pass through a dichroic mirror, which allows only the amplified idler beam to transmit. The power amplifier pump beam is then overlapped temporally and spatially with the returning idler beam in the BBO crystal for the final amplification. The generated near IR signal and idler beams are then difference frequency mixed in a silver gallium sulfide crystal ($AgGaS_2$, 0.5 mm thick). The mid-IR pulses generated have a pulse duration of about 90 fs with a bandwidth of 200 cm^{-1}. The frequency of the mid-IR light can be tuned to the resonant vibration of interest (the probe) by changing the angles of the BBO and $AgGaS_2$ crystals. After the generation of the mid-IR light, the light is collimated and sent to the 2D-IR setup.[8,13]

The 2D-IR experiment setup is shown in Figure 2.5. The collimated near-IR light is sent into three zinc selenide (ZnSe) beam splitters producing three near-equal in power beams (A, B, and C) and a significantly weaker local oscillator (LO, approximately 0.01% of incoming beam) as shown in Figure 2.5. The pulses for each beam are temporally separated using four delay stages labeled as A, B, C, and LO. Beams C and LO both use delay stage C, which has a piezo-electric actuator (PZA) attached to the stage.[8,13,151]

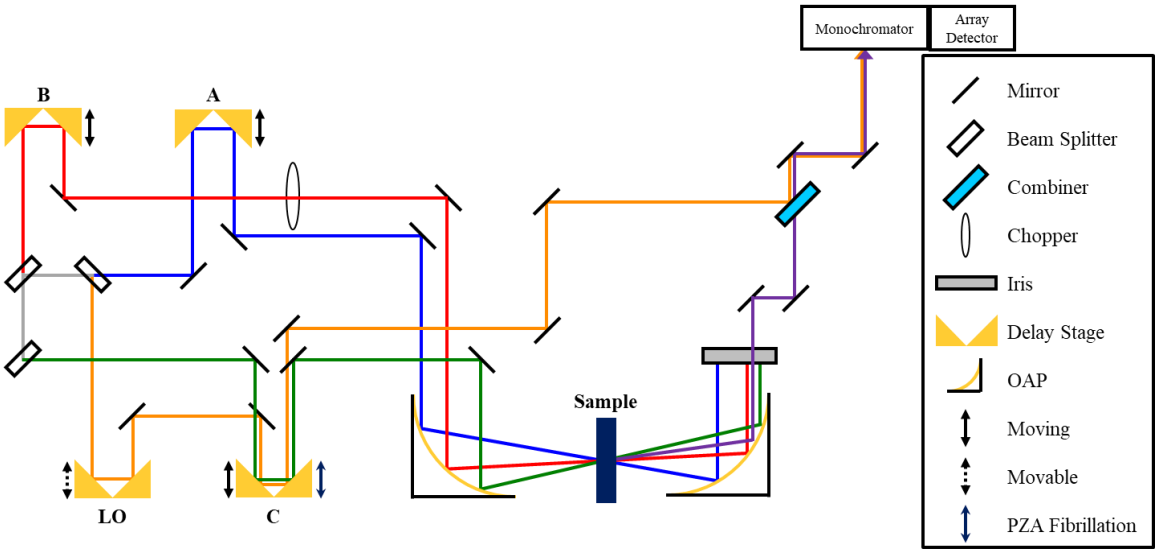

Figure 2.5. 2D-IR experimental setup showing the beams baths as labeled on the delay stages. Near-IR beam from OPA is grey, Beam A is red, Beam B is blue, Beam C is green, the LO is orange, the generated vibrational echo is purple. The sample (represented as a dark blue rectangle) is located between the two off-axis parabolic (OAP) mirrors. The legend on the right of the figure shows what each of the shapes represents in the experimental setup.

Delay stages A, B, and C move during an experiment, while the LO delay stage remains stationary during data collection but can be moved for timing. Previously discussed in Section 2.3.2, the timing between the pulses are labeled as t_1, t_2, and t_3 as shown in Figure 2.3. A new timing convention shall be used where the timing between the first and second pulses, t_1, will be referred to as τ, and the timing between the second and third pulses, t_2, will be referred to as the waiting time, T_w. The timing between the third pulse and the emitted echo will still be labelled as t_3. The new timing scheme is shown in Figure 2.6 with the pulses labeled as A, B, and C to correspond to the delay stages shown in Figure 2.5.[8,13,151]

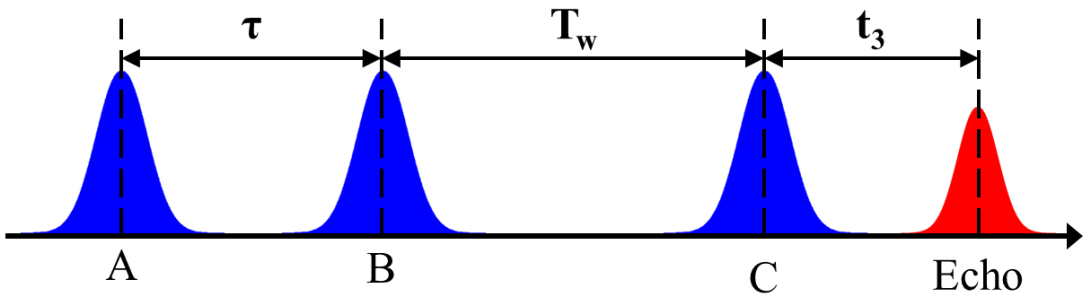

Figure 2.6. The labeling of the time between pulses for a 2D-IR experiment with the pulses labeled as A, B, C, and Echo.

Beam B is chopped at 500 Hz to allow the chopped signal to be divided by the laser spectrum to account for laser power differences across the range of frequencies examined, which will be shown later.[8,13,151] Beams A-C are crossed and focused in a BOXCARS geometry, as seen in Figure 2.7, onto a sample using an off-axis parabolic (OAP) reflector.[152]

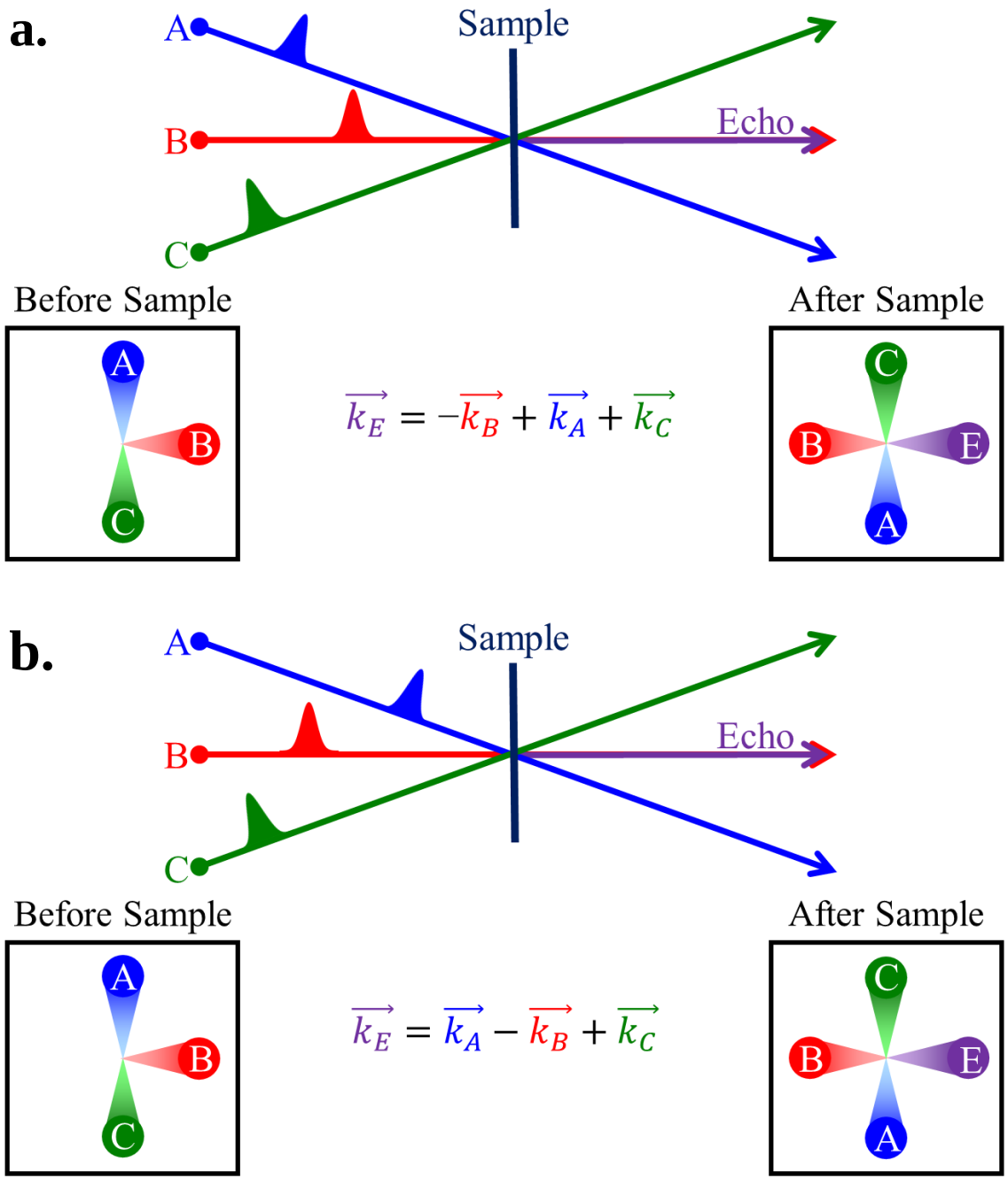

Figure 2.7. A diagram of the BOXCARS beam geometry for 2D-IR spectroscopy. The pulse sequence determines if τ will be negative or positive (non-rephasing and rephasing, respectively). (a) Positive τ is obtained with a pulse sequence of BAC, while (b) negative τ is obtained with a pulse sequence of ABC. For both cases, the desired signal is emitted in the same phase matched direction.

Both the rephasing and non-rephasing signals need to be collected to obtain the phase information within a spectrum. As discussed in Section 2.3.2., the rephasing processes (Figure 2.4 for R_1 through R_3) result in an echo signal being emitted in the $-\vec{k}_1 + \vec{k}_2 + \vec{k}_3$ phase matched direction, while the non-rephasing processes (Figure 2.4 for R_4 through R_6) result in the echo signal being emitted in the $\vec{k}_1 - \vec{k}_2 + \vec{k}_3$ phase matched direction. The BOXCARS beam geometry (as shown in Figure 2.7) allows both the rephasing and non-rephasing signals to be collected in the same phase matched direction by simply changing the order of the pulses. The three beams are aligned to three corners of a square before the OAP reflector, which will overlap the beams spatially onto the sample. The generated echo signal appears on the fourth corner of the square due to the positioning of the beams. When the pulse sequence proceeds as BAC, as shown in Figure 2.7a, the rephasing signal proceeds in the $-\vec{k}_B + \vec{k}_A + \vec{k}_C$ direction, while the non-rephasing signal proceeds in the $\vec{k}_B - \vec{k}_A + \vec{k}_C$ direction (not shown). When the pulse sequence order proceeds as ABC, as shown in Figure 2.7b, the non-rephasing signal now proceeds in the $\vec{k}_A - \vec{k}_B + \vec{k}_C$ (same as $-\vec{k}_B + \vec{k}_A + \vec{k}_C$) direction, while the rephasing signal proceeds in the $-\vec{k}_A + \vec{k}_B + \vec{k}_C$ (same as $\vec{k}_B - \vec{k}_A + \vec{k}_C$) direction. Therefore, the rephasing and non-rephasing signals can be collected in the $-\vec{k}_B + \vec{k}_A + \vec{k}_C$ phase matched direction just by changing the timing of the beams. The ordering of the pulses changes the origins of the echo, so there needs to be a reference for the timing between the first and second pulses, τ. When the pulse B is first (rephasing signal), τ is positive, while τ is negative when pulse A is first (non-rephasing signal).[36,152]

The generated vibrational echo signal in the phase-matched direction from the sample has zero-background, due to the signal being isolated from other signals that are produced. The echo signal is spatially coaligned with the LO using an uncoated ZnSe window as a combining optic, where the echo is transmitted and the LO is partially reflected. The echo signal is heterodyned with the LO (0.3-0.5 nJ per pulse, approximately 100 times larger than echo signal) to produce a signal of combined intensity that is spectrally resolved in a 0.32 meter monochromator with a 75 line/mm grating. The signal is detected with a liquid N_2 cooled 64-element mercury cadmium telluride (MCT) linear array detector (Infrared Associates, Inc.) with a resolution of 4 cm^{-1}.[8,13,151]

The echo signal is measured by heterodyne detection, as a result of the interference between the echo signal and the LO. The signal from the detector is the square of the sum of the echo and the LO electric fields:

$$S(t) = |E_{echo} + E_{LO}|^2 = E_{LO}^2 + 2E_{echo}E_{LO} + E_{echo}^2 \quad (2.23)$$

where $S(t)$ is the signal, E_{echo} is the electric field of the echo, and E_{LO} is the electric field of the local oscillator. When there is good temporal and spatial overlap of the LO and echo signal, the third term becomes very small compared to the other two terms. Also, the third term is usually quite small due to the echo electric field being orders of magnitude weaker than the LO electric field. The first term is eliminated by subtracting off a reference spectrum, which is the laser spectrum of the LO on the detector when the echo signal is not being emitted. When the data are collected, the signal is recorded as:

$$S_{data} = \frac{S_{unblocked} - S_{blocked}}{S_{blocked}} \quad (2.24)$$

where S_{data} is the signal of interest, $S_{unblocked}$ is the signal of the LO and the echo signal, and $S_{blocked}$ is the signal of the LO. The subtraction process clearly gives the signal that is only present when all the beams are reaching the sample. The division by the blocked signal is also done to account for laser fluctuations and the shape of the laser spectrum across the wavelength of interest. This leaves Eq. 2.23 with the second term, the cross term, left over, which results in the phase information contained in the echo electric field being preserved due to the cross term being linear with the two electric fields and no longer being squared.[36,138]

The purpose of beams C and LO reflecting off the same delay stage with the PZA is to cancel scatter from certain samples. Scatter in this case means that the sample sends additional "pulses" in the phase direction of the echo, leading to undesired interferences between each scattered pump beam (beams A-C in Figure 2.5) and the LO as well as between the scattered beams and the echo signal. As seen in Eq. 2.23, the signal from the detector is the squared modulus of the sum of the echo and LO electric fields. However, the intensity reaching the detector includes both the desired and undesired interferences between all the fields:[151]

$$S(t) \propto \left|E_{echo} + E_{LO} + E_{A,scatter} + E_{B,scatter} + E_{C,scatter}\right|^2 \qquad (2.25)$$

where E is the electric field and the subscripts describe its origin: echo is for the echo signal generated, LO is the local oscillator, scatter is the signal produced from the scatter of beams A-C. Eq. 2.25 produces 25 terms in total, but some of these terms are eliminated by chopping one of the beams (in this case, beam B). The remaining 16 terms either have an E_{echo} or $E_{B,scatter}$ term in them. To counteract the scattering in a heterodyne detection system, both beam C and the LO are "fibrillated." Fibrillation refers to the modulation of the arrival

of one pulse at a sample by a fraction of a wavelength. The interference between the LO and echo produces a spectrum, so there would be total signal cancelation if the LO was left stationary. Beams A and B cannot be modulated due to the τ period being changed. The phase relationship between beam C (and its scatter), the LO, and the echo signal fields has to be maintained.[151] Beam C can be fibrillated, since the echo signal is phase locked to the third pulse (Beam C).[137] The phase relationship between these two fields will be maintained, while the echo amplitude will decrease slightly. Beam C and the LO are fibrillated by both reflecting off of delay stage C, which has a PZA attached. The PZA is driven by a triangle-wave wave-form generated at ~17 Hz to cancel the scatter from the LO and beam C, leading to cleaner spectra. The drawback is that T_w resolution is lost when using fibrillation.[151]

Once the echo signal and the LO arrive at the detector, the detector performs an optical Fourier transform of t_3 time variable to the frequency domain, ω_m, for each pixel of the detector. To obtain a 2D-IR spectrum, τ is scanned from negative values to positive values while T_w is held constant to obtain both the rephasing and non-rephasing decays. The rephasing and non-rephasing regions of the interferogram produced at a given T_w are separately Fourier transformed. The original time axis, τ, is Fourier transformed to become a frequency axis, ω_τ. This process is repeated for different values of T_w.[8,13]

The emitted echo signal is complex with both the real and imaginary terms containing a combination of absorptive and dispersive lineshapes. Adding the complex rephasing and non-rephasing spectra together cancels out the dispersive components of the lineshape, leaving the purely absorptive lineshape/spectrum of the echo signal. The purely absorptive spectrum offers a significant improvement in the spectral resolution to

distinguish peaks.[36,153] However, there are phase errors with the purely absorptive spectra obtained with our experimental setup, but weaker oscillators (weak transition dipole moments) can be detected more easily with heterodyne detection.[154] Correcting the spectra after data collection is called phasing or phasing processing, since it corrects the errors in the relative phases of each of the pulses.[36,153,155-156]

2.3.4. Phasing 2D-IR Spectra

To account for the error in the phase of the spectra, phase corrections are applied. The errors being accounted for are the chirp of the pulses and the timing error from the relative timing of the pulses. Chirp is the time dependence of the instantaneous frequencies due to the pulse passing through a medium with a frequency dependent refractive index. The number of beam splitters and slightly different optics between each of the beams makes matching the chirp difficult. The timing error is caused by the movement of the delay stages and is proportional to their movement. However, the movements are dynamic and are not corrected for directly. The timing error deals more with the relative timing of the beams, more specifically when t = 0 is defined.[36,153,155-156]

The equations used for phasing are:

$$S_{PA}(\omega_m, \omega_\tau) = S_R(\omega_m, \omega_\tau)e^{i\Phi_R(\omega_m,\omega_\tau)} + S_{NR}(\omega_m, \omega_\tau)e^{i\Phi_{NR}(\omega_m,\omega_\tau)} \quad (2.26)$$

$$\Phi_R(\omega_m, \omega_\tau) = \omega_m\Delta\tau_{3,LO} + \omega_\tau\Delta\tau_{1,2} + \mathrm{Q}_1\omega_m^2 + Q_2\omega_m\omega_\tau \quad (2.27)$$

$$\Phi_{NR}(\omega_m, \omega_\tau) = \omega_m\Delta\tau_{3,LO} - \omega_\tau\Delta\tau_{1,2} + \mathrm{Q}_1\omega_m^2 + Q_2\omega_m\omega_\tau \quad (2.28)$$

where S stands for spectrum, the subscript PA stands for purely absorptive spectrum, the subscript R stands for rephasing, the subscript NR stands for non-rephasing, and Φ is the phase correction for the corresponding spectrum. Both the rephasing and non-rephasing spectra in Eq. 2.26 have slightly different phase correction defined in Eqs. 2.27 and 2.28. In Eqs. 2.27 and 2.28, $\Delta\tau_{1,2}$ is the correction for errors associated with the relative timing between the first and second pulses (hence negative for non-rephasing due to how we defined the τ), $\Delta\tau_{3,LO}$ is the correction for errors associated with the relative timing between the third pulse and local oscillator, Q_1 is the correction for chirp due to the propagation of the echo signal through the back window of the sample cell, and Q_2 is the correction for chirp due to propagation of the echo signal through sample itself.[155-156] In addition, the final terms in Eqs. 2.27 and 2.28 are thought to also correct for the errors in the actual versus expected dispersion of the monochromator.

Constraints must be applied to the phasing process to lower the error involved. The first constraint is the pump-probe projection theorem, which involves pump-probe spectra. The projection of the 2D-IR plot onto the ω_m axis should overlap with the pump-probe spectrum of the same sample at a given T_w.[156-158] The pump-probe projection theorem requires having a pump-probe spectrum for each time point corresponding to each T_w that was collected.[158] This method is the most widely accepted method for phasing data as well as the most important metric of well-phased data. An assumption for this method is that the pump-probe spectrum is free of phase errors, which is based on the fact that the same four-wave mixing processes that give rise to the vibrational echo signal, also produce pump-probe signal as discussed later in section 2.4.1. The pump-probe signal should have a constant value of $\tau = 0$, meaning it is insensitive to phase errors during the coherence

times that matter for 2D-IR spectroscopy.[36,137,157] To lower the error in the correction applied, the 2D-IR projection should match the phase perfect pump-probe spectrum.

The projection is sensitive to the values of $\Delta\tau_{3,LO}$ and the chirp phasing parameters Q_1 and Q_2. However, there is less sensitivity to the $\Delta\tau_{1,2}$ parameter.[157-158] Therefore, there needs to be an additional phasing constraint, which is to compare the purely absorptive spectrum to the absolute value spectrum (addition of the absolute values of the rephasing and non-rephasing signals).[42] The absolute value spectrum has no dependence on the phase errors but is sensitive to the $\Delta\tau_{1,2}$ parameter unlike the pump-probe projection theorem.[42] The peak values of the absolute value spectrum for each value of ω_m are found and compared with the peak values of the absolute value of the purely absorptive spectrum to minimize the difference.

In addition to these two constraints, it is important to check the quality of the phasing. There are two important qualities to a 2D-IR spectrum: (1) the 0-1 (positive-going) and 1-2 (negative-going) peaks should be centered vertically over one another, and (2) the peaks should be symmetrical if there is only a single ensemble/population and the bond has sufficient anharmonicity. The specific information of what the 2D-IR spectrum contains will be discussed later in Section 2.3.5.

Due to the LO not passing through the sample in the 2D-IR experimental setup while the probe beam in the pump-probe setup does, irregularities rise when the pump-probe projection theorem is applied. Distortion of the pump-probe signal relative to the 2D-IR signal occurs due to the division of the blocked signal (Eq. 2.24) where there is absorption of the sample as well as any solvent peaks for the pump-probe signal. The spectrum of the probe is a better approximation of the light interacting with the sample than

the LO, so the 2D-IR spectra were corrected. Due to the division by the blocked signal, the denominator needs to be changed for the 2D-IR spectra. Therefore, the raw 2D-IR data before phasing were multiplied by the FTIR spectrum to account for the probe beam passing through the sample while the LO does not in our setup.[157] Once the 2D-IR spectra are fully phased and corrected, they can be correctly interpreted and analyzed.

2.3.5. Interpretation of the 2D-IR Data

A sample of 2D-IR data that can be obtained are shown in Figure 2.8. Each 2D-IR spectrum has two axes, which can be labeled differently but ultimately are the same. The x-axis can be labeled as ω_τ due to being the Fourier transform of the τ axis, and the y-axis can be labeled as ω_m due to being the optical transform of the heterodyned echo signal with the LO. On the other hand, the x-axis and y-axis are labelled as ω_1 and ω_3, respectively, to elucidate more of the information contained in the spectrum. The x-axis corresponds to the frequencies at which a subensemble of oscillators is excited by the first IR pulse, and the y-axis is the range of frequencies that a specific subensemble exhibits after sampling its surroundings for a specific waiting time, T_w. Hence, a 2D-IR spectrum can be considered as a correlation plot between the frequencies absorbed and emitted during a specific T_w.[2,38,141,153,159-161]

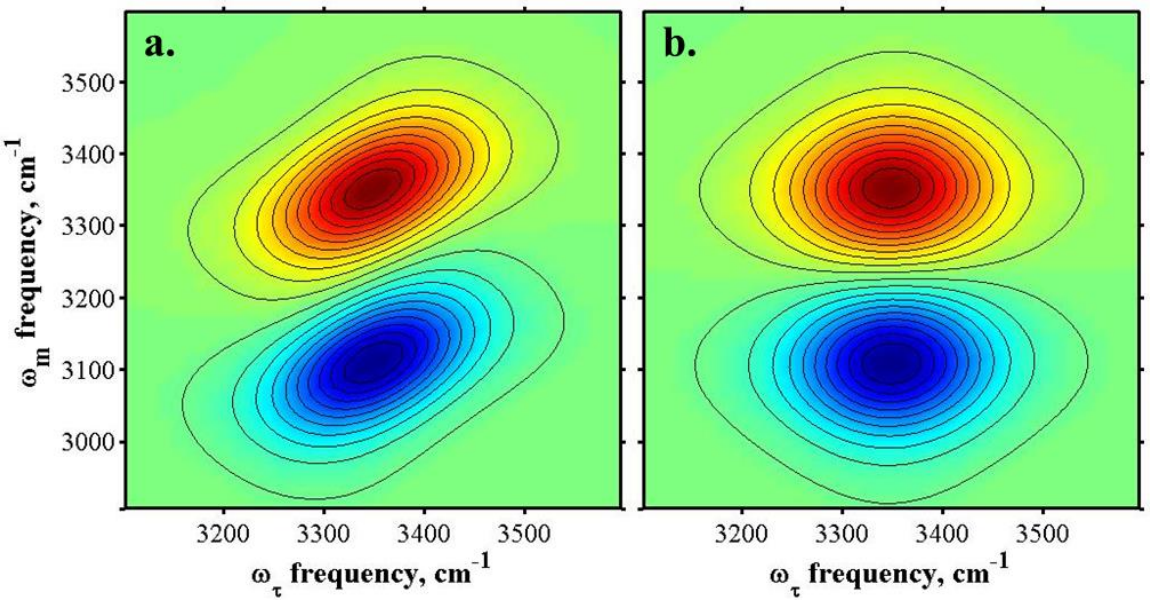

Figure 2.8. Purely absorptive 2D-IR spectra at a) early T_w and b) late T_w of the O-H stretch mode in water to emphasize the differences in the peak shape as a function of T_w.[36]

Each spectrum has a positive-going (red) v = 0-1 peak that lies on or above the diagonal and a negative-going (blue) v = 1-2 peak that is shifted by the anharmonicity to lower frequencies along the ω_m axis. The 0-1 peak is found centered on $\langle\omega_{01}\rangle$ due to the final emission of the echo signal in R_1, R_2, R_4, and R_5 coming from the first vibrational excited state and relaxing to the ground state. The 1-2 peak is found to be centered on $\langle\omega_{01}\rangle$ due to R_3 and R_6 coming from the second vibrational excited state and relaxing to the first excited state, where the energy difference will be lower. R_3 and R_6 are opposite in sign of the other response functions, which is why the 0-1 and the 1-2 peaks are opposite in the sign in their signals. Also, this reveals that ground state bleach and stimulated emission of the 0-1 transition are contributing to the 0-1 peak, but only excited state absorption of the 1-2 transition contributes to the 1-2 peak. Both peaks will have roughly the same intensity due to the 1-2 excited state absorption being twice as strong as the 0-1 transition.[36] This is a simplistic view with just one vibrational mode. There are many 2D-IR studies that involve

multiple modes which results in peaks that lie off-diagonally whenever modes are coupled, which are called cross peaks. Cross peaks will not be discussed here, but there are many detailed descriptions elsewhere.[36-37,162]

A diagonal slice through the 0-1 peak reflects the range of frequencies captured by the linear FTIR lineshape, assuming there is sufficient separation between the 0-1 and 1-2 peaks. This represents the chemical heterogeneity of the sample. The antidiagonal width represents the portion of the available frequencies that have been sampled during a given T_w period. This antidiagonal width contains contributions from very fast pure dephasing (T_2*) and vibrational relaxation (T_1), as well as spectral diffusion caused by interconversion of molecular subensembles and driven by the reorganization of the molecules in the environment.[36,163-164]

At short T_ws (Figure 2.8a), the peak shape is diagonally elongated or highly correlated, indicating that the oscillators have not yet sampled the full range of chemical environments. As the waiting time increases (Figure 2.8b), the peak shape becomes circular or uncorrelated, indicating that the oscillators have sampled a greater range of the available configurations, which is spectral diffusion. A peak could be highly correlated at early T_w but become uncorrelated at a later T_w. 2D-IR spectra need to be collected at various T_ws to understand the dynamics that are occurring in the system.[36,138] The peak shape in a 2D-IR contour plot holds the information about the dynamics in the system. Therefore, there needs to be a way to quantify the peak shape and relate it back to the underlying dynamics of the system, which is part of the frequency-frequency correlation function (FFCF). The FFCF can be obtained from 2D-IR spectroscopy.[2,38,141,153,159-161]

2.3.6. Quantifying 2D-IR Data

To understand the frequency-frequency correlation function (FFCF), consider a vibrational mode being surrounded by a local molecular environment that is continuously in motion, on many different timescales. Each molecule in the system and the probe molecules have an associated electric dipole due to partial charges. Therefore, local net electric fields are created throughout the sample. When the system is moving, the local net electric fields are subject to change. As the projection of the net electric field vector onto the transition dipole of the oscillator varies, the frequency changes. Therefore, the FFCF captures the frequency response of the vibrational mode to the environment dynamics and is more of a time dependent vibrational Stark effect, which states the vibrational frequency of the oscillator changes in the presence of an electric field.[36,138]

The FFCF fits to a multi-exponential decay of the following form due to the inherent nature of a correlation function:

$$C_{FFCF}(t) = \frac{\delta(t)}{T_2} + \sum_i \Delta_i^2 \exp\left(\frac{-t}{\tau_i}\right) \tag{2.29}$$

Here, δ(t) is a delta function and T_2 is the total dephasing time, which has been described in Section 2.3.1.[163-164] This first term represents the homogeneous component of the FFCF, since it contains T_2. The second component is comprised of a sum of i exponential decays. Each of the decays has a specific τ_i with a corresponding Δ_i. τ_i is the timescale of fluctuations to which the mode is sensitive, and Δ_i is the magnitude of frequency fluctuations induced by the surroundings. In other words, it is the change in frequency that occurs when a specific fluctuation happens. A larger Δ_i means that the specific fluctuation has a stronger effect on the frequency. The number of decays depends on the complexity

of the sample and how sensitive the mode is to the environment. In other words, the second component of Eq 2.29 describes the spectral diffusion of the system.[163-164]

The Δ_is obtained are the standard deviations of the Gaussian distribution of the Si-H frequencies. To obtain the total standard deviation (Δ), the Δ_is must be added in quadrature. The FWHM of the Gaussian lineshape, f_g, is related to Δ through the relation $2\Delta\sqrt{2\ln(2)}$.[36,165] The total FWHM of the lineshape, which is a Voigt profile, can be found using the approximation of $\frac{\Gamma}{2} + \sqrt{\frac{\Gamma^2}{4} + f_g^2}$, where Γ is the homogeneous linewidth and was defined earlier in Eq. 2.20.[166] Therefore, the FFCF details the contribution of both the homogeneous and inhomogeneous broadening to the linear lineshape. However, the 2D-IR peak shape is not directly related to the full FFCF, but a peak shape analysis method can relate the respective metric to the full FFCF.

Many methods exist for extracting the FFCF from 2D-IR data, but it depends on how the data were collected and corrected. If the data did not need phase corrections, the amplitude of the rephasing and non-rephasing spectra could be related.[37,153] If the anharmonicity of the mode is small where the 1-2 peak can interfere with the shape of the 0-1 peak, the angle of the node between the two peaks is used.[36,167] If the peaks are well-separated and isolated, the ellipticity can be calculated, which compares the diagonal and antidiagonal widths.[7,36,168] The method that will be used here is the center line slope (CLS) method due to many using this method and has been shown to be robust.[163-164]

For the CLS method, the 0-1 peak is analyzed by taking slices through the peak along the ω_τ axis with the slices being parallel to the ω_m axis, which can be seen in Figure 2.9 as the dashed gray lines. With each slice, a Gaussian is fit to the 0-1 peak to find the

center of the Gaussian peak at a specific ω_τ. The centers of the fits are then plotted as a function of ω_τ (as shown as the white circles in Figure 2.9), which are then fit to a line (as shown as the solid black lines in Figure 2.9).[163-164]

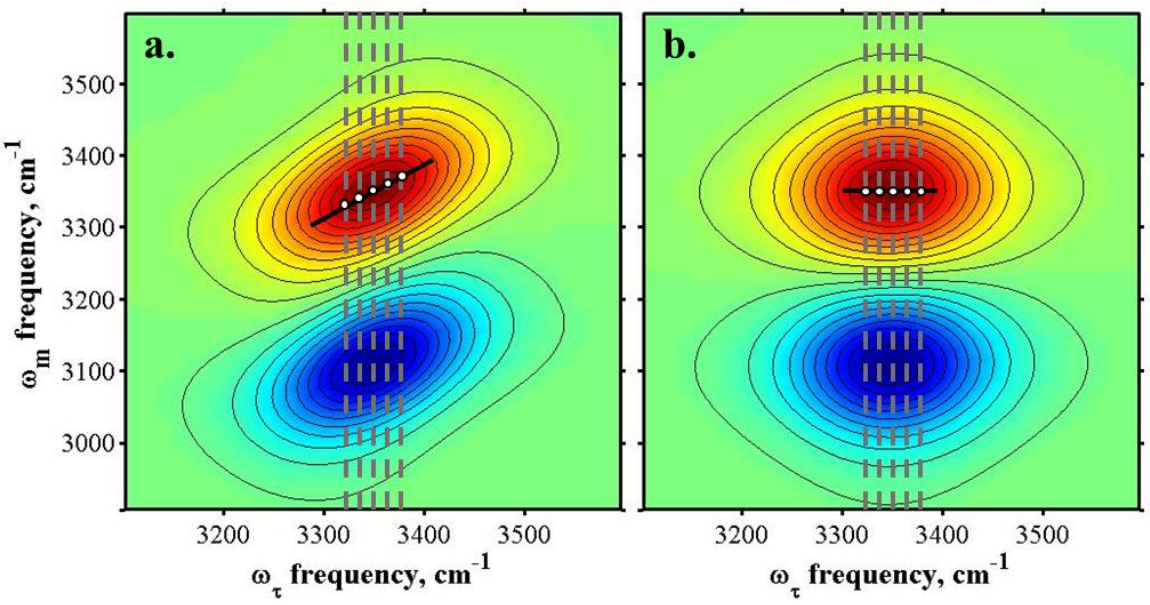

Figure 2.9. The CLS methods for the 0-1 peak for a) early T_w and b) later T_w. The dashed gray lines represent the slices that are along ω_τ and parallel to ω_m. The white circles represent the centers of the fitted gaussians. The black line represents the fitted line obtained from the centers plotted as a function of ω_τ.[36]

The slope of the line is called the center line slope, hence the name of the method. The CLS can vary from zero to one depending on the peak shape as can be seen in Figure 2.9. The CLS is one when the peak is highly correlated, meaning the peak is elongated along the diagonal as seen in Figure 2.9a. The CLS is zero when the peak is uncorrelated or circular as seen in Figure 2.9b. A peak is circular when the diagonal width is the same as the antidiagonal width. The CLS is found for each T_w collected. The CLS values are plotted as a function of T_w, which can be fit to an exponential decay.[163-164] The CLS method is quite popular, since the fit has a direct relationship to the normalized FFCF:[164]

$$\overline{C_{FFCF}}(t) = CLS(T_w) = \frac{C_{FFCF}(T_w)}{C_{FFCF}(0)} = \sum{}_i \Delta_i^2 \exp\left(\frac{-t}{\tau_i}\right). \quad (2.30)$$

The normalized FFCF is able to capture the time constants contributing to the spectral diffusion in the full FFCF in Eq. 2.29, which has been shown to be highly accurate.[163-164] However, the amplitudes of the exponential contributions (Δ_i) assume a FFCF normalized to unity and a y-intercept that is likewise normalized, meaning the amplitudes are not in balance with the homogeneous component. The CLS procedure cannot distinguish the homogeneous broadening from fast spectral diffusion, causing the initial values of the amplitudes to be incorrect. The full FFCF can be found from the normalized one though. The amplitudes from the CLS decay fits and the linear FTIR FWHM are first used to calculate approximate values for Δ_is and T_2 of the full FFCF by following the procedure by Kwak and co-workers.[163-164] These initial values are then applied to a full FFCF, where the Fourier transform of the first-order response function (Eqs. 2.18 and 2.19) is used to reproduce the linear FTIR lineshape.[137,139] The lineshape was fit by iteratively varying the amplitudes, T_2, as well as the central frequencies but keeping the time constants the same. The CLS method was developed using the short-time approximation, so the values for Δ_is and T_2 are underestimated due to the method's inability to distinguish between homogeneous terms and fast spectral diffusion (compared with the FID). Therefore, the floated Δ_is and T_2 are constrained to only increase from the estimated values.[163-164] The FFCF parameters reveal the timescales for the motions occurring but not what those motions are. Molecular dynamic simulations must be performed to reveal the microscopic picture of what is occurring in the system.

2.4. Infrared Pump-Probe Spectroscopy

Infrared pump-probe (IPP) spectroscopy is another technique that is a third order process and obtains $P^{(3)}$ as seen in Eq. 2.21. An assumption is that there are only three states in the system: the ground state, the first excited state, and the second excited state, as was the case in the 2D-IR spectroscopy theory. As mentioned earlier in Section 2.3.4, IPP data is needed for phasing of the 2D-IR data due to not having phase errors.

2.4.1. Theory

IPP spectroscopy involves two beams, usually a strong pump beam and a weak probe beam, where the signal comes from the interactions of three electric fields as mentioned previously. Therefore, the Feynman diagrams from Figure 2.4 apply here as well. However, the first two interactions come from the pump beam versus from two separate beams, meaning that $R_1 = R_4$ and $R_2 = R_5$ and $R_3 = R_6$. The three remaining pathways belong to processes described before: stimulated emission, ground state bleach, and excited state absorption. The double-sided Feynman diagrams for these processes are shown in Figure 2.10, where the solid blue arrows indicate the pump beams and interact at the sample at the same time. The signal is once again emitted in the $\pm\vec{k}_1 \pm \vec{k}_2 + \vec{k}_3$ direction. For IPP though, $\vec{k}_1 = \vec{k}_2$ meaning the signal's phase-matched direction is in the same direction as the probe. Therefore, IPP spectroscopy is self-heterodyning and does not require the use of an external LO.[36,137-138]

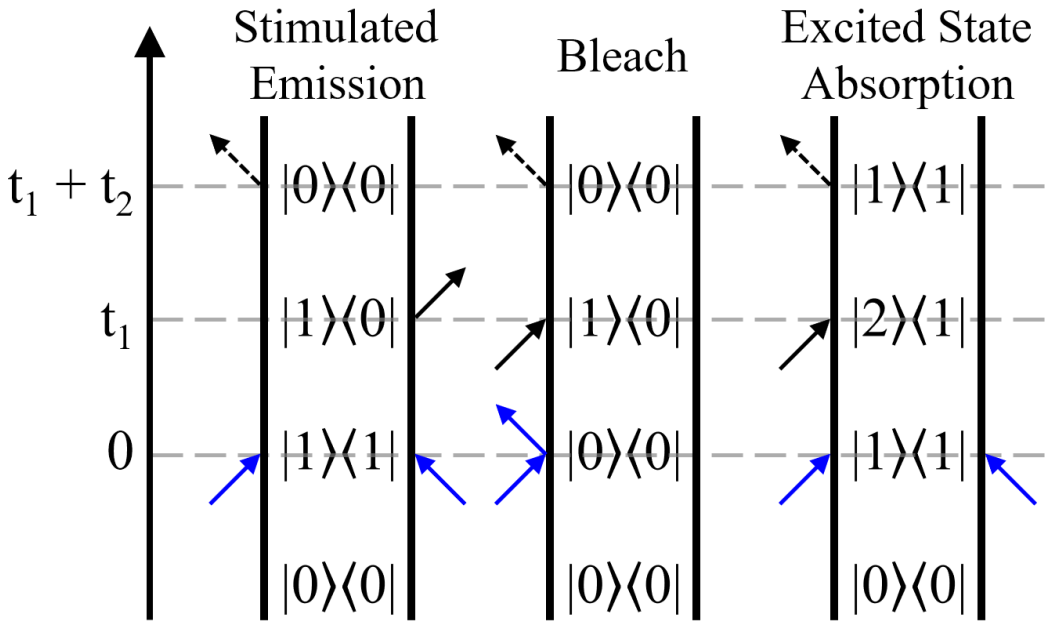

Figure 2.10. Double-sided Feynman diagrams for producing IPP signal. The diagrams are labeled based on the physical process that occurs. The solid blue arrows represent the pump beam and the solid black arrows represent the probe beam. The dashed black arrows show the emitted signal.

2.4.2. Experimental Setup

Experimentally, IPP involves two laser pulses, where one is higher in power (pump) and a weaker one (probe beam). The two pulses are separated by a time delay, called T_w. The T_w here is directly related to the T_w used in 2D-IR spectroscopy. The IPP experiment is performed on the same laser system as described previously and in Section 2.3.3.[4] In brief, different beam splitters are used to produce the strong pump and weak probe beams and utilizing two delay stages. The probe beam is sent into the detector where a difference spectrum is obtained with the pump on/off due to chopping the pump beam. Chopping the pump beam is necessary to subtract any signal arising from interactions of the probe beam with the system.[137,169-170] The IPP signal is negative with excited state absorption and is positive with ground state bleach and stimulated emission to remain consistent with the previous conventions of the 2D-IR spectra.

The IPP signal obtained is expected to decay due to vibrational relaxation of the excited states. However, mostly in solution phase, orientational relaxation may also contribute to this decay, causing the vibrational lifetime not to be accurate. A common and simple method to remove the orientational contribution to the IPP signal is to perform the experiment with magic angle polarization.[171] By setting the polarization of the pump and probe beams to be 54.7º relative to one another, the orientational changes occurring can cancel one another, leaving the population relaxation due to the molecules rotating in and out of being aligned with the electric fields. To implement this, polarizers are placed on the pump and probe beams immediately before the sample and placing a polarizer on the probe beam after the sample. The polarizers on the probe beams are set to the same angle, while the pump beam is set 54.7º from the probe polarizers. The resulting IPP signal has no orientational dependence.[171]

2.4.3. Analyzing IR Pump-Probe Spectra

The IPP data obtained can be presented in two different ways as seen in Figure 2.11. Figure 2.11a shows the IPP spectra over a range of T_ws. There is a positive 0-1 transition peak and the negative 1-2 peak shifted anharmonically downward in frequency, which lines up with the 2D-IR spectra. As T_w increases, the IPP signal approaches zero due to the relaxation of the excited states which is due to the vibrational relaxation. Figure 2.11b shows the IPP decay at a certain frequency obtained by taking a slice of the IPP spectra in Figure 2.11a at that frequency. In order to calculate the vibrational lifetime, T_1, of a system, the pump-probe decays over a range of frequencies are fit to a single exponential function. This means at each frequency over the 0-1 transition, the decays are

fit to a single exponential where the time constants are averaged to find T_1. T_1 can be found for both the first and second excited states but are found to be similar.[137,169-170]

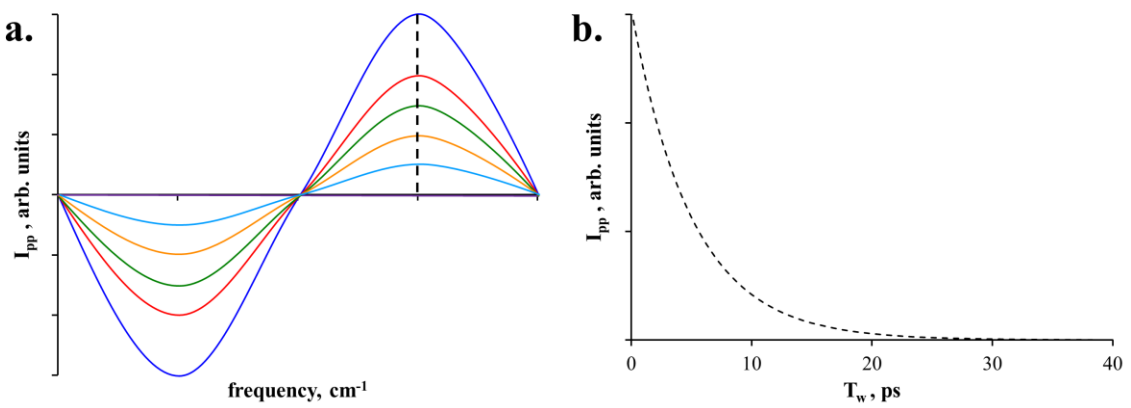

Figure 2.11. Different representation of IPP data obtained. a) Simulation of pump-probe spectra where the intensity of the signal is plotted against the frequency. The T_w is increasing as the signal reaches zero. The progression of T_w is in the order of blue, red, green, orange, light blue, and purple. b) Simulation of a pump-probe decay where the intensity of the signal is plotted against the waiting time. The data is represented as a dashed black line. The pump-probe decay is obtained by taking a slice of the pump-probe spectra at a specific frequency as shown in (a) by a dashed black line. The decay will give the vibrational lifetime, T_1, for that transition.

Chapter 3. Enhanced Vibrational Solvatochromism and Spectral Diffusion by Electron Rich Substituents on Small Molecule Silanes

Reproduced from

Olson, C. M.; Grofe, A.; Huber, C. J.; Spector, I. C.; Gao, J.; Massari, A. M., Enhanced vibrational solvatochromism and spectral diffusion by electron rich substituents on small molecule silanes. *J. Chem. Phys.* **2017**, *147* (12), 124302.

with permission of AIP Publishing.

This work was performed in collaboration with the Gao group at the University of Minnesota – Twin Cities. All calculations were performed by Adam Grofe.

3.1. Chapter Summary

FTIR and two-dimensional IR (2D-IR) spectroscopies were applied to two different silanes in three different solvents. The selected solutes exhibit different degrees of vibrational solvatochromism for the Si-H vibration. Density functional theory calculations confirm that this difference in sensitivity is the result of higher mode polarization with more electron withdrawing ligands. This mode sensitivity also affects the extent of spectral diffusion experienced by the silane vibration, offering a potential route to simultaneously optimize the sensitivity of vibrational probes in both steady-state and time-resolved measurements. Frequency-frequency correlation functions obtained by 2D-IR spectroscopy show that both solutes experience dynamics on similar timescales and are consistent with a picture in which weakly interacting solvents produce faster, more homogeneous fluctuations. Molecular dynamics simulations confirm that the frequency-frequency correlation function obtained by 2D-IR spectroscopy is sensitive to the presence of hydrogen bonding dynamics in the surrounding solvation shell.

3.2. Introduction

Solvent motions play a critical role in chemical reactivity and solvation dynamics.[172-175] Perhaps the most obvious example is found in electron transfer reactions in which solvent shell dynamics contribute the energy needed to reach the transition state geometries of the donor and acceptor species.[170,176] In fact, for any condensed phase reaction, solvent-solute interactions can stabilize or destabilize the transition state, thereby directly influencing the rate coefficient.[11,14,16-17,177] For example, in biomacromolecules,

key structural motions for the function of proteins or enzymes can be slaved to the dynamics of the surrounding solvation layer.[178-183] Likewise, catalytic rate constants are always specific to a solvent system,[184-187] and ultrafast dynamics in the solvation shell have been directly correlated with proposed mechanistic steps for organometallic catalysts.[140,188]

A variety of approaches have been used to characterize solvent dynamics.[38,43-44,141,153,159,189-194] All of these techniques report some facet of solvent motions, but none of them delivers the full dynamic picture. Complete structural evolution is filtered by the sensitivity of the reporter to each dynamic component, and only a subset of the coupled dynamics is visible through the lens of a particular measurement technique. For example, two-dimensional infrared (2D-IR) spectroscopy monitors the time dependent frequency fluctuations of a vibrational mode on a solvated solute species.[38,141,153,159-160] Changes in the vibrational frequency are dependent on the timescales of solvent motions in the proximal solvation shell and the degree to which those motions perturb the vibrations of the solute. The latter effect depends on solvent polarity and the strength of solute-solvent interactions – generally only the closest solvation shells exert a measurable influence on frequency fluctuations of the solute.[140,172-173,175] Therefore, the 2D-IR spectrum of a particular solute vibrational mode is blind to solvent motions in the bulk and even excludes dynamics in the solvation shell that do not perturb its vibrational frequency. In this context, molecular dynamics (MD) simulations can complement experimental measurements to provide detailed, structural insights into the microscopic mechanism of solvation.[39-40,195-203]

In this chapter, I describe a combined experimental and computational investigation of vibrational solvatochromism and spectral diffusion in small silane molecules in various solvents using Fourier transform infrared (FTIR) and 2D-IR spectroscopies. To elucidate substituent effects on solvation dynamics, trimethoxysilane (TriMOS) and triphenylsilane (TriPS) were chosen, since the same vibrational mode can be monitored in the presence of different electron withdrawing ligands, giving rise to different solvatochromic responses. The study of these model molecules reveals the role of substituents on spectral diffusion in different solvents. The timescales and amplitudes of spectral diffusion are extracted from the 2D-IR data, which are further analyzed through molecular dynamics (MD) simulations, in which each solute molecule is represented explicitly by a quantum mechanical method, embedded in the solvent environment approximated by a molecular mechanics force field. Such a combined QM/MM treatment of solute-solvent interactions allows a direct probe of the effect of solvent dynamics on the instantaneous change of the solute potential energy surface and its vibrational frequency as measured experimentally.

3.3. Experimental Materials and Methods

Trimethoxysilane (TriMOS, 95%, Sigma-Aldrich), triphenylsilane (TriPS, 97%, Sigma-Aldrich), chloroform (99.9% purity, anhydrous, Acros Organics), isopropanol (99.5%, anhydrous, Sigma-Aldrich), and pentane (*n*-pentane, 98%, Sigma-Aldrich) were used as received.

TriPS and TriMOS solutions were prepared in each solvent as 5 m/m % and 5 v/v % solutions, respectively, giving absorbances of 100–200 mOD for the Si-H vibration on

both solutes. Solutions were used within 1 week of preparation. Spectroscopic studies were performed on solutions sandwiched between two 3 mm CaF_2 windows with a 50 μm Teflon spacer to define the sample path length.

Fourier transform infrared (FTIR) spectra were collected on a Nicolet 6700 FTIR spectrometer (Thermo Scientific) with at least 16 scans and a resolution of 1 cm^{-1}. A background spectrum of each of the solvents was subtracted from the respective TriMOS and TriPS spectra.

3.3.1. Details of 2D-IR and IR Pump-Probe Measurements

The 2D-IR instrument was described previously in Section 2.3.3.[204] Briefly, a regeneratively amplified Ti:Sapphire laser (Spectra-Physics, 800 nm, 40 fs pulse duration, 500 mW, 1 kHz repetition rate) pumped an optical parametric amplifier (OPA, Spectra-Physics), and the near-IR signal and idler beams were difference frequency mixed in a silver gallium sulfide crystal ($AgGaS_2$, 0.5 mm thick) to generate mid-IR pulses (3 μJ /pulse, 90 fs FWHM, ~200 cm^{-1} bandwidth FWHM). The mid-IR pulses were tuned to the silane (Si-H) stretching frequency (2200 cm^{-1} for TriMOS and 2130 cm^{-1} for TriPS), divided into three ~1 μJ p-polarized pulses, and focused at the sample in a BOXCARS geometry.[152] The generated vibrational echo signal was heterodyne detected with a liquid N_2 cooled MCT linear array detector (Infrared Associates, Inc.) with spectral resolution of ~4 cm^{-1}. The system was continuously purged with dry air (-100 °F dew point) during data collection from the OPA to the detector.

The first frequency dimension (x-axis, ω_τ) was achieved by scanning the time delay between pulses 1 and 2, τ, in increments of 5 fs and subsequent Fourier transformation.[36,38,160] The second dimension (y-axis, ω_m) was obtained by optical Fourier transform of the heterodyne detected vibrational echo signal by dispersing it from the monochromator diffraction grating. Each 2D-IR spectrum was collected while the time delay between pulses 2 and 3, T_w, was maintained at a fixed value. The resulting data were processed to obtain the purely absorptive 2D-IR spectrum,[153,205] and phase corrected using the pump-probe projection theorem and the absolute value center as constraints as described in Section 2.3.4.[164,206] The FTIR spectrum of the sample was used as an absorption correction prior to phasing, since the probe beam passes through the sample while the local oscillator does not in our setup.[157]

The 2D-IR spectra were analyzed using the centerline slope (CLS) method to obtain the frequency-frequency correlation function (FFCF).[163-164] For the CLS analysis, the maximum intensity for the 0-1 and its central frequency were found for each of the systems. The frequency range for the CLS was ± 8 cm^{-1} from the central frequency. Other ranges were chosen, but the CLS did not change significantly. So, this range was used for the final analysis. More details are provided in the subsequent section.

IR pump-probe spectroscopy was carried out with the pump and probe beams polarized at the magic angle to remove contributions from orientational relaxation,[171] as described previously.[4] The data were fit from 1 to 75 ps to determine the population relaxation times (lifetime, T_1) for the v = 0-1 and 1-2 transitions. The vibrational relaxation

times for these two transitions consistently showed the same trends, and the 0-1 values were used in data analyses, which can be found in Table 3.1.

3.3.2. Analysis of Frequency-Frequency Correlation Functions

The FFCF was modeled according to Equation 3.1. However, only the first two terms were necessary for the molecules in chloroform and pentane.

$$FFCF(t) = \frac{\delta(t)}{T_2} + \Delta_1^2 \exp\left(\frac{-t}{\tau_1}\right) + \Delta_2^2 \exp\left(\frac{-t}{\tau_2}\right) \quad (3.1)$$

The time constants (τ_1 and τ_2) in this equation were obtained directly from fitting the CLS decays, which has been shown to be highly accurate.[163-164] However, the amplitudes of each exponential contribution (Δ_1 and Δ_2) assume a FFCF normalized to unity and a y-intercept that is likewise normalized. The amplitudes from the fits of the CLS decays and the linear FTIR full widths at half maximum (FWHMs) were used to calculate approximate values for the amplitudes (Δ_i) and T_2 of the full FFCF by following the procedure by Kwak and co-workers.[163-164] These initial values were then applied to a FFCF, and the first-order response function was used to reproduce the linear FTIR lineshape. The lineshape was fit by iteratively varying the amplitudes, as well as the central frequencies. The CLS method was developed using the short-time approximation, so the values for Δ_i and T_2 are underestimated due to the method's inability to distinguish between homogeneous terms and fast spectral diffusion (compared with the FID) as described in Section 2.3.6. Therefore, the floated Δ_i and T_2 were constrained to only increase from the estimated values.

3.3.3. Electronic Structure and Molecular Dynamics Simulation

The computational analysis followed a two-pronged approach: (1) quantum mechanical electronic calculations both in the gas phase and in solutions represented by continuum solvation models to elucidate solvent polarization effects on the vibrational mode, and (2) combined quantum mechanical and molecular mechanical (QM/MM) molecular dynamics simulations were carried out to understand the microscopic solvation dynamics of the vibrational chromophore.

In the gas-phase and continuum solvation QM calculations, density functional theory (DFT) calculations were performed using the M06-2X functional along with the 6-31+G(d,p) basis set. Both the Minnesota solvation model (SMD) and polarizable continuum model (PCM) were examined using the Gaussian software package, with the latter employing the default isoelectron density surface.[207] All structures were optimized at each level of theory, and normal mode analysis was performed to obtain the vibrational frequency of the silicon hydride mode. In addition, charge analysis was performed by the CHELPG (charges from electrostatic potentials using a grid based method) electrostatic potential fitting procedure,[208] and the interaction between molecular orbitals was modeled using natural bonding orbital (NBO).[209-210]

The QM/MM simulations were performed using CHARMM,[211] in which the solute is treated by the semiempirical Austin Model 1 (AM1) method[212] to provide an adequate sampling of the configuration space. The solute molecules were placed in the center of a previously equilibrated solvent box (~50 Å in each length). All solvent molecules within 3.0 Å of the solute were removed. The bond lengths of the solvent were held constant using

the SHAKE algorithm.[213] The coordinates were minimized for 50 steps using the steepest descent algorithm followed by 50 steps, using the adopted basis Newton-Raphson algorithm. Long-range electrostatic interactions were feathered to zero at 12 Å by a switching function. The simulations box was equilibrated employing the isothermal-isobaric (NPT) ensemble at 1 atm and 25 ℃ by performing molecular dynamics for 1.0 ns. The production dynamics trajectory was acquired similarly for 2.0 ns. Coordinates were saved every 10 fs, resulting in a total of 200,000 configurations, which were used for all subsequent analyses.

3.3.4. Instantaneous Vibrational Frequency Calculations

The instantaneous vibrational frequency of the silicon hydride mode at a given solvent configuration was determined using a vibration quantum-mechanical perturbation theory (QVP) that was developed recently by Xue and coworkers.[214] In this approach, the effects of solute-solvent interactions on the vibrational wave function and transition energies of the solute are treated as a perturbation to a reference state. The main purpose of the QVP method was to increase the performance of solving the nuclear wave function on the Born-Oppenheimer potential energy surface to calculate a large number of frequencies (10^5-10^7) precisely and quantum mechanically. This was accomplished by using two numerical procedures: (1) the nuclear wave function and properties were obtained using a potential-optimized discrete variable representation (PO-DVR),[215-217] and (2) the effects of solvent dynamic fluctuations were determined using perturbation theory. Overall, this method allows for the efficient computation of vibrational frequencies with

systematic improvement by increasing either the number of PO-DVR points or increasing the order of the perturbation.

Several improvements from the initial report by Xue and coworkers[214] were made in the present study. First, rather than using the gas-phase wave function and PO-DVR points as the reference for solvent perturbation, an initial (after the equilibration) solvent configuration in the dynamics trajectory was used to define the QVP reference Hamiltonian to further enhance convergence in the perturbation calculations. Therefore, the solvent effects in the instantaneous vibrational frequency calculations is reduced to contributions due to solvent fluctuations with respect to the initial solvent configuration. Typically, the solvent configuration frame in the beginning of each restart of the trajectory was used to optimize the PO-DVR reference state.

Second, a localized normal mode was used as the coordinate of the nuclear displacement. Both TriMOS and TriPS presented a particular challenge if the Si-H stretch normal coordinate was used because of internal dihedral rotations that will move atoms away from the vector coordinate in the initial mode analysis. This issue was avoided using a localized mode in which the movements of the free atoms were projected out of the Si-H stretching mode. In the case of TriMOS, the free atoms are those in the methyl groups, and for TriPS, the majority of the phenyl rings are included. The atoms that were included in the local mode are the silicon, hydrogen, and adjacent atoms that are covalently bonded to the silicon; oxygen for TriMOS, carbon for TriPS. The local mode was determined using a mobile block Hessian (MBH)[218-219] to reduce the magnitude of displacement for the frozen atoms in the mode. MBH allows for a block of atoms to be defined which act like a

single particle. Because the mass of the block of frozen atoms is relatively large, the displacement of these atoms in the normal mode becomes small, and thus, will have a diminished effect when these displacements are zeroed out. The MBH calculations were performed on the probes in the gas phase owing to cost limitations the MBH implementation in CHARMM. Therefore, this local mode is used in all solvents for each probe.

Although the same local mode was used in the instantaneous frequency calculation using QVP throughout each trajectory, the positions of the atoms were allowed to freely move during MD simulations. The coordinate projection to the local mode was performed using a least squares procedure in which the optimal rotation matrix was determined from a singular value decomposition (SVD).[220] This algorithm has three steps: (1) move the center of both the reference point set and the instantaneous point set to the origin, (2) calculate the covariance matrix between the two sets of coordinates, (3) perform SVD on the covariance matrix. The optimal rotation matrix is calculated by multiplying the U and V matrices. In order to introduce molecular symmetry effects into the least squares procedure and to place the most emphasis on the hydrogen stretch, which has the largest displacement, the covariance matrix was mass weighted. The center of mass was used to center the coordinates rather than the centroid used by Arun et al.[220]

The third difference from the work of Xue et al. [214] is the precision to which we are calculating the frequencies. The hybrid AM1/CHARMM Hamiltonian used in our simulation affords us the opportunity to calculate the vibrational frequencies to high precision (less than 0.5 cm^{-1}) owing to the low cost of the QM/MM energy evaluation.

Here, we used 10 PO-DVR points to represent the wavefunction, and the perturbation was calculated to the fourth order (QVP4) for all frequencies. Because we were dealing with a space that only contained 10 vibrational states, the fourth order in the perturbation could be calculated quite rapidly. In fact, the majority of the cost of the QVP calculation was the cost of minimizing the normal mode atoms. For the PO-QVP optimization, 500 steps of adopted basis Newton-Raphson minimization were called for, but the energy typically converged around 400-450 steps on average.

One concern in the atomic configurations of the dynamics trajectory is that the bond lengths of the solvent molecules remain constrained throughout the trajectory, which precludes any coupling from being introduced into the calculations of the vibrational frequencies. In this simulation, we chose to work under the assumption that coupling with the solvent coordinates was small enough to disregard. However, it is possible to include coupling into the QVP method by using vibrational configuration interaction on the QVP wavefunction. If this were implemented, then the nuclear configurations for the mode would displace from their minima, which would not be overly affected by constraining the bond lengths of the solvent molecules.

Overall, the reference vibrational state was the vibrational wave function at time zero after the initial equilibration for data collection (which can be regarded as an arbitrary moment in time during the MD simulation). Numerically, the wave function of the reference state was modeled using the PO-DVR. In this manner, the changes in wave function for the ground state and the first two excited states due to the instantaneous solvent fluctuations as well as the change in solute geometry at future times were determined by

perturbation theory. Although second-order perturbation yields sufficient precision (~1 cm^{-1}), we used the fourth-order perturbation theory (QVP4) thanks to the computational efficiency using the present QM/MM potential, which ensures that the computed vibrational frequencies are within 0.5 cm^{-1} of the exact result for each configuration. Because a discrete variable representation is employed, the calculation of the perturbation operator only requires single point energy calculations at the PO-DVR points without the need to explicitly solve the vibrational Schrödinger equations. Consequently, the QVP4 approach is computationally efficient, providing the instantaneous, on-the-fly transition energies of the solute for the 0-1 and 1-2 excitations. Importantly, nuclear quantum mechanical effects as well as solvent dynamics on the solute potential energy surface are explicitly included in the computation, although nuclear quantum effects on solute-solvent coupling are neglected. A complementary alternative approach is the widely used electrostatic potential mapping procedure. The QVP4 calculations captured the time-dependent evolution of the vibration excitation energies of the solute, which were used to model the linear and nonlinear absorption spectra and the FFCF, where the linear spectra were calculated using:[221]

$$I(\omega) \approx \int_0^\infty e^{-i\omega t} \langle \exp\left(\int_0^t dt' \omega(t')\right) \rangle e^{-\frac{t}{2T_1}} dt \tag{3.2}$$

where ω is the angular frequency, and T_1 is the experimental pump probe lifetime.

3.3.5. Calculation of the Hydrogen Bonding Lifetime

The hydrogen bonding lifetime (τ_{HB}) of the solvent was determined by calculating the hydrogen bond correlation function.[222-223]

$$C(t) = \left\langle \frac{\sum h_{ij}(t_0) h_{ij}(t+t_0)}{\sum h_{ij}(t_0)^2} \right\rangle \tag{3.3}$$

where $h_{ij}(t)$ is unity when the pair of solvent molecules i and j are hydrogen bonded, and zero otherwise. The computed correlation function was fit to a set of three exponentials,[222-224] and the average τ_{HB} was determined by integrating the correlation function. For these calculations, a hydrogen bond was defined by geometrical criteria such that the donor-acceptor distance was less than 3.0 Å and the OH–O angle was greater than 130°. This methodology has been implemented into the MdAnalysis library in Python[224] and possibly underestimates the lifetime, since it does not take into account instances of transient breaking and reforming of the same bond.

Before concluding this section, we make a distinction in the trajectories used to determine correlation functions. First, there is the molecular dynamics trajectory, which encompasses the entirety of the dataset from which the correlation function is calculated. Second, there are correlation trajectories, which are a subset of the molecular dynamics trajectory, upon which the correlation function is averaged at each point in the correlation function. In the calculation of the hydrogen bond correlation function, correlation trajectories were only accepted if the hydrogen bond was continuous throughout the correlation trajectory. This could in principle underestimate the hydrogen bond lifetime, because it does not include transient breaks of the hydrogen bond. However, this is compensated for by using a generous hydrogen bond geometric criteria of 3 Å for the hydrogen-acceptor distance and 130° for the donor-hydrogen-acceptor angle. This algorithm was further modified to calculate the hydrogen bond lifetime at the solute-solvent interface by only including correlation trajectories that were within the first shell

of the solvent. The first shell was determined by having any distance between the atoms of the solute and the atoms of each solvent molecule be less than 6 Å, the minimum following the first peak of the radial distribution function (Figure 3.7c) between the central carbon of isopropanol and the hydride hydrogen.

The radial distribution function between the oxygen atom of TriMOS and the hydroxy hydrogen of isopropanol (Si-O---HOPr) is shown in Figure 3.7b. Hydrogen bonding interactions between the isopropanol and the acceptor in TriMOS are clearly revealed by the strong first peak in the Si-O---HOPr radial distribution function. Integration to the first minimum at 2.8 Å yields an average of 1.08 coordination numbers per solute molecule, due to hydrogen bonding interaction. Overall, this suggests that out of the six possible accepting sites from TriMOS, only 1 is occupied on average.

3.4. Results and Discussion

3.4.1. Analysis of FTIR Solvatochromism of TriMOS and TriPS

Figure 3.1 shows the solvent-subtracted FTIR spectra for the silicon hydride, Si-H, stretching vibration of TriMOS and TriPS in three different solvents: isopropanol, chloroform, and pentane. The center frequencies and FWHMs can be found in Table 3.1. A most striking finding is the large substituent effect on the silane stretch mode; its vibrational frequency is blue-shifted by 74 cm^{-1} when the phenyl groups of TriPS are replaced with the electron-withdrawing substituents in TriMOS in the non-polar solvent pentane. The experimental finding on the effect of the CH_3O-substitution on the Si-H frequency in pentane is reproduced by the computational results of 78 and 81 cm^{-1} using,

respectively, the Minnesota solvation model (SMD)[225] and the polarizable continuum model (PCM)[226] at the M06-2X/6-31+G(d,p) level of theory (Table 3.2). The corresponding change of 59 cm^{-1} was obtained from QM/MM molecular dynamics simulations (Table 3.3). The TriMOS hydride stretch frequency (ν_{Si-H}) also exhibits a strong hypsochromic change with absorption peak maxima at 2194.6, 2203.2, and 2207.2 cm^{-1} in isopropanol, pentane, and chloroform, respectively. Similarly, the corresponding values for TriPS are 2125.7, 2129.2, and 2131.1 cm^{-1}. The experimental trend of solvatochromic shift in order of isopropanol < pentane < chloroform for ν_{Si-H} is surprising, since it does not follow any solvent polarity scales. Continuum model calculations, explicit MD simulations, and experiments predict the vibrational frequency to decrease monotonically with the solvent polarity (polarity trend: pentane < chloroform < isopropanol), in accordance with the Stark effect.[227] Interestingly, although the trend is the same, TriMOS and TriPS experience different degrees of solvatochromism. It has been established that ν_{Si-H} is tuned by the inductive effect of the substituents.[228-232] A major difference between TriMOS and TriPS is the presence of electronegative oxygen atoms in the methoxy ligands that strongly polarize the Si-O bonds; the partial atomic charge on silicon changes from 0.08 *e* in TriPS to 1.03 *e* in TriMOS (Table 3.2). Previous analysis showed that the hydrogen bonding ability of the solvent was correlated with solvatochromic shifts of ν_{Si-H} on silanes and silica sol-gels.[168] Consequently, I hypothesized that the solvent interactions with the oxygen atoms would have the greatest influence on the vibrational mode due to the inductive effect.[168,233] Yet, the fact that the solvatochromic

trend in Figure 3.1 is the same for TriPS, which lacks oxygen atoms in its ligands, indicates that the solvent influence is not limited to this specific interaction.

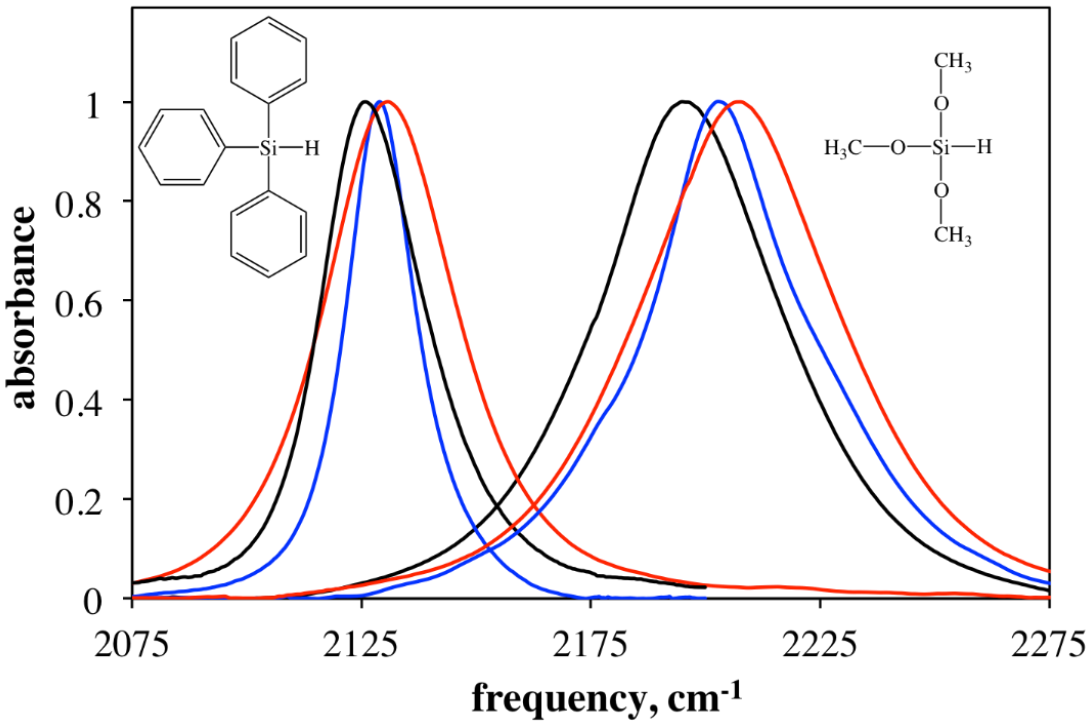

Figure 3.1. Solvent subtracted, baselined, and normalized FTIR spectra of the Si-H vibration for TriPS (left) and TriMOS (right) in isopropanol (black), chloroform (red), and pentane (blue).

Table 3.1. Experimental Si-H vibrational center frequency (ν_{Si-H}, cm^{-1}), FWHM (cm^{-1}), and vibrational lifetime (T_1, ps) of TriMOS and TriPS in various solvents.

molecule	solvent	ν_{SiH} (cm^{-1})	FWHM (cm^{-1})	T_1 (ps)[a]
TriMOS	pentane	2203.2	41	9.8 ± 0.2
	chloroform	2207.2	50	9.9 ± 0.2
	isopropanol	2194.6	46	6.0 ± 0.1
TriPS	pentane	2129.2	18	20.0 ± 0.5
	chloroform	2131.1	35	17.2 ± 0.4
	isopropanol	2125.7	27	15.3 ± 0.3

[a] Standard error of the fit

Table 3.2. Normal mode vibrational frequencies for the Si-H stretch (ν_{Si-H}, cm^{-1}) and CHELPG partial atomic charges (a.u.) of TriMOS and TriPS in the gas phase and in pentane, chloroform, and isopropanol solution using M06-2X/6-31+G(d,p) along with SMD and PCM solvation models.

molecule	solvent	ν_{SiH} SMD (cm^{-1})	$\Delta\nu_{SiH}$ SMD (cm^{-1})	ν_{SiH} PCM (cm^{-1})	$\Delta\nu_{SiH}$ PCM (cm^{-1})	Si Charge SMD	H Charge SMD
TriMOS	gas	2342.3	0.0	2342.3	0.0	1.03	-0.17
	pentane	2337.0	-5.3	2339.6	-2.7	1.05	-0.17
	chloroform	2334.8	-7.5	2338.3	-4.0	1.05	-0.16
	isopropanol	2342.1	-0.2	2338.8	-3.5	1.05	-0.15
TriPS	gas	2260.8	0.0	2260.8	0.0	0.08	-0.08
	pentane	2258.7	-2.1	2258.6	-2.2	0.08	-0.08
	chloroform	2256.3	-4.5	2257.5	-3.1	0.09	-0.08
	isopropanol	2255.6	-5.2	2257.1	-3.7	0.04	-0.07

Table 3.3. Computed Si-H stretch vibrational frequencies (ν_{Si-H}, cm^{-1}) and FWHM (cm^{-1}) of TriMOS and TriPS in the gas phase and in pentane, chloroform, and isopropanol solution using quantum vibrational perturbation theory in combined QM/MM molecular dynamics simulations. The solute is treated by the AM1 Hamiltonian and the solvents are represented by the CHARMM force field. The experimental data (same as Table 3.1) are also listed for convenience of comparison.

molecule	solvent	experiment		calculation		
				M06-2X/6-31+G(d,p)/SMD	AM1/CHARMM	
		ν_{SiH} (cm^{-1})	FWHM (cm^{-1})	ν_{SiH} (cm^{-1})	ν_{SiH} (cm^{-1})	FWHM (cm^{-1})
TriMOS	gas	---	---	2342.3	2206.2	9.1
	pentane	2203.2	41	2337.0	2222.4	19.3
	chloroform	2207.2	50	2334.8	2219.1	19.8
	isopropanol	2194.6	46	2342.1	2220.9	22.5
TriPS	gas	---	---	2260.8	2154.2	7.8
	pentane	2129.2	18	2258.7	2163.2	19.3
	chloroform	2131.1	35	2256.3	2165.2	19.8
	isopropanol	2125.7	27	2255.6	2165.6	22.5

To gain insights into the solvatochromism for TriMOS and TriPS, we modeled the $\nu_{Si\text{-}H}$ vibrations through a combination of DFT calculations on solutes using two continuum solvent models (SMD[225] and PCM[226]) and MD simulations. Continuum solvation methods introduce the equilibrium electric polarization into the Born-Oppenheimer surface, probing the Stark effect on the vibrational frequency, but the unusual trend of the Si-H vibrational frequency shifts observed experimentally was not fully reproduced by either continuum model as shown in Table 3.2. In particular, the simulation yielded the correct relative frequency shifts for TriPS between pentane and chloroform solvents but not in isopropanol, and for TriMOS, the order between pentane and isopropanol was correct yet not in $CHCl_3$. We suspect that the large dispersion contributions from chloroform are partly responsible for the unusual experimental findings. The DFT/SMD calculations yielded a blue shift for TriMOS in isopropanol, a clear departure from other computational methods and experiments.

The discrepancy between the continuum solvation results and the experimental data suggests that there are probably other factors affecting the solvatochromic shifts in addition to solvent dielectric effects. Figure 3.2 displays the absorption spectra from combined QM/MM molecular dynamics simulations, which were calculated using Equation 3.2. For TriMOS, the computed frequency shifts are too small to make a conclusive assessment of the origin of the unusual experimental trends, since the computed blue shift in isopropanol is not sufficiently large. On the other hand, the trend for TriPS from MD simulations failed to reproduce experiments completely. Further analyses of intermolecular interactions suggest that the computed red spectral shifts are due to van der Waals interactions that are

not compensated by dispersion interactions, which are not included in the QM/MM potential. Nevertheless, the trends obtained using the PCM model and QM/MM simulations are in agreement with each other, suggesting that dielectric and electrostatic interactions are consistently represented. The SMD model includes contributions due to surface tension terms, which may be too sensitive in the Hessian for the present systems.

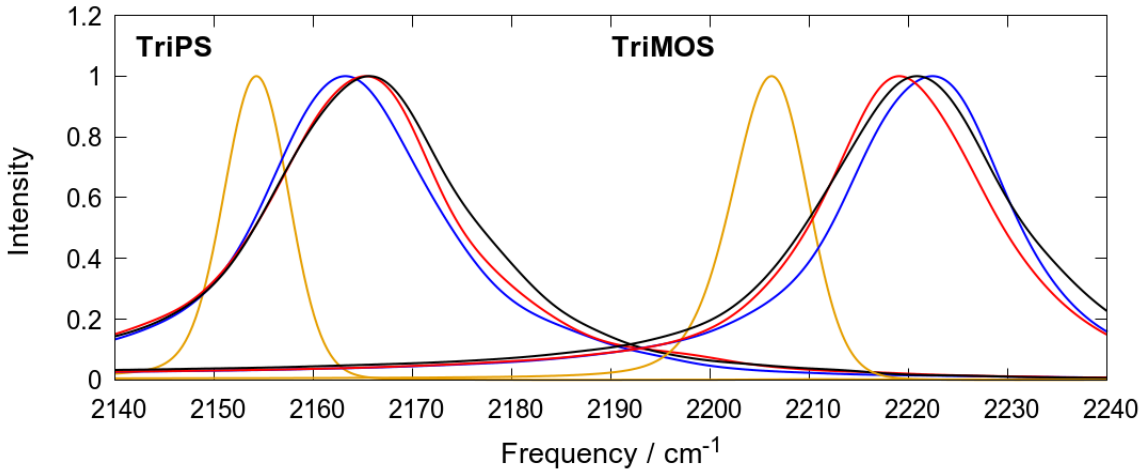

Figure 3.2. Computed linear IR spectra in the Si-H stretch vibrational frequency region for TriPS (left) and TriMOS (right) in the gas phase (orange), isopropanol (black), chloroform (red), and pentane (blue).

Figure 3.3 depicts the computed instantaneous Si-H vibrational frequencies of TriMOS in the gas phase and in pentane, along with the forces due to the Lennard-Jones terms, projected on the vibrational mode. It is readily observed that a spectral variation with relatively small fluctuations punctuated by large and short-lived fluctuations in pentane solution (similar behaviors are found in other solvents). However, there is no large fluctuations in the gas phase frequency trajectory (orange curve in Figure 3.3). Thus, instantaneous close van der Waals (VdW) contacts causes a sharp increase in the force on the mode coordinates, thus the slope of the potential energy surface, leading to a large

increase in the frequency. In fact, Figure 3.3 shows that large fluctuations in vibrational frequency coincide exactly with spikes in the VdW forces. These fluctuations have direct effects both on the spectral diffusion (lineshape) and average vibrational frequencies. Notice that the frequency fluctuations due to van der Waals collisions are on the order of hundreds of wavenumbers, much greater than the FTIR linewidths and solvatochromic shifts. Furthermore, these fluctuations are rather common throughout the trajectories, and are similarly found in the other two condensed phase simulations. It is possible that magnitude of the fluctuation due to a VdW contact is overestimated, since the repulsive wall for the Lennard-Jones potential is known to be too steep compared to the exact potential.

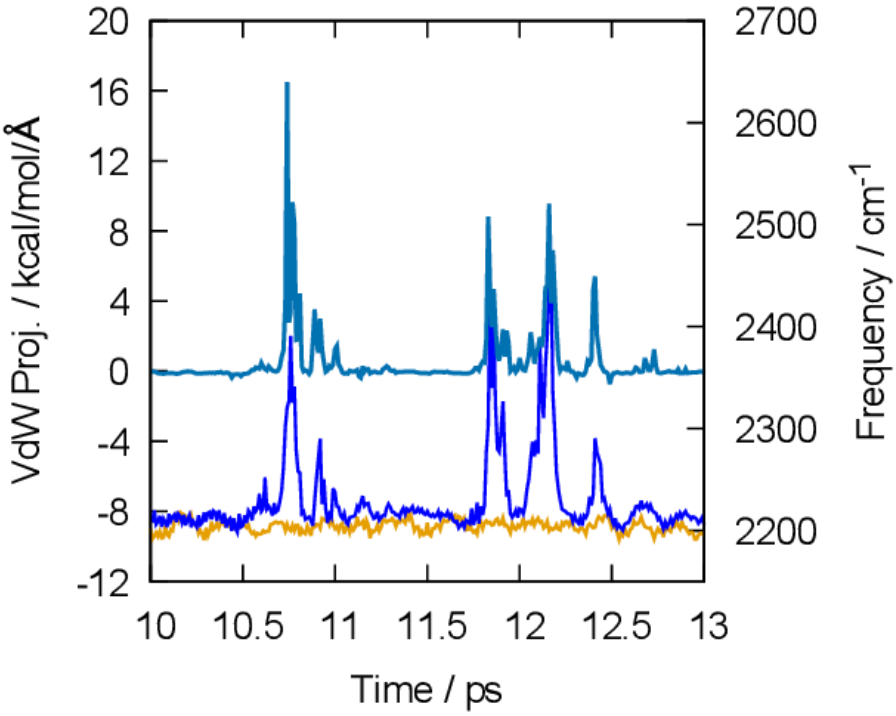

Figure 3.3. Snapshot of computed instantaneous Si-H vibrational frequency (cm^{-1}) along a segment of molecular dynamic trajectories of TriMOS in the gas phase (orange) and in pentane solution (dark blue) and the Van der Waals force on the local mode coordinate (light blue).

It should be noted that there are a few instances when a fluctuation in frequency does not correlate exactly with a fluctuation in the VdW force. It is possible that these are due to intramolecular overlaps that are not being accounted for in the projection procedure for the VdW forces. The absence of these large fluctuations in the gas phase seems to suggest that the intramolecular collisions occur more often in solution due to a cage effect from the solvent.

We have performed an analysis by computing the full vibrational spectra based on Equation 3.2 without van der Waals contributions (Figure 3.4, dashed lines) from the solvent in QM/MM interactions. Since only the QM/MM electrostatic terms enters into the QM calculation, the computed spectra are purely a reflection of the electric field projected on the stretch model. As can be seen, the average (and maximum) frequencies are shifted to smaller values, but the relative shifts in the three solvents are not affected. Importantly, the line widths are significantly reduced. These are consistent with the findings presented in Figure 3.3 due to collision with the solvent.

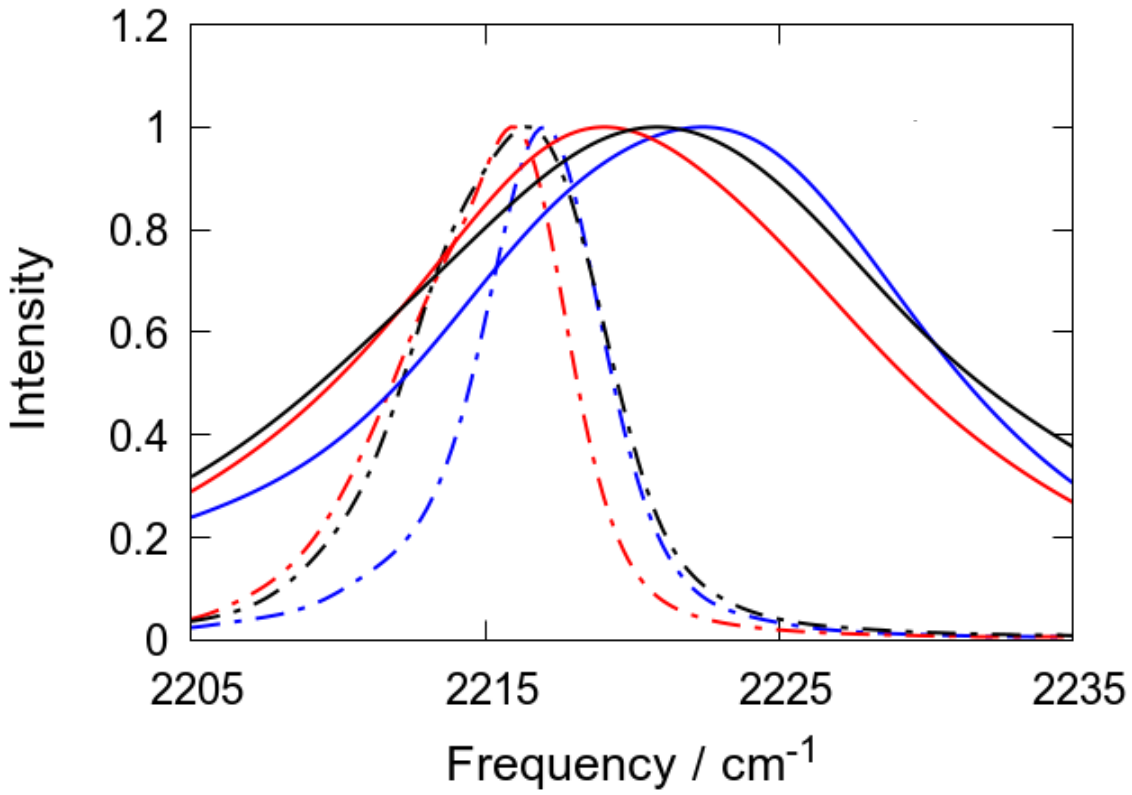

Figure 3.4. Computed Si-H vibrational spectra for TriMOS with (solid curves) and without (dashed curves) inclusion of van der Waals interaction energies where the color of the line denotes the environment: black for isopropanol, red for chloroform, and blue for pentane.

Returning to Table 3.3, the QM/MM molecular dynamics simulations results exhibited increased Si-H stretch frequencies (blue shifts) in solutions relative to that in the gas phase, whereas the continuum model yielded red shifts. As in Figure 3.3, the instantaneous collision (i.e., steric restriction that increases the slope of the potential along the stretch mode) between solute and solvent leads to significant increase in the stretch frequency, which, when averaged over the MD trajectory, yields an increase in frequency. This is also consistent with vibrational frequencies/spectra computed using the same trajectory, without including van der Waals energies (Figure 3.4), which are smaller than those computed using the full potential. For the continuum solvation model, it lacks such

instantaneous collision effects (Figure 3.3). Thus, a continuum model gives a "pure" reflection of the dielectric medium in a fixed solvent cavity. Unfortunately, to our knowledge, there is no experimental data in the "gas-phase" results for comparison. It would be interesting if a gas-phase measurement were performed to compare with this computational prediction. Thus, we attribute the opposite trends in the simulation results and continuum data for TriPS to the same reason, i.e., instantaneous collision with solvent to increase the Si-H stretch frequency, since there is small solvent (electrostatic) effects for TriPS.

To understand the effects of conformational preference of the three methoxy groups in TriMOS in different solvents, we have computed the potential of mean forces (PMFs) as a function of the H-Si-O-C dihedral angle, which are displayed in Figure 3.5. Shown also are the occupation numbers in the bonding and antibonding natural orbitals from the natural bond orbital (NBO) analysis. Clearly, there is a solvent effect on the equilibrium distribution between the two conformational minima. As the polarity of the solvent increases, 0° conformation is stabilized, although the overall stability remains in the anti (180^{o}) conformation. The results in Figure 3.5 may be attributed to potentially enhanced solvent and solute dipolar interactions.

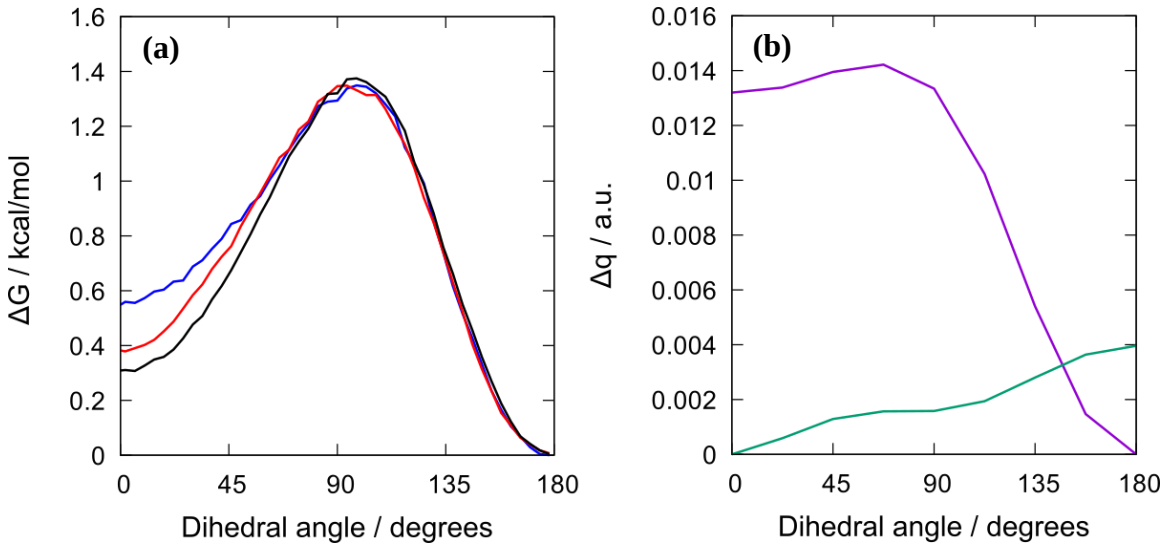

Figure 3.5. Analysis of H-Si-O-C dihedral angle of TriMOS. (a) Potential of mean force computed directly from the simulations results where the color of the line denotes the environment: black for isopropanol, red for chloroform, and blue for pentane. (b) Change in the occupation of the bonding (light green) and antibonding orbitals (light purple) of Si-H calculated in the gas phase at the level of M06-2X/6-31+G(d,p).

The effect that the dihedral angles have on the frequency can be seen by performing natural bond orbital analysis (NBO). NBO determines the best unitary transformation between the molecular orbitals determined from self-consistent field to the Lewis structure representation. Overall, this analysis allows us to compute the occupation of the bonding and anti-bonding orbital of the Si-H bond. Furthermore, if we compute this value as we perform a relaxed scan of a single dihedral angle, we see that the occupation of the anti-bonding orbital changes as a function of the angle. At zero degrees, (oxygen-methyl bond is parallel to the silicon-hydrogen bond) hyperconjugation interactions, i.e., the delocalization of the lone-pair electrons on the oxygen atom to the antibonding orbital of the Si-H bond reaches maximum, but the orbital overlap is diminished as the torsional angle is changed, and hyperconjugation stabilization is at minimum. Thus, the vibrational frequency of the Si-H mode will be red shifted at 0° due to weakening in its bond strength

compared to that at 180°. This hypothesis was confirmed by normal mode analysis at each of the configurations.

We believe that the hyperconjugation with the anti-bonding orbital has the most significant effect, leading to a red shift. The instantaneous vibrational frequencies plotted against the methoxy torsion angles showed weak dependence using the combined AM1/CHARMM potential, weaker than the M06-2X results in the gas phase. It possible that AM1 is not adequately mixing the orbitals as in higher level methods, and this could explain why the solvent shifts are small from QM/MM simulations and why they do not fully follow the experimental trends. To examine the effect of the conformational distribution of the three methoxy groups (the three ligands to the Si-H unit), we determined the average torsional angles of these groups over the dynamics trajectories in all three solvents studied (pentane, chloroform, and isopropanol). The results show that there is negligible effect on the observed solvatochromic shifts as a result of the variations in the methoxy conformation distribution in these solvents (Figure 3.5).

A plausible explanation for the unusual frequency trends is that specific solvent-solute interactions that were not captured by implicit solvent modeling might be needed to reproduce the experimental order of spectral change. In calculations with TriMOS, the inclusion of an explicit H-bond donor (methanol) near the oxygen atoms of the methoxy ligands was able to yield the red spectral shift observed in isopropanol relative to that in pentane (Table 3.4). All calculations were performed using M06-2X/6-31+G(d,p)/SMD. The methanol molecule, acting as a hydrogen bond donor, was placed in different locations to test its effect on the vibrational frequency. A total of six configurations for TriMOS were

constructed, which are displayed in Figure 3.6. Considering the plane defined by the three oxygen atoms in TriMOS, we classify the direction of the Si-H bond vector as above this plane. Table 3.4 suggests that there is no uniform preference for a consistent orientation. Nevertheless, the combination of two methanol molecules in the above and below configurations appears to display a rough cancellation on frequency shift, and the above/above and below/below configurations display opposite signs in the frequency shift. The inclusion of an explicit H-bond donor near the oxygen atoms of the methoxy ligands was able to yield the red spectral shift observed in isopropanol relative to that in pentane. This suggests that the effect of explicit hydrogen bond donation on the TriMOS vibrational frequency is dependent upon which lone pair the donor interacts with at any given time.

Table 3.4. Computed normal mode frequencies and shifts due to hydrogen bonding interactions for TriMOS using M06-2X/6-31+G(d,p) embedded in the SMD solvent model. Only methanol as a solvent is used in this analysis. Structure numbers are defined in Figure 3.6.

system	ν_{SiH} (cm^{-1})	$\Delta\nu_{SiH}$ (cm^{-1})	Figure 3.6
TriMOS/continuum	2320.64	0.0	1
TriMOS/continuum +1 explicit donor (above)	2314.63	-6.01	2
TriMOS/continuum +1 explicit donor (below)	2311.59	-9.05	3
TriMOS/continuum +2 explicit donors (above/above)	2307.21	-13.43	4
TriMOS/continuum +2 explicit donors (above/below)	2321.34	0.7	5
TriMOS/continuum +2 explicit donors (below/below)	2336.13	15.49	6

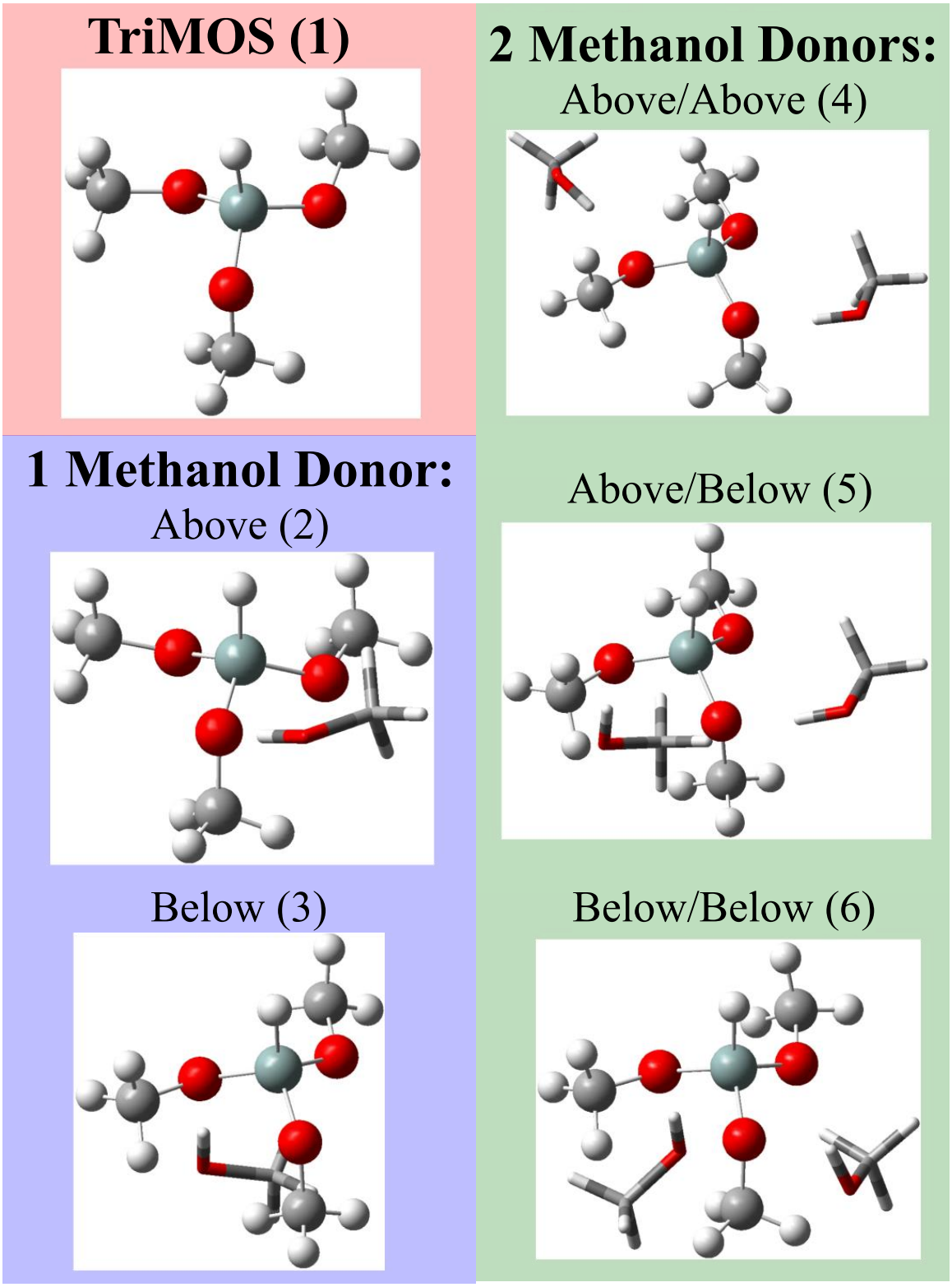

Figure 3.6. Optimized configurations of TriMOS with the explicit hydrogen bond donors given with the respective label used in Table 3.4. Note: the donor molecules were drawn using tubes for clarity purposes only (all atoms were treated at the same level of DFT).

In an effort to test the potential effect of halogen bonding[30-31] on the Si-H mode, another series of normal mode analyses were performed on TriMOS in chloroform. These calculations were performed using MP2/6-31+G(d,p)/IEFPCM so that dispersion between the solute and the donor was explicitly included. First, the TriMOS structure in the continuum was optimized and the frequency was calculated as shown in Table 3.5. Next, an explicit chloroform molecule was placed in the continuum such that an intermolecular halogen bond was formed with the hydrogen of the mode. The formation of a halogen bond is possible in this case because the hydrogen has a slight negative charge and could potentially act as an electron donor to one of the chlorine atoms of chloroform. The result of the unconstrained optimization was a structure in which the halogen bond was broken. Nonetheless, a slight blue shift of less than 1 cm^{-1} was calculated for the Si-H mode. Another geometry optimization was performed with the same starting structure except that two angles were constrained to maintain the halogen bond. Those angles were: (1) Si-H-Cl, (2) H-Cl-C, where the silicon and hydrogen are in the TriMOS and carbon and chlorine are in the explicit chloroform. Overall, these two constraints maintained the linear arrangement between the chlorine and Si-H mode and yielded a hydrogen chlorine distance of 2.9 Å. Although the unconstrained optimization did not maintain the halogen bond (suggesting that it is a less stable structure) solvent packing effects in the condensed phase could lead to this interaction being more significant. In addition, the radial distribution functions between the hydrogen of the silane mode for both TriMOS and TriPS and the chlorine of $CHCl_3$ (Figure 3.7a) show a moderate peak at roughly the distance of the halogen bond determined by the constrained QM geometry optimization. Furthermore, the

integral of the peak shows that this occupation is greater than one, which suggests that on average the halogen bond is maintained through most of the simulation. The results of the normal mode analysis are presented in Table 3.5 and show that there is a 7.8 cm^{-1} blue shift when an explicit halogen bond donor molecule is added to the system. When the system is optimized without constraints, the blue shift is relatively small, but constrained halogen bond system showed a significant blue shift. Therefore, introducing an explicit $CHCl_3$ solvent molecule in the solvation shell of TriMOS led to a mild blue shift, which could be further enhanced by constraining the solvent geometry to maintain a halogen bonding configuration to the hydride.[30-31] We conclude that the unusual experimental solvatochromic trend for ν_{Si-H} is understood as arising from specific hydrogen and halogen bonding interactions with the solute. Given that the solvatochromism is not fully reproduced from QM/MM suggests that non-electrostatic effects, such as dispersion and charge transfer, also play a role for $CHCl_3$.

Table 3.5. Computed normal mode frequencies and shifts due to halogen bonding interactions for TriMOS using MP2/6-31+G(d,p)/IEFPCM. Only chloroform was investigated for this analysis.

system	ν_{SiH} (cm^{-1})	$\Delta\nu_{SiH}$ (cm^{-1})
TriMOS/PCM	2359.6369	0.0
TriMOS / PCM + donor (unconstrained optimization)	2360.3402	+ 0.7033
TriMOS / PCM + donor (constrained)	2367.4177	+ 7.7808

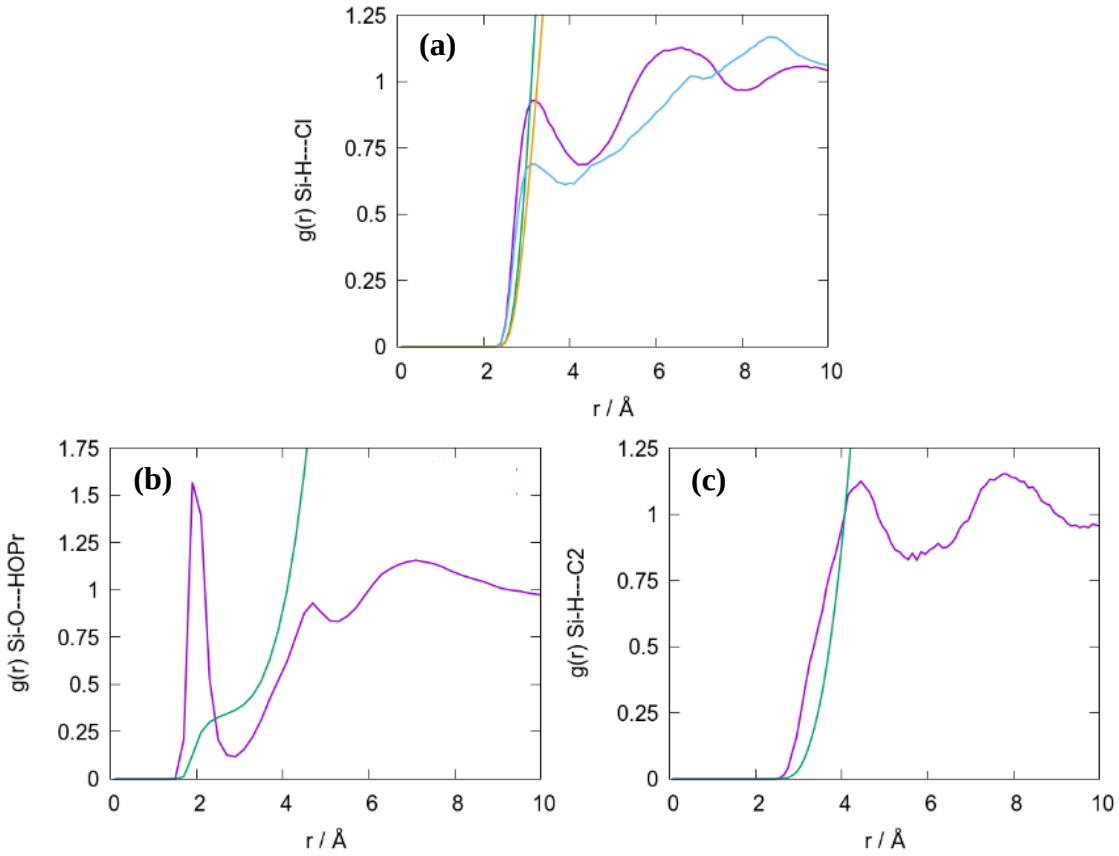

Figure 3.7. (a) Radial distribution functions for TriMOS (purple) and TriPS (light blue) and integrated radial distribution functions for TriMOS (light green) and TriPS (orange) between the hydrogen of the silane mode and the chlorine of the chloroform. (b) Radial distribution function (purple) and integrated radial distribution function (green) between the hydrogen bond acceptor in TriMOS (oxygen) and the hydrogen donor in isopropanol (hydrogen on the hydroxyl). (c) Radial distribution function (purple) and integrated radial distribution function (green) between the silane hydrogen and the central carbon of isopropanol. The functions were computed from AM1/CHARMM MD simulations.

An interesting finding from our analyses is that the magnitudes of the partial atomic charges for silicon and hydrogen – the main components of the normal mode vector – increase with the electronegativity of the ligands (Table 3.2). This provides an explanation for the greater solvatochromic effects in TriMOS than in TriPS: the electron withdrawing methoxy ligands lead to a greater charge separation and electrostatic coupling to the solvent reaction field.[227] Consequently, the average dipole moment for TriMOS is increased from

1.8 D in pentane to 2.5 D in isopropanol, whereas the corresponding values are 0.8 and 1.2 D, respectively, for TriPS.

One key question is whether a change in solvatochromism correlates with increased sensitivity to ultrafast structural dynamics leading to spectral diffusion. If so, this would provide a strategy to designing vibrational probes with enhanced sensitivity to solvent dynamics by tuning peripheral ligands. As a starting point, the FTIR peak widths vary considerably among the three solvents for both compounds, increasing in order of pentane (blue) < isopropanol (black) < chloroform (red) as seen in Figure 3.1. The TriPS peak widths are generally narrower than those of TriMOS, though the broadening trend with solvent remains the same. The FTIR peak widths are influenced by the range of chemical environments as well as the time dependent fluctuations of the vibrational frequencies that are driven by solvent dynamics (spectral diffusion and homogeneous broadening). Broader peaks in more polar solvents suggest that their solvation environments are more heterogeneous and/or dynamic than that of pentane. 2D-IR spectroscopy enables one to decompose the FTIR lineshapes into their homogeneous and inhomogeneous contributions, and MD simulations can be used to understand the molecular origins of the experimental data.[36,38,160] The full widths at half maximum (FWHMs) determined from molecular dynamics simulations show similar trends both for the two solutes and in different solvents, although the linewidths are somewhat smaller than those from experiments (Table 3.3). Thus, the present QM/MM simulations can provide useful insights on properties of solvent dynamics.

3.4.2. Solution Dynamics Studied via 2D-IR Spectroscopy and MD Simulations

Figure 3.8 shows the 2D-IR spectra at T_w = 0.3 ps (left column) and 3 ps (right column) for TriMOS in isopropanol (top row) and pentane (bottom row). All 2D-IR spectra acquired for both molecules in all solvents are provided in Figure 3.13 through Figure 3.18. An intuitive interpretation of these spectra is that the x-axis (ω_1) corresponds to the frequencies at which a subensemble of oscillators is excited by the first IR pulse, and the y-axis (ω_3) is the range of frequencies that this subensemble exhibits after sampling its surroundings for a specific waiting time, T_w. Hence, the 2D-IR spectrum yields a frequency-frequency time correlation for the subensembles beneath the FTIR lineshape.[38,141,153,159-161] Each spectrum has a positive-going (red) v = 0-1 peak that lies on or above the diagonal and a negative-going (blue) v = 1-2 peak that is shifted by the anharmonicity to lower frequencies along the ω_3 axis. A diagonal slice through the 0-1 peak reflects the range of frequencies captured by the linear FTIR lineshape (assuming sufficient separation between the 0-1 and 1-2 peaks); the antidiagonal width represents the portion of the available frequencies that have been sampled during a given T_w period. This antidiagonal width contains contributions from very fast pure dephasing (T_2^*) and relaxation (T_1), as well as spectral diffusion caused by interconversion of molecular subensembles and driven by the reorganization of solvent molecules.[36,163-164]

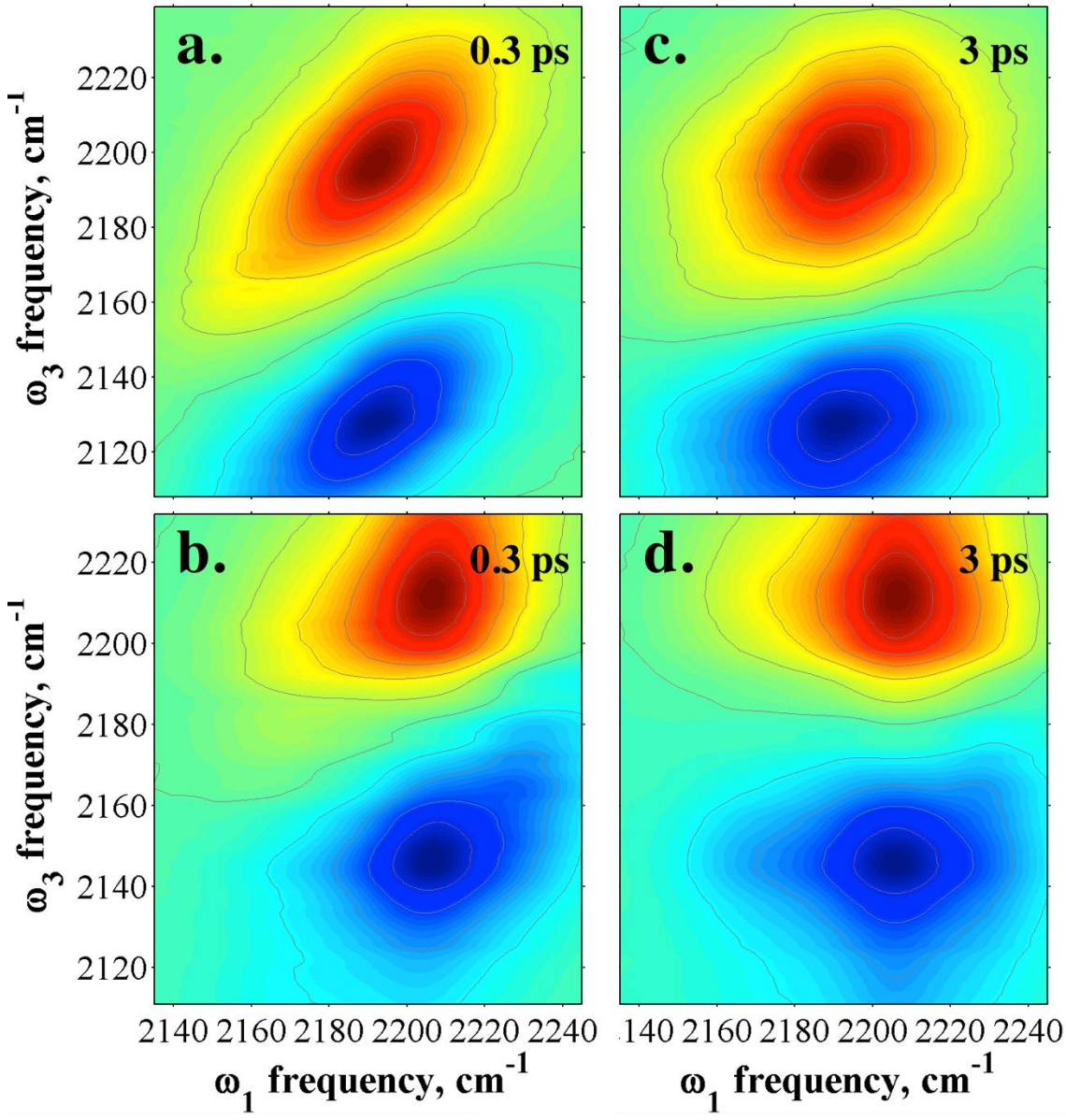

Figure 3.8. 2D-IR spectra collected at T_w = 0.3 (left column) and 3 ps (right column) for the ν_{Si-H} mode on TriMOS in isopropanol [(a) and (c)] and pentane [(b) and (d)].

For TriMOS, I observe in Figure 3.8a and 3.8b that at short T_ws, the peak shape is diagonally elongated, indicating that the Si-H oscillators have not yet sampled the full range of solvation environments. Comparison of these two contour plots reveals that the spectrum in isopropanol is more elongated along the diagonal direction than that in

pentane; the Si-H mode of TriMOS has either sampled a greater range of the available solvent configurations in pentane than in isopropanol in the first 300 fs, or there are less structural dynamics in the non-polar solvent. As the waiting time increases, the 2D-IR contour shapes become more circular, reflecting the loss of correlation due to spectral diffusion of the $\nu_{Si\text{-}H}$ oscillators (Figure 3.8c and 3.8d). By 3 ps, the 2D-IR spectral shape in pentane is nearly circular while some diagonal elongation persists in isopropanol at this T_w, revealing that the timescale of solvent shell rearrangements is slower in isopropanol.

To quantify these dynamic differences, I analyzed the centerline slope (CLS) for the v = 0-1 peaks at all T_ws for both molecules in all three solvents. Figure 3.9 shows the CLS values as a function of T_w along with multiexponential fits for TriMOS and TriPS in isopropanol, chloroform, and pentane. The CLS decays in isopropanol can be adequately represented by a double exponential fit for both TriMOS and TriPS, while a single exponential function is sufficient for the CLS decays in chloroform and pentane. This suggests that the solvent dynamics in chloroform and pentane enable all of the Si-H oscillators for both TriMOS and TriPS to experience all of the available frequencies under the linear lineshape by about 5 ps. In contrast, some $\nu_{Si\text{-}H}$ oscillators remain partially correlated with their starting frequencies in isopropanol for both molecules since the CLS decays have not yet reached the baseline.

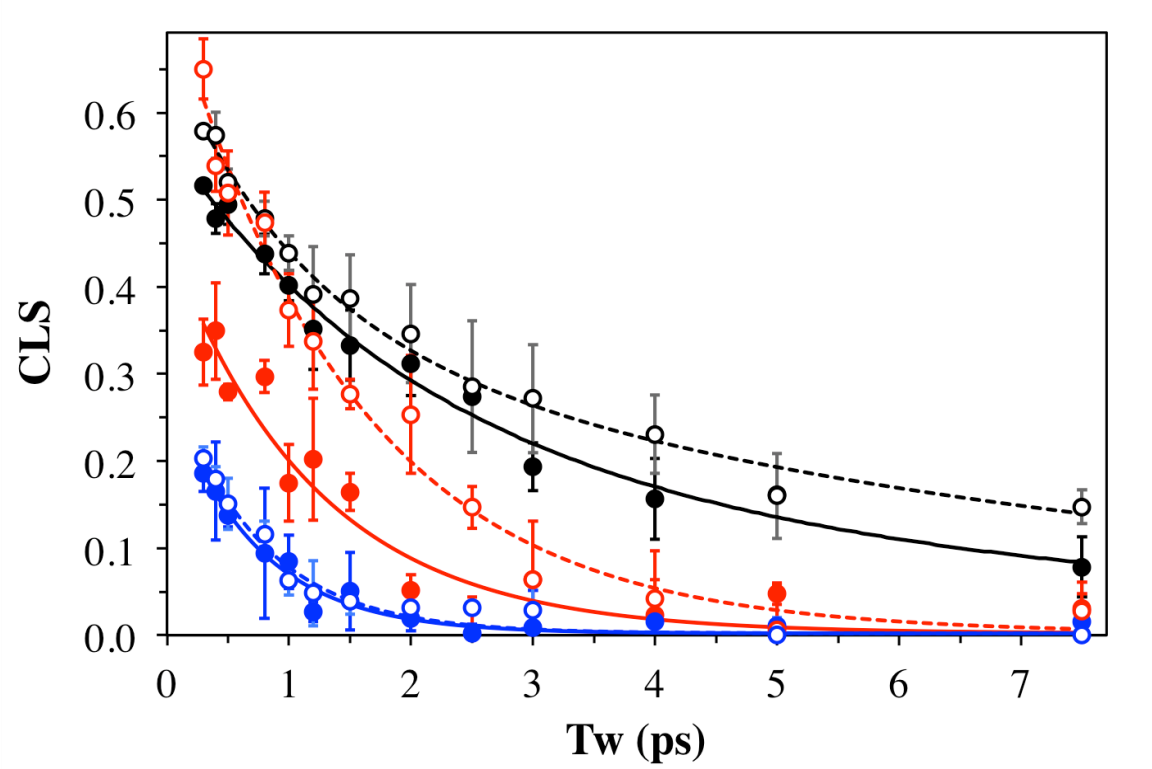

Figure 3.9. CLS decays as a function of T_w for TriMOS (solid markers) and TriPS (open markers) in isopropanol (black), chloroform (red), and pentane (blue). Overlaid are solid curves (TriMOS) and dotted curves (TriPS) to show multiexponential fits to the data described in the text. The markers are the average CLS values and the error bars are the standard deviations.

The CLS decays represent the normalized FFCFs, but they can be used to obtain the full FFCFs by iteratively fitting the CLS decays and the linear lineshapes,[163-164] thereby separating the homogeneous and inhomogeneous contributions to the FTIR spectra. The resulting FFCF parameters are given in Table 3.6 and can be categorized as unresolvably fast (Γ), fast spectral diffusion (~1 ps), and slow spectral diffusion (~10 ps). Vibrational dynamics are the fastest and the lowest amplitude in pentane, characteristic of a solvent that interacts very weakly with itself and couples very weakly to the $\nu_{Si\text{-}H}$ mode. Polar and strongly interacting solvents such as chloroform (weak H-bond donor) and isopropanol (strong H-bond donor and acceptor) exhibit slower, larger amplitude frequency

fluctuations in the FFCF. The homogeneous linewidths are similar for molecules in the same solvent and track inversely with the solvent polarity. Pentane exhibits the widest homogeneous linewidths for both solute molecules, despite having the narrowest FTIR peak widths; the $\nu_{Si\text{-}H}$ mode in TriPS is more homogeneously broadened. The FTIR lineshapes in chloroform and isopropanol are dominated by inhomogeneous broadening.

Table 3.6. FFCF parameters for TriPS and TriMOS in isopropanol, chloroform, and pentane.

solute	solvent	Δ_1 (cm^{-1})[a]	τ_1 (ps)[b]	Δ_2 (cm^{-1})[a]	τ_2 (ps)[b]	Γ (cm^{-1})[a]
TriMOS	isopropanol	16 (±4)	2.0 (±0.5)	12 (±4)	7 (±2)	6 (±2)
	chloroform	23 (±5)	1.2 (±0.2)	---	---	7 (±3)
	pentane	10 (±4)	0.7 (±0.1)	---	---	13 (±2)
TriPS	isopropanol	8 (±3)	1.1 (±0.6)	8 (±2)	8 (±3)	5 (±1)
	chloroform	15 (±2)	1.5 (±0.09)	---	---	6.1 (±0.7)
	pentane	8 (±1)	0.72 (±0.07)	---	---	7.9 (±0.2)

[a] Errors show the range of which that parameter could be increased while the other parameters floated to fit the FTIR lineshape 98% as well as the best value
[b] Standard error of the exponential fit.

Interestingly, the amplitudes are statistically greater for TriMOS than TriPS in isopropanol and chloroform. The timescales of the dynamics sensed by these two species are the same, but they apparently have a larger influence on the Si-H mode for TriMOS. We have hypothesized previously that specific solvent-solute interactions with the oxygen atoms bound to a silicon site might be responsible for the enhanced solvatochromism in molecules such as TriMOS.[7,233] However, the FFCFs presented here for TriMOS, which

has oxygen-bearing ligands, and TriPS, which lacks oxygen atoms, disprove this hypothesis, since the ν_{Si-H} on both molecules senses the same dynamics. Recall that DFT calculations above showed that enhanced solvatochromism arises from increased coupling of ν_{Si-H} to the reaction field due to mode polarization by the substituents. Here, we find that this polarization also enhances spectral diffusion.

The FFCFs for ν_{Si-H} on TriPS and TriMOS in isopropanol also exhibit a similar, slower dynamic contribution (Δ_2 and τ_2). Since the hydrogen atom of the Si-H group carries a negative partial charge (Table 3.2), it is not expected to donate a hydrogen bond to isopropanol, and such binding interactions have not been observed in silanes.[231] Similarly, hydrogen bonding interactions with the ligands are also ruled out by the lack of a hydrogen-bond acceptor in TriPS. Consequently, we attribute the slower component to the hydrogen bonding dynamics of isopropanol with itself since the timescale is similar to what has been reported.[234-237] To confirm this hypothesis, we computed the FFCFs' overall 2 ns trajectories shown in Figure 3.10 from QM/MM simulations, which were fitted to a combination of three exponentials plus a constant offset (shown by the thicker lines). The gas phase FFCF display notable beat behavior suggesting that the mode is oscillating in an underdamped manner compared to the mode in the solvents. The instantaneous frequencies along the dynamics trajectories of the TriMOS in the gas phase and in pentane in Figure 3.3 show that the gas phase trajectory exhibits roughly periodic spectral diffusion depending on the intramolecular interactions at each configuration, and this is present in its FFCF where we observe noticeable and regular fluctuations. Furthermore, the condensed phase simulations display similarly regular fluctuations in the FFCF, but there

is additional noise introduced by the solvent. To verify the convergence of the computed FFCFs, we compared the results averaged over 2 ns to that obtained using just half of the trajectory (1 ns) as shown in Figure 3.11. The results do not show appreciable changes in the timescales, although the fast fluctuations show some differences. Thus, within the timescale of our interest, the results are adequately converged. Overall, the parameters obtained from the computed FFCFs (Table 3.7) are in accord with those determined from experiment (Table 3.6). Similar to experiment, both probes in isopropanol required two additional inhomogeneous exponential terms to describe the FFCF, while all of the other FFCFs only required one. Additionally, the time constants for the second exponential are in reasonable accord with the lifetime of hydrogen bonds.[234-237] The third exponential contains dynamics that are motionally narrowed and would contribute to the homogeneous linewidth (Γ).

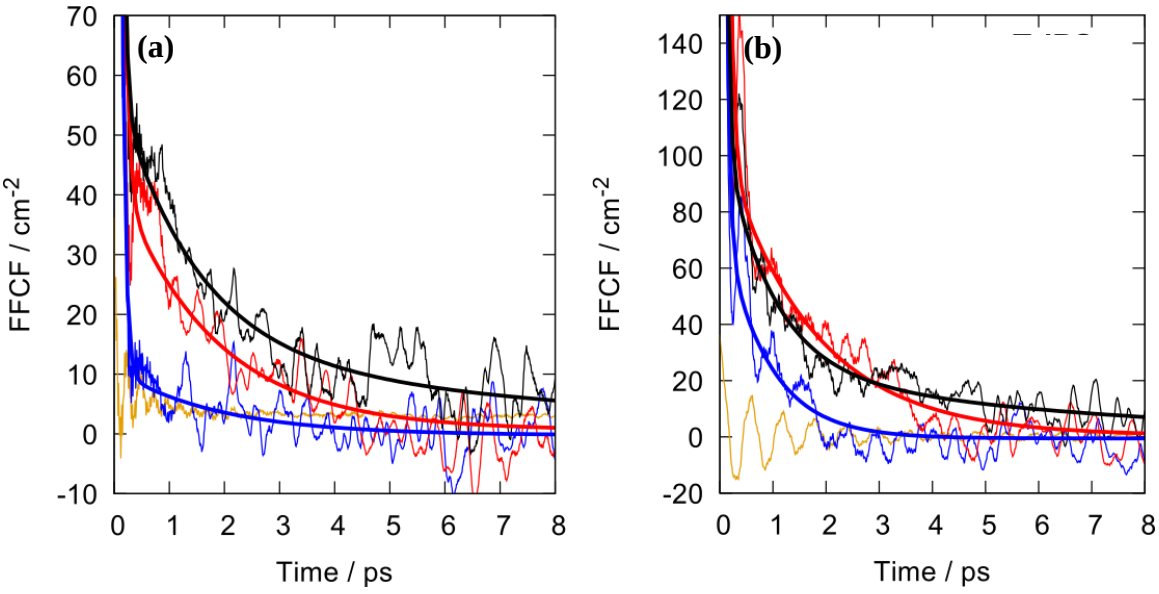

Figure 3.10. Computed FFCF from AM1/CHARMM vibrational dynamics trajectory for TriMOS (a) and TriPS (b) in in the gas phase (orange), isopropanol (black), chloroform (red), and pentane (blue).

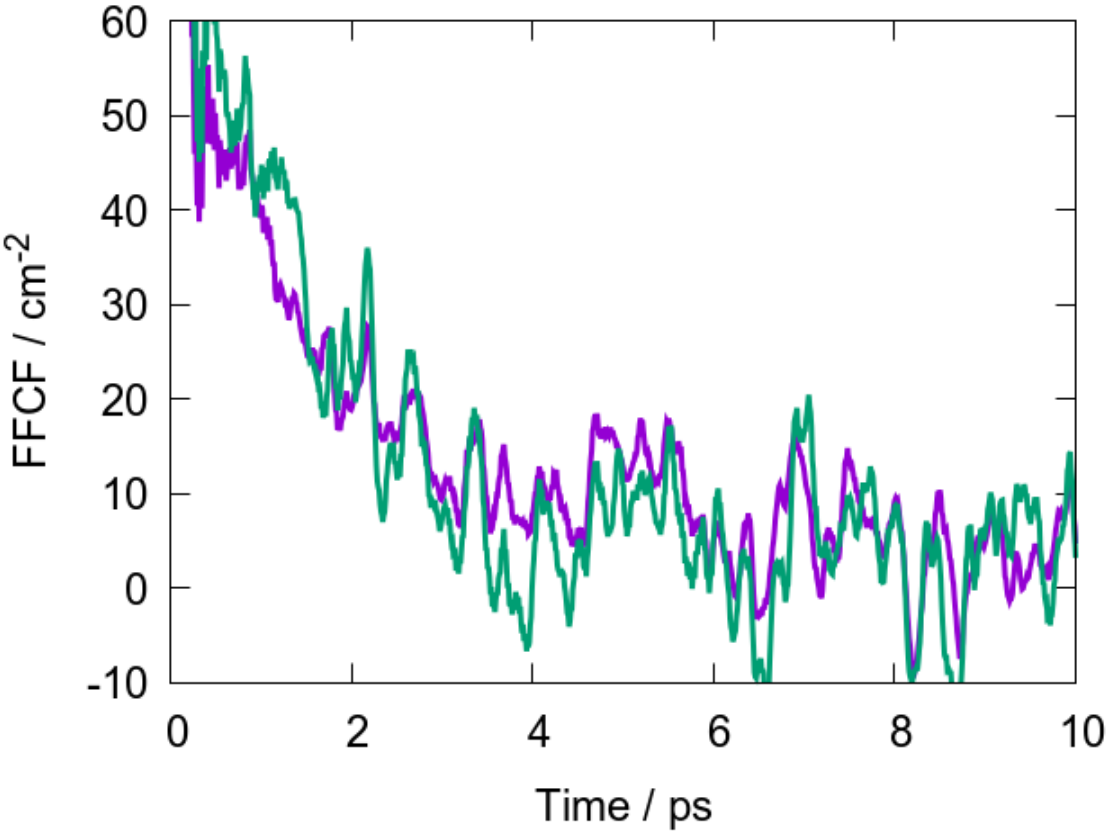

Figure 3.11. Frequency-frequency autocorrelation functions averaged over 1 ns trajectories (light green) and 2 ns trajectories (purple) from AM1/CHARMM simulations for TriMOS in isopropanol.

Table 3.7. Computed FFCF parameters for TriPS and TriMOS in the three solvents.

solute	solvent	Δ_1 (cm^{-1})	τ_1 (ps)	Δ_2 (cm^{-1})	τ_2 (ps)	Δ_3 (cm^{-1})	τ_3 (ps)
TriMOS	isopropanol	6.8	1.4	3.8	9.3	28.1	0.06
	chloroform	6.6	1.7	---	---	25.1	0.07
	pentane	3.3	1.9	---	---	27.1	0.06
TriPS	isopropanol	9.3	0.90	5.0	6.3	30.4	0.06
	chloroform	10.3	1.67	---	---	32.4	0.08
	pentane	8.9	0.84	---	---	29.56	0.06

The fast inhomogeneous spectral diffusion component (Δ_1 and τ_1) is ascribed to collective motions of bulk solvent molecules approximately resembling a dielectric continuum. Here, solvent molecules are indistinguishable, and coherent movement of the collection together leads to a variance in the electric field that is higher than the noise of the individual molecules. Spectral diffusion can be modeled here as a time-dependent Stark effect: the motions that lead to the largest variance in the electric field on the mode are those that contribute most strongly to the FFCF and are the basis for attribution of the signal lifetimes.

The FFCFs for the simulated solutes in isopropanol require a (Δ_2 and τ_2) with a correlation time that is longer than the continuum motions. This is attributed to the reorganization of the isopropanol hydrogen bond network. It cannot be due to hydrogen bonding with the solute, since it is present in the TriPS/isopropanol system as well. The hydrogen bond lifetime (τ_{HB}) of isopropanol was calculated as described in Section 3.3.5. Calculation of the Hydrogen Bonding Lifetime. Table 3.8 presents the τ_{HB} values for the first solvation shell molecules (defined as having a distance less than 6.0 Å to the solute) around TriMOS and TriPS, as well as for the bulk solvent. Hydrogen bonds exchange faster in the bulk solvent, but the τ_{HB} of the first solvation shell species are more relevant to the FFCF of $\nu_{Si\text{-}H}$ on the solutes. τ_{HB} in the first solvation shell are in excellent agreement with τ_2 in the FFCFs obtained by MD simulations (Table 3.7), strongly supporting the assignment that τ_2 dynamics in the experimental FFCFs originate from solvent shell hydrogen bond dynamics.

Table 3.8. Hydrogen bond lifetimes (τ_{HB}) in isopropanol simulations.

solvent environment	$\tau_{HB/bulk}$ (ps)	$\tau_{HB/first\ shell}$ (ps)
TriMOS / isopropanol	4.15	9.3
TriPS / isopropanol	4.18	8.3
Bulk isopropanol	4.88	---

The autocorrelation functions of solvent dipole moments [(dipole autocorrelation functions (DAFs)] were calculated for individual solvent molecules in the solvation shell around TriMOS and TriPS (Figure 3.12). Because the bond lengths of the solvent molecules are constrained using SHAKE,[238] the DAFs only contain angle bending, torsional modes, and rotational motions of each solvent molecule. Isopropanol and chloroform both display exponential decay behavior, characteristic of rotational motions. Pentane shows damped oscillatory behavior, suggesting that the DAF is dominated by torsional and bending modes rather than rotation. The DAFs of chloroform and isopropanol were fitted to a sum of three and four exponentials, respectively, to adequately quantify the dipole dynamics (Table 3.9).

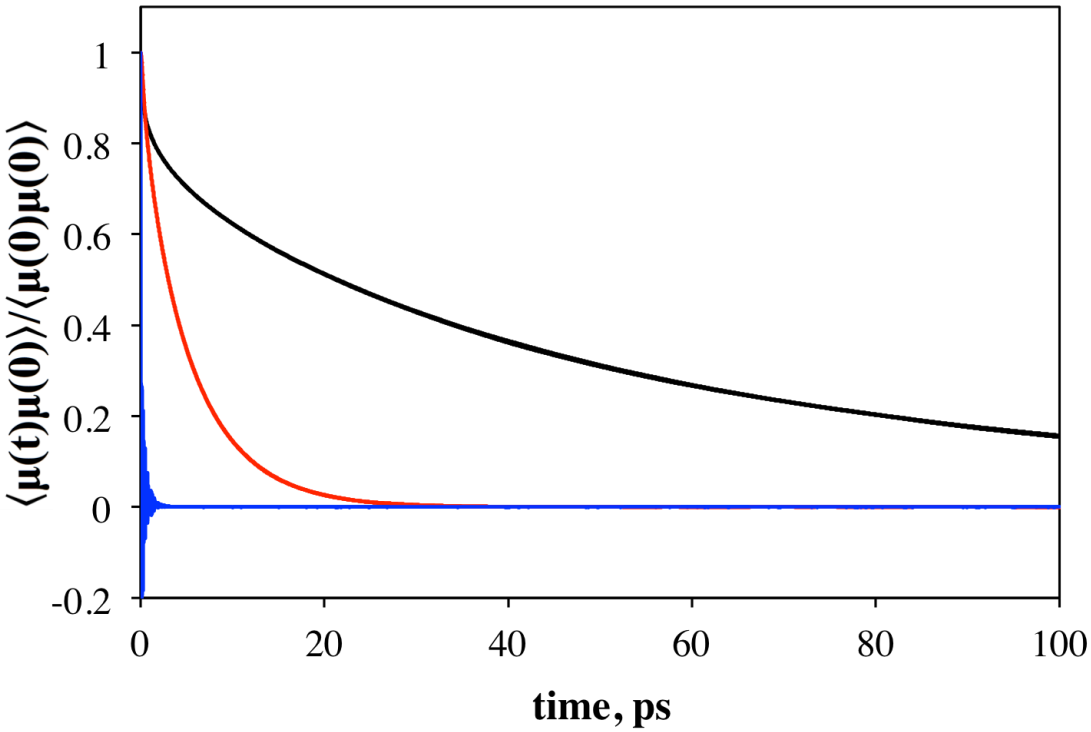

Figure 3.12. Normalized dipole autocorrelation functions (DAF) for individual solvent molecules in isopropanol (black), chloroform (red), and pentane (blue).

Table 3.9. Fitted parameters to the computed molecular dipole autocorrelation functions for TriMOS and TriPS in chloroform and isopropanol solutions.

chloroform				**isopropanol**			
TriMOS		**TriPS**		**TriMOS**		**TriPS**	
A	**τ (ps)**	**A**	**τ (ps)**	**A**	**τ (ps)**	**A**	**τ (ps)**
0.80	5.85	0.78	5.89	0.36	99.41	0.48	86.26
0.12	1.76	0.13	2.18	0.38	35.70	0.28	27.42
0.09	0.46	0.24	0.51	0.11	4.09	0.11	3.04
---	---	---	---	0.12	0.34	0.12	0.27

The DAF parameters for chloroform and isopropanol show the largest contribution to decorrelation from the slowest process (Table 3.9), which we attribute to rotation of the

whole molecule. Of the two solvents, molecular rotation in chloroform is significantly faster than that in isopropanol since chloroform is smaller, more spherical, and lacks restriction by hydrogen bonding interactions. Previous deuteron scattering studies reported that the rotational correlation times for deuterated isopropanol and $CDCl_3$ differed by a factor of 6,[239] which is relatively consistent with the slowest time coefficients obtained from the DAFs. Isopropanol displays two longer lifetimes of ~32 ps and ~92 ps that we tentatively attribute to rotational motions within a hydrogen bonded network. These assignments are consistent with experimental rotational correlation times of 22 ps and 91 ps that were measured by NMR[239-240] and dielectric spectroscopies,[240-241] respectively. Meanwhile, we conjecture that the shortest lifetime (~0.4 ps) is dominantly due to fast intramolecular motions such as angle bending or dihedral rotations.

Isopropanol also contains a time coefficient that is comparable to the hydrogen bond lifetime. A similar value has been reported in the rotational correlation times measured by dielectric spectroscopy.[242] The largest DAF lifetime in isopropanol is on the order of 100 ps, indicating that there is no significant rotation of the dipole when isopropanol exchanges hydrogen bonds. This is most likely due to the size of isopropanol. The lifetime that is on the same order as the hydrogen bond lifetime only accounts for about 10% of the change in the dipole. Furthermore, the large amount of time it takes for isopropanol to rotate suggests that it is hindered by hydrogen bonding interactions. Isopropanol maintains its orientation for a long time by exchanging hydrogen bonds with a close neighbor.

3.5. Conclusions

Proper interpretation of static and time-resolved vibrational spectroscopic data requires an understanding of the ways in which homogeneous and inhomogeneous effects are manifested in spectral change. In this study, TriMOS and TriPS provided an opportunity to monitor the same probe, the Si-H vibrational mode, with two different ligand sets and three solvent systems by steady-state FTIR and time-resolved 2D-IR spectroscopies. DFT calculations provided insight into the differences in silicon hydride sensitivity to solvent through increased mode polarization with more electron withdrawing ligands. Calculations and simulations revealed that the solvatochromic trends of the hydride mode arise from specific hydrogen and halogen bonding interactions with the solute. Spectral diffusion experienced by $\nu_{Si\text{-}H}$ was found to be characteristic of the solvent type rather than the solute structure, yet showed the same sensitivity observed in the FTIR solvatochromic shifts. Therefore, the solvent motions are dominated by their interactions with neighboring solvent molecules rather than with the solute. MD simulations confirmed that the dynamics experienced in isopropanol were due to hydrogen bonding fluctuations in the surrounding solvation shell. This was further corroborated by the calculation of the dipole autocorrelation function of individual solvent molecules throughout the bulk. These results showed the principle motions experienced by isopropanol molecules, which included a lifetime of similar magnitude to the hydrogen bonding lifetime. The remaining motions include rotational diffusion, and low frequency intramolecular motions.[a]

[a] The authors gratefully acknowledge partial supports from the National Science Foundation (NSF) under CHE-0847356 and CHE-1464416 (to A.M.M.), the National Natural Science Foundation of China under Grant No. 21533003, and the National Institutes of Health under Grant No. GM46376 (to J.G.). C.M.O. and I.C.S. were supported by a NSF Graduate Student Research Fellowship Grant Number 00039202.

3.6. Full Set of 2D-IR Spectra

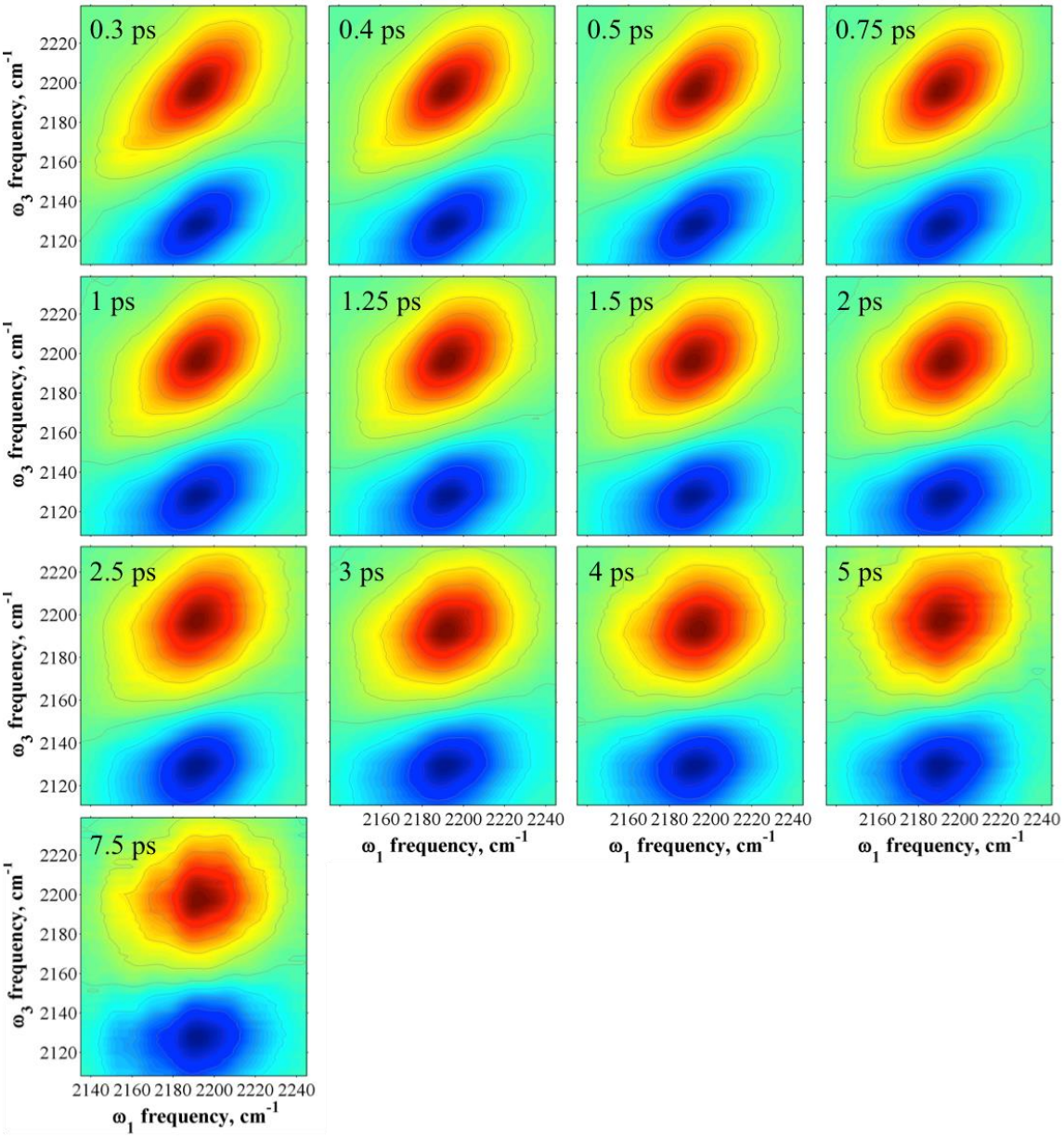

Figure 3.13. 2D-IR spectra of TriMOS in isopropanol for all T_w values of TriMOS.

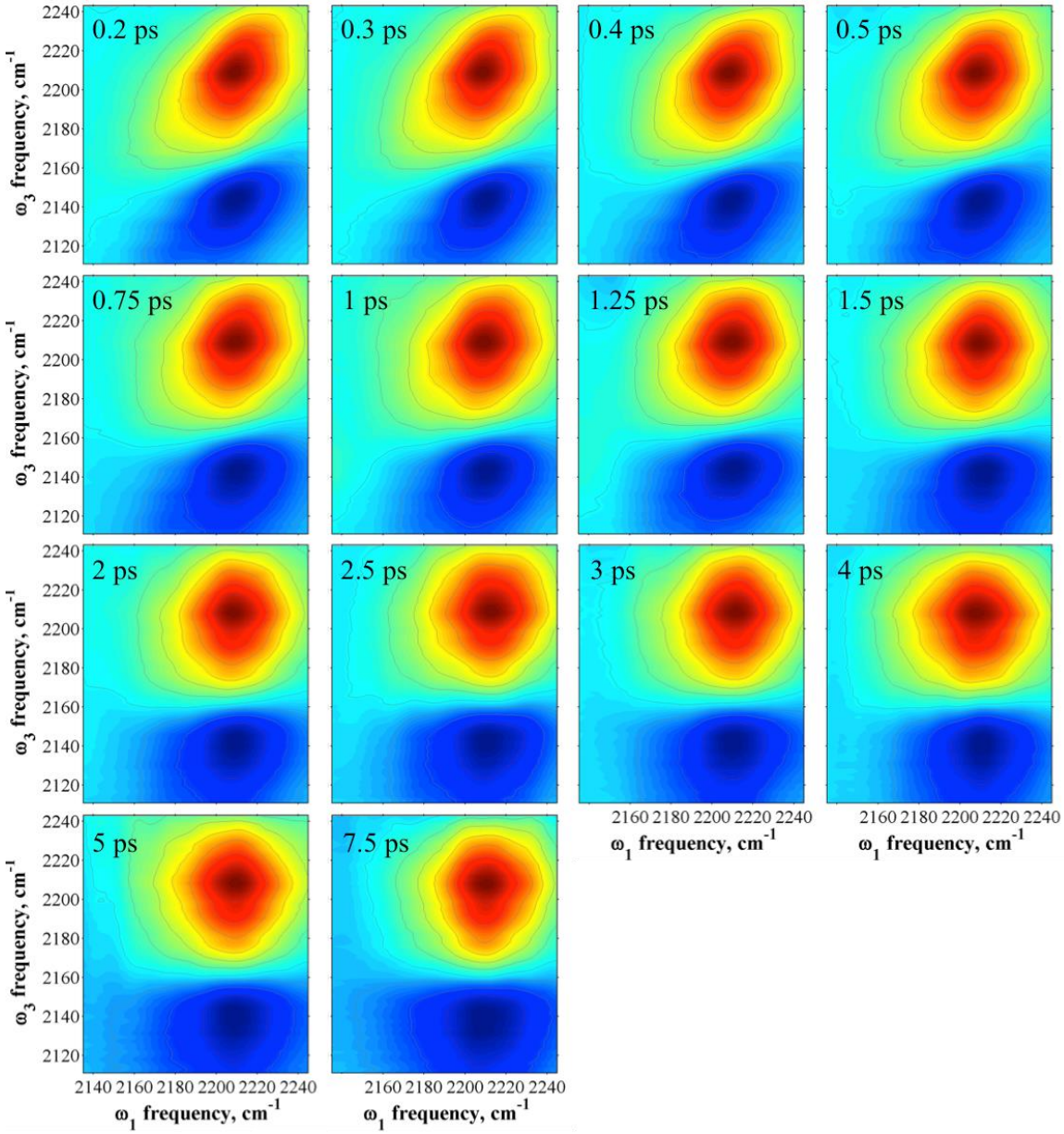

Figure 3.14. 2D-IR spectra of TriMOS in chloroform for all T_w values.

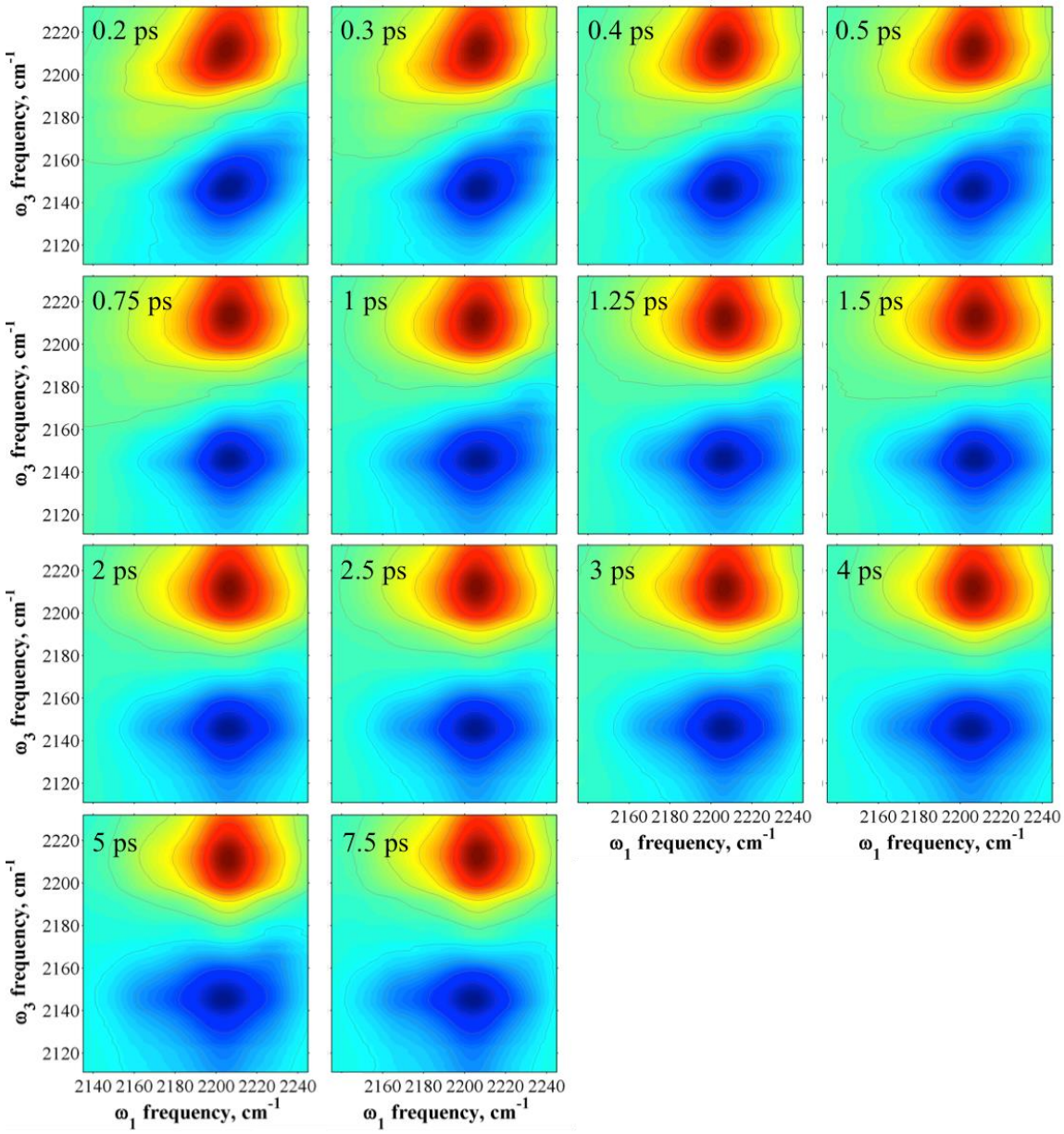

Figure 3.15. 2D-IR spectra of TriMOS in pentane for all T_w values.

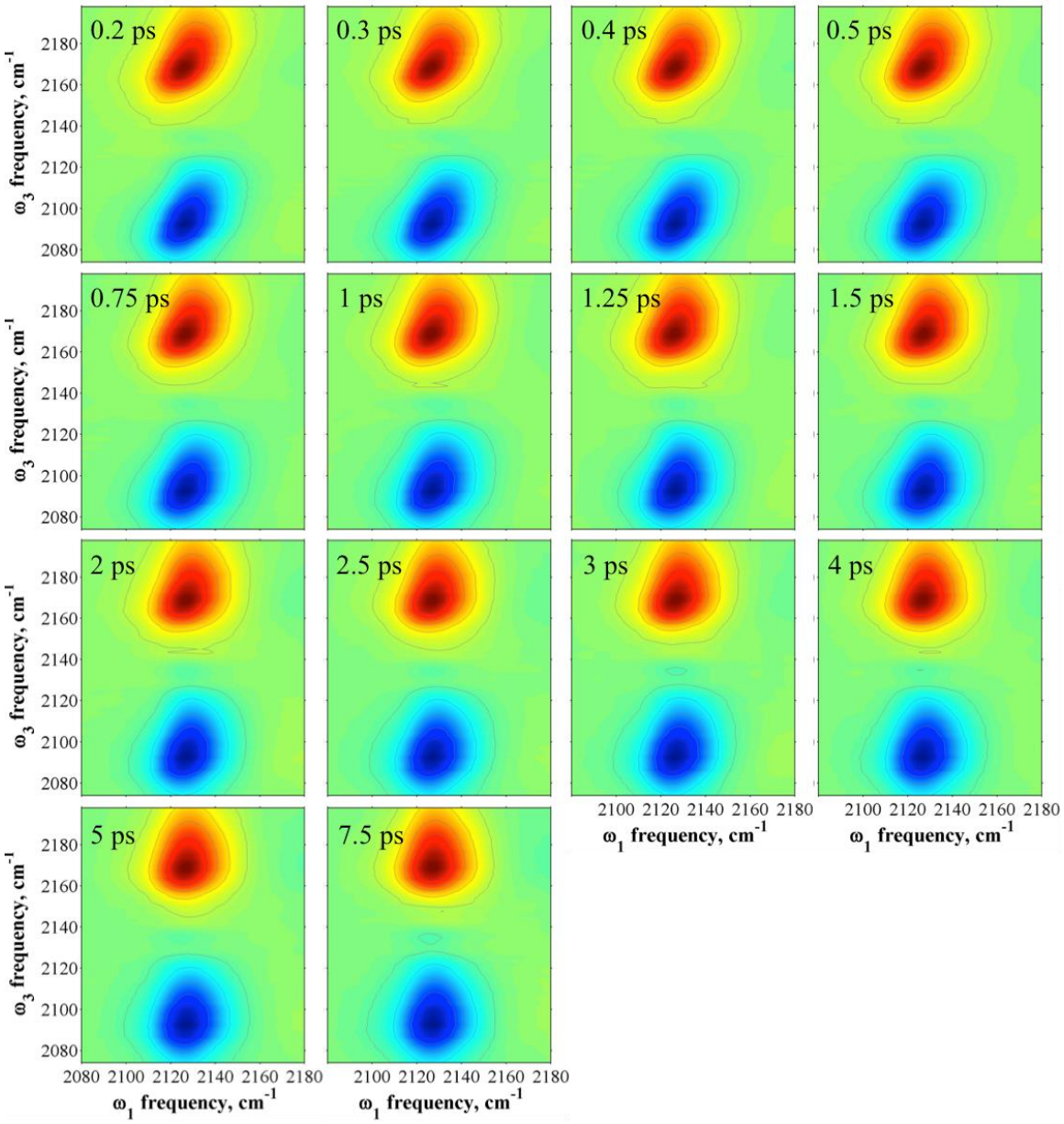

Figure 3.16. 2D-IR spectra of TriPS in pentane for all T_w values.

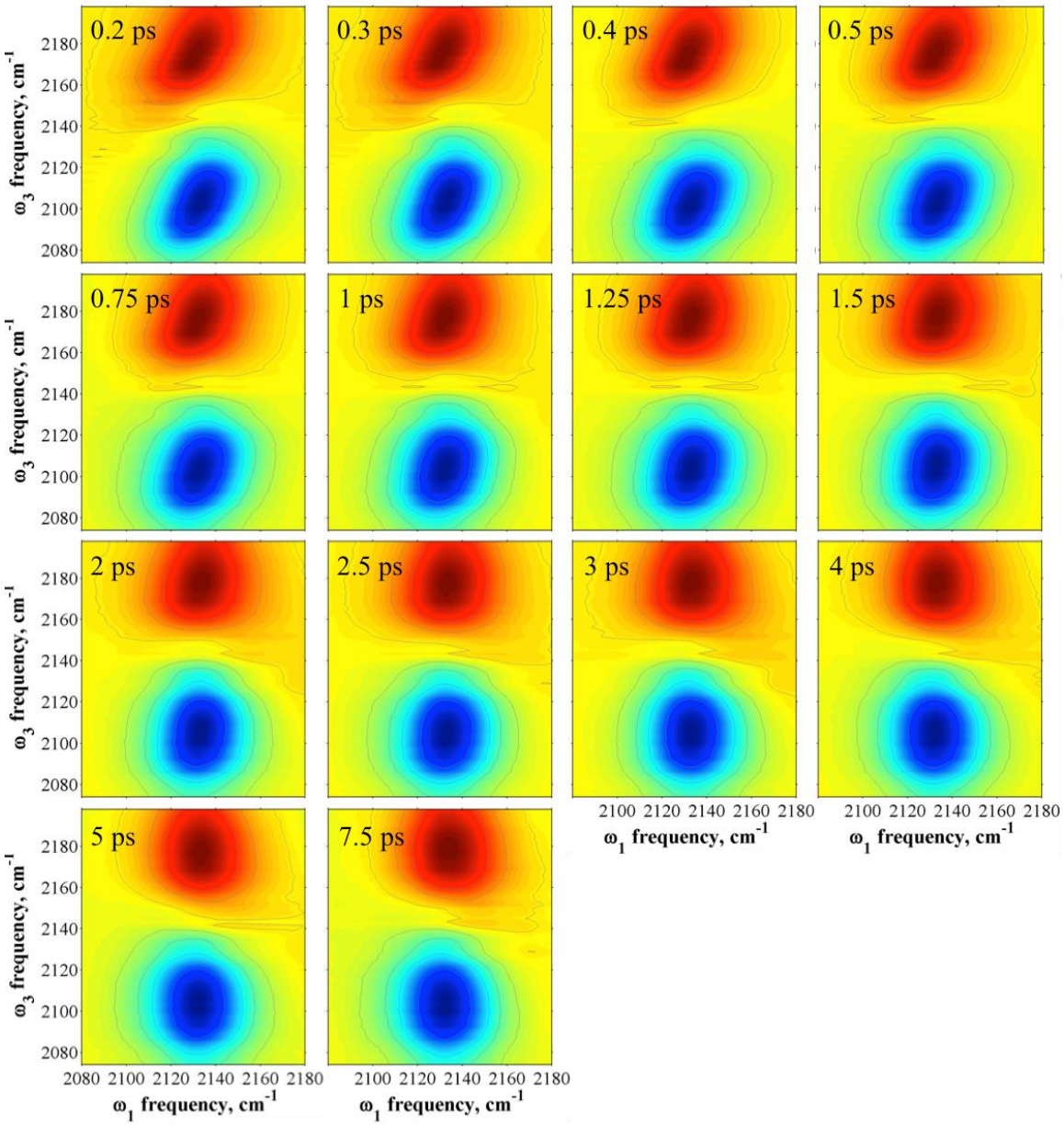

Figure 3.17. 2D-IR spectra of TriPS in chloroform for all T_w values.

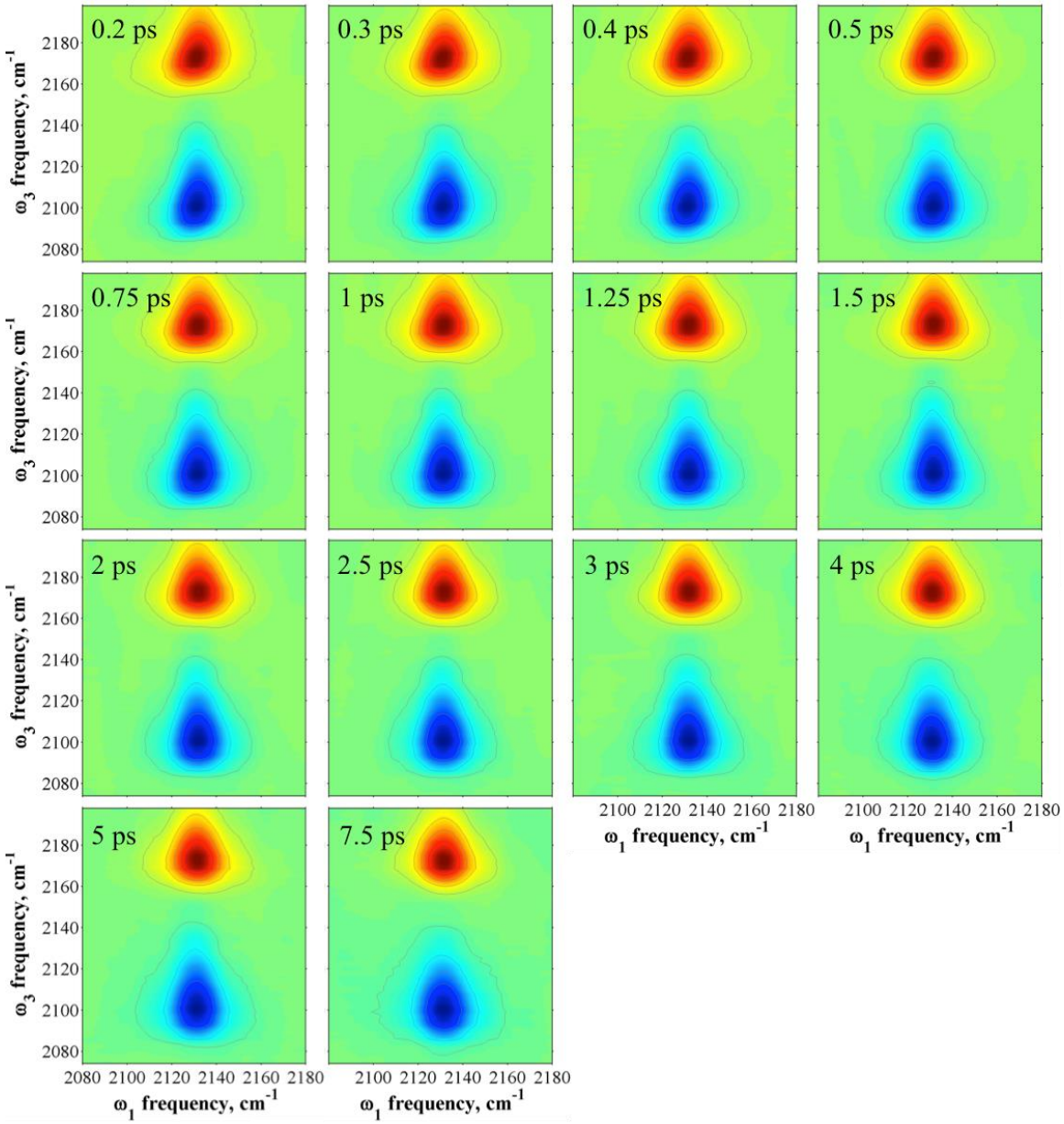

Figure 3.18. 2D- IR spectra of TriPS in pentane for all T_w values.

Chapter 4. Influence of Solvent Swelling on Ultrafast Structural Dynamics in Polydimethylsiloxane Thin Films by Two-Dimensional IR Spectroscopy

Reproduced with permission from

Olson, C. M.; Massari, A. M., Influence of Solvent Swelling on Ultrafast Structural Dynamics in Polydimethylsiloxane Thin Films by Two-Dimensional IR Spectroscopy. *J Phys. Chem. A* **2018**, *122* (6), 1592-1599.

4.1. Chapter Summary

Fourier transform infrared and two-dimensional IR (2D-IR) spectroscopies were applied to polydimethylsiloxane (PDMS) cross-linked elastomer and a siloxane oligomer without solvent and swollen or dissolved in various solvents. The silicon hydride, which is covalently bound to the polymer chains, was the vibrational probe for the systems studied. There is almost an absence of vibrational solvatochromism in these systems. Frequency-frequency correlation functions obtained by 2D-IR spectroscopy show that the insensitivity of the FTIR spectra is due to overwhelming heterogeneity. However, the homogeneous contribution to the FTIR spectrum is smaller for the elastomer than the oligomer showing that the cross-linking process restricts the frequency fluctuations that are experienced by the hydride mode. The silicon hydride mode in a cross-linked, solvent-free PDMS film also exhibits spectral diffusion that must be due to polymer structural motions on the ultrafast timescale that are active above the glass transition temperature. Once solvents penetrate and swell the elastomer, the polymer likely continues to experience these polymer structural motions. However, I find that the vibrational dynamics are characteristic of the infiltrating solvents, showing that at least some fraction of the measured dynamics originate in solvent motions.

4.2. Introduction

Elastomer networks are formed by covalently cross-linking high molecular weight polymer chains in a random fashion.[64] Poly(dimethylsiloxane) (PDMS) is one of the simplest non-hydrocarbon elastomers that has found a wide range of applications such as

adhesives, sealants, coatings, and encapsulants.[51-53] It has a characteristically low glass transition temperature due to a high degree of backbone flexibility.[51,53-56] This structural flexibility has important ramifications for its permeability to gases and other small molecule penetrants, such as solvent molecules.[130-135,243-244] It also has excellent thermal and oxidative stability,[55] optical transparency, and biocompatibility, and is simple and inexpensive to synthesize.[58-60,65] The properties of PDMS elastomers can be further tuned by varying chain lengths and cross-linking density, or by adding fillers to the network.[61-63,80]

In recent years, PDMS has found great utility in water-based microfluidic devices. However, the elastomer swells in common organic solvents, which leads to deformation, distortion, and even collapse of microfluidic channels.[81,124,245] Swelling has also been exploited for certain applications such as chemical sensors[120] and pervaporative membranes.[128] Elastomer swelling is driven by thermodynamics. The free energy of mixing promotes expansion through enthalpic contributions from solvent-polymer interactions that stabilize extended chain conformations and entropic contributions due to chain extension.[87,91,121,123] For a hydrophobic polymer like PDMS, nonpolar solvents are the most favorable and contribute to the enthalpy of mixing through dispersion interactions.[124-126] Network expansion equilibrates with the retractive forces imposed by the physical cross-links to reach a final, average polymer structure.[118,120-122]

The structural changes that accompany swelling have been described by the Flory-Rehner[83,87-88] and James-Guth models.[85,98] The Flory-Rehner model assumes that the movement of the cross-links are completely suppressed and that the microscopic

deformation of the elastomer network is proportional to the macroscopic deformation of the sample. On the other hand, the James-Guth model allows the cross-links to fluctuate around their mean positions and move freely through one another. Both models assume an ideal, homogeneous network. In real polymer networks, imperfections cause polymer chain entanglements that decreases the swelling capacity of a polymer. Some have argued that the contribution of these entanglements act like pseudo-crosslinks,[110-112] while others believe the entanglements restrict the fluctuations of the cross-links.[102-103,109] Flory and Erman modified the original model to rationalize these discrepancies by including a force from the entanglements.[101-102,246]

Although the average polymeric structures before and after swelling are dictated by thermodynamics, the kinetics of reaching those states and many of their final properties are dictated by structural dynamics.[127] Polymer dynamics span many orders of magnitude in time from milliseconds[114-115] to picoseconds.[115-116] The swelling process itself requires diffusion of solvent penetrants through the polymeric matrix, which is facilitated by local backbone and side chain motions.[128-135] MD simulations by Müller-Plathe showed that the infiltrating solvent has a plasticizing effect on polymer motions leading to increased structural flexibility.[128-129] Once enhanced in the swollen state, the same segmental motions that were integral to the swelling process itself, serve to further increase permeability of the polymer to other small molecule penetrants.[129,133] Solid-state NMR,[63,132] neutron scattering measurements,[115-116,247] and MD simulations[128-129,131-132,243-244] have shown conclusively that there is a direct correlation between penetrant diffusion and picosecond polymer dynamics. For this reason, it is important to characterize not only the average

polymeric structure but also the time-dependent structural motions of the polymer and its associated solvent penetrants.

In this chapter, vibrational solvatochromism and spectral diffusion of the silicon hydride in siloxane oligomer solutions and PDMS elastomer films in three different solvents and in the absence of solvent were investigated using Fourier transform infrared (FTIR) and two-dimensional infrared (2D-IR) spectroscopies. These complementary approaches provide molecular level insights into the interactions between the polymer and the solvent as well as the structural dynamics that accompany the swollen and contracted states.[248]

4.3. Experimental Materials and Methods

Chloroform (99.9% purity, anhydrous, Acros Organics), isopropanol (99.5%, anhydrous, Sigma-Aldrich), and *n*-pentane (98%, Fisher) were used as received. A Sylgard® 184 silicone elastomer kit from Dow Corning was used to fabricate thin cross-linked PDMS elastomer films.[66-68] The kit consisted of an elastomer base (Sylgard-184A) and a curing agent (Sylgard-184B). The elastomer based contained >60 wt% dimethylvinyl-terminated poly(dimethylsiloxane) oligomers, 30-60 wt% dimethylvinylated and trimethylated silica, 1-5 wt% tetra(trimethoxysiloxy)silane, and a Pt-based catalyst. The curing agent contains 40-70 wt% poly(dimethyl, methylhydrogensiloxane), 15-40 wt% dimethylvinyl-terminated poly(dimethylsiloxane) oligomers, 10-30 wt% dimethylvinylated and trimethylated silica, and 1-5 wt% tetramethyl tetravinyl cyclotetrasiloxane.[60-62,69] Poly(dimethyl, methylhydrogensiloxane) in the curing

agent is the cross-linking species and contains the silicon hydride group that serves as the vibrational probe in this study.[60-62]

The curing agent contains the cross-linker, which is poly(dimethyl, methylhydrogen siloxane) due to the silicon hydride (see structure in Figure 4.1). Dimethylvinyl-terminated poly(dimethylsiloxane) oligomers and tetramethyl tetravinyl cyclotetrasiloxane are used to create the polymer network with the cross-linker. Dimethylvinylated and trimethylated silica are used as reinforcing materials to improve the mechanical properties of the elastomer.[60,66-67] The tetra(trimethoxysiloxy)silane acts as a modulator which inhibits fast cross-linking at room temperature as to allow more time to prepare the samples.[71]

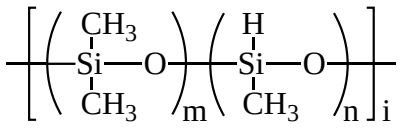

Figure 4.1. Poly(dimethyl, methylhydrogen siloxane)

The elastomer base and curing agent were mixed with a 10:1 mass ratio. Upon mixing, the vinyl groups and the silicon hydride hydrogens underwent a platinum-catalyzed hydrosilylation reaction.[61,71] The mixture was then doctor-bladed in a 5 mm x 5 mm square opening in the middle of a piece of Magic tape (~38 μm thick) on a 3 mm CaF_2 window. The sample cured under ambient conditions for 2 days.

The PDMS elastomer was studied spectroscopically by sandwiching the window that had the film with a clean CaF_2 window and a 50 μm Teflon spacer between the two.

The space between the windows was filled with one of three solvents or just air. The PDMS elastomer was immersed in solvent throughout data collection to ensure that the system stayed swollen. The PDMS cross-linker oligomer (in Sylgard-184B) was also studied dissolved in each solvent as a 5 wt % solution and used within 1 week of preparation. Spectroscopic studies were performed on the solutions sandwiched between two 3 mm CaF_2 windows with a 50 μm Teflon spacer. To study the cross-linker oligomer with no solvent, the curing agent was placed between two 3 mm CaF_2 windows with no spacer to reduce the IR absorbance of the sample.

Fourier transform infrared (FTIR) spectra were collected on a Nicolet 6700 FTIR spectrometer (Thermo Scientific) with at least 16 scans and a resolution of 1 cm^{-1}. A background spectrum of each of the solvents was subtracted from the respective PDMS elastomer and cross-linker oligomer IR spectra.

The 2D-IR instrument has been described previously in Section 2.3.3.[4,13] A regeneratively amplified Ti:Sapphire laser (Spectra-Physics, 800 nm, 40 fs pulse duration, 500 mW, 1 kHz repetition rate) pumped an optical parametric amplifier (OPA, Spectra-Physics), and the near-IR signal and idler beams were difference frequency mixed in a silver gallium sulfide crystal ($AgGaS_2$, 0.5 mm thick) to generate mid-IR pulses (3 μJ /pulse, 90 fs FWHM, ~200 cm^{-1} bandwidth FWHM). The mid-IR pulses were tuned to the silane (Si-H) stretching frequency of 2160 cm^{-1}. The pulses were then divided into three ~1 μJ p-polarized pulses and focused at the sample in a BOXCARS geometry.[152] The generated vibrational echo signal was heterodyned with a local oscillator and detected with a liquid N_2 cooled MCT linear array detector (Infrared Associates, Inc.) with a spectral

resolution of ~4 cm^{-1}. The system was continuously purged with dry air (-100 °F dew point) during data collection from the OPA to the detector.

The first frequency dimension (x-axis, ω_τ or ω_1) was achieved by scanning the time delay between pulses 1 and 2, τ, in increments of 5 fs and subsequent Fourier transformation.[36,38,160] The second dimension (y-axis, ω_m or ω_3) was obtained by an optical Fourier transform of the heterodyne detected vibrational echo signal by dispersing it from the monochromator diffraction grating. Each 2D-IR spectrum was collected while the time delay between pulses 2 and 3, T_w, was maintained at a fixed value. The resulting data were processed to obtain the purely absorptive 2D-IR spectrum[153,205] and phase corrected using the pump-probe projection theorem and the absolute value center as constraints as described in Section 2.3.4.[164,206] The FTIR spectrum of the sample was used as an absorption correction prior to phasing due to the probe beams passing through the sample while the local oscillator does not in our experimental setup.[157]

IR pump-probe spectroscopy was carried out with the same laser system as described above.[4] The data were fit from 1 to 75 ps to determine the population relaxation times (lifetime, T_1) for the v = 0-1 and 1-2 transitions. The vibrational relaxation times for these two transitions consistently showed the same trends, and the 0-1 values were used in data analyses. The T_1 values were found by fitting the decays to single exponentials and are shown later in Table 4.1.

The 2D-IR spectra were analyzed using the centerline slope (CLS) method to obtain the frequency-frequency correlation function (FFCF).[163-164] For the CLS analysis, the maximum intensity for the 0-1 and its associated central frequency on the ω_1 axis were

found for all the 2D-IR spectra for each of the systems. The frequency range used to find the CLS was the central frequency +/- 8 cm^{-1}. Other ranges were chosen, but the CLS did not change significantly. Therefore, this range was used for the final analysis.

The FFCF was modeled according to the following equation:

$$FFCF(t) = \frac{\delta(t)}{T_2} + \Delta_1^2 \exp\left(\frac{-t}{\tau_1}\right) + \Delta_o^2 \quad (4.1)$$

Here, δ(t) is a delta function and T_2 is the total dephasing time, which has contributions from the vibrational and orientational relaxations as well as the pure dephasing time, T_2^*.[163-164] In the current study, orientational relaxation has a negligible contribution due to the cross-linker oligomer being a large molecule (MW over 1000 g/mol according to a personal communication with the manufacturer)[68] and the PDMS elastomer having all of the oligomers linked together via the cross-links. The relationship between T_2, T_2^*, and the vibrational relaxation lifetime, T_1 is:

$$\frac{1}{T_2} = \frac{1}{T_2^*} + \frac{1}{2T_1} \quad (4.2)$$

The pure dephasing time, T_2^*, is the time it takes for the oscillators that comprise the macroscopic polarization to lose the phase relationship without the loss of excitation. The pure dephasing time arises from fast intramolecular dynamics and intermolecular interactions that cause random, fast fluctuations in the vibrational frequency of the mode.[143] T_2 defines the homogenous line width, Γ, through the relation: $\Gamma = \frac{1}{\pi T_2}$.[36,138] Δ_o is the contribution from pseudo-static inhomogeneous broadening due to the structural dynamics in the elastomer, cross-linker, and solvent that influence the Si-H frequency but evolve on a much slower timescale than our measurements. Δ_1 is the average amplitude frequency

shifts caused by a particular frequency-perturbing process with correlation time τ_1.[163-164] Therefore, Δ_1 and Δ_o are the standard deviations of the Gaussian distribution of the Si-H frequencies. To obtain the total standard deviation (Δ), Δ_1 and Δ_o must be added in quadrature. The FWHM of the Gaussian lineshape, f_g, is related to Δ through the relation $2\Delta\sqrt{2\ln(2)}$.[36,165] The total FWHM of the lineshape, which is a Voigt profile, can be found using the approximation of $\frac{\Gamma}{2} + \sqrt{\frac{\Gamma^2}{4} + f_g^2}$.[166]

The time constant (τ_1) in the FFCF was obtained directly from fitting the CLS decays, which has been shown to be highly accurate.[163-164] However, the amplitude of the exponential contribution (Δ_1) and the offset (Δ_o) assume a FFCF normalized to unity and a y-intercept that is likewise normalized. The amplitude from the CLS decay fits and the linear FTIR FWHM were used to calculate approximate values for Δ_1, Δ_o, and T_2 of the full FFCF by following the procedure by Kwak and co-workers.[163-164] These initial values were then applied to a FFCF, where the first-order response function was used to reproduce the linear FTIR lineshape.[137] The lineshape was fit by iteratively varying the amplitudes, as well as the central frequencies. The CLS method was developed using the short-time approximation, so the values for Δ_1, Δ_o, and T_2 are underestimated due to the method's inability to distinguish between homogeneous terms and fast spectral diffusion (compared with the FID) as described in Section 2.3.6. Therefore, the floated Δ_1, Δ_o, and T_2were constrained to only increase from the estimated values.

4.4. Results and Discussion

The solvent-subtracted FTIR spectra for the silicon hydride stretching vibration (ν_{Si-H}) on the PDMS elastomer without solvent and swollen with 2-propanol, chloroform, and pentane are shown in Figure 4.2a. These solvents were chosen due to the range of swelling induced in the elastomer, and because they offer a diverse palette of solvent-solute interactions. Pentane is nonpolar and aprotic; 2-propanol is polar and protic, readily donating and accepting hydrogen bonds; chloroform is polar but a poor hydrogen bonding solvent. In previous work, these three solvents were found to span the range of solvatochromic shifts for silicon hydride vibrations.[249] The ν_{Si-H} on PDMS is nearly insensitive to the different solvent environments. A slight solvatochromic trend (less than a wavenumber) is seen in order of increasing frequency: chloroform (red) < 2-propanol (black) < pentane (blue) < no solvent (green). In small molecules, ν_{Si-H} is tuned by the inductive effect of the substituents that are attached to the silicon,[6-7,229,231-232,250-251] but in this case the substituents are the same. Therefore, any spectral changes must be due to structural changes induced by swelling and the influence of the infiltrating solvent on the hydride vibration. Recent work from our group has shown that the solvatochromic effect for the silicon hydride can be explained by a vibrational Stark effect with the addition of specific solvent-solute interactions in the case of hydrogen and halogen bond donors.[249] The FTIR peak widths in Figure 4.2a are slightly more sensitive to the different solvent environments, increasing in the order of none (green) < pentane (blue) < 2-propanol (black) < chloroform (red) and consistent with our previous report (excluding the solvent-free sample).[249]

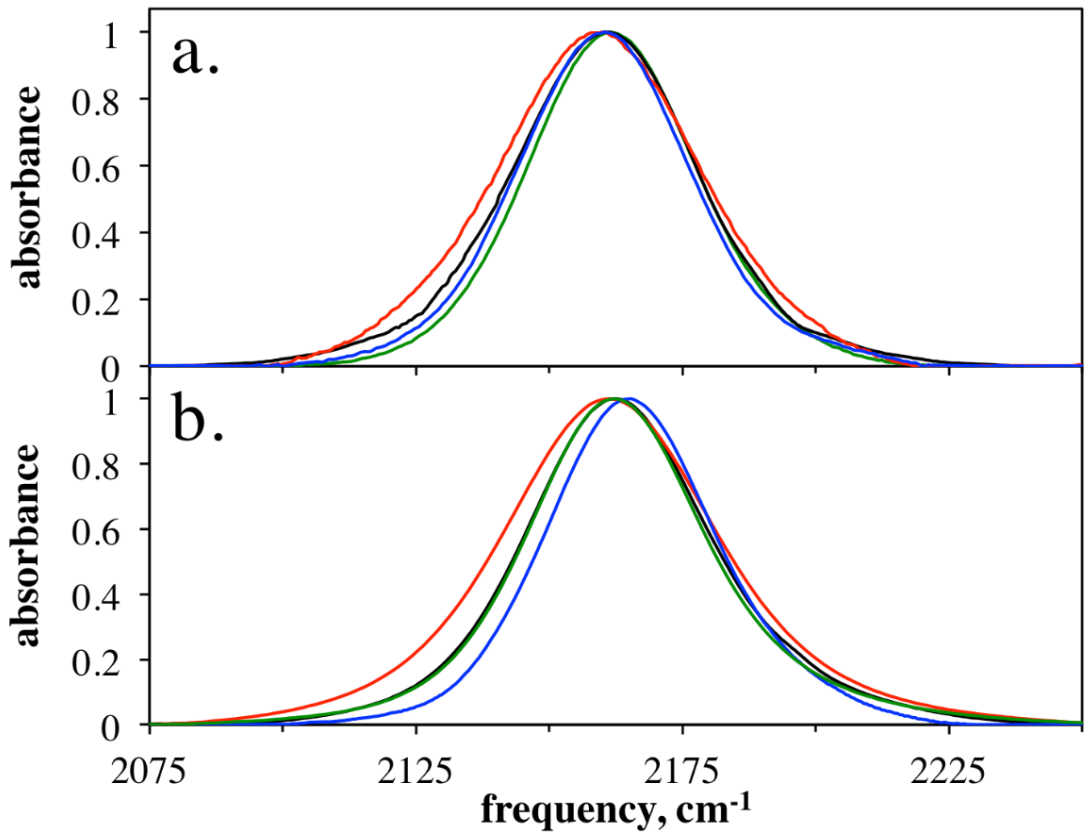

Figure 4.2. Solvent subtracted, baselined, and normalized FTIR spectra of the Si-H vibration for PDMS elastomer (a) and cross-linking oligomer (b). In both frames, the spectra correspond to no solvent (green), isopropanol (black), chloroform (red), and pentane (blue). Note that the spectrum for the cross-linker in no solvent.

For comparison, Figure 4.2b shows the FTIR spectra of oligomeric cross-linking species in the same solvents prior to being polymerized into the PDMS elastomer. The hydride on the cross-linker oligomer is only slightly more solvatochromic with its frequency shifts spanning a range of 4 cm^{-1} and has the same trend except for a higher frequency in pentane than without solvent. As with the elastomer, the peak widths for the hydride on the cross-linker are somewhat more sensitive to the different solvent environments than the central frequency and follow the same trend observed in the elastomer except that the cross-linker in no solvent is slightly wider than the cross-linker

in pentane. The center frequencies and peak widths of the ν_{Si-H} in the various systems are provided in Table 4.1.

Table 4.1. Center frequency (ν_{Si-H}), peak width (FWHM), and vibrational lifetime (T_1) values for the PDMS elastomer and cross-linker oligomer without solvent and swollen or dissolved in various solvents.

sample	solvent	ν_{Si-H} (cm^{-1})	FWHM (cm^{-1})	T_1 (ps)[a]
PDMS elastomer	none	2161.3	36.9	5.0 (± 0.2)
	isopropanol	2160.2	39.8	4.69 (± 0.08)
	chloroform	2159.9	44.2	4.90 (± 0.05)
	pentane	2160.4	37.6	4.72 (± 0.06)
cross-linker oligomer	none	2162.5	38.5	5.2 (± 0.1)
	isopropanol	2162.3	39.9	5.0 (± 0.1)
	chloroform	2161.3	46.4	5.1 (± 0.1)
	pentane	2165.2	36.8	5.0 (± 0.2)

a. Standard error of the fit.

The insensitivity of ν_{Si-H} can be interpreted in the context of solvatochromism on small silane molecules in these same solvents[249] and when bound to a porous silica surface.[7] When comparing the PDMS elastomer to the silica sol-gel study performed by our group previously,[6] the Si-H frequency is much lower in frequency suggesting that the silicon atom in the elastomer is more electron rich than it is in the silica sol-gels. The frequency of the silicon hydride mode in the PDMS systems is closer to that for triphenylsilane (TriPS) than to those for silica sol-gels and trimethoxysilane (TriMOS).[6, 249] The electron withdrawing methoxy ligands of TriMOS lead to a greater charge separation and electrostatic coupling to the solvent reaction field, whereas TriPS does not have either of these benefits. In the

PDMS elastomer and the cross-linker oligomer, the silicon atom bearing the hydride is bound to two oxygen atoms and one methyl group, likely rendering it less polarized and therefore less sensitive to the solvent environment.

The FTIR peak widths reflect the range of chemical environments around the hydride groups as well as spectral diffusion and homogeneous broadening. Spectral diffusion and homogeneous broadening are measures of the time-dependent fluctuations of the vibrational frequencies that are driven by the solvent and/or polymer dynamics. Despite the structural changes that occur in the elastomer upon swelling, the FTIR spectrum of $\nu_{Si\text{-}H}$ is insensitive to these changes. This is likely due to the fact that the linear lineshape is a reflection of the time-averaged molecular configurations. Therefore, 2D-IR spectroscopy was employed to see if there were differences in the dynamics that accompany these average structures.

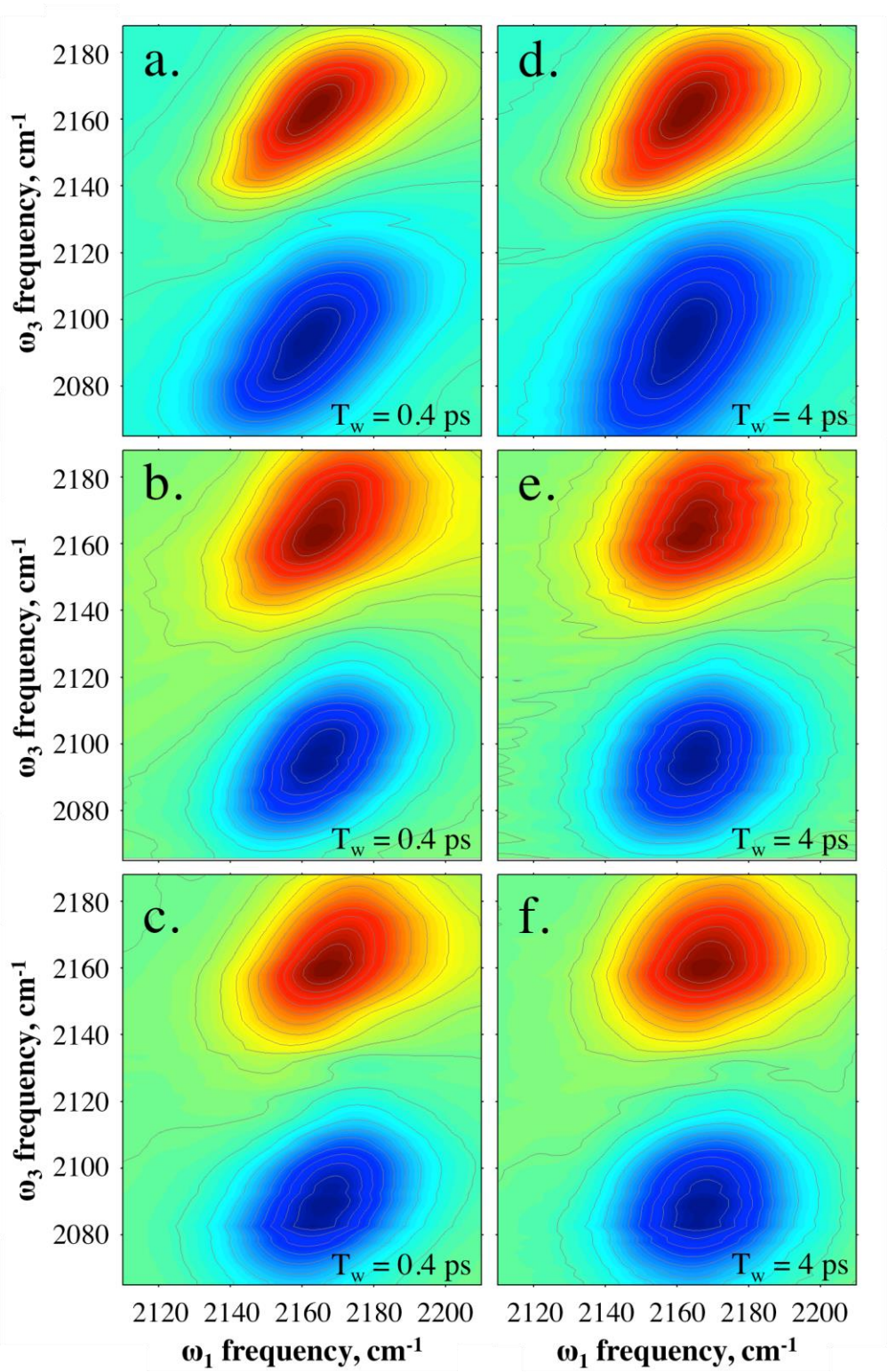

Figure 4.3. 2D-IR spectra collected at T_w = 0.4 (left column) and 4 ps (right column) for the ν_{Si-H} mode on the PDMS elastomer in no solvent (a,d) and in pentane (b,e) and on the cross-linker oligomer in pentane (c,f).

Figure 4.3 shows the 2D-IR spectra at T_w = 0.4 ps (left column) and 4 ps (right column) for the PDMS elastomer in no solvent (top row), elastomer in pentane (middle), and cross-linking oligomer in pentane (bottom row). All 2D-IR spectra are shown in Figure 4.6 through Figure 4.13 provided in the Supporting Information. In a 2D-IR spectrum, the x-axis (ω_1) corresponds to the frequencies at which a subensemble of oscillators is excited by the first IR pulse, and the y-axis (ω_3) is the range of frequencies that this subensemble exhibits after sampling its surroundings for a specific waiting time, T_w. Hence, the 2D-IR spectrum yields the frequency-frequency time correlation for the subensembles beneath the FTIR lineshape.[2,38,141,153,159] Each spectrum has a positive-going (red) v = 0-1 peak that lies on or above the diagonal, and a negative-going (blue) v = 1-2 peak that is anharmonically shifted to lower frequencies along the ω_3 axis. When the 0-1 and 1-2 peaks are sufficiently separated, a diagonal slice through the 0-1 peak reflects the range of frequencies captured by the linear FTIR lineshape. The antidiagonal width represents the portion of the available frequencies that have been sampled during a given T_w period. It contains contributions from very fast pure dephasing (T_2^*), vibrational relaxation (T_1), and spectral diffusion caused by interconversion of molecular subensembles and driven by the reorganization of solvent molecules.[36,163-164]

In Figure 4.3a-c, the peak shape is diagonally elongated at short T_ws, indicating that the Si-H oscillators have not yet sampled the full range of local and/or solvation environments. The solvent-free PDMS elastomer is more broadened along the diagonal direction than the other two systems at both short and long T_ws; the presence of solvent enables new dynamics that perturb the $\nu_{Si\text{-}H}$ on multiple timescales. As the waiting time

increases, the 2D-IR contour shapes become more round, reflecting the loss of correlation due to spectral diffusion of the ν_{Si-H} oscillators (Figure 4.3d-f). By 4 ps, the 2D-IR spectral shape of the elastomer and cross-linker in pentane are nearly circular. Qualitatively, it appears that the timescales of structural rearrangements in the solvent-free elastomer are slower than those occurring in the solvated samples.

To quantify these dynamic differences, the v = 0-1 peaks at all T_ws were analyzed using the CLS method for both the elastomer and cross-linker with and without solvents. Figure 4.4 shows the CLS values as a function of T_w for the PDMS elastomer and cross-linking oligomer without solvent (green), and swollen or dissolved in 2-propanol (black), chloroform (red), and pentane (blue). Compared to the FTIR spectra in Figure 4.2, the CLS decays are more sensitive to changes occurring during the swelling process. A single exponential function with an offset was sufficient to model the CLS data for all samples. The solvent-free elastomer is the least dynamic sample on the timescale of this measurement. Since none of the CLS decays reached the baseline, the Si-H oscillators must remain somewhat correlated with their starting frequencies even after 10 ps; there are structural dynamics that occur on the timescales that are much longer than tens of picoseconds and appear as pseudo-static inhomogeneity.

The CLS decays can be used to obtain the full FFCFs, thereby separating the homogeneous and inhomogeneous contributions to the FTIR lineshapes.[163-164] The resulting FFCF parameters are given in Table 4.2.

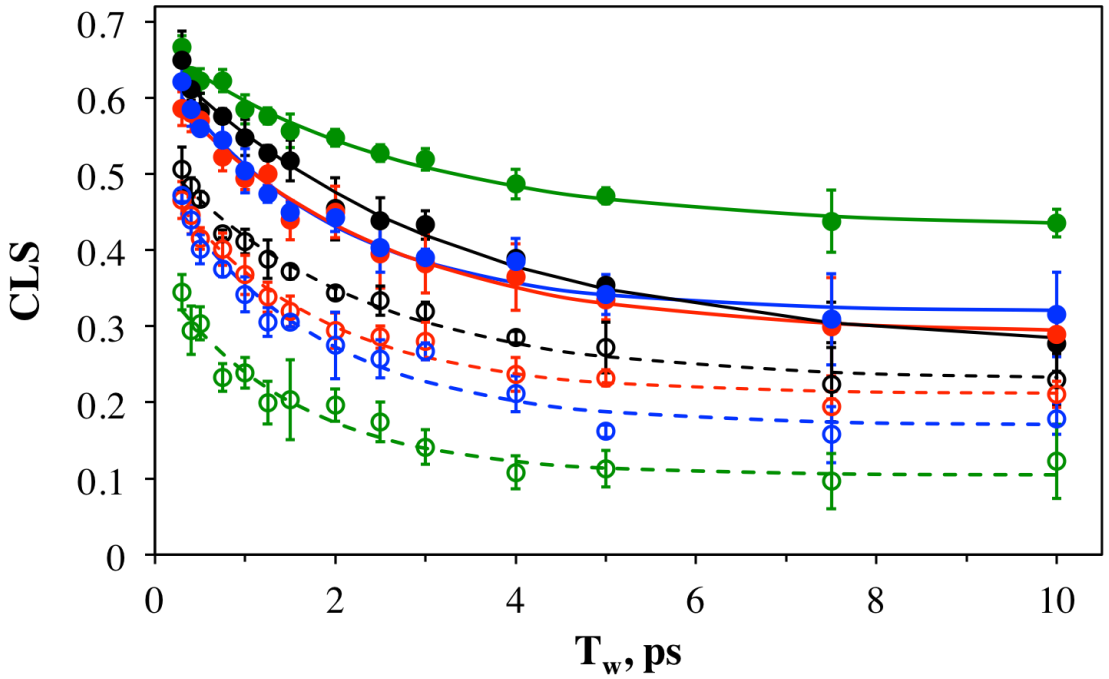

Figure 4.4. CLS decays as a function of T_w for PDMS elastomer (solid markers) and cross-linker oligomer (open markers) in no solvent (green), 2-propanol (black), chloroform (red), and pentane (blue). Overlaid are solid lines (elastomer) and dashed lines (cross-linker) to show the multiexponential fits to the data described in the text. The markers are the average CLS values and the error bars are the standard deviations.

Table 4.2. FFCF parameters for the PDMS elastomer and cross-linker oligomer without solvent and swollen or dissolved in various solvents.

sample	solvent	Δ_1 (cm^{-1})[a]	τ_1 (ps)[b]	Δ_0 (cm^{-1})[a]	Γ (cm^{-1})[a]
PDMS elastomer	none	9 (± 2)	2.7 (± 0.4)	13 (± 1)	1.5 (± 0.3)
	2-propanol	13 (± 2)	3.2 (± 0.4)	11 (± 2)	2.4 (± 0.5)
	chloroform	14 (± 2)	2.3 (± 0.4)	13 (± 2)	2.2 (± 0.5)
	pentane	11 (± 1)	1.8 (± 0.2)	12 (± 2)	2.0 (± 0.3)
cross-linker oligomer	none	14 (± 2)	1.5 (± 0.2)	9 (± 2)	4.7 (± 0.6)
	2-propanol	13 (± 2)	2.2 (± 0.3)	11 (± 2)	3.3 (± 0.5)
	chloroform	15 (± 2)	1.7 (± 0.2)	13 (± 2)	3.8 (± 0.7)
	pentane	13 (± 2)	1.7 (± 0.2)	9 (± 2)	3.4 (± 0.4)

[a] Errors show the range over which the parameter could be increased while other parameters floated to fit the FTIR lineshape 98% as well as the best value
[b] Standard error of the exponential fit

Comparing the top four and bottom four samples in Table 4.2, we can look at the impact of polymerizing the hydride probe into an elastomer. The homogeneous linewidths, Γ, which represent unresolvably fast dynamics, are consistently narrower for the elastomer than that of the cross-linker in the same solvents and in the absence of solvent. This shows that the frequency fluctuations experienced by the hydride mode are either consistently slower or lower amplitude when the cross-linking oligomer is incorporated into the PDMS matrix.

Inhomogeneous contributions to the FTIR linewidth can be separated into spectral diffusion (Δ_1 and τ_1) and pseudo-static inhomogeneity (Δ_o). Spectral diffusion is uniformly lower in amplitude (Δ_1) and slower (τ_1) when the hydride is a part of the elastomer. The structural motions that perturb $\nu_{Si\text{-}H}$ in the PDMS elastomer induce smaller, less frequent stochastic frequency shifts than when the cross-linking oligomer chains are free in solution. Still comparing the elastomer (top four rows in Table 4.2) to the cross-linker (bottom four rows in Table 4.2) in the same solvent environment, the pseudostatic inhomogeneity (Δ_o) has a larger contribution on average to the FTIR linewidth for the elastomer. Collectively, the top and bottom halves of Table 4.2 show that the $\nu_{Si\text{-}H}$ experiences slowing and damping of structural dynamics on all timescales probed by 2D-IR spectroscopy in all solvents when the cross-linking oligomer is incorporated into the elastomer. The oligomer chains have more freedom of movement, since they are unrestricted by the cross-links that are found in the elastomer. The total inhomogeneous amplitudes ($\Delta_o + \Delta_1$) reproduce the trends observed in peak widths in Figure 4.2 demonstrating that the peak width is dominated by

heterogeneity and that those subtle differences in the FTIR spectra in different solvents are due to inhomogeneous broadening effects.

The FTIR lineshapes for both the elastomer and oligomer across all solvents are dominated by inhomogeneous broadening (spectral diffusion and pseudostatic inhomogeneity). In the case of the elastomer, this is due, in part, to the fact that the cross-linking reaction does not react homogeneously. However, most models use an ideal homogeneous network when describing the swelling process, where the swelling ratio is a direct function of cross-linking density.[83,85,87-88,98] This direct relationship predicts that one should be able to determine the cross-linking density of elastomers by performing swelling experiments. Due to the large inhomogeneity present in the PDMS elastomer, the swelling experiment is not a good metric – the swelling of the elastomer is inhibited by heterogeneities making the cross-linking density appear higher than the actual value.[123] In principle, the heterogeneity experienced by the silicon hydride that was obtained by 2D-IR spectroscopy could be used as a measure of structural heterogeneity to improve the accuracy of cross-linking determined from swelling measurements.

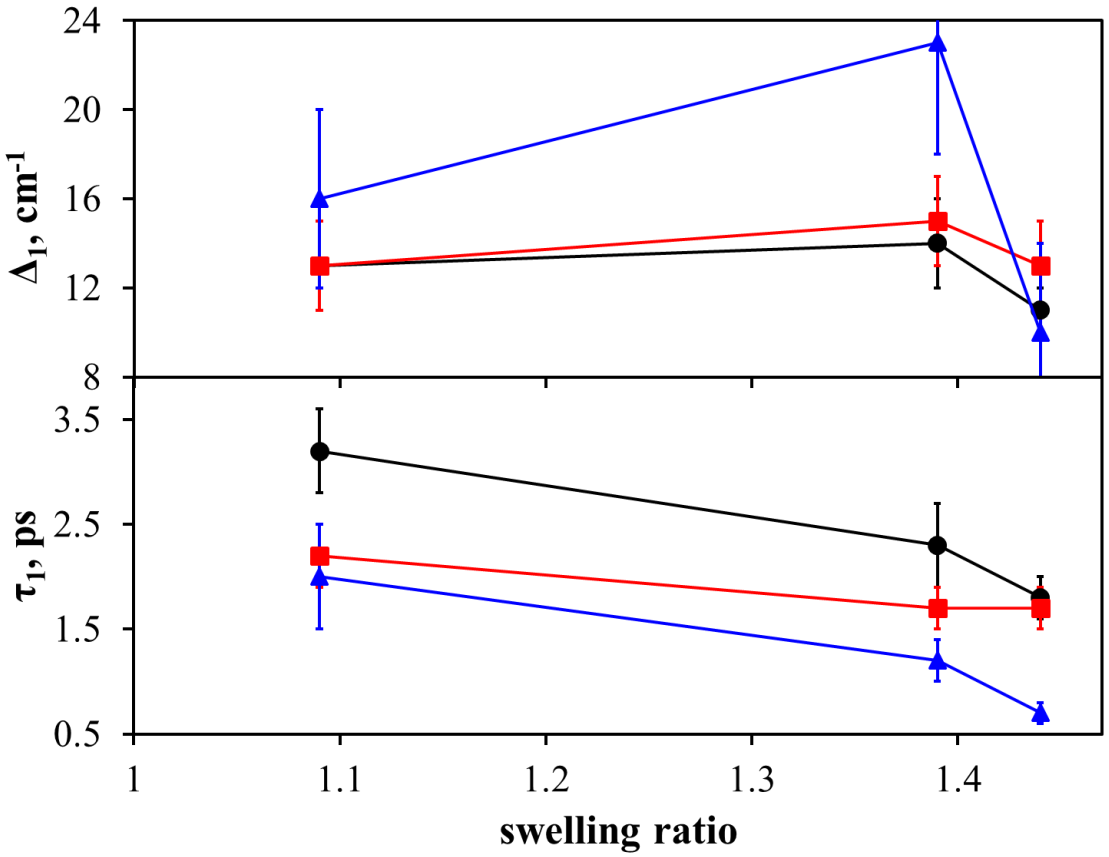

Figure 4.5. Amplitudes (a) and correlation times (b) for spectral diffusion determined for PDMS elastomer (black circles), cross-linking oligomer (red squares), and TriMOS (blue triangles).[249] The x-axis uses normalized swelling ratios for 2-propanol (1.09), chloroform (1.39), and pentane (1.44) in PDMS, as reported elsewhere,[124] as a measure of solvent interaction strength.

A relevant comparison can be made to the fast spectral diffusion for a small molecule silane reported previously by our group.[249] Trimethoxysilane (TriMOS) is a simpler system with the silicon hydride bearing three methoxy groups. The spectral diffusion amplitudes and correlation times for TriMOS in 2-propanol, chloroform, and pentane are plotted in Figure 4.5a and Figure 4.5b, respectively, along with the corresponding parameters from Table 4.2 as a function of the swelling ratios for the PDMS systems. Strictly speaking, the swelling ratio is only relevant to PDMS but is used here as a general metric for solvent interaction strength. The Δ_1 values in Figure 4.5a reveal

identical trends among the cross-linker, elastomer, and TriMOS: pentane < isopropanol < chloroform. Similarly, the τ_1 values in Figure 4.5b show that the correlation times decrease monotonically from 2-propanol to chloroform to pentane. The amplitude changes are more dramatic and the correlation times are faster for TriMOS, but the fact that these parameters change in the same ways shows that the hydride in the elastomer and cross-linker experiences spectral diffusion that is characteristic of these three solvents. The lack of quantitative agreement may be ascribed to the possibility that the solvation shell around the silicon hydride is partly occupied by the globular oligomer in the cross-linker or adjacent polymer chains in the elastomer. This can also be seen more clearly when comparing the elastomer swollen in 2-propanol is compared to the other scenarios. The degree of swelling $\left(\frac{\text{final weight-initial weight}}{\text{initial weight}} \times 100\right)$ of the elastomer in 2-propanol is less than 20%, but exceeds over 100% in chloroform and pentane.[124,245,252] The correlation time is the longest compared to those of the other solvents (and is close to that of the elastomer in the absence of solvent), suggesting that the hydride mode is influenced by nearby polymer chains as well, making the correlation time seem slower. Nonetheless, the trends in Figure 4.5 provide compelling evidence that a significant portion of the solvation shell around the silicon hydride includes the swelling solvent.

The Δ_o and Γ values for $\nu_{Si\text{-}H}$ in either the elastomer or the cross-linker in the three different solvents are the same within error. However, there is a distinct increase in Γ upon going from no-solvent to any of the three solvents. This shows that there are some characteristic dynamics experienced by $\nu_{Si\text{-}H}$ due solely to the motions of PDMS or cross-linking oligomer. MD simulations showed that swollen polymer chains experience fewer

polymer-polymer interactions due to the presence of the liquid solvation layer.[129] As the polymer chains become solvated, the solvent shell proximal to the hydride is at least partly replaced by solvent molecules that bring their own characteristic dynamics to influence the hydride frequency fluctuations. Note that Γ was not independent of solvent type in the FFCF of TriMOS,[249] adding further support to the hypothesis that the hydride may not be fully accessible to the swelling solvent, thereby retaining some influence from the nearby polymeric dynamics.

4.5. Conclusions

This study viewed the structural dynamics of an oligomeric cross-linker and a cross-linked elastomer from the perspective of a covalently bound silicon hydride. A subset of the full palette of dynamics in these systems was reported through the lens of ultrafast frequency fluctuations experienced by the hydride mode. When immersed in solvents with a range of free energies of mixing, the siloxane chains extended to reach new thermodynamically favored conformations with modified structural motions. I have fully characterized the static and dynamic structural effects reflected in the silicon hydride vibration for the initial and final thermodynamic states of swelling in three different solvents. The FTIR spectra of this mode were broad and relatively insensitive to swelling; 2D-IR analysis showed that this was due to overwhelming chemical heterogeneity. Importantly, spectral diffusion experienced by the hydride mode in solvent swollen elastomers and solvent dissolved cross-linker matched the characteristics expected for the three solvents studied. Even in the absence of solvent, I observed structural dynamics of

the polymer chains on the same timescale as the solvent dynamics. Hence, when the elastomer was swollen, I could not fully rule out the possibility that polymer dynamics contributed to the observed measurements; there may be underlying polymer motions for the swollen/dissolved species that explain some deviations from the previous values for TriMOS. However, to further the understanding of the underlying microscopic processes involved in the swelling process, MD simulations would need to be implemented.[2,36,38] The influx of solvent during elastomer swelling is known to be moderated by polymer backbone and side chain dynamics such as those measured in this study. From an applications perspective, this work shows that solvent motions themselves may play a critical role in the rate of swelling by modulating elastomer permeability. Therefore, modeling polymer side chain dynamics in the absence of solvent may not be sufficient to predict accurately polymer permeabilities.[b]

[b] The authors gratefully acknowledge partial supports from the National Science Foundation under CHE-0847356 and CHE-1464416 (to A.M.M.). C.M.O. was supported by a National Science Foundation Graduate Student Research Fellowship Grant Number 00039202.

4.6. Full Set of 2D-IR Spectra

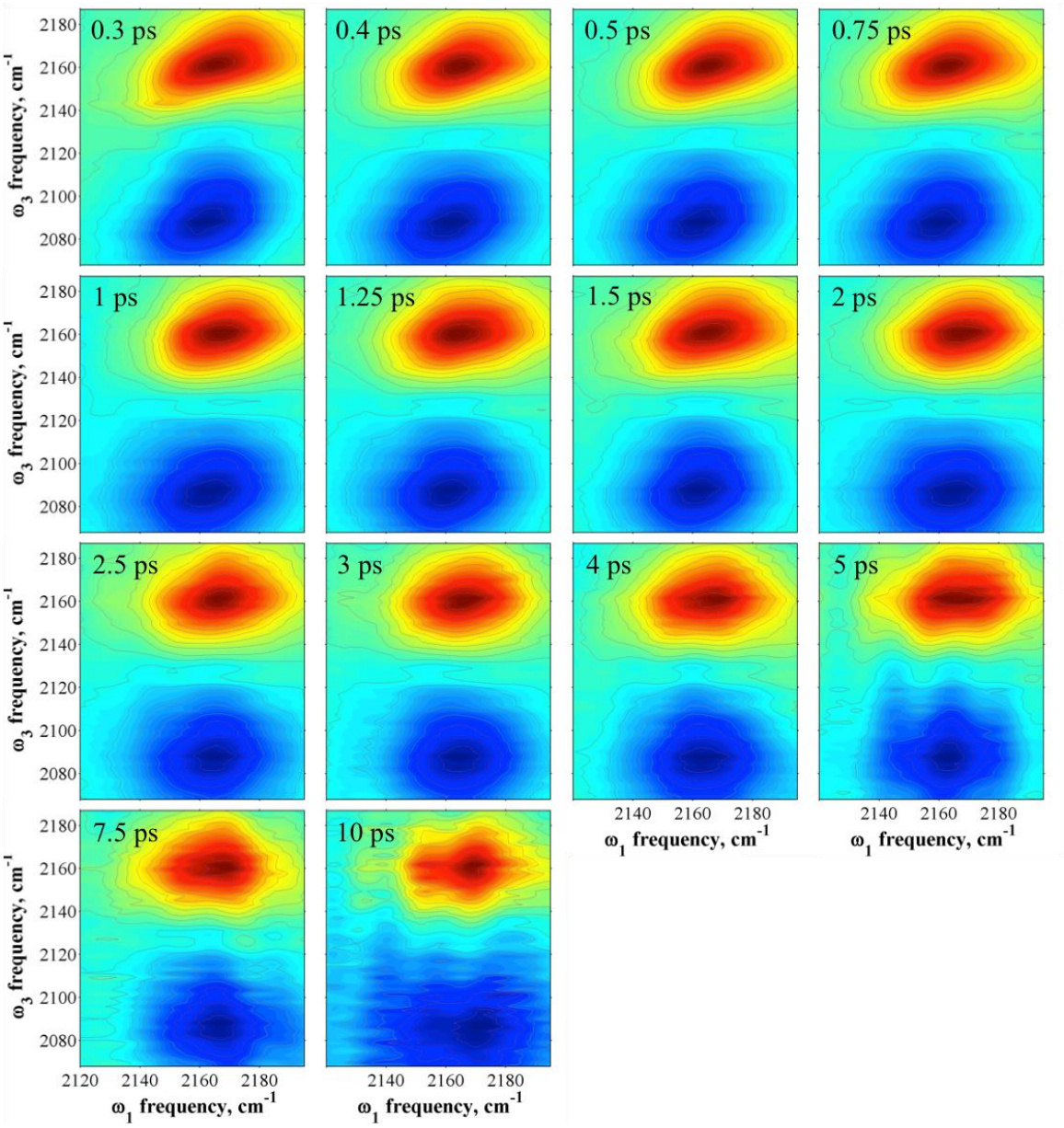

Figure 4.6. All 2D-IR spectra collected for pure cross-linking oligomer, no additional solvent.

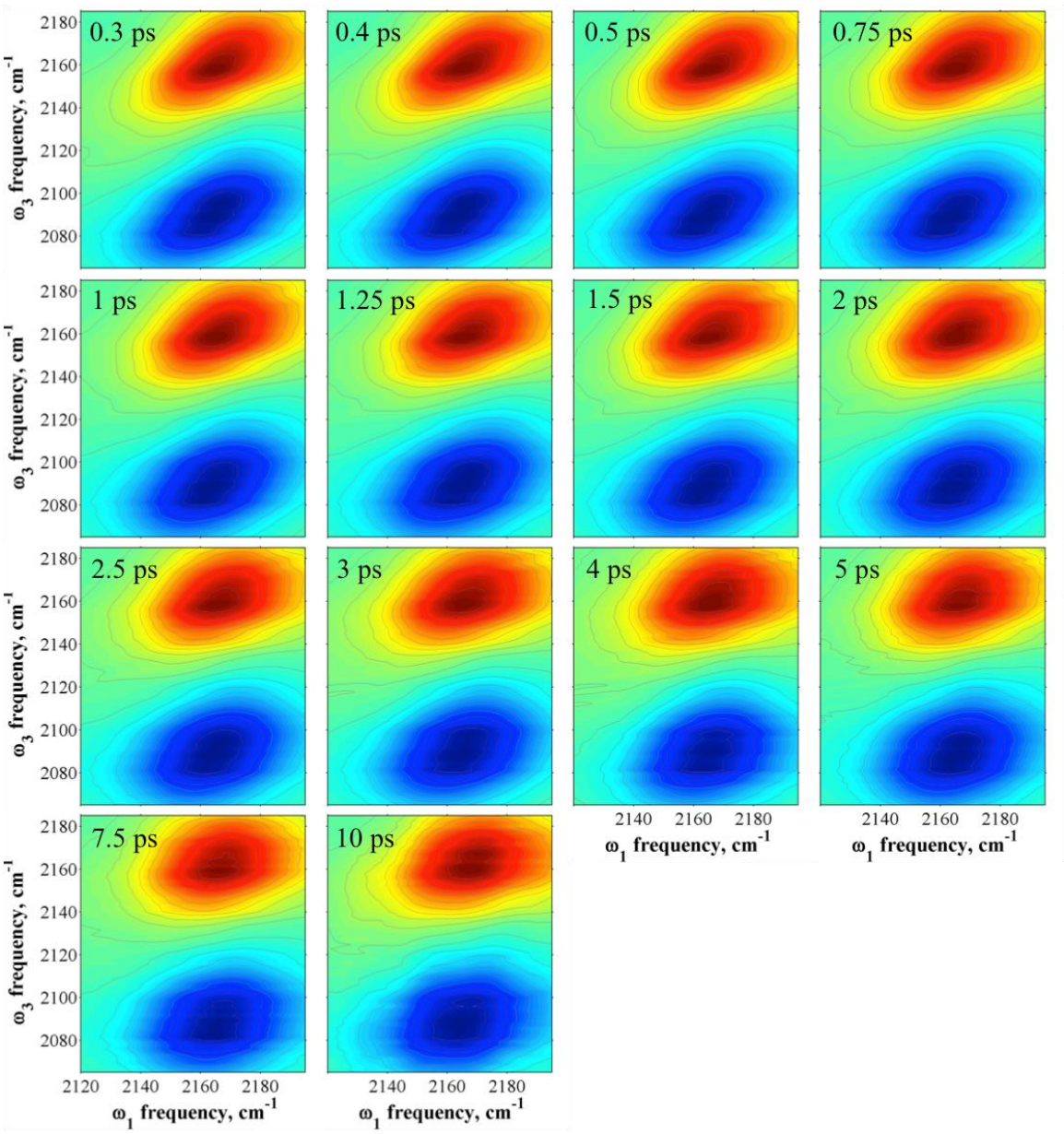

Figure 4.7. All 2D-IR spectra collected for cross-linking oligomer in isopropanol.

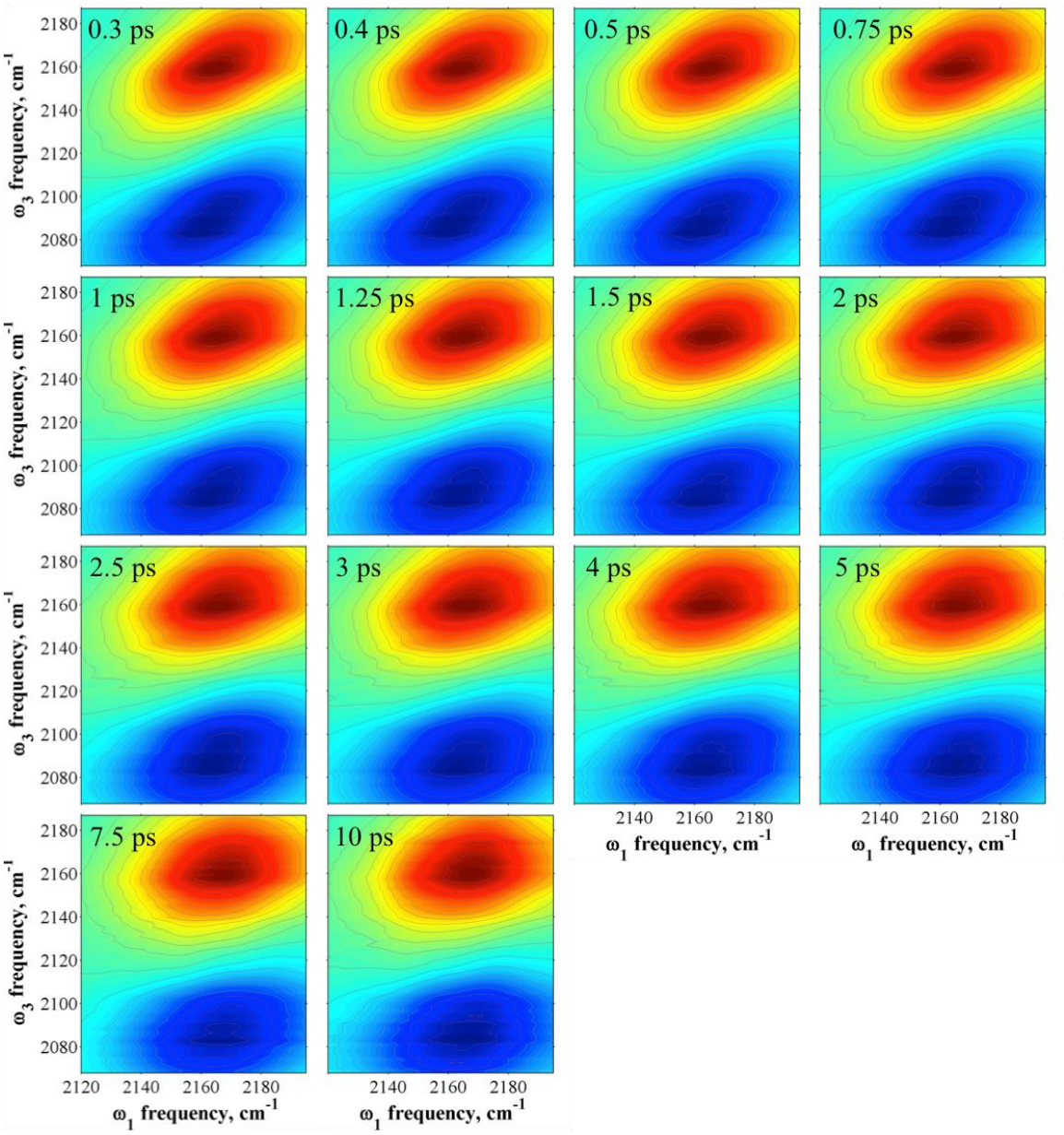

Figure 4.8. All 2D-IR spectra collected for cross-linking oligomer in chloroform.

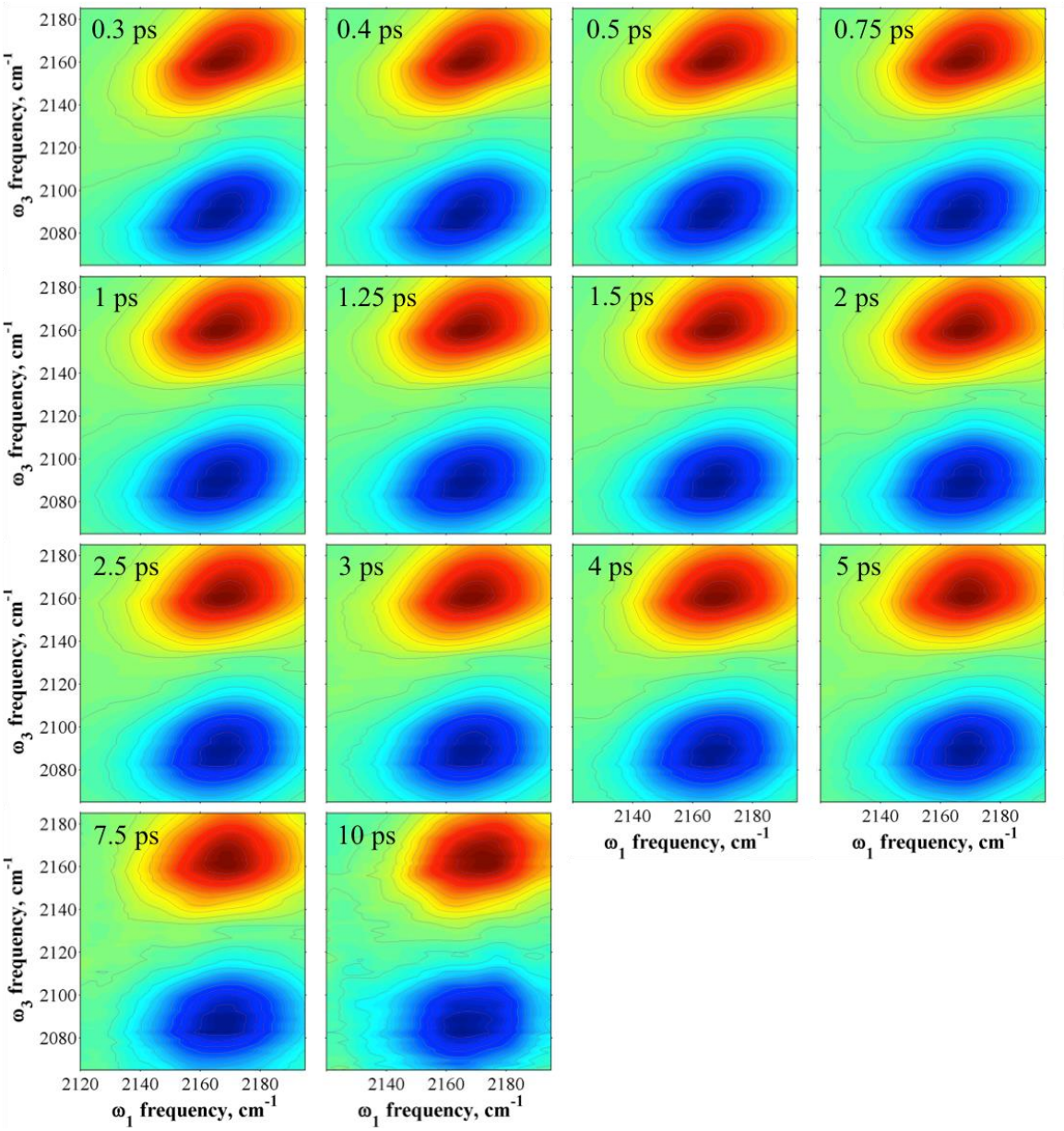

Figure 4.9. All 2D-IR spectra collected for cross-linking oligomer in pentane.

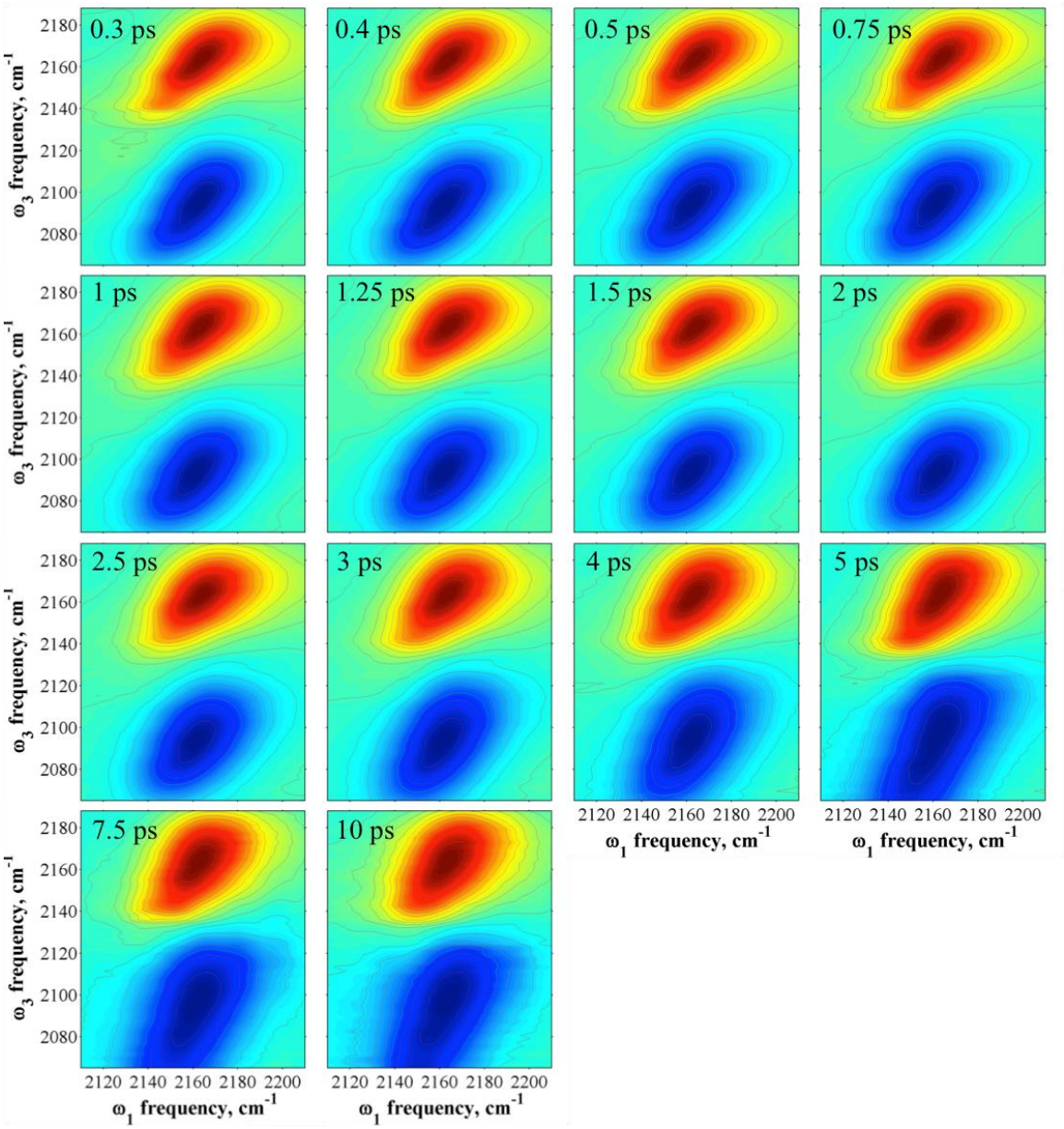

Figure 4.10. All 2D-IR spectra collected for PDMS with no added solvent.

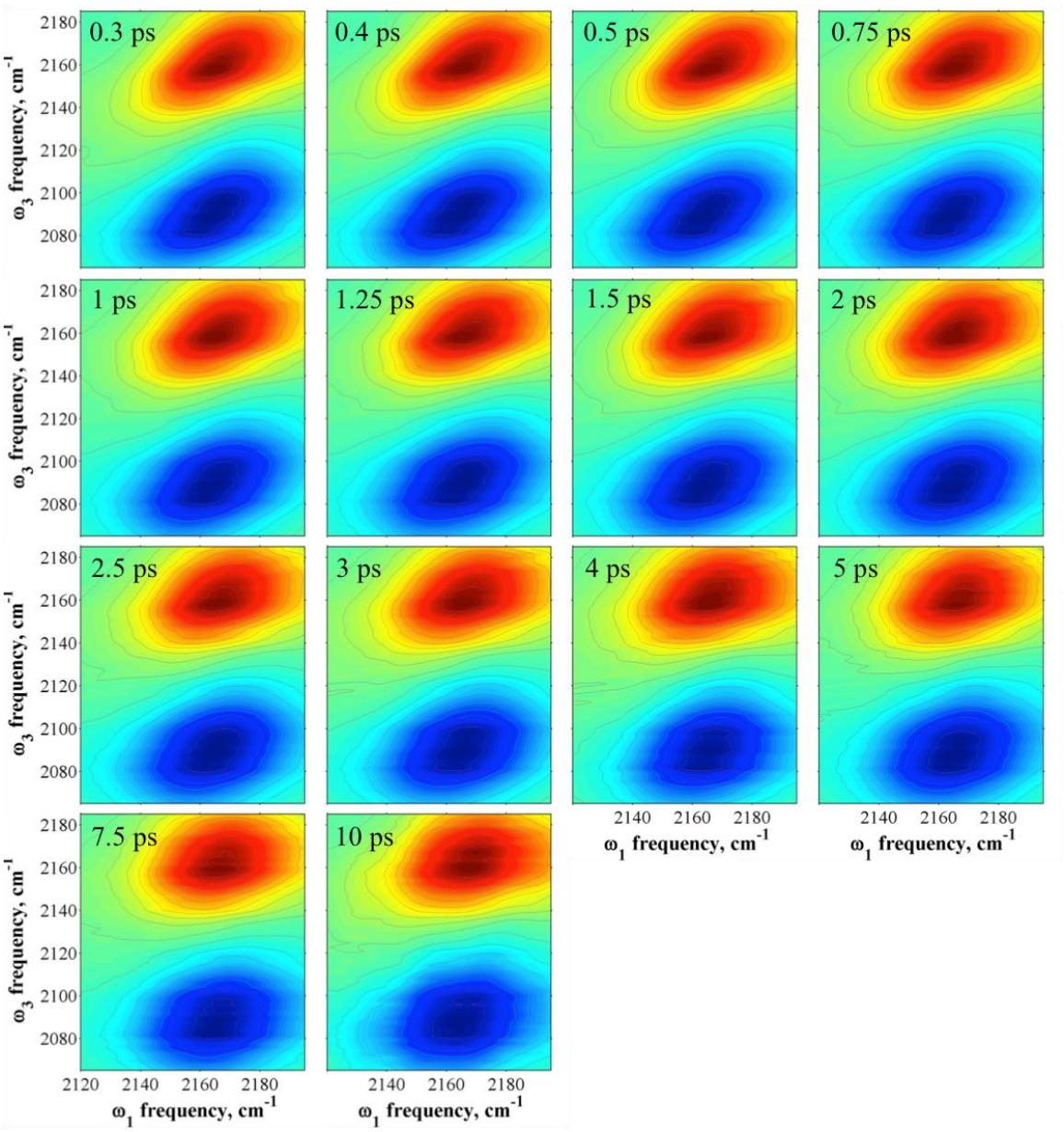

Figure 4.11. All 2D-IR spectra collected for PDMS swollen in isopropanol.

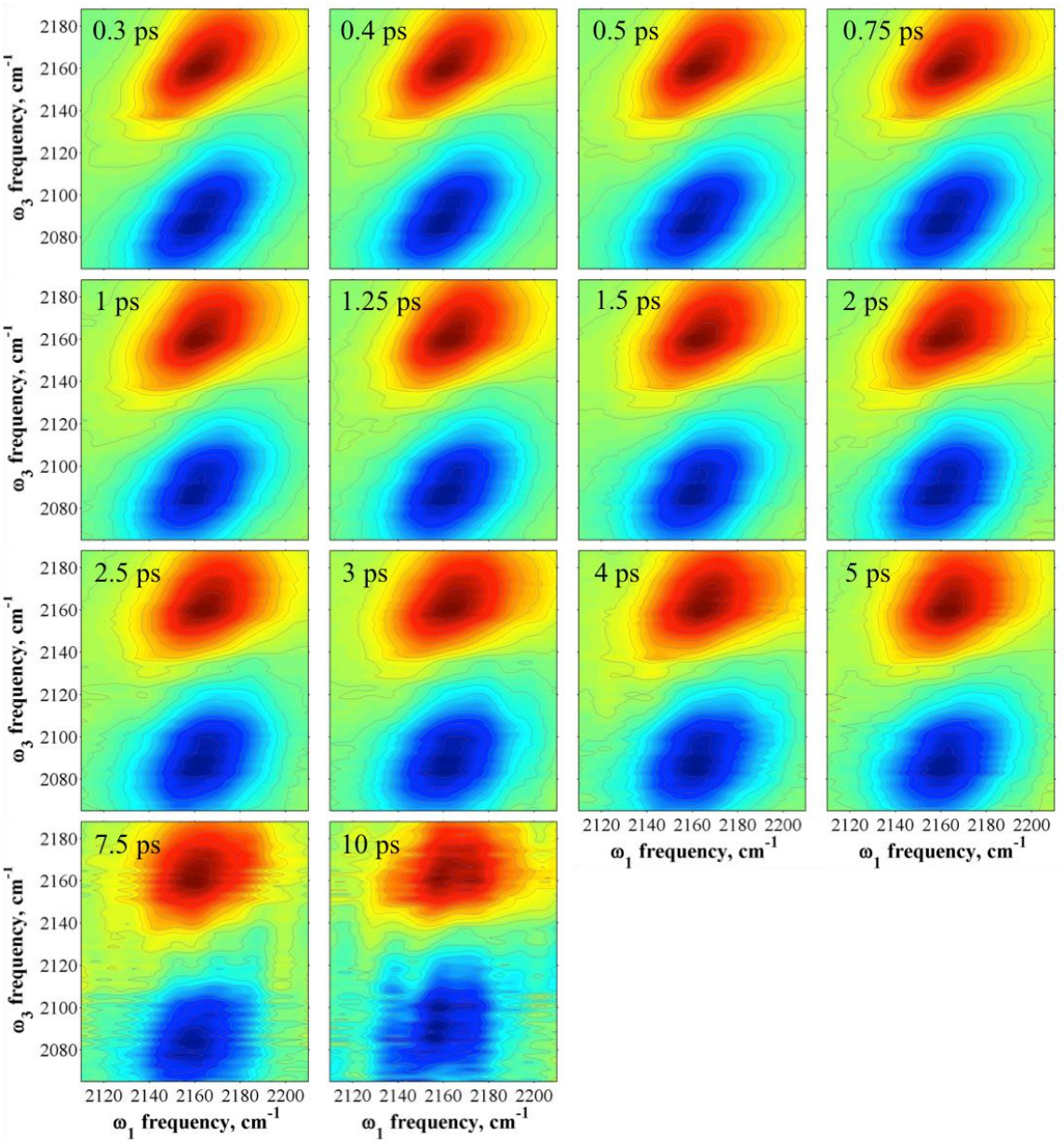

Figure 4.12. All 2D-IR spectra collected for PDMS swollen in chloroform.

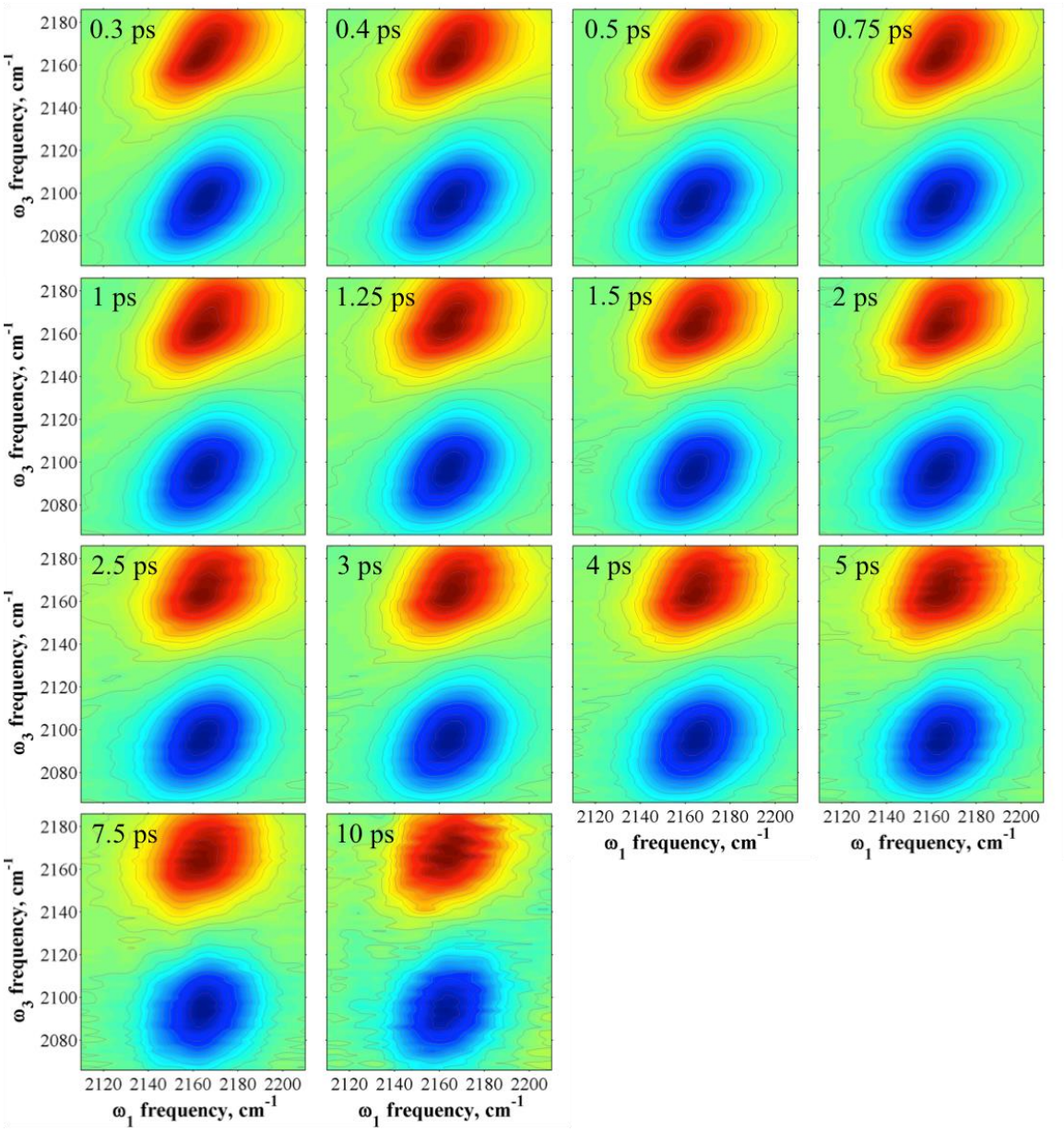

Figure 4.13. All 2D-IR spectra collected for PDMS swollen in pentane.

Chapter 5. The Role of Ultrafast Structural Dynamics with Physical and Chemical Changes in Polydimethylsiloxane Thin Films by Two-Dimensional IR Spectroscopy

Reproduced with permission from Journal of Physical Chemistry B, ‘submitted for publication.’

5.1. Chapter Summary

Fourier transform infrared (FTIR) and two-dimensional IR (2D-IR) spectroscopies were applied to polydimethylsiloxane (PDMS) cross-linked elastomer films. The vibrational probe for the systems studied was a silicon hydride mode that was covalently bound to the polymer chains. The structure and dynamics reported by this mode were measured in response to a wide range of chemical and physical perturbations, including elevated curing temperature, increased curing agent concentration, mechanical compression, and cooling to near the glass transition temperature. The FTIR spectra were found to be relatively insensitive to all of these perturbations, and 2D-IR spectroscopy revealed that this was due to the overwhelming influence of heterogeneity on the spectral lineshape. Surprisingly, the deconvoluted spectral lineshapes showed that there were only slight differences in the heterogeneous and homogeneous dynamics even with the drastic macroscopic changes occurring in the different systems. In the context of modeling polymer behavior, the results confirm that dynamics on the ultrafast timescale need not be included to properly model PDMS elasticity.

5.2. Introduction

The macroscopic properties of polymer networks originate from microscopic behavior for most cases. For example, solute diffusion through polymer membranes is intimately tied to the side-chain dynamics that open and close transient conduits through the matrix.[130-132,134-135,244] Likewise, the recoverability of an elastomer network from macroscopic deformation, or elasticity, likely has some relationship to microscopic

molecular rearrangements. There have been many theories describing how the molecular environment at the cross-links influences the elasticity of an elastomer but the degree to which the cross-link fluctuations must be included is debated.[83,92,94-95] On some timescales, the molecular dynamics at the cross-links must influence the elasticity of elastomers, as seen by the slower segmental motions.[93,114,117,253-254] On the other hand, fast structural motions monitored indirectly by rotations of a probe molecule at a cross-link had no correlation with the macroscopic properties of polymers.[113]

Elastomers have technological importance due to the wide range of applications like adhesives, sealants, coatings, and enapsulants.[51-53] Each of these applications requires different mechanical properties that can be altered by changing the polymer chain lengths, cross-linking density, cure temperature, and the additional fillers added during the cross-linking reaction.[61-63,80] Altering the elastomer film in this manner results in a material with the desired properties but lacking a well-understood microscopic structure.[63] Ultimately, the underlying network structure and dynamics dictate the performance of the elastomer, so there is a need to improve the understanding between the microscopic polymer network and the macroscopic properties in order to manufacture better materials.

The elastic modulus is one way to quantify the elasticity of an elastomer by measuring the resistance to deformation in one dimension.[94-95] Over the years, many theories have been developed to explain the contributions that the microscopic environment has on this macroscopic property. Flory developed the affine network model,[83,86-89] which assumed no fluctuations of the cross-links due to being suppressed by local intermolecular entanglements; the microscopic deformation of the elastomer network is proportional to

the macroscopic deformation of the sample. There is no contribution of the cross-link junctions to the modulus due to the cross-links being static. However, the cross-links in the network should be able to fluctuate inside the polymer matrix due to thermal fluctuations, so Guth developed the phantom network model[83,89,98] in which the cross-links contribute to the modulus due to the cross-links moving freely. The microscopic deformation of the mean positions of the cross-links is proportional to the macroscopic deformation, while the fluctuations are independent of this strain. Both models apply to monodisperse networks and neglect both the excluded volume of chains and entanglement effects, hence assuming an ideal homogeneous network.

The affine network model and the phantom network model are the two descriptions of the modulus in the limits of no fluctuations or maximum fluctuations of the cross-links. Intermediate models exist in which the cross-links are constrained within the polymer network. To allow for partial fluctuations of the cross-links, Flory and Erman developed the constrained junction model.[101-103] This model assumes that the cross-links fluctuate like the phantom network model, but can be hindered somewhat by the entanglements like the affine network model. Therefore, the elastic modulus is found to be intermediate to those predicted by the affine and phantom network models. Entanglements could be permanently trapped during network formation, so Langley and Graessley[104-105] included the contributions of these trapped entanglements to the modulus. This approach allowed separation of the contributions from the chain entanglements due to chemical cross-links and the permanently trapped physical entanglements.

The preponderance of elasticity models highlights the challenges to describing how polymer structure and cross-link dynamics contribute to the elastic modulus. Previous experiments have found that the elastic modulus is not modeled well using the affine network or the phantom network models and needed to include entanglements.[89] However, the nature of the cross-links and the entanglements found in the elastomer are not defined. Some believe that the entanglements affect the properties by restricting the fluctuations,[109] while others argue that they contribute more to the cross-link contribution by acting like pseudo-cross-links.[110-112] Excluding the affine network model, the macroscopic elastic moduli of elastomer networks are believed to be governed to varying degrees by molecular dynamics at the cross-links.[93,113] Polymer structural dynamics span many orders of magnitude in time from milliseconds[114-115] to picoseconds.[115-116] Skeletal and lattice vibrations have typical periods of 0.1 ps to 1 ps.[115] The reorientation of groups, drifting of chains, rotations of internal segments, or slow changes in conformation occur on the timescale of 1 μs to 10 μs.[115] In this chapter, Fourier transform infrared (FTIR) and two-dimensional infrared (2D-IR) spectroscopies were used to characterize ultrafast structural dynamics in a PDMS elastomer network in response to a range of chemical and physical perturbations that modulate the elastic modulus. Vibrational solvatochromism and spectral diffusion for the intrinsic silicon hydride (Si-H) vibrational mode served as markers for the interdependence of microscopic and macroscopic properties, allowing us to test the hypotheses asserted by several of the elasticity models described above.

5.3. Experimental Materials and Methods

Cross-linked PDMS elastomer thin films were fabricated using a Sylgard® 184 silicone elastomer kit from Dow Corning, consisting of an elastomer base (Sylgard-184A) and a curing agent (Sylgard-184B).[66-68] The elastomer base contained >60 wt% vinyl-terminated oligomers, 30-60 wt% dimethylvinylated and trimethylated silica, 1-5 wt% tetra(trimethoxysiloxy)silane, and a Pt-based catalyst. The curing agent contained 40-70 wt% poly(dimethyl, methylhydrogensiloxane), 15-40 wt% dimethylvinyl-terminated poly(dimethylsiloxane) oligomers, 10-30 wt% dimethylvinylated and trimethylated silica, and 1-5 wt% tetramethyl tetravinyl cyclotetrasiloxane.[60-62]

The curing agent contains the cross-linker, which is poly(dimethyl, methylhydrogen siloxane) due to the silicon hydride (see Figure 4.1). The silicon hydride also serves as the vibrational probe in this study due to not fully reacting. The polymer network is created by the cross-linker reacting with the dimethylvinyl-terminated poly(dimethylsiloxane) oligomers and tetramethyl tetravinyl cyclotetrasiloxane. The kit also contains dimethylvinylated and trimethylated silica as reinforcing materials to improve the mechanical properties of the elastomer.[60,66-67] A modulator, tetra(trimethoxysiloxy)silane, is needed to inhibit the fast cross-linking at room temperature to allow more time to prepare the samples.[71]

The elastomer base and curing agent were mixed with a 10:1 mass ratio. The samples that have 20% and 30% curing agent, however, had the elastomer base and curing agent mixed in 10:2 and 10:3 mass ratios, respectively. Upon mixing, a platinum-catalyzed hydrosilylation reaction occurs between the vinyl groups in the elastomer base and the

silicon hydrides in the curing agent.[61,71] The mixture was then doctor-bladed in a 5 mm x 5 mm square opening in the middle of a piece of Magic or Scotch tape (~38 or ~51 μm thickness, respectively) on a 3 mm CaF_2 window. The thin films that underwent compression required the films to be thicker than ~51 μm, so three pieces of Scotch tape stacked upon one another (~151 μm thickness) were used instead. A circular opening with a 1.5 cm diameter in the middle of a single piece of scotch tape was needed for the PDMS cooled below room temperature to allow a larger sample surface required for the VPF-100 Cryostat. The temperature of the Cryostat was controlled with a Lake Shore Model 325 Temperature Controller. The samples cured under ambient conditions for 2 days, except for the heat cured samples. The heat cured samples cured for 35 min when heated at 100°C, for 20 min when heated at 125°C, and for 10 min when heated at 150°C, following the product information sheet.[68] For clarity, throughout this study an "unaltered" PDMS sample is defined as using 10% curing agent and being cured at room temperature for 2 days.

The PDMS elastomer films were studied spectroscopically by lightly pressing the CaF_2 window containing the sample against a clean CaF_2 window with a 50 μm Teflon spacer between the two in air. The compressed samples did not use a spacer due to the design of the compression cell as shown in Figure S1. The compression cell (Figure 5.1) was designed to allow IR beams to pass through as well as letting the user see the lateral expansion of the sample during compression. A Force Sensing Resistor (FSR)® was implemented into the compression cell to measure the pressure that was being applied to the polymer thin films. The resistance of the FSR decreases with an increase in the

force/pressure being applied to the sensor. The Interlink Electronics FSR® 404 was used for this experiment due to its donut shape allowing light to pass through the center hole. The FSR had to be calibrated to give accurate force/pressure reading for the resistances measured with the calibration curve shown in Figure S2. The pressures used will be discussed later.

Figure 5.1. Compression cell schematic. From left to right: aluminum plate with screw holes, rubber o-ring, CaF_2 window, CaF_2 window with sample, 50 μm Teflon spacer, 3/8 in. flat washer (1-inch diameter), ¼ in. flat washer (5/8 inch diameter), ¼ in black neoprene washer (1 inch diameter), FSR® 404, ¼ in. flat washer, 3/8 in. flat washer, rubber o-ring, and aluminum plate with screw holes. By tightening the two aluminum plates together, the sample can be compressed between the two CaF_2 windows with the FSR® 404 measuring the amount of force/pressure being applied to the sample.

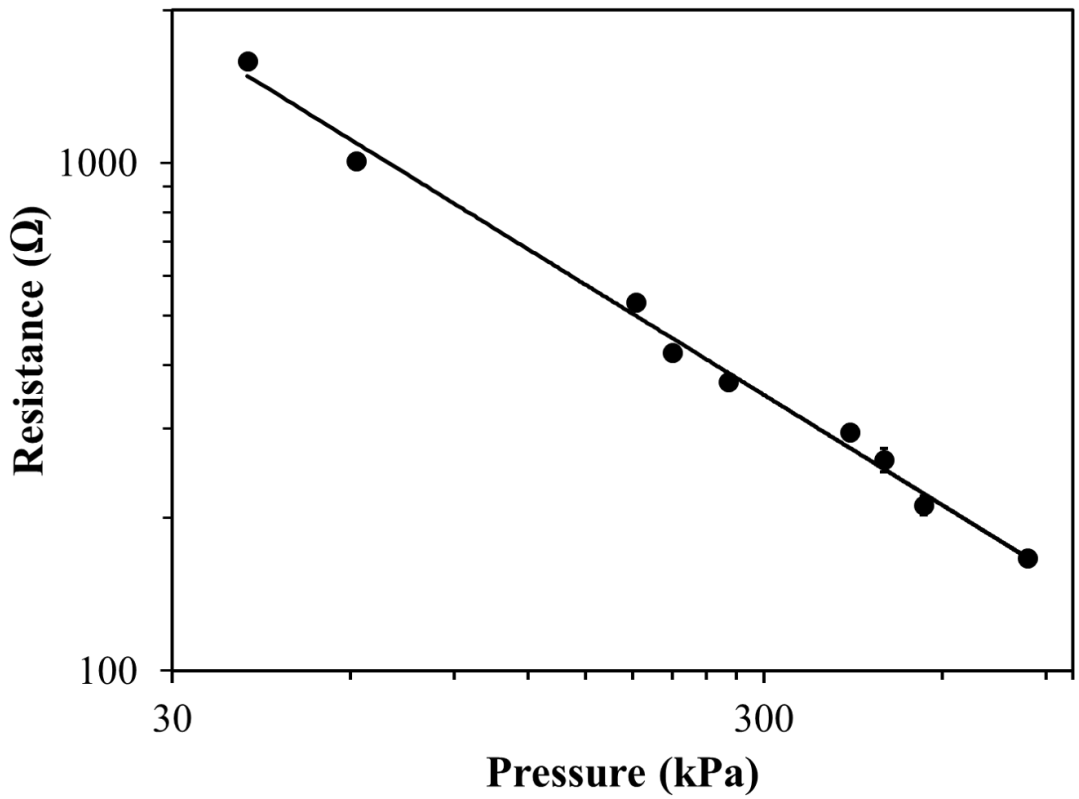

Figure 5.2. Resistance versus pressure calibration curve for the FSR® 404 plotted on a logarithmic scale. The pressure was calculated using an active area of 1.60 cm^2 for the actuator on the FSR® 404. The fit was found to be log(R) = (-0.71979 ± 0.013408)P + (4.32617 ± 0.03231231) with an R^2 value of 0.991.

Fourier transform infrared (FTIR) spectra were collected on a Nicolet 6700 FTIR spectrometer (Thermo Scientific) with at least 16 scans and a resolution of 1 cm^{-1}. A background spectrum was not needed due to the samples being solvent-free. However, the data were baselined with a polynomial in the 2075 to 2250 cm^{-1} range.

The 2D-IR instrument has been described previously in Section 2.3.3.[4,13] A regeneratively amplified Ti:Sapphire laser (Spectra-Physics, 800 nm, 40 fs pulse duration, 500 mW, 1 kHz repetition rate) pumped an optical parametric amplifier (OPA, Spectra-Physics) to generate near-IR beams. The near-IR signal and idler beams were difference

frequency mixed in a silver gallium sulfide crystal ($AgGaS_2$, 0.5 mm thick) to generate mid-IR pulses (3 μJ /pulse, 90 fs FWHM, ~200 cm^{-1} bandwidth FWHM) tuned to the silicon hydride (Si-H) stretching frequency of ~2160 cm^{-1}. The pulses were then divided into three ~1 μJ p-polarized pulses and focused at the sample in a BOXCARS geometry.[152] The generated vibrational echo signal was heterodyned with a local oscillator and detected with a liquid N_2 cooled MCT linear array detector (Infrared Associates, Inc.) with a spectral resolution of ~4 cm^{-1}. The system was continuously purged with dry air (-100 °F dew point) during data collection from the OPA to the detector.

For each 2D-IR spectrum, the time delay between pulses 2 and 3, T_w, was maintained at a fixed value while the time delay between pulses 1 and 2, τ, was scanned in increments of 5 fs to subsequently Fourier transform into the first frequency dimension (x-axis, ω_τ, or ω_1).[2,36,38] The second dimension (y-axis, ω_m, or ω_3) was obtained by an optical Fourier transform of the heterodyne detected vibrational echo signal by dispersing it from the monochromator diffraction grating. The resulting data were processed to obtain the purely absorptive 2D-IR spectrum[153,205] and phase corrected using the pump-probe projection theorem and the absolute value center as constraints due to the BOXCARS geometry as described in Section 2.3.4.[158,164] Due to the local oscillator not passing through the sample, the FTIR spectrum of the sample was used as an absorption correction prior to phasing the 2D-IR spectra.[157]

The 2D-IR spectra were analyzed using the centerline slope (CLS) method to obtain the frequency-frequency correlation function (FFCF).[163-164] For the CLS analysis, the maximum intensity for the 0-1 and its associated central frequency on the ω_1 axis were

found for all the 2D-IR spectra for each of the systems. The frequency range used to find the CLS was the central frequency ± 8 cm^{-1}, since a wider/narrower range did not change the CLS values significantly.

The FFCF was modeled according to the following equation:

$$FFCF(t) = \frac{\delta(t)}{T_2} + \Delta_1^2 \exp\left(\frac{-t}{\tau_1}\right) + \Delta_0^2 \quad (5.1)$$

δ(t) is a delta function and T_2 is the total dephasing time, which has contributions from the vibrational and orientational relaxations as well as the pure dephasing time, T_2^*.[163-164] The orientational relaxation has negligible contribution in PDMS elastomer films due to the polymer chains being linked together via cross-links to make a solid film, hindering rotations of the polymer chains. The relationship between T_2, T_2^*, and the vibrational relaxation lifetime, T_1, is:

$$\frac{1}{T_2} = \frac{1}{T_2^*} + \frac{1}{2T_1} \quad (5.2)$$

The pure dephasing time, T_2^*, is the time it takes for the oscillators that comprise the macroscopic polarization to lose the phase relationship without the loss of excitation. The pure dephasing time arises from fast intramolecular dynamics and intermolecular interactions that cause random, fast fluctuations in the vibrational frequency of the mode.[143] T_2 defines the homogeneous line width at half-maximum, Γ, through the relation: $\Gamma = \frac{1}{\pi T_2}$.[36,138] Δ_0 is the contribution from pseudo-static inhomogeneous broadening due to the structural dynamics in the elastomer that influence the Si-H frequency but evolve on a much slower timescale than our measurements. Δ_1 is the average amplitude frequency shifts caused by a particular frequency-perturbing process with correlation time τ_1.[163-164]

Therefore, Δ_1 and Δ_0 are the standard deviations of the Gaussian distribution of the Si-H frequencies. To obtain the total standard deviation (Δ), Δ_1 and Δ_0 must be added in quadrature. The FWHM of the Gaussian lineshape, f_g, is related to Δ through the relation $2\Delta\sqrt{2\ln(2)}$.[36,165] The total FWHM of the lineshape, which is a Voigt profile, can be found using the approximation of $\frac{\Gamma}{2} + \sqrt{\frac{\Gamma^2}{4} + f_g^2}$.[166]

The time constant (τ_1) in the FFCF parameters was obtained directly from fitting the CLS decays, which has been shown to be highly accurate.[163-164] However, the amplitude of the exponential contribution (Δ_1) and the offset (Δ_0) assume a FFCF normalized to unity and a y-intercept that is likewise normalized. The amplitude from the CLS decay fits and the linear FTIR FWHM were used to calculate approximate values for Δ_1, Δ_0, and T_2 of the full FFCF by following the procedure by Kwak and co-workers.[163-164] These initial values were then applied to a FFCF, where the first-order response function was used to reproduce the linear FTIR lineshape.[137] The lineshape was fit by iteratively varying the amplitudes, as well as the central frequencies, while holding the time constant. The CLS method was developed using the short-time approximation, so the values for Δ_1, Δ_0, and T_2 are underestimated due to the method's inability to distinguish between homogeneous terms and fast spectral diffusion (compared with the FID) as described earlier in Section 2.3.6. Therefore, the floated Δ_1, Δ_0, and T_2were constrained to only increase from the estimated values.

IR pump probe spectroscopy was carried out with the same laser system described above.[4,13] The data were fit from 1 to 100 ps to determine the population relaxation times (lifetime, T_1) for the v = 0-1 and 1-2 transitions. The vibrational relaxation times for these

two transitions consistently showed the same trends; the 0-1 values were used in data analyses. The T_1 values were found by fitting the decays to single exponentials (values provided in Table 5.1.

5.4. Results and Discussion

PDMS elastomer films in this work were prepared with a range of curing temperatures and amounts of cross-linker agent, and then characterized at room and low temperatures, and with and without mechanical compression in one dimension. Increasing the curing temperature increases the cross-linking density of the polymer due to having more of the Si-H moieties react with the vinyl functional groups. The higher curing temperatures also cause loops to form in the polymer network, while decreasing the number of dangling or unreacted ends of polymer chains when compared to lower curing temperatures.[123] Previous studies have found that higher curing temperatures (along with longer curing times) do have an effect on the modulus of the films.[255-258] Changing the mass ratio between the elastomer base and the curing agent also has an effect on the physical characteristics of the films. Increasing the cross-linker agent percentage makes a material more rigid (higher modulus) due to increasing the cross-linking density by adding more Si-H groups that can react with the vinyl groups.[59,259-260] However, increasing the curing concentration beyond 10% could leave an excess of unreacted curing agent in the system, which could in turn make the modulus decrease when compared to the manufacturer ratio of 10%.[261-262] In addition to chemically altering the polymer network, the samples were compressed to actively strain the polymer. Compressing the elastomer

films in one dimension stretches it uniformly in the other two dimensions, causing the film to be under active stress during measurements. The range of pressures ranged from barely squeezing (232 kPa) the polymer to being on the brink of breaking CaF_2 windows (651 kPa). Even with the higher pressure, the elastomer was able to recover its original shape (by eye) after the stress was removed. Cooling a polymer towards its glass transition temperature (T_g) causes the elastomer to become more glass-like, more brittle with a higher modulus. For example, the shear elastic modulus is 250 kPa for PDMS and changes at a small rate of 1.1 kPa/°C.[263] T_g for uncross-linked PDMS is -123°C with a melting temperature, T_m, around -40°C. [57,263] When the polymer is cross-linked, T_g changes slightly but not a significant amount.[264]

The baselined and normalized FTIR spectra for the silicon hydride vibration, $\nu_{Si\text{-}H}$, on the PDMS elastomer thin films under various perturbations are shown in Figure 5.3a-d. The center frequencies ($\nu_{Si\text{-}H}$) and peak widths (full width at half maximum, FWHM) of the $\nu_{Si\text{-}H}$ in the various systems are provided in Table 5.1 for comparison. The $\nu_{Si\text{-}H}$ frequency has been shown to be tuned by the inductive effect of the substituents attached to the silicon in small molecules,[229,231,249-251] but is found here to be relatively insensitive to these macroscopic perturbations. When the PDMS elastomer is swollen with different solvents, the center frequency was also insensitive.[265] However, the largest peak shift is 5 cm^{-1} for the film heat cured at 150°C (Figure 5.3b), which is larger than any of the swollen elastomer systems. The compressed elastomer thin films also experience a similar peak shift. Slight changes in the local electrostatic environment around the vibrational oscillator induce these shifts in the vibrational transition energies. The insensitivity of the mean Si-

H stretching frequencies demonstrates that there are similar average local environments in the various elastomer films.

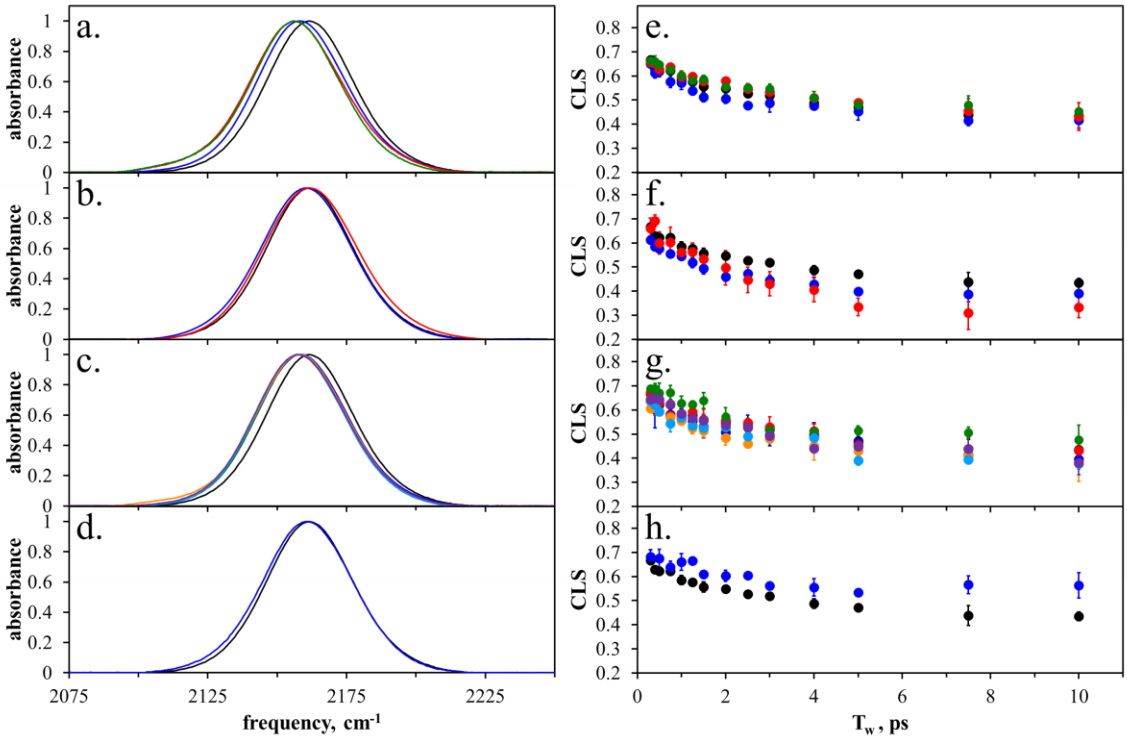

Figure 5.3. Baselined and normalized FTIR spectra of the Si-H vibration for PDMS elastomer thin films with a) increasing curing temperature, b) increasing curing agent percentage, c) increasing pressure, and d) being cooled, with the CLS decays as a function of T_w for each respective perturbation (e-h). Black lines/markers denote unaltered PDMS in all plots; blue, red, and green represent 100°C, 125°C, and 150°C in plots (a) and (e); blue and red represent 20% and 30% curing agent in plots (b) and (f); blue, red, green, orange, light blue, and purple represent 232, 249, 299, 371, 478, and 651 kPa in plots (c) and (g); and red for PDMS cooled to -43°C for plots (d) and (h). The markers are the average CLS values with the error bars as the standard deviations. The unaltered PDMS elastomer thin film FTIR spectrum and CLS data are shown in all of the respective frames to show the slight differences occurring.

Table 5.1. Frequency (ν_{Si-H}), peak width (FWHM), and vibrational lifetime (T_1) values for the PDMS elastomer thin films under various perturbations.

sample	conditions	ν_{Si-H} (cm^{-1})	FWHM (cm^{-1})	T_1 (ps)[a]
Unaltered PDMS		2161.3	36.9	5.0 (± 0.2)
PDMS Heat Cured	100 ℃	2158.0	37.7	4.86 (± 0.08)
	125 ℃	2155.5	38.9	4.9 (± 0.1)
	150 ℃	2156.0	37.6	4.89 (± 0.07)
Increased Cross-Linker	20% (10:2)	2160.4	38.6	5.05 (± 0.07)
	30% (10:3)	2161.8	39.8	5.3 (± 0.7)
Compressed PDMS	232 (± 6) kPa	2158.4	38.3	4.91 (± 0.09)
	249 (± 7) kPa	2158.0	38.0	-
	299 (± 8) kPa	2157.5	37.8	4.9 (± 0.4)
	371 (± 9) kPa	2158.0	38.5	4.96 (± 0.09)
	478 (± 12) kPa	2157.0	37.9	4.85 (± 0.08)
	651 (± 16) kPa	2157.5	38.5	4.9 (± 0.1)
Cooled PDMS	-43 ℃	2160.8	38.3	4.9 (± 0.2)

a. Standard error of the fit.

The peak width of the FTIR spectrum has a similar insensitivity to the perturbations. The FTIR peak widths reflect the range of chemical environments around the silicon hydride groups contained in the sample as well as the time-dependent fluctuations of the vibrational frequencies that are driven by the polymer structural dynamics. Spectral diffusion and homogeneous broadening are measures of these fluctuations. Increasing the percentage of the curing agent had the largest change of 3 cm^{-1}. These slight differences could be due to the local environment or the structural dynamics changing. Even with the silicon atom being less polarized and less sensitive to the

environment,[265] the $\nu_{Si\text{-}H}$ is still sensing slight differences. Overall, the FTIR spectrum is relatively insensitive to the macroscopic changes that are occurring across these different alterations due to the linear lineshape reflecting the time-average molecular configurations.

2D-IR spectroscopy was implemented to separate contributions to the FTIR lineshapes for the $\nu_{Si\text{-}H}$ into slow, pseudo-static and dynamic heterogeneity, and homogeneous dynamics. Figure 5.5 through Figure 5.17 show all of the collected 2D-IR spectra. A 2D-IR spectrum has two frequency axes. The x-axis (ω_1) corresponds to the frequencies at which a subensemble of oscillators is excited by the first IR pulse. The y-axis (ω_3) is the range of frequencies that this subensemble exhibits after sampling its surroundings for a specific waiting time, T_w. The longer the waiting time, the longer the subensemble has had to sample its surroundings. Therefore, the 2D-IR spectrum yields the frequency-frequency time correlation for the subensembles beneath the FTIR lineshape.[2,38,141,153,159] Each spectrum has a positive- and negative-going peak. The red positive-going peak corresponds to the v=0-1 transition (ground-state bleach) and lies on or above the diagonal. The blue negative-going peak corresponds to the v=1-2 transition (excited-state absorption) and is anharmonically shifted to lower frequencies along the ω_3 axis. When a large anharmonicity is present, a diagonal slice through the 0-1 peak reflects the range of frequencies captured by the linear FTIR lineshape. The antidiagonal width of the 0-1 peak represents the portion of the available frequencies that have been sampled during a given T_w, containing the contributions from very fast pure dephasing (T_2^*), vibrational relaxation (T_1), and spectral diffusion caused by interconversion of molecular subensembles and driven by reorganization of the local environment.[36,163-164]

Qualitatively, all of the 2D-IR spectra look similar to one another. The peaks are diagonally elongated at early T_ws, meaning that the modes are strongly correlated to their initial frequencies; the Si-H oscillators have not yet sampled the full range of local environments at early waiting times. As the waiting time increases, the 2D-IR peak shapes become slightly rounder, reflecting the loss of correlation due to spectral diffusion of the Si-H oscillators. The polymer structural motions must have an influence on the frequencies if spectral diffusion is occurring. The 2D-IR spectra for all the systems seem well-correlated even after 5 ps; no subensemble of Si-H oscillators in the films is able to experience all of the local environments that are present.

The v=0-1 peaks in the 2D-IR spectra for all T_ws for the PDMS elastomer films under the various perturbations were analyzed using the CLS method to quantify the subtle differences between them.[163-164] Figure 5.3e-h shows the CLS values as a function of T_w, where a single exponential function with an offset was sufficient to model the CLS data for all the systems studied. The CLS decays confirm that much of the dynamic processes on these timescales are insensitive to the macroscopic perturbations imposed upon PDMS in this study. However, there are slight differences that can be discussed. The CLS decays do not reach the baseline for any of the samples, so the Si-H oscillators must remain somewhat correlated with their starting frequencies even after 10 ps. There are structural dynamics that occur on timescales that are much longer than tens of ps and appear as a pseudo-static inhomogeneity. This pseudo-static inhomogeneity was also present when the PDMS elastomer films were swollen in various solvents.[265] The pseudo-static inhomogeneity in the CLS decay decreased when solvent was introduced to the elastomer

network, but did not vary with solvent. In Figure 5.3e, the CLS decay is not sensitive to the increase in the cross-link density when the films are heat cured. Heat curing the samples causes the modulus of the films to increase (from 1.32 MPa with 25℃ cure to 2.59 MPa with 150℃),[258] but the dynamics remained unchanged. Increasing the curing agent percentage, however, caused the dynamics to become faster as shown in Figure 5.3f with a lower offset. The modulus also increases with the curing agent percentage, but not as much as heat curing the samples (1 MPa with 10% curing agent to 1.3 MPa with 20% curing agent). If the dynamics to which the $\nu_{Si\text{-}H}$ is sensitive were correlated to the elastic modulus, then both the heat cured samples and increased curing agent samples would have had similar changes in their CLS decays. However, the CLS decays are not similar, meaning whatever fast structural motions are reported by the Si-H are not involved in the elastic properties of the polymer. Straining the polymer with the compression confirms this as well. Figure 5.3g shows the polymer being compressed by different pressures, while the CLS decay remains unchanged; the Si-H mode is insensitive to this macroscopic change. The $\nu_{Si\text{-}H}$ seems to be more sensitive to the local microscopic environment changing due to the increase of the cross-linker component than the macroscopic environment changing. In Figure 5.3h, cooling the PDMS elastomer film had an effect on the dynamics by increasing the offset. The slower dynamics captured in this offset cannot be due to the macroscopic changes, since the vibrational mode was not sensitive to the elastic properties changing with all the other samples studied. Cooling the PDMS elastomer film makes a more glassy polymer, but the damping of the dynamics must be due to the thermal fluctuations of the polymer decreasing, which decreases the amount of motion in the polymer films. However,

the elastomer films being swollen with various solvents had more of a dramatic change to the CLS decays.[265] This confirms our hypothesis in that previous study that the differences in the dynamics must have been due to changes in the local environment with the inclusion of the solvent rather than the polymer network expanding during the swelling process. The CLS decays for the $\nu_{Si\text{-}H}$ in PDMS are more sensitive to the local chemical environment changing than the macroscopic environment.

The full FFCFs are obtained by using the CLS decays along with the FTIR lineshape, which separates the homogeneous and inhomogeneous contributions to the FTIR lineshapes.[163-164] The resulting FFCF parameters are given in Table 5.2. Overall, the values are similar to one another for each of these parameters, but there are slight differences. To highlight these slight differences, Figure 5.4 shows the inhomogeneous and homogeneous contributions to the FTIR lineshape with the various perturbations.

Table 5.2. FFCF Parameters for the PDMS elastomer thin films under various perturbations.

sample	conditions	Δ_1 (cm^{-1})[a]	τ_1 (ps)[b]	Δ_0 (cm^{-1})[a]	Γ (cm^{-1})[a]
Unaltered		9 (± 2)	2.7 (± 0.4)	13 (± 1)	1.5 (± 0.3)
Heat Cured	100℃	10 (± 2)	1.7 (± 0.3)	13 (± 2)	1.7 (± 0.4)
	125℃	10 (± 2)	3.9 (± 0.7)	13 (± 2)	1.5 (± 0.7)
	150℃	9 (± 2)	2.6 (± 0.5)	13 (± 2)	1.4 (± 0.6)
Curing Agent Percentage	20% (10:2)	10 (± 1)	2.0 (± 0.3)	13 (± 1)	1.8 (± 0.2)
	30% (10:3)	13 (± 2)	2.4 (± 0.4)	11 (± 2)	2.0 (± 0.3)
Compressed	232 (± 6) kPa	10 (± 2)	4 (± 1)	13 (± 2)	1.0 (± 0.4)
	249 (± 7) kPa	10 (± 2)	4 (± 1)	13 (± 2)	1.0 (± 0.4)
	299 (± 8) kPa	9 (± 2)	1.9 (± 0.4)	13 (± 2)	1.4 (± 0.3)
	371 (± 9) kPa	10 (± 2)	2.3 (± 0.4)	13 (± 2)	1.4 (± 0.4)
	478 (± 12) kPa	11 (± 2)	3.4 (± 0.8)	12 (± 2)	1.1 (± 0.4)
	651 (± 16) kPa	11 (± 2)	2.9 (± 0.5)	12 (± 2)	1.1 (± 0.2)
Cooled	-43℃	8 (± 1)	1.7 (± 0.5)	14 (± 1)	1.5 (± 0.2)

a. Errors show the range over which the parameter could be increased while the other parameters floated to fit the FTIR lineshape 98% as well as the best value

b. Standard error of the exponential fit

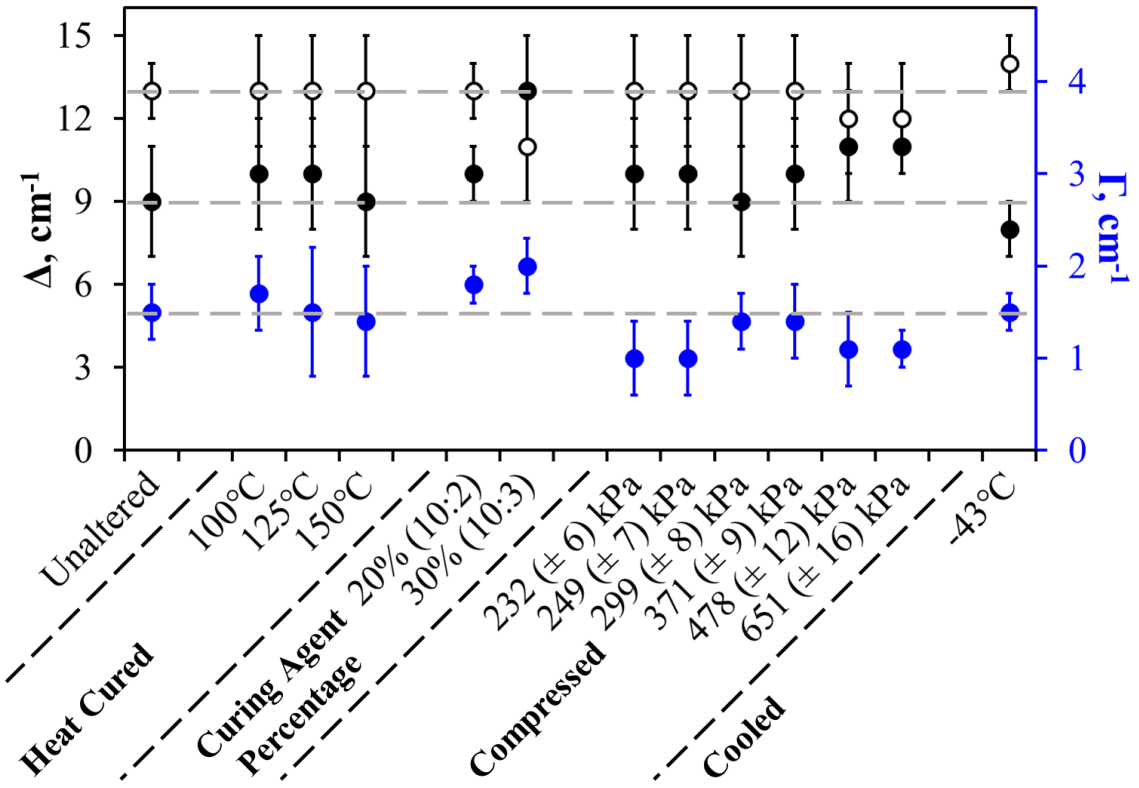

Figure 5.4. Amplitudes (black circles) and homogenous linewidth (blue circles) determined for PDMS elastomer thin films under various perturbations. The x-axis shows the systems studied in order of unaltered, heat cured, curing agent percentage, compressed, and cooled as labeled. Δ_1 (filled black circles) and Δ_0 (open black circles) are plotted along the black y-axis on the left of the plot. Γ (filled blue circles) is plotted along the blue y-axis on the right of the plot. The dashed grey lines show the unaltered PDMS FFCF parameters across the plot for comparison.

The homogeneous linewidth, Γ, represents the unresolvably fast dynamics in the elastomer films. The homogeneous linewidth is the same within error for all the alterations performed on the PDMS films, but there are slight trends that can be seen in Figure 5.4. Elevated curing temperatures and cooling the PDMS elastomer had no effect on the homogeneous linewidth. Even when cooling the polymer to the point of crystallization, there are many fast structural motions occurring in the polymer due to T_g being so low, causing the homogeneous dynamics to remain unchanged. Heat curing did increase the

cross-linker density along with increasing the heterogeneity of the sample by forming loops in the chains, but the homogeneity remains the same. The homogeneous linewidth broadens with increasing curing agent percentage, showing that the frequency fluctuations experience by the $\nu_{Si\text{-}H}$ are either consistently faster or higher in amplitude. This may be due to having an increase in the curing agent component in the polymer network, since the elevated curing temperature samples did not have a significant change in the homogeneous linewidth. In the previous swelling study of PDMS, the curing agent on its own had a larger homogeneous linewidth.[265] Therefore, the Si-H oscillators may be experiencing more of the curing agent environment than the oligomer chains found in the base. However, the broadening of the FTIR peak for the increased curing agent percentage samples cannot be due to the macroscopic properties of the elastomer changing, since the heat cured samples relatively have no change in the linewidth but experience a change in the elastic modulus. Compressing the elastomer seemed to narrow the homogeneous linewidth, but there is no correlation with the amount of pressure applied to the samples. The ultrafast dynamics sensed by the $\nu_{Si\text{-}H}$ must be disconnected from the stress applied to the polymeric chains. This may be evidence that the dynamics reported in the FFCF are in fact not polymer backbone movements but rather the methyl side chain motions that do not bear the stress during compression. Overall, the small contributions of the homogeneous linewidth to the broad FTIR lineshape shows the large inhomogeneity of the elastomer networks that should properly be included in elasticity models.

The inhomogeneous contributions to the FTIR lineshape can be separated into spectral diffusion (Δ_1 and τ_1) and pseudo-static inhomogeneity (Δ_0). The correlation time,

τ_1, was shown to be influenced by nearby polymer chains when the PDMS elastomer was swollen in different solvents.[265] The correlation times across all samples and perturbation ranged from 1.7 to 4.0 ps. This may seem like a large variation, but the errors are large on some of these values. Also, the variation of the correlation time may be due to the range of polymer motions that could be occurring at room temperature. Overall, there seems to be no trends with the variables tested.

Elevating the curing temperature and compressing the polymer films had no effect on Δ_1, again showing that the macroscopic changes do not have a large effect on the local environment. However, I do find that Δ_1 increases slightly as the number of cross-linker molecules increases, meaning that the motion occurring is producing larger stochastic frequency shifts. In other words, the motion has more of an effect on the local environment, or there are more Si-H modes near each other where a fluctuation can have more of an effect on the frequency. The increase in the amplitude was also seen in the pure curing agent and the curing agent solutions.[265] Therefore, the increase in the amplitude shown here is most likely due to the Si-H oscillators experiencing more of the curing agent environment than the elastomer network. On the other hand, cooling the elastomer films causes Δ_1 to decrease due to the thermal energy of the system being much lower.

The pseudo-static inhomogeneity (Δ_0) also shows some slight trends. Like Δ_1, heat curing and compressing the sample have no effect on the amplitude but increasing the curing agent percentage lowers the pseudo-static inhomogeneity while cooling the polymer increases the pseudo-static inhomogeneity. The reasoning is the same as in the previous paragraph. The Si-H oscillators are experiencing more of the curing agent oligomers than

the elastomer network causing the pseudo-static inhomogeneity to decrease. The pure curing agent also had a lower pseudo-static inhomogeneity in the previous paper.[265] Cooling the PDMS elastomer causes the polymer chains to move slower overall, so those ultrafast motions are slower. The FFCF parameters show that the macroscopic property of the films is not dependent on the ultrafast structural dynamics of the polymer. The differences in the dynamics are more due to the local environment changing chemically than physically. The large values of the inhomogeneous amplitudes show that the peak width is dominated by the heterogeneity and that the differences are mostly due to the inhomogeneous broadening effects.

Finally, the FTIR lineshapes are dominated by inhomogeneous broadening (spectral diffusion and pseudo-static inhomogeneity). The inhomogeneity of the films must be due to the cross-linking reaction not reacting homogeneously, which was discussed previously when the PDMS elastomer films were swollen in different solvents.[265] 2D-IR spectroscopy is able to show that the elastomer network remains heterogeneous over the different physical and chemical perturbations. The heterogeneity remaining relatively unchanged shows the difficulty of measuring and modeling the underlying microscopic motions that result in the macroscopic properties. It is likely that a complete and predictive model of elastomer behavior will need to account for this heterogeneity.

5.5. Conclusions

This study viewed the structural dynamics of a cross-linked elastomer from the perspective of a covalently bound silicon hydride. The macroscopic properties of the films

were altered by heat curing, increasing the curing agent percentage, mechanical compression, and cooling the elastomer near T_g. The FTIR spectra of the silicon hydride mode were broad and relatively insensitive to the macroscopic changes occurring, which is due to the overwhelming chemical heterogeneity demonstrated by 2D-IR spectroscopy. There are ultrafast dynamics occurring in PDMS to which the Si-H mode is sensitive, yet, these dynamics have minimal connections to the macroscopic elastic properties of the polymer. Even though the polymer films were macroscopically perturbed, the microscopic picture remained relatively unchanged. The phantom network model or some intermediate model may be necessary to properly model the elasticity but the dynamics on the ultrafast timescale need not be included. From the perspective of the ultrafast dynamics, the affine network model would be a good approximation.

The ultrafast dynamics that influence $\nu_{Si\text{-}H}$ do not contribute to the elasticity of the polymer network, but they are still important for other polymer properties, such as gas and liquid transport.[93,114,117,253-254] One interesting prediction that one could make is that such processes would be independent of film deformation, since the current results show that the driving dynamics are unchanged by these macroscopic perturbations.[c]

[c] The authors gratefully acknowledge partial support from the National Science Foundation under CHE-0847356 and CHE-1464416 (to A.M.M.). C.M.O. was supported by a National Science Foundation Graduate Student Research Fellowship Grant Number 00039202. Any opinions, findings, and conclusions or recommendations expressed in this material are those of the author(s) and do not necessarily reflect the views of the National Science Foundation.

5.6. Full Set of 2D-IR Data

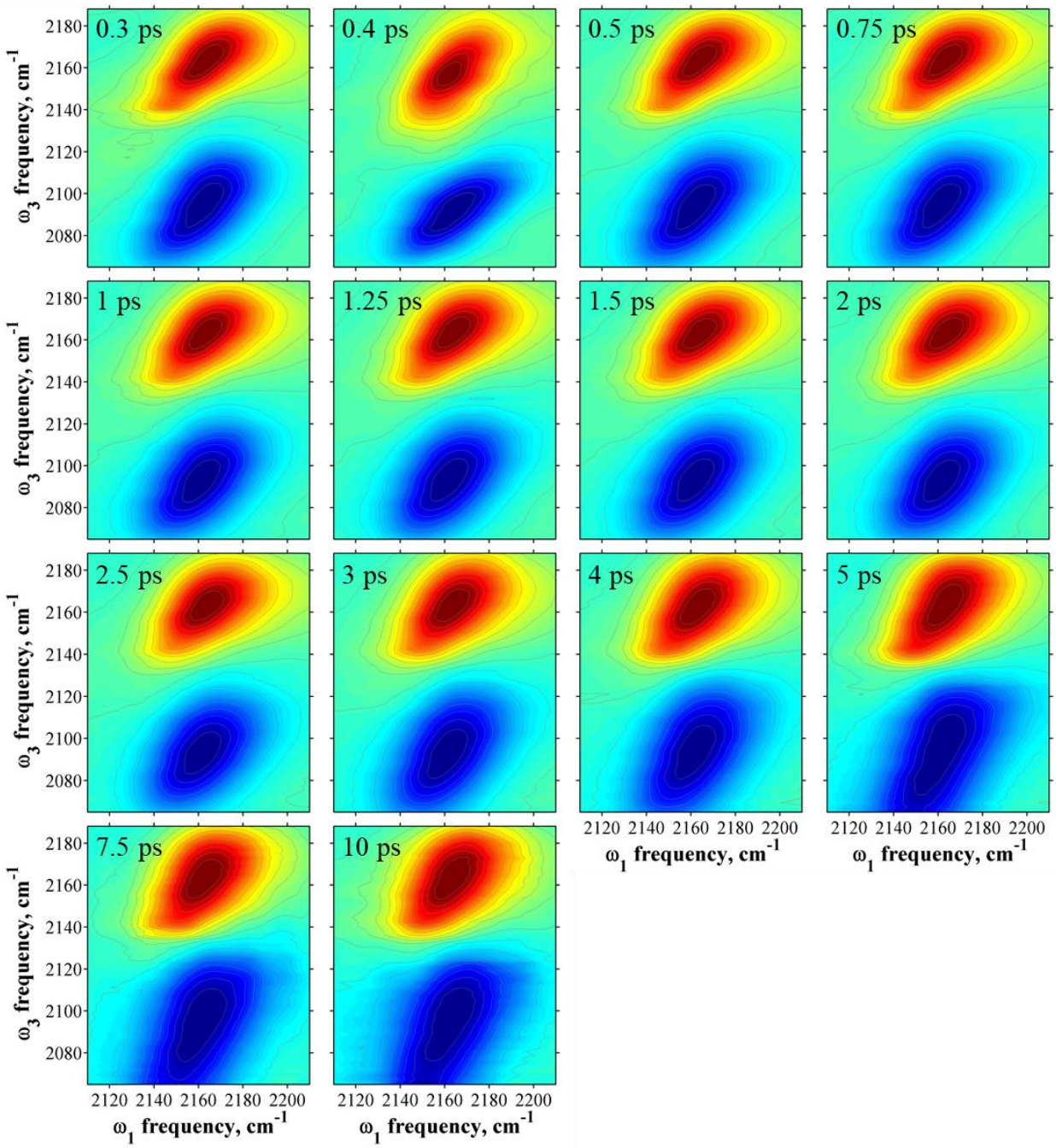

Figure 5.5. All 2D-IR spectra collected for unaltered PDMS.

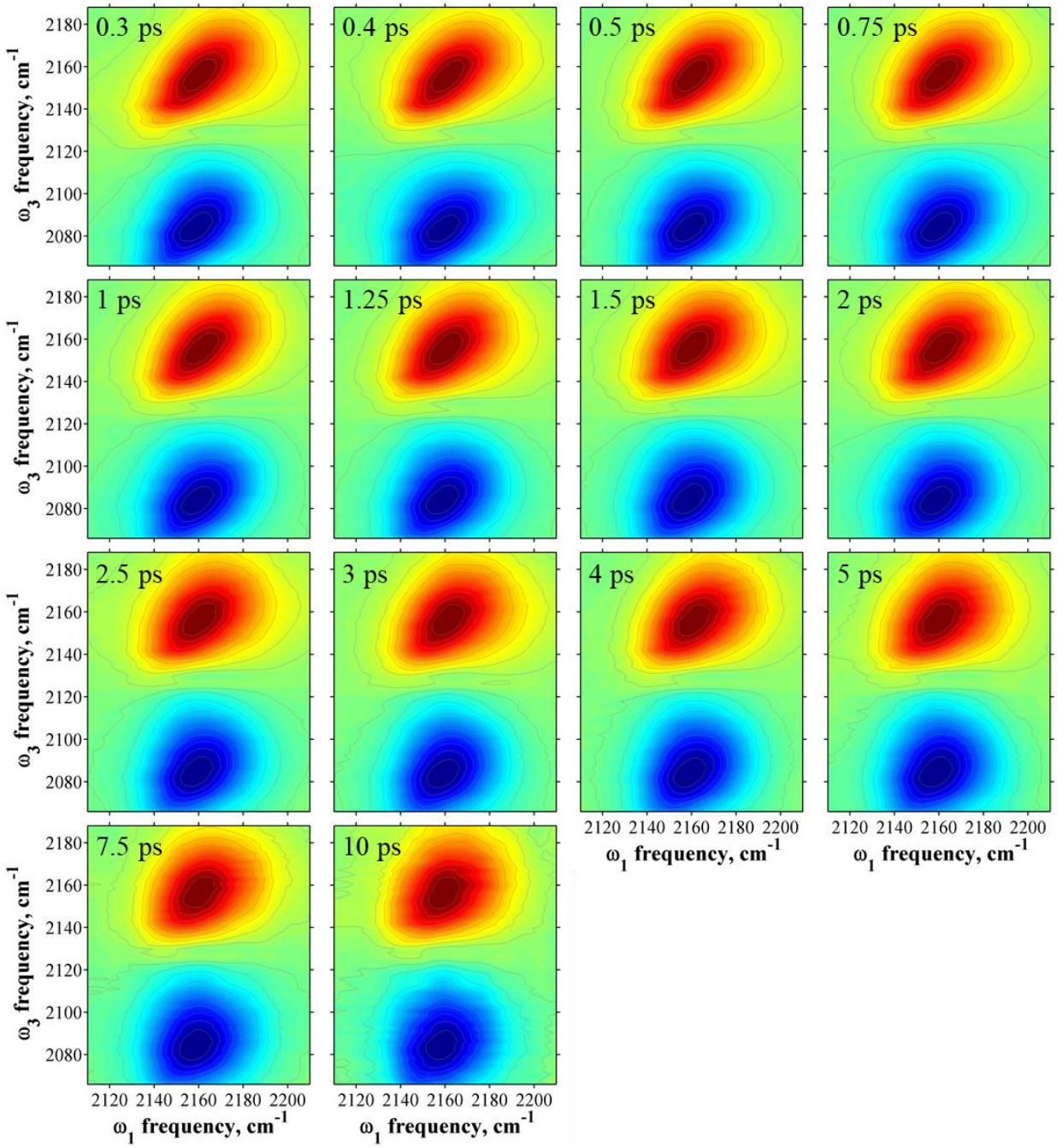

Figure 5.6. All 2D-IR spectra collected for PDMS heat cured at 100°C.

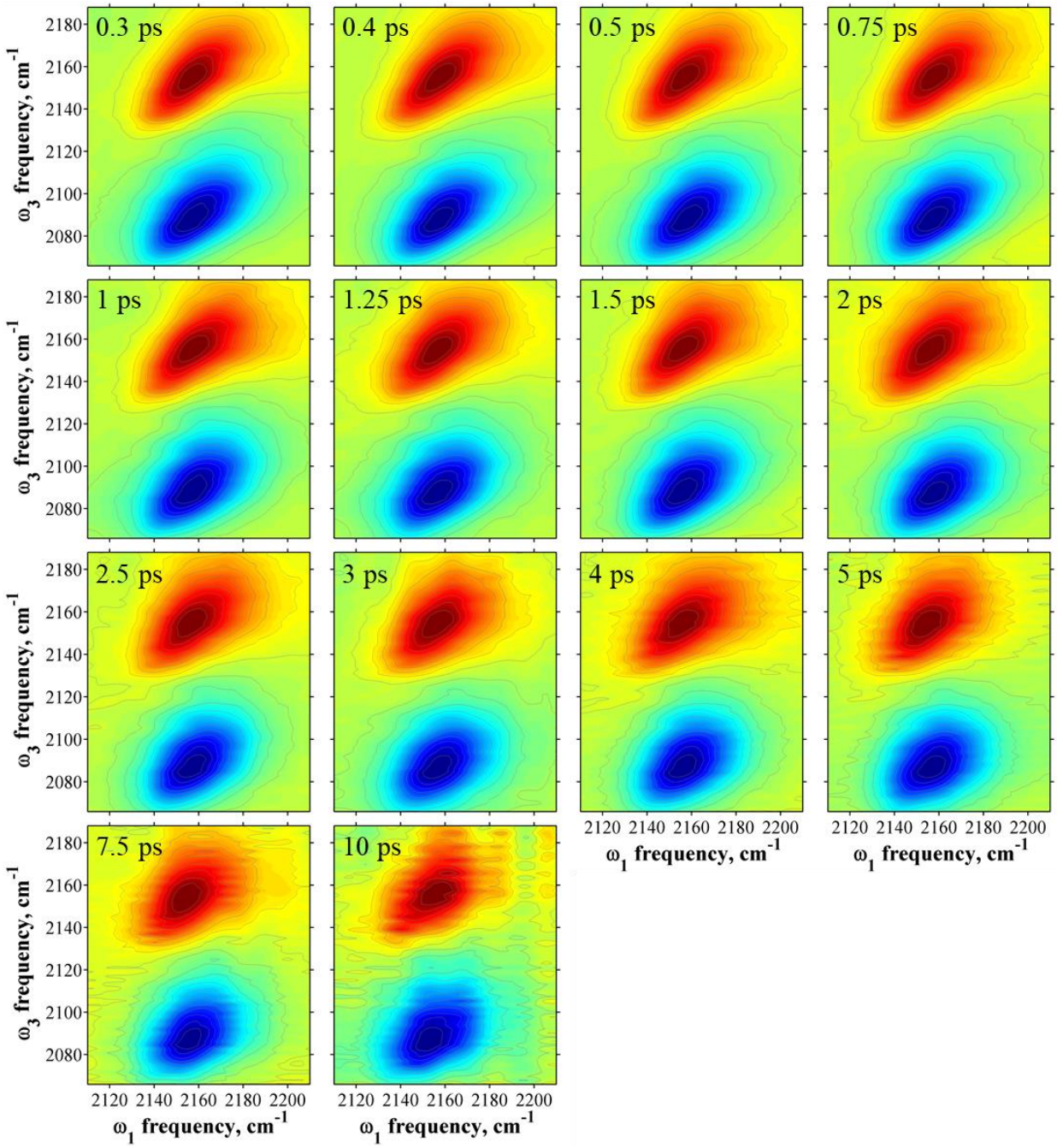

Figure 5.7. All 2D-IR spectra collected for PDMS heat cured at 125°C.

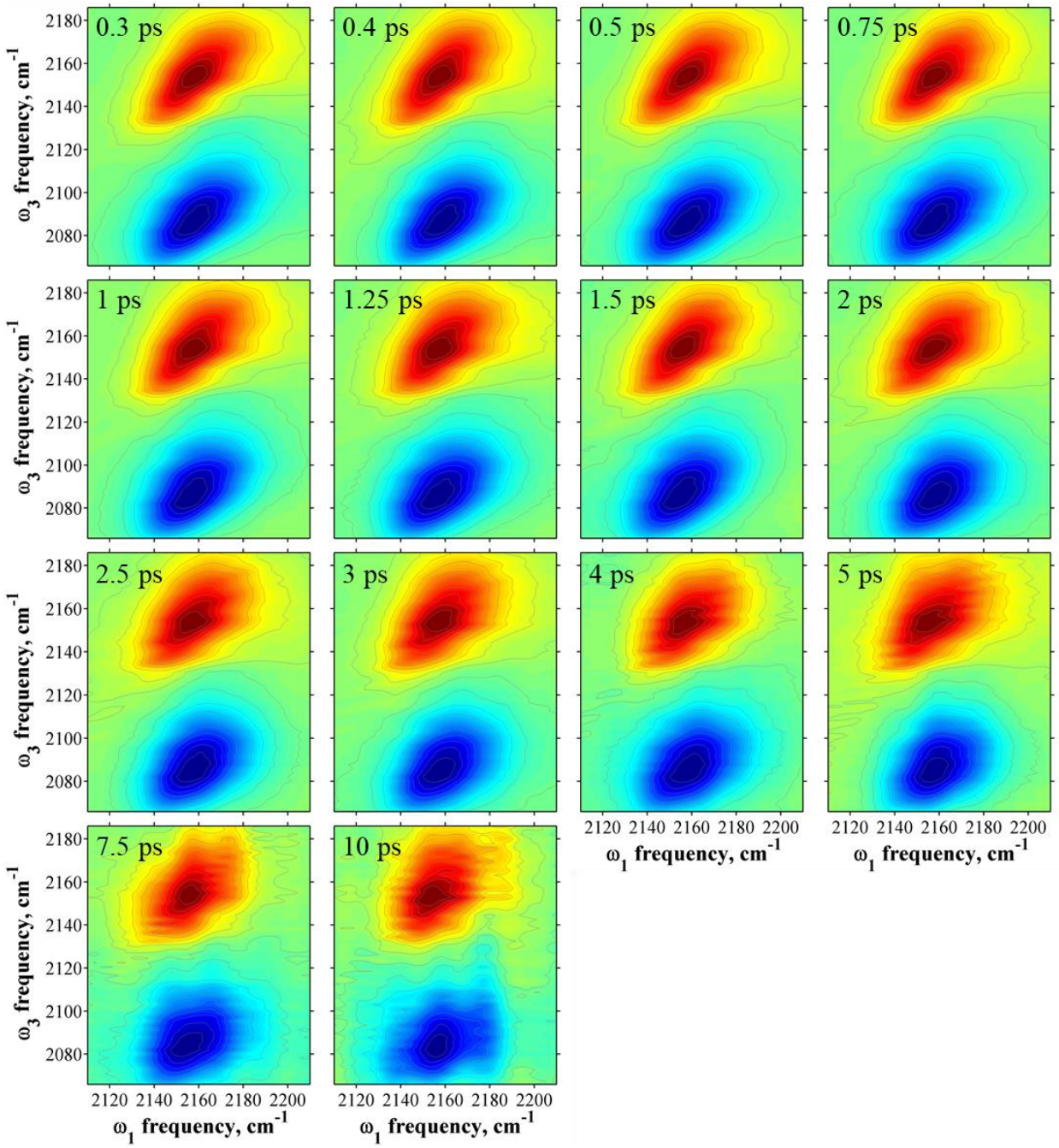

Figure 5.8. All 2D-IR spectra collected for PDMS heat cured at 150°C.

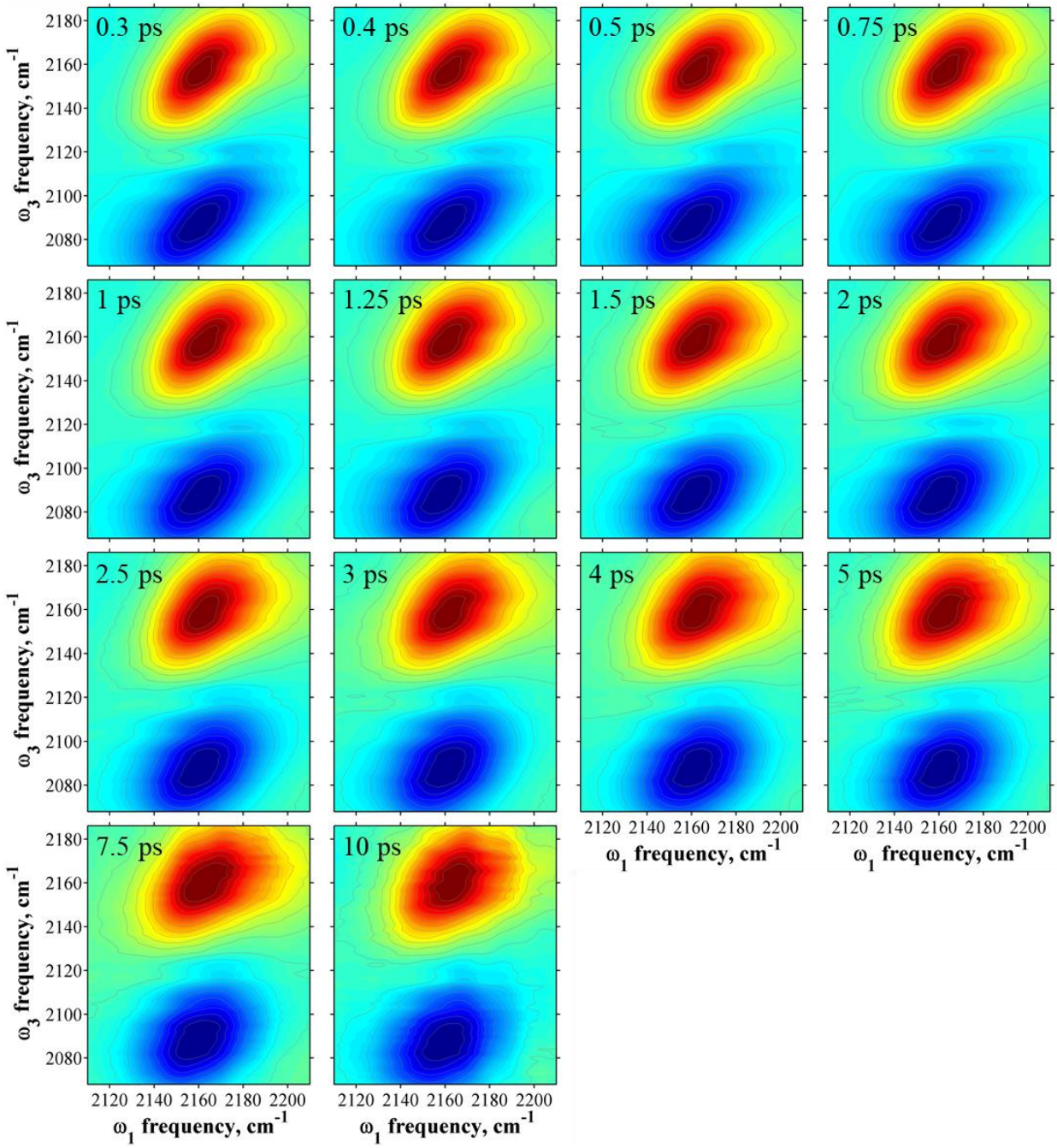

Figure 5.9. All 2D-IR spectra collected for PDMS with 20% curing agent.

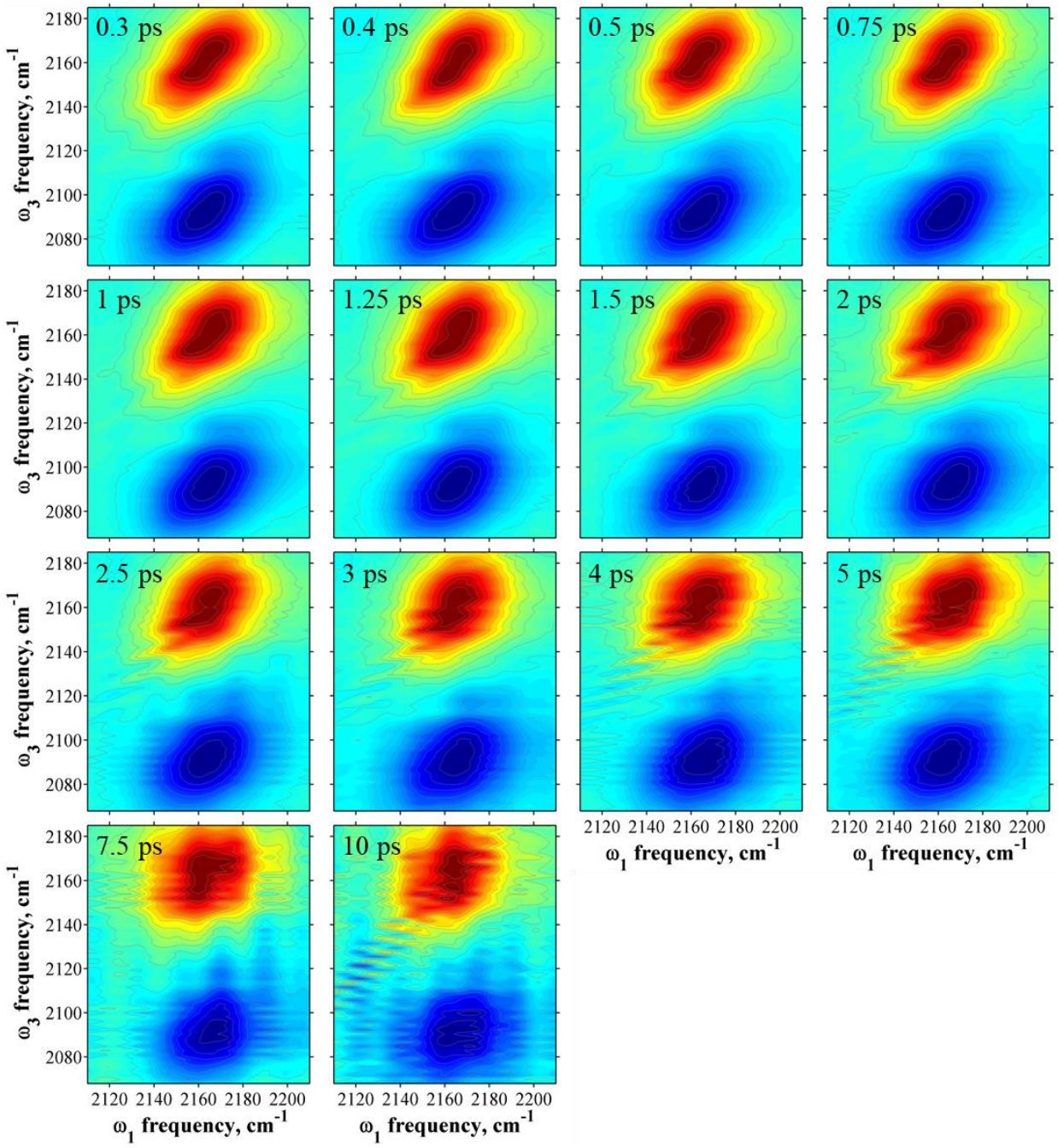

Figure 5.10. All 2D-IR spectra collected for PDMS with 30% curing agent.

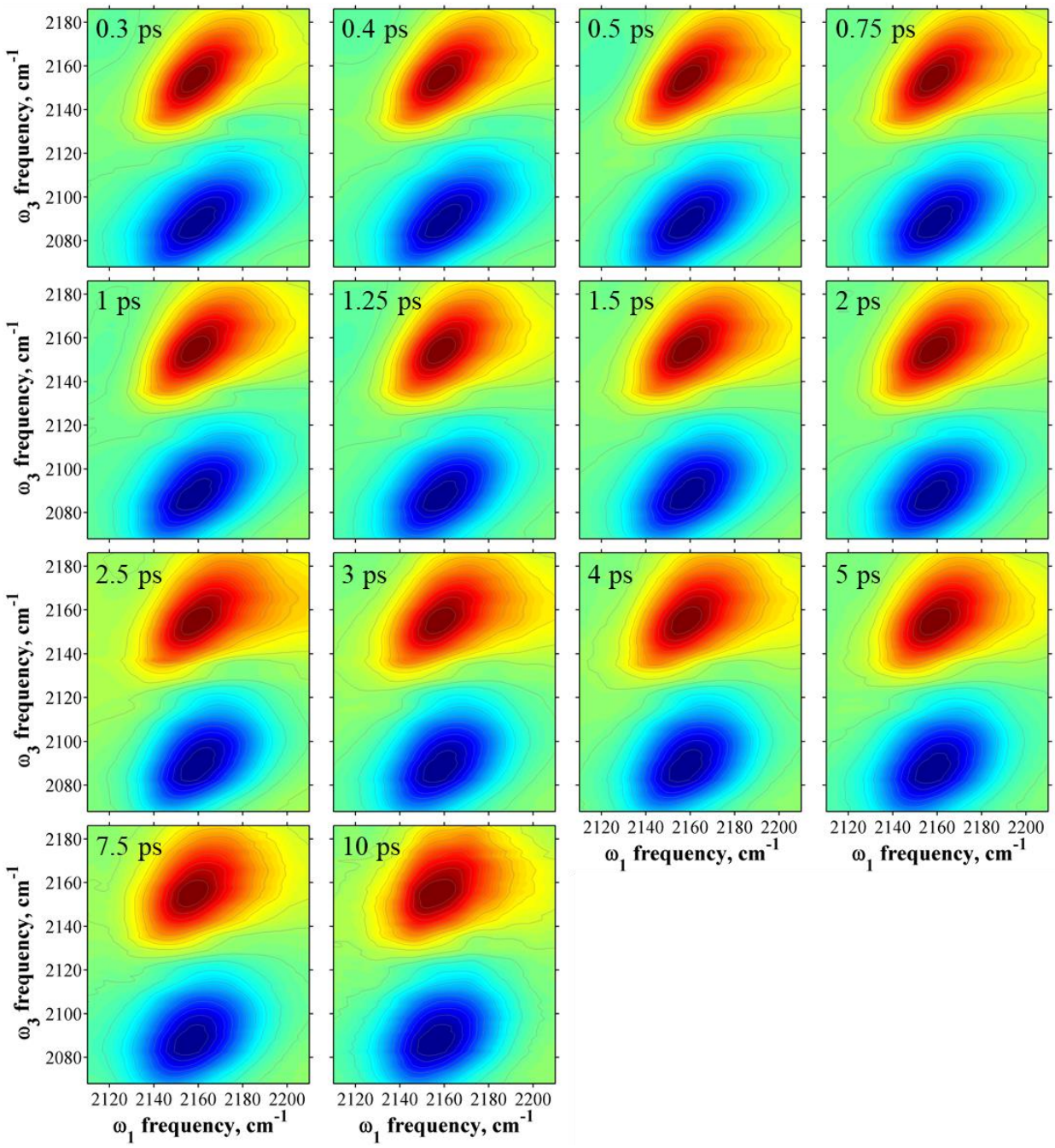

Figure 5.11. All 2D-IR spectra collected for PDMS compressed to 232 kPa.

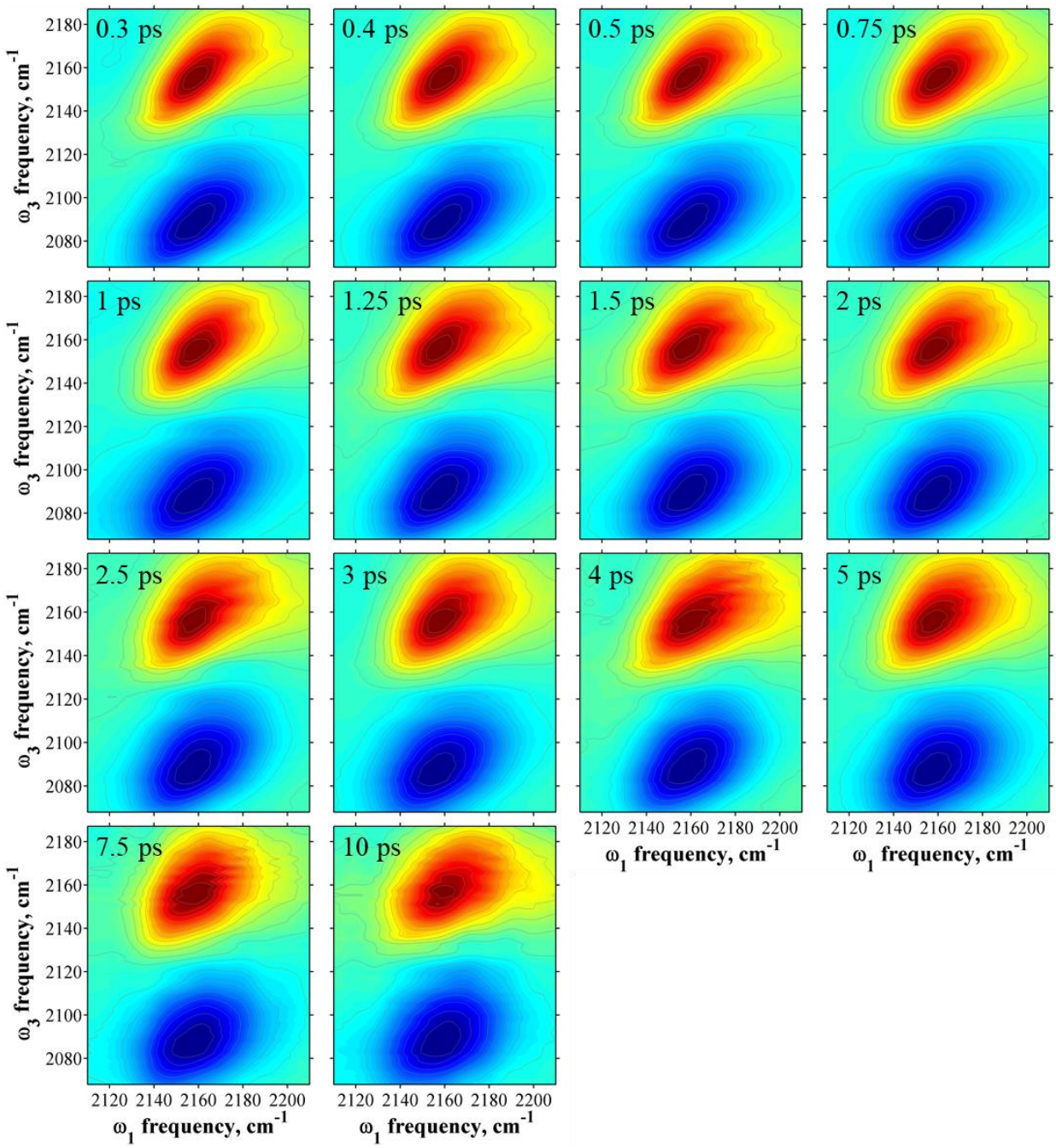

Figure 5.12. All 2D-IR spectra collected for PDMS compressed to 249 kPa.

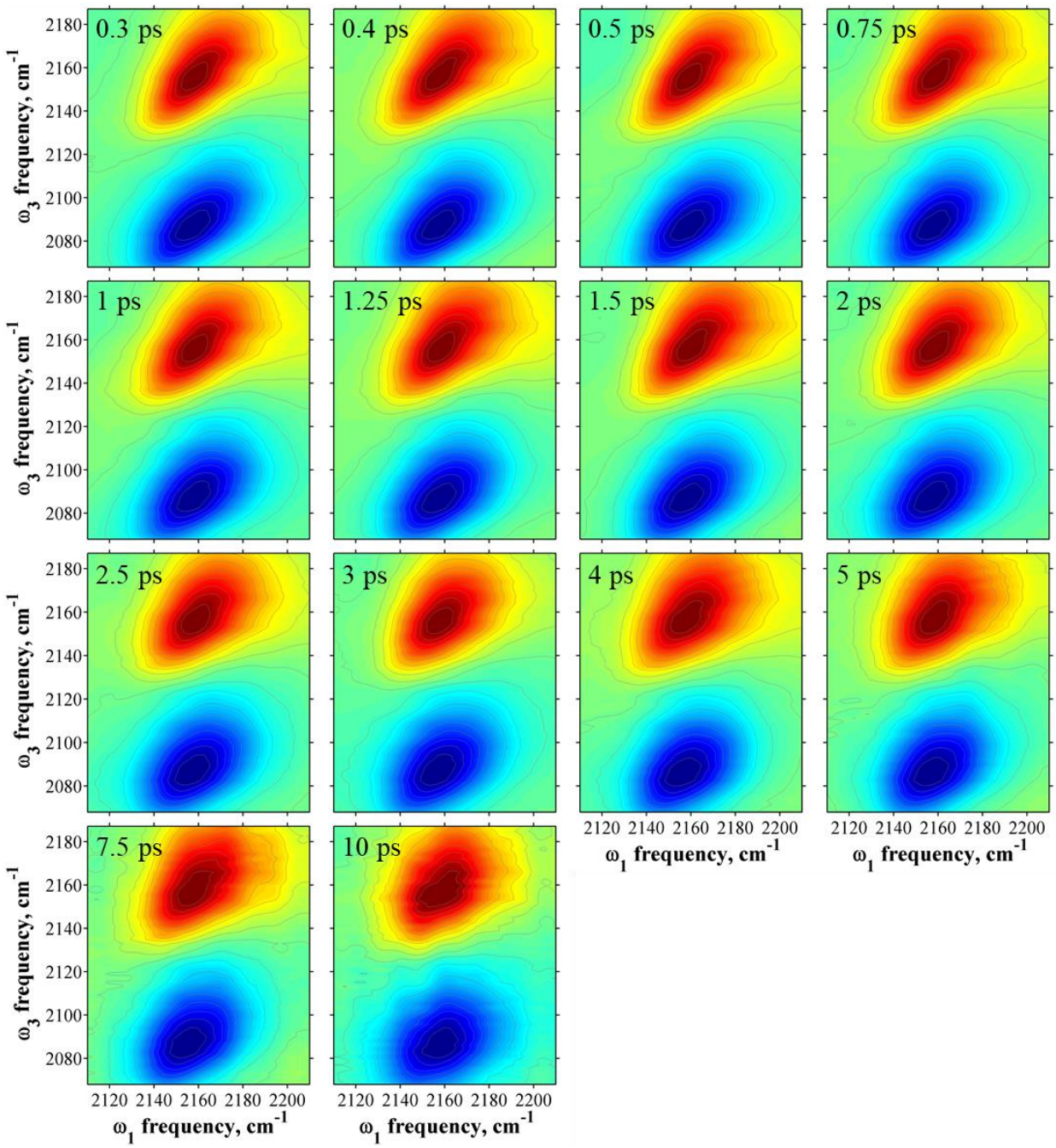

Figure 5.13. All 2D-IR spectra collected for PDMS compressed to 299 kPa.

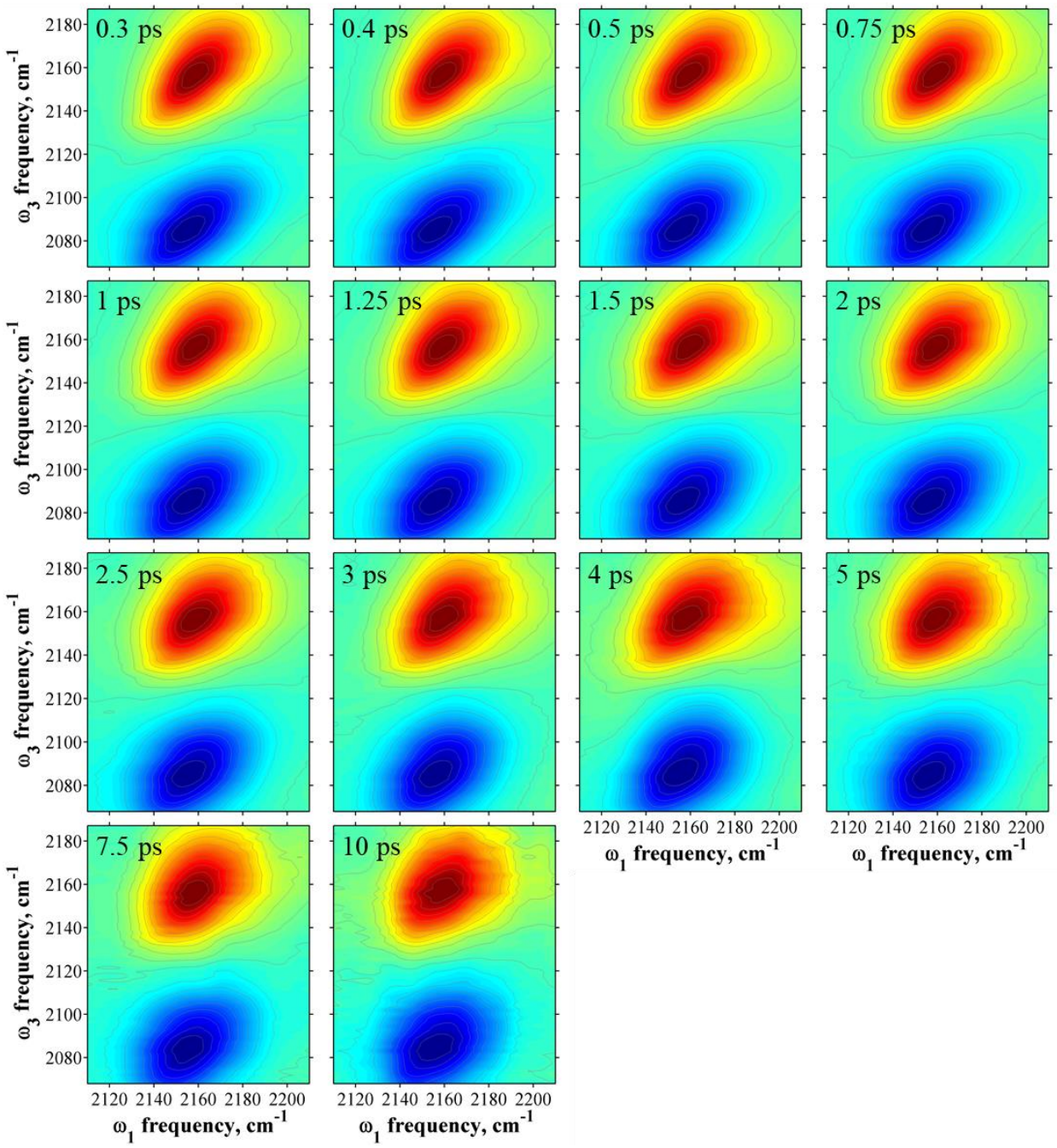

Figure 5.14. All 2D-IR spectra collected for PDMS compressed to 371 kPa.

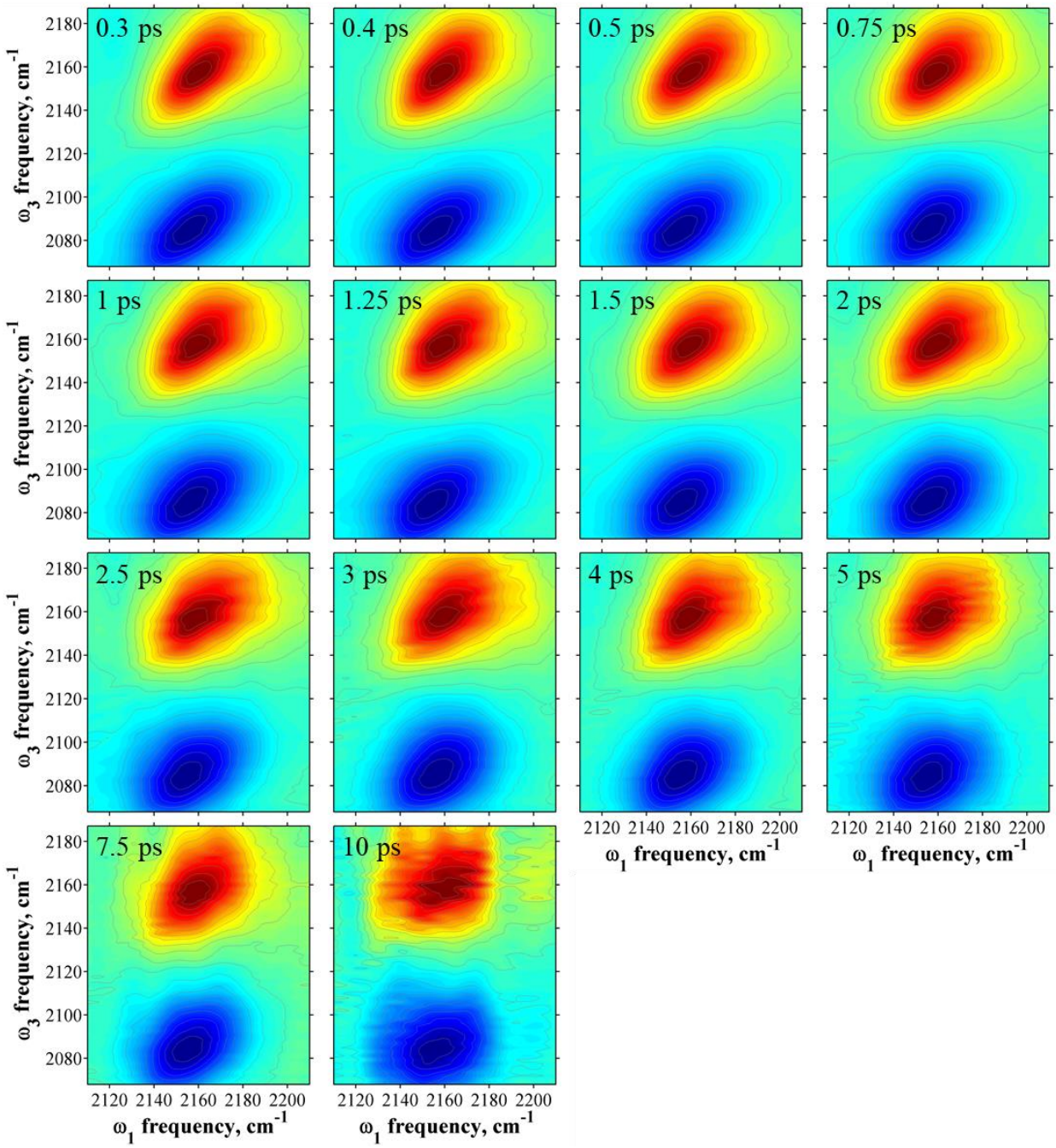

Figure 5.15. All 2D-IR spectra collected for PDMS compressed to 478 kPa.

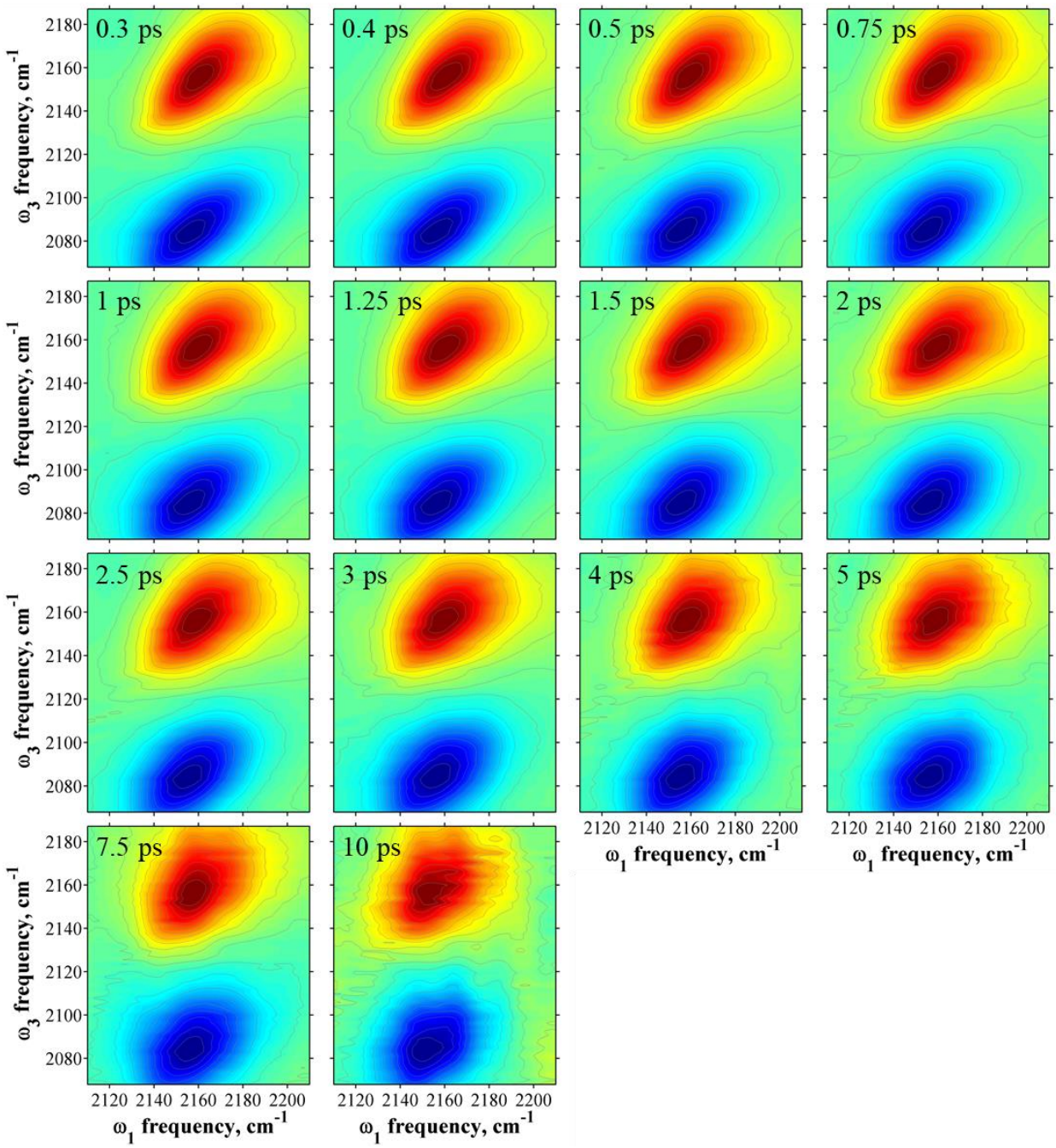

Figure 5.16. All 2D-IR spectra collected for PDMS compressed to 651 kPa.

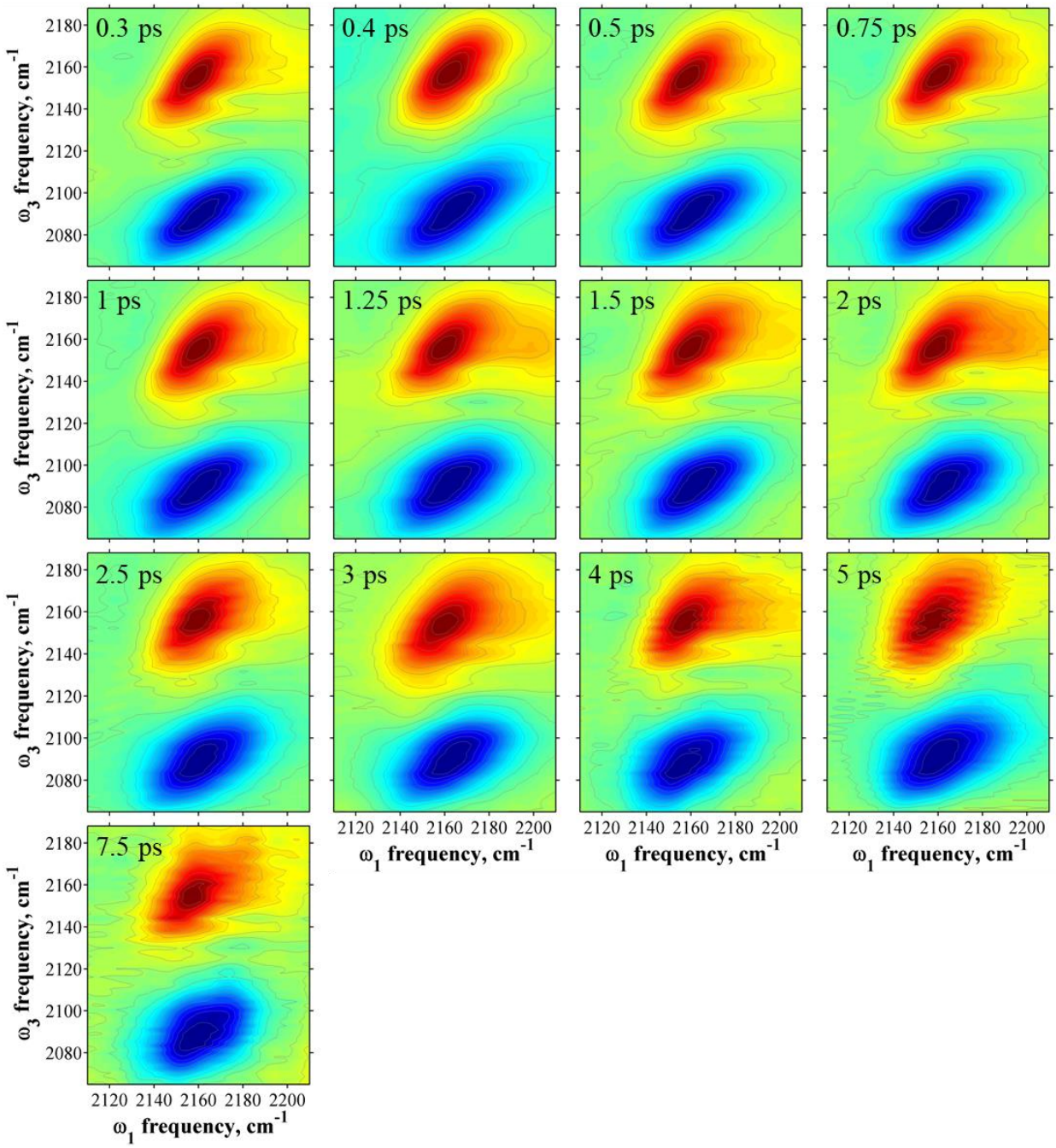

Figure 5.17. All 2D-IR spectra collected for PDMS cooled to -45°C.

Bibliography

1. Reichardt, C., *Solvents and Solvent Effects in Organic Chemistry.* 2nd ed.; VCH: 1988.
2. Hamm, P.; Lim, M.; Hochstrasser, R. M., Structure of the Amide I Band of Peptides Measured by Femtosecond Nonlinear-Infrared Spectroscopy. *J. Phys. Chem. B* **1998**, *102*, 6123-6138.
3. King, J. T.; Anna, J. M.; Kubarych, K. J., Solvent-Hindered Intramolecular Vibrational Redistribution. *Phys. Chem. Chem. Phys.* **2011**, *13*, 5579-5583.
4. Jones, B. H.; Huber, C. J.; Massari, A. M., Solvent-Mediated Vibrational Energy Relaxation from Vaska's Complex Adducts in Binary Solvent Mixtures. *J. Phys. Chem. A* **2013**, *117*, 6150-6157.
5. Brookes, J. F.; Slenkamp, K. M.; Lynch, M. S.; Khalil, M., Effect of Solvent Polarity on the Vibrational Dephasing Dynamics of the Nitrosyl Stretch in an Fe(II) Complex Revealed by 2D IR Spectroscopy. *J. Phys. Chem. A* **2013**, *117*, 6234-6243.
6. Huber, C. J.; Massari, A. M., Characterizing Solvent Dynamics in Nanoscopic Silica Sol–Gel Glass Pores by 2D-IR Spectroscopy of an Intrinsic Vibrational Probe. *J. Phys. Chem. C* **2014**, *118*, 25567-25578.
7. Huber, C. J.; Egger, S. M.; Spector, I. C.; Juelfs, A. R.; Haynes, C. L.; Massari, A. M., 2D-IR Spectroscopy of Porous Silica Nanoparticles: Measuring the Distance Sensitivity of Spectral Diffusion. *J. Phys. Chem. C* **2015**, *119*, 25135-25144.
8. Eigner, A. A.; Anglin, T. C.; Massari, A. M., 2D-IR Studies of Annealing-Induced Changes to Structural Dynamics in Organic Semiconductor Thin Films. *J. Phys. Chem. C* **2010**, *114*, 12308-12315.
9. Eigner, A. A.; Jones, B. H.; Koprucki, B. W.; Massari, A. M., Ground-State Structural Dynamics in Doped and Undoped Polyaniline Films Probed by Two-Dimensional Infrared Vibrational Echo Spectroscopy. *J. Phys. Chem. B* **2011**, *115*, 4583-4591.
10. Eigner, A. A.; Jones, B. H.; Koprucki, B. W.; Massari, A. M., Static and Dynamic Structural Memory in Polyaniline Thin Films. *J. Phys. Chem. B* **2011**, *115*, 8686-8695.
11. Casey, C. P.; Beetner, S. E.; Johnson, J. B., Spectroscopic Determination of Hydrogenation Rates and Intermediates During Carbonyl Hydrogenation Catalyzed by Shvo's Hydroxycyclopentadienyl Diruthenium Hydride Agrees with Kinetic Modeling Based on Independently Measured Rates of Elementary Reactions. *J. Am. Chem. Soc.* **2008**, *130*, 2285-2295.
12. Anna, J. M.; Baiz, C. R.; Ross, M. R.; McCanne, R.; Kubarych, K. J., Ultrafast Equilibrium and Non-Equilibrium Chemical Reaction Dynamics Probed with Multidimensional Infrared Spectroscopy. *Int. Rev. Phys. Chem.* **2012**, *31*, 367-419.
13. Jones, B. H.; Huber, C. J.; Massari, A. M., Solvation Dynamics of Vaska's Complex by 2D-IR Spectroscopy. *J. Phys. Chem. C* **2011**, *115*, 24813-24822.
14. Chock, P. B.; Halpern, J., Kinetics of the Addition of Hydrogen, Oxygen, and Methyl Iodide to Some Square-Planar Iridium(I) Complexes. *J. Am. Chem. Soc.* **1966**, *88*, 3511-3514.

15. Stieger, H.; Kelm, H., Effect of Solvent and Pressure on the Rates of the Oxidative Addition Reactions of Methyl Iodide and Oxygen to Chlorocarbonylobis(Triphenylphosphine)Iridium(I). *J. Phys. Chem.* **1973**, *77*, 290-294.
16. Ugo, R.; Pasini, A.; Fusi, A.; Cenini, S., Kinetic Investigation of Some Electronic and Steric Factors in Oxidative Addition Reactions to Vaska's Compound. *J. Am. Chem. Soc.* **1972**, *94*, 7364-7370.
17. Cainelli, G.; Galletti, P.; Giacomini, D., Solvent Effects on Stereoselectivity: More Than Just an Environment. *Chem. Soc. Rev.* **2009**, *38*, 990-1001.
18. El Seoud, O. A., Understanding Solvation. *Pure Appl. Chem.* **2009**, *81*, 697-707.
19. Reichardt, C., Solvatochromic Dyes as Solvent Polarity Indicators. *Chem. Rev.* **1994**, *94*, 2319-2358.
20. Sakurai, M.; Yoshimori, A., Selective Solvation Caused by Size Effects. *Chem. Phys. Lett.* **2003**, *371*, 23-28.
21. Sadek, P. C.; Carr, P. W.; Doherty, R. M.; Kamlet, M. J.; Taft, R. W.; Abraham, M. H., Study of Retention Processes in Reversed-Phase High-Performance Liquid Chromatography by the Use of the Solvatochromic Comparison Method. *Anal. Chem.* **1995**, *57*, 2971-2978.
22. Snyder, L. R.; Carr, P. W.; Rutan, S. C., Solvatochromically Based Solvent-Selectivity Triangle. *J. Chromatogr. A* **1993**, *656*, 537-547.
23. Taft, R. W.; Pienta, N. J.; Kamlet, M. J.; Arnett, E. M., Linear Solvation Energy Relationships. 7. Correlations between the Solvent-Donicity and Acceptor-Number Scales and the Solvatochromic Parameters, Π*, A, and B. *J. Org. Chem.* **1981**, *46*, 661-667.
24. Kamlet, M. J.; Abboud, J.-L. M.; Abraham, M. H.; Taft, R. W., Linear Solvation Energy Relationships. 23. A Comprehensive Collection of the Solvatochromic Parameters, Π*, A, and B, and Some Methods for Simplifying the Generalized Solvatochromic Equation. *J. Org. Chem.* **1983**, *48*, 2877-2887.
25. Katritzky, A. R.; Fara, D. C.; Yang, H.; Tämm, K.; Tamm, T.; Karelson, M., Quantitative Measures of Solvent Polarity. *Chem. Rev.* **2004**, *104*, 175-198.
26. Rosés, M.; Ràfols, C.; Ortega, J.; Bosch, E., Solute–Solvent and Solvent–Solvent Interactions in Binary Solvent Mixtures. Part 1. A Comparison of Several Preferential Solvation Models for Describing Et(30) Polarity of Bipolar Hydrogen Bond Acceptor-Cosolvent Mixtures. *J. Chem. Soc., Perkin Trans. 2* **1995**, *1*, 1607-1615.
27. Jauquet, M.; Laszlo, P., Influence of Solvents on Spectroscopy. In *Solutions and Solubilities Part 1*, Dack, M. R. J., Ed. John Wiley & Sons: 1975; pp 195-298.
28. Coleman, M. M.; Skrovanek, D. J.; Hu, J.; Painter, P. C., Hydrogen Bonding in Polymer Blends. 1. FTIR Studies of Urethane-Ether Blends. *Macromolecules* **1988**, *21*, 59-65.
29. Skrovanek, D. J.; Howe, S. E.; Painter, P. C.; Coleman, M. M., Hydrogen Bonding in Polymers: Infrared Temperature Studies of an Amorphous Polyamide. *Macromolecules* **1985**, *18*, 1676-1683.
30. Beale, T. M.; Chudzinski, M. G.; Sarwar, M. G.; Taylor, M. S., Halogen Bonding in Solution: Thermodynamics and Applications. *Chem. Soc. Rev.* **2013**, *42*, 1667-1680.
31. Politzer, P.; Murray, J. S.; Clark, T., Halogen Bonding and Other Sigma-Hole Interactions: A Perspective. *Phys. Chem. Chem. Phys.* **2013**, *15*, 11178-11189.

32. Martí, J.; Lledós, A.; Bertrán, J.; Duran, M., Vibrational Stark Effect: Theoretical Determination through the Semiempirical Am1 Method. *J. Comput. Chem.* **1992**, *13*, 821-829.
33. Bishop, D. M., The Vibrational Stark Effect. *J. Chem. Phys.* **1993**, *98*, 3179-3184.
34. Schneider, S. H.; Boxer, S. G., Vibrational Stark Effects of Carbonyl Probes Applied to Reinterpret IR and Raman Data for Enzyme Inhibitors in Terms of Electric Fields at the Active Site. *J. Phys. Chem. B* **2016**, *120*, 9672-9684.
35. Irish, D. E., Part 2: Infrared and Raman Spectroscopy. In *Physical Chemistry of Organic Solvents*, Covington, A. K.; Dickinson, T., Eds. Plenum Publishing Company Ltd.: 1973; pp 433-459.
36. Hamm, P.; Zanni, M. T., *Concepts and Methods of 2D Infrared Spectroscopy.* Cambridge University Press: 2011.
37. King, J. T.; Baiz, C. R.; Kubarych, K. J., Solvent-Dependent Spectral Diffusion in a Hydrogen Bonded "Vibrational Aggregate". *J. Phys. Chem. A* **2010**, *114*, 10590-10604.
38. Fayer, M. D., Dynamics of Liquids, Molecules, and Proteins Measured with Ultrafast 2D IR Vibrational Echo Chemical Exchange Spectroscopy. *Annu. Rev. Phys. Chem.* **2009**, *60*, 21-38.
39. Medders, G. R.; Paesani, F., Water Dynamics in Metal-Organic Frameworks: Effects of Heterogeneous Confinement Predicted by Computational Spectroscopy. *J. Phys. Chem. Lett.* **2014**, *5*, 2897-2902.
40. Pieniazek, P. A.; Lin, Y. S.; Chowdhary, J.; Ladanyi, B. M.; Skinner, J. L., Vibrational Spectroscopy and Dynamics of Water Confined inside Reverse Micelles. *J. Phys. Chem. B* **2009**, *113*, 15017-15028.
41. Rothschild, W. G., Solvation by Benzene: Molecular Dynamics Simulation of Orientational Motion, Translational Diffusion, and Site–Site Radial Distributions of the Solutes Di- and Trichloromethane (Chloroform). *Mol. Phys.* **2007**, *105*, 1003-1011.
42. Asbury, J. B.; Steinel, T.; Fayer, M. D., Vibrational Echo Correlation Spectroscopy Probes of Hydrogen Bond Dynamics in Water and Methanol. *J. Lumin.* **2004**, *107*, 271-286.
43. Farrer, R. A.; Fourkas, J. T., Orientational Dynamics of Liquids Confined in Nanoporous Sol-Gel Glasses Studied by Optical Kerr Effect Spectroscopy. *Acc. Chem. Res.* **2003**, *36*, 605-612.
44. Jaye, A. A.; Hunt, N. T.; Meech, S. R., Temperature- and Solvation-Dependent Dynamics of Liquid Sulfur Dioxide Studied through the Ultrafast Optical Kerr Effect. *J. Chem. Phys.* **2006**, *124*, 024506.
45. Zhong, Q.; Fourkas, J. T., Optical Kerr Effect Spectroscopy of Simple Liquids. *J. Phys. Chem. B* **2008**, *112*, 15529-15539.
46. Klimov, V. I.; McBranch, D. W.; Leatherdale, C. A.; Bawendi, M. G., Electron and Hole Relaxation Pathways in Semiconductor Quantum Dots. *Phys. Rev. B* **1999**, *60*, 13740-13749.
47. Ramsteiner, I. B.; Hartschuh, A.; Port, H., Relaxation Pathways and Fs Dynamics in a Photoswitchable Intramolecular D→a Energy Transfer System. *Chem. Phys. Lett.* **2001**, *343*, 83-90.

48. Tokmakoff, A.; Fayer, M. D., Homogeneous Vibrational Dynamics and Inhomogeneous Broadening in Glass-Forming Liquids: Infrared Photon Echo Experiments from Room Temperature to 10 K. *J. Chem. Phys.* **1995**, *103*, 2810-2826.
49. Zimdars, D.; Tokmakoff, A.; Chen, S.; Greenfield, S. R.; Fayer, M. D.; Smith, T. I.; Schwettman, H. A., Picosecond Infrared Vibrational Photon Echoes in a Liquid and Glass Using a Free Electron Laser. *Phys. Rev. Lett.* **1993**, *70*, 2718-2721.
50. Massari, A. M.; Finkelstein, I. J.; McClain, B. L.; Goj, A.; Wen, X.; Bren, K. L.; Loring, R. F.; Fayer, M. D., The Influence of Aqueous Versus Glassy Solvents on Protein Dynamics: Vibrational Echo Experiments and Molecular Dynamics Simulations. *J. Am. Chem. Soc.* **2005**, *127*, 14279-14289.
51. Ismail, A. E.; Grest, G. S.; Heine, D. R.; Stevens, M. J.; Tsige, M., Interfacial Structure and Dynamics of Siloxane Systems: PDMS−Vapor and PDMS−Water. *Macromolecules* **2009**, *42*, 3186-3194.
52. Esteves, A. C. C.; Brokken-Zijp, J.; Laven, J.; Huinink, H. P.; Reuvers, N. J. W.; Van, M. P.; de With, G., Influence of Cross-Linker Concentration on the Cross-Linking of PDMS and the Network Structures Formed. *Polymer* **2009**, *50*, 3955-3966.
53. Owen, M. J., Properties and Applications of Silicones. In *In Progess in Silicones and Silicone-Modified Materials*, Clarson, S. J.; Fitzgerald, J. J.; Owen, M. J.; Smith, S. D., Eds. American Chemical Society: 2010; pp 13-18.
54. Yoo, J. S.; Kim, S. J.; Choi, J. S., Swelling Equilibria of Mixed Solvent/Poly(Dimethylsiloxane) Systems. *J. Chem. Eng. Data* **1999**, *44*, 16-22.
55. Kim, C.; Gurau, M. C.; Cremer, P. S.; Yu, H., Chain Conformation of Poly(Dimethyl Siloxane) at the Air/Water Interface by Sum Frequency Generation. *Langmuir* **2008**, *24*, 10155-10160.
56. Tosaka, M.; Noda, M.; Ito, K.; Senoo, K.; Aoyama, K.; Ohta, N., Strain- and Temperature-Induced Polymorphism of Poly(Dimethylsiloxane). *Colloid. Polym. Sci.* **2013**, *291*, 2719-2724.
57. Heimenz, P. C.; Lodge, T. P., *Polymer Chemistry*. CRC Press: 2007.
58. Liu, M.; Sun, J.; Chen, Q., Influences of Heating Temperature on Mechanical Properties of Polydimethylsiloxane. *Sens. Actuators, A* **2009**, *151*, 42-45.
59. Kim, T. K.; Kim, J. K.; Jeong, O. C., Measurement of Nonlinear Mechanical Properties of PDMS Elastomer. *Microelectron. Eng.* **2011**, *88*, 1982-1985.
60. Bistričić, L.; Borjanović, V.; Mikac, L.; Dananić, V., Vibrational Spectroscopic Study of Poly(Dimethylsiloxane)-ZnO Nanocomposites. *Vib. Spectrosc.* **2013**, *68*, 1-10.
61. Wu, Y.; Huang, Y.; Ma, H., A Facile Method for Permanent and Functional Surface Modification of Poly(Dimethylsiloxane). *J. Am. Chem. Soc.* **2007**, *129*, 7226-7227.
62. Palchesko, R. N.; Zhang, L.; Sun, Y.; Feinberg, A. W., Development of Polydimethylsiloxane Substrates with Tunable Elastic Modulus to Study Cell Mechanobiology in Muscle and Nerve. *PLoS One* **2012**, *7*, e51499.
63. Lewicki, J. P.; Harley, S. J.; Finnie, J. A.; Ashmore, M.; Bell, C.; Maxwell, R. S., NMR Investigations of Network Formation and Motional Dynamics in Well-Defined Model Poly(Dimethylsiloxane) Elastomers. In *Progress in Silicones and Silicone-Modified Materials*, Clarson, S. J.; Owen, M. J.; Smith, S. D.; Van Dyke, M.; Brook, M.; Mabry, J., Eds. American Chemical Society: 2013; Vol. Vol. 1154, pp 133-154.

64. Mark, J. E.; Sullivan, J. L., Model Networks of End-Linked Polydimethylsiloxane Chains. I. Comparisons between Experimental and Theoretical Values of the Elastic Modulus and the Equilibrium Degree of Swelling. *J. Chem. Phys.* **1977**, *66*, 1006-1011.
65. Seo, J. H.; Matsuno, R.; Konno, T.; Takai, M.; Ishihara, K., Surface Tethering of Phosphorylcholine Groups onto Poly(Dimethylsiloxane) through Swelling-Deswelling Methods with Phospholipids Moiety Containing ABA-Type Block Copolymers. *Biomaterials* **2008**, *29*, 1367-1376.
66. *Sylgard® 184 Silicone Elastomer Kit (Base)*; 802554-00011; Dow Corning; Midland, Michigan, Sept. 13, 2017
67. *Sylgard® 184 Silicone Elastomer Kit (Curing Agent)*; 743649-00010; Dow Corning; Midland, Michigan, March 3, 2017
68. *Sylgard® 184 Silicone Elastomer*; 11-3184B-01; Dow Corning; Midland, Michigan, April 2, 2014
69. *Dow Corning® 3-6559 Cure Accelerator*; 802554-00011; Dow Corning; Midland, Michigan, Sept. 6, 2017
70. Clarson, S. J.; Semlyen, J. A., *Siloxane Polymers.* Prentice Hall: 1993.
71. Lewis, L. N.; Stein, J.; Gao, Y.; Colborn, R. E.; Hutchins, G., Platinum Catalysts Used in the Silicone Industry: Their Synthesis and Activity in Hydrosilylation. *Platinum Met. Rev.* **1997**, *41*, 66-75.
72. Simpson, T. R. E.; Parbhoo, B.; Keddie, J. L., The Dependence of the Rate of Crosslinking in Poly(Dimethyl Siloxane) on the Thickness of Coatings. *Polymer* **2003**, *44*, 4829-4838.
73. Giorgi, G.; De Angelis, F.; Re, N.; Sgamellotti, A., A Theoretical Investigation of the Chalk–Harrod and Modified Chalk–Harrod Mechanisms Involved in Hybrid Integrated Circuit Building. *Future Generation Computer Systems* **2004**, *20*, 781-791.
74. Chalk, A. J.; Harrod, J. F., Homogeneous Catalysis. II. The Mechanism of the Hydrosilation of Olefins Catalyzed by Group VIII Metal Complexes. *J. Am. Chem. Soc.* **1965**, *87*, 16-21.
75. Schroeder, M. A.; Wrighton, M. S., Pentacarbonyliron (0) Photocatalyzed Reactions of Trialkylsilanes with Alkenes. *Journal of Organometallic Chemistry* **1977**, *128*, 345-358.
76. Reichel, C. L.; Wrighton, M. S., Photochemistry of Cobalt Carbonyl Complexes Having a Cobalt-Silicon Bond and Its Importance in Activation of Catalysis. *Inorganic Chemistry* **1980**, *19*, 3858-3860.
77. Randolph, C. L.; Wrighton, M. S., Photochemical Reactions of (H^5-Pentamethylcyclopentadienyl)Dicarbonyliron Alkyl and Silyl Complexes: Reversible Ethylene Insertion into an Iron-Silicon Bond and Implications for the Mechanism of Transition-Metal-Catalyzed Hydrosilation of Alkenes. *J. Am. Chem. Soc.* **1986**, *108*, 3366-3374.
78. Karlsson, A.; Singh, S. K.; Albertsson, A.-C., Controlled Destruction of Residual Crosslinker in a Silicone Elastomer for Drug Delivery. *J. Appl. Polym. Sci.* **2002**, *84*, 2254-2264.
79. Mark, J. E.; Erman, B., *Rubberlike Elasticity: A Molecular Primer.* Second ed.; Cambridge University Press: 2007.

80. Seethapathy, S.; Górecki, T., Applications of Polydimethylsiloxane in Analytical Chemistry: A Review. *Anal. Chim. Acta* **2012**, *750*, 48-62.
81. Dangla, R.; Gallaire, F.; Baroud, C. N., Microchannel Deformations Due to Solvent-Induced PDMS Swelling. *Lab Chip* **2010**, *10*, 2972-2978.
82. Billmeyer, F. W., *Textbook of Polymer Science.* John Wiley & Sons: 1984.
83. Flory, P. J., *Principles of Polymer Chemistry*. Cornell University Press: 1953.
84. Rubinstein, M.; Colby, R. H., *Polymer Physics.* Oxford University Press: 2003.
85. James, H. M.; Guth, E., Theory of the Elastic Properties of Rubber. *J. Chem. Phys.* **1943**, *11*, 455-481.
86. Wall, F. T., Statistical Thermodynamics of Rubber. III. *J. Chem. Phys.* **1943**, *11*, 527-530.
87. Flory, P. J.; Rehner, J., John, Statistical Mechanics of Cross-Linked Polymer Networks II. Swelling. *J. Chem. Phys.* **1943**, *11*, 521-526.
88. Flory, P. J., Statistical Mechanics of Swelling of Network Structures. *J. Chem. Phys.* **1950**, *18*, 108-111.
89. Patel, S. K.; Malone, S.; Cohen, C.; Gillmor, J. R.; Colby, R. H., Elastic Modulus and Equilibrium Swelling of Poly(Dimethylsiloxane) Networks. *Macromolecules* **1992**, *25*, 5241-5251.
90. Wang, P.; Wunder, S. L., The Effects of Solution Concentration on Network Properties of Thin Films of Polyorganosiloxanes Crosslinked in the Solid State. *Polymer* **1997**, *38*, 3417-3421.
91. Nandi, S.; Winter, H. H., Swelling Behavior of Partially Cross-Linked Polymers: a Ternary System. *Macromolecules* **2005**, *38*, 4447-4455.
92. Kloczkowski, A.; Mark, J. E.; Erman, B., A Diffused-Constraint Theory for the Elasticity of Amorphous Polymer Networks. 1. Fundamentals and Stress-Strain Isotherms in Elongation. *Macromolecules* **1995**, *28*, 5089-5096.
93. Eichinger, B. E., The Theory of High Elasticity. *Annu. Rev. Phys. Chem.* **1983**, *34*, 359-387.
94. Akagi, Y.; Gong, J. P.; Chung, U.-i.; Sakai, T., Transition between Phantom and Affine Network Model Observed in Polymer Gels with Controlled Network Structure. *Macromolecules* **2013**, *46*, 1035-1040.
95. Mark, J. E., Rubber Elasticity. *J. Chem. Educ.* **1981**, *58*, 898-903.
96. Villar, M. A.; Vallés, E. M., Influence of Pendant Chains on Mechanical Properties of Model Poly(Dimethylsiloxane) Networks. 2. Viscoelastic Properties. *Macromolecules* **1996**, *29*, 4081-4089.
97. Heine, D. R.; Grest, G. S.; Lorenz, C. D.; Tsige, M.; Stevens, M. J., Atomistic Simulations of End-Linked Poly(Dimethylsiloxane) Networks: structure and Relaxation. *Macromolecules* **2004**, *37*, 3857-3864.
98. James, H. M.; Guth, E., Theory of the Increase in Rigidity of Rubber During Cure. *J. Chem. Phys.* **1947**, *15*, 669-683.
99. Kloczkowski, A.; Mark, J. E.; Erman, B., Chain Dimensions and Fluctuations in Random Elastomeric Networks. 1. Phantom Gaussian Networks in the Undeformed State. *Macromolecules* **1989**, *22*, 1423-1432.

100. Beltzung, M.; Herz, J.; Picot, C., Investigation by Small-Angle Neutron Scattering of the Chain Conformation in Equilibrium-Swollen Poly(Dimethylsiloxane) Networks. *Macromolecules* **1983**, *16*, 580-584.
101. Flory, P. J., Theory of Elasticity of Polymer Networks. The Effect of Local Constraints on Junctions. *J. Chem. Phys.* **1977**, *66*, 5720-5729.
102. Flory, P. J.; Erman, B., Theory of Elasticity of Polymer Networks. 3. *Macromolecules* **1982**, *15*, 800-806.
103. Mark, J. E., The Use of Model Polymer Networks to Elucidate Molecular Aspects of Rubberlike Elasticity. *Adv. Polym. Sci.* **1982**, *44*, 1-26.
104. Dossin, L. M.; Graessley, W. W., Rubber Elasticity of Well-Characterized Polybutadiene Networks. *Macromolecules* **1979**, *12*, 123-130.
105. Langley, N. R., Elastically Effective Strand Density in Polymer Networks. *Macromolecules* **1968**, *1*, 348-352.
106. Edwards, S. F.; Vilgis, T. A., The Tube Model Theory of Rubber Elasticity. *Rep. Prog. Phys.* **1988**, *51*, 243-297.
107. Edwards, S. F.; Vilgis, T., The Effect of Entanglements in Rubber Elasticity. *Polymer* **1986**, *27*, 483-492.
108. de Gennes, P.-G., *Scaling Concepts in Polymer Physics*. Cornell University Press: 1979.
109. Brotzman, R. W.; Flory, P. J., Elastic Behavior of Cis-1,4-Polybutadiene. *Macromolecules* **1987**, *20*, 351-356.
110. Macosko, C. W.; Benjamin, G. S., Modulus of Three and Four Functional Poly(Dimethylsiloxane) Networks. *Pure Appl. Chem.* **1981**, *53*, 1505-1518.
111. Gnanou, Y.; Hild, G.; Rempp, P., Molecular Structure and Elastic Behavior of Poly(Ethylene Oxide) Networks Swollen to Equilibrium. *Macromolecules* **1987**, *20*, 1662-1671.
112. Meyers, K. O.; Bye, M. L.; Merrill, E. W., Model Silicone Elastomer Networks of High Junction Functionality: Synthesis, Tensile Behavior, Swelling Behavior, and Comparison with Molecular Theories of Rubber Elasticity. *Macromolecules* **1980**, *13*, 1045-1053.
113. Stein, A. D.; Hoffman, D. A.; Frank, C. W.; Fayer, M. D., Reorientational Motion of a Cross-Link Junction in a Poly(Dimethylsiloxane) Network Measured by Time-Resolved Fluorescence Depolarization. *J. Chem. Phys.* **1992**, *96*, 3269-3278.
114. Menge, H.; Hotopf, S.; Pönitzsch, S.; Richter, S.; Arndt, K.-F.; Schneider, H.; Heuert, U., Investigation on the Swelling Behaviour in Poly(Dimethylsiloxane) Rubber Networks Using NMR and Compression Measurements. *Polymer* **1999**, *40*, 5303-5313.
115. Henry, A. W.; Safford, G. J., Study of Low-Frequency Molecular Motions in Polydimethylsiloxane Polymers by Neutron Inelastic Scattering. *J. Polym. Sci., Part A-2: Polym. Phys.* **1969**, *7*, 433-462.
116. Fujara, F.; Petry, W., Fast Local Motion around T_g in a Molecular Glass as Observed by Incoherent Neutron Scattering. *Europhys. Lett.* **1987**, *4*, 921-927.
117. Stein, A. D.; Hoffmann, D. A.; Marcus, A. H.; Leezenberg, P. B.; Frank, C. W.; Fayer, M. D., Dynamics in Poly(Dimethylsiloxane) Melts: Fluorescence Depolarization Measurements of Probe Chromophore Orientational Relaxation. *J. Phys. Chem.* **1992**, *96*, 5255-5263.

118. Royer, J. R.; DeSimone, J. M.; Khan, S. A., Carbon Dioxide-Induced Swelling of Poly(Dimethylsiloxane). *Macromolecules* **1999**, *32*, 8965-8973.
119. Rodriguez, F.; Cohen, C.; Ober, C., K.; Archer, L. A., *Principles of Polymer Systems.* 6th ed.; CRC Press: 2015.
120. Lavine, B. K.; Kaval, N.; Westover, D. J.; Oxenford, L., New Approaches to Chemical Sensing-Sensors Based on Polymer Swelling. *Anal. Lett.* **2006**, *39*, 1773-1783.
121. Lavine, B. K.; Oxenford, L.; Kim, M.; Kaval, N.; Benjamin, M.; Seitz, W. R., Novel Turbidimetric Method to Study Polymer Swelling. *Microchem. J.* **2012**, *103*, 97-104.
122. Singh, A.; Mukherjee, M., Swelling Dynamics of Ultrathin Polymer Films. *Macromolecules* **2003**, *36*, 8728-8731.
123. Kroll, D. M.; Croll, S. G., Heterogeneity in Crosslinked Polymer Networks: Molecular Dynamics Simulations. In *Protective Coatings: Film Formation and Properties*, 1 ed.; Wen, M.; Dušek, K., Eds. Springer International Publishing: 2017; pp 39-65.
124. Lee, J. N.; Park, C.; Whitesides, G. M., Solvent Compatibility of Poly(Dimethylsiloxane)-Based Microfluidic Devices. *Anal. Chem.* **2003**, *75*, 6544-6554.
125. Bueche, A. M., Interaction of Polydimethylsiloxanes with Swelling Agents. *J. Polym. Sci.* **1955**, *15*, 97-103.
126. Errede, L. A., Polymer Swelling. 7. A Molecular Interpretation of Polymer Swelling. *J. Phys. Chem.* **1989**, *93*, 2668-2671.
127. McCrum, N. G.; Read, B. E.; Williams, G., *Anelastic and Dielectric Effects in Polymeric Solids.* Wily-Interscience: 1967.
128. Müller-Plathe, F., Local Structure and Dynamics in Solvent-Swollen Polymers. *Macromolecules* **1996**, *29*, 4782-4791.
129. Müller-Plathe, F., Microscopic Dynamics in Water-Swollen Poly(Vinyl Alcohol). *J. Chem. Phys.* **1998**, *108*, 8252-8263.
130. Sonnenburg, J.; Gao, J.; Weiner, J. H., Molecular Dynamics Simulations of Gas Diffusion through Polymer Networks. *Macromolecules* **1990**, *23*, 4653-4657.
131. Charati, S. G.; Stern, S. A., Diffusion of Gases in Silicone Polymers: Molecular Dynamics Simulations. *Macromolecules* **1998**, *31*, 5529-5535.
132. Takeuchi, H.; Okazaki, K., Molecular Dynamics Simulation of Diffusion of Simple Gas Molecules in a Short Chain Polymer. *J. Chem. Phys.* **1990**, *92*, 5643-5652.
133. Wind, J. D.; Sirard, S. M.; Paul, D. R.; Green, P. F.; Johnston, K. P.; Koros, W. J., Relaxation Dynamics of CO 2diffusion, Sorption, and Polymer Swelling for Plasticized Polyimide Membranes. *Macromolecules* **2003**, *36*, 6442-6448.
134. Freeman, B. D., Basis of Permeability/Selectivity Tradeoff Relations in Polymeric Gas Separation Membranes. *Macromolecules* **1999**, *32*, 375-380.
135. Kanaya, T.; Tsukushi, I.; Kaji, K.; Sakaguchi, T.; Kwak, G.; Masuda, T., Role of Local Dynamics in the Gas Permeability of Glassy Substituted Polyacetylenes. A Quasielastic Neutron Scattering Study. *Macromolecules* **2002**, *35*, 5559-5564.
136. Fayer, M. D., *Elements of Quantum Mechanics.* Oxford University Press: 2001.
137. Mukamel, S., *Principles of Nonlinear Optical Spectroscopy.* Oxford University Press: 1995.
138. Rector, K. D.; Fayer, M. D.; Hamm, P.; Hochstrasser, R. M., *Ultrafast Infrared and Raman Spectroscopy.* Marcel Dekker, Inc.: 2001.

139. Fenn, E. E.; Fayer, M. D., Extracting 2D IR Frequency-Frequency Correlation Functions from Two Component Systems. *J. Chem. Phys.* **2011**, *135*, 074502.
140. Kiefer, L. M.; Kubarych, K. J., Solvent-Dependent Dynamics of a Series of Rhenium Photoactivated Catalysts Measured with Ultrafast 2DIR. *J. Phys. Chem. A* **2015**, *119*, 959-965.
141. Jones, B. H.; Massari, A. M., Origins of Spectral Broadening in Iodated Vaska's Complex in Binary Solvent Mixtures. *J. Phys. Chem. B* **2013**, *117*, 15741-15749.
142. Ren, Z.; Ivanova, A. S.; Couchot-Vore, D.; Garrett-Roe, S., Ultrafast Structure and Dynamics in Ionic Liquids: 2D-IR Spectroscopy Probes the Molecular Origin of Viscosity. *J. Phys. Chem. Lett.* **2014**, *5*, 1541-1546.
143. Shelby, R. M.; Harris, C. B.; Cornelius, P. A., The Origin of Vibrational Dephasing of Polyatomic Molecules in Condensed Phases. *J. Chem. Phys.* **1979**, *70*, 34-41.
144. Gershgoren, E.; Wang, Z.; Ruhman, S.; Vala, J.; Kosloff, R., Investigating Pure Vibrational Dephasing of I_3^- in Solution: Temperature Dependence of T_2* for the Fundamental and First Harmonic of ν_1. *J. Chem. Phys.* **2003**, *118*, 3660-3667.
145. Vöhringer, P.; Westervelt, R. A.; Yang, T. S.; Arnett, D. C.; Feldstein, M. J.; Scherer, N. F., Solvent and Frequency Dependence of Vibrational Dephasing on Femtosecond Time-Scales. *J. Raman Spectrosc.* **1995**, *26*, 535-551.
146. Berg, M.; Vanden Bout, D. A., Ultrafast Raman Echo Measurements of Vibrational Dephasing and the Nature of Solvent−Solute Interactions. *Acc. Chem. Res.* **1997**, *30*, 65-71.
147. Orr-Ewing, A. J., Perspective: Bimolecular Chemical Reaction Dynamics in Liquids. *J. Chem. Phys.* **2014**, *140*, 090901.
148. Wang, S. P.; Schwartz, M., Reorientational Diffusion of Tungsten Hexacarbonyl in Solution. *J. Mol. Liq.* **1990**, *47*, 121-128.
149. Shirota, H.; Fujisawa, T.; Fukazawa, H.; Nishikawa, K., Ultrafast Dynamics in Aprotic Molecular Liquids: A Femtosecond Raman-Induced Kerr Effect Spectroscopic Study. *Bull. Chem. Soc. Jpn.* **2009**, *82*, 1347-1366.
150. Sturlaugson, A. L.; Fruchey, K. S.; Lynch, S. R.; Aragón, S. R.; Fayer, M. D., Orientational and Translational Dynamics of Polyether/Water Solutions. *J. Phys. Chem. B* **2010**, *114*, 5350-5358.
151. Spector, I. C.; Olson, C. M.; Huber, C. J.; Massari, A. M., Simple Fully Reflective Method of Scatter Reduction in 2D-IR Spectroscopy. *Opt. Letters* **2015**, *40*, 1850-1852.
152. Eckbreth, A. C., BOXCARS: Crossed-Beam Phase-Matched CARS Generation in Gases. *Appl. Phys. Lett.* **1978**, *32*, 421-423.
153. Khalil, M.; Demirdöven, N.; Tokmakoff, A., Coherent 2D IR Spectroscopy: Molecular Structure and Dynamics in Solution. *J. Phys. Chem. A* **2003**, *107*, 5258-5279.
154. Rock, W.; Li, Y. L.; Pagano, P.; Cheatum, C. M., 2D IR Spectroscopy Using Four-Wave Mixing, Pulse Shaping, and IR Upconversion: A Quantitative Comparison. *J. Phys. Chem. A* **2013**, *117*, 6073-6083.
155. Asbury, J. B.; Steinel, T.; Kwak, K.; Corcelli, S. A.; Lawrence, C. P.; Skinner, J. L.; Fayer, M. D., Dynamics of Water Probed with Vibrational Echo Correlation Spectroscopy. *J. Chem. Phys.* **2004**, *121*, 12431-12446.
156. Park, S.; Kwak, K.; Fayer, M. D., Ultrafast 2D-IR Vibrational Echo Spectroscopy: A Probe of Molecular Dynamics. *Laser Phys. Lett.* **2007**, *4*, 704-718.

157. Jonas, D. M., Two-Dimensional Femtosecond Spectroscopy. *Annu. Rev. Phys. Chem.* **2003**, *54*, 425-463.
158. Gallagher Faeder, S. M.; Jonas, D. M., Two-Dimensional Electronic Correlation and Relaxation Spectra: Theory and Model Calculations. *J. Phys. Chem. A* **1999**, *103*, 10489-10505.
159. Baiz, C. R.; McRobbie, P. L.; Anna, J. M.; Geva, E.; Kubarych, K. J., Two-Dimensional Infrared Spectroscopy of Metal Carbonyls. *Acc. Chem. Res.* **2009**, *42*, 1395-1404.
160. Hamm, P.; Lim, M. H.; Hochstrasser, R. M., Structure of the Amide I Band of Peptides Measured by Femtosecond Nonlinear-Infrared Spectroscopy. *J. Phys. Chem. B* **1998**, *102*, 6123-6138.
161. Kolano, C.; Helbing, J.; Kozinski, M.; Sander, W.; Hamm, P., Watching Hydrogen-Bond Dynamics in a Beta-Turn by Transient Two-Dimensional Infrared Spectroscopy. *Nature* **2006**, *444*, 469-472.
162. Kim, Y. S.; Hochstrasser, R. M., Chemical Exchange 2D IR of Hydrogen-Bond Making and Breaking. *Proc. Natl. Acad. Sci. U. S. A.* **2005**, *102*, 11185-11190.
163. Kwak, K.; Park, S.; Finkelstein, I. J.; Fayer, M. D., Frequency-Frequency Correlation Functions and Apodization in Two-Dimensional Infrared Vibrational Echo Spectroscopy: A New Approach. *J. Chem. Phys.* **2007**, *127*, 124503.
164. Kwak, K.; Rosenfeld, D. E.; Fayer, M. D., Taking Apart the Two-Dimensional Infrared Vibrational Echo Spectra: More Information and Elimination of Distortions. *J. Chem. Phys.* **2008**, *128*, 204505.
165. Shin, J. Y.; Yamada, S. A.; Fayer, M. D., Carbon Dioxide in a Supported Ionic Liquid Membrane: Structural and Rotational Dynamics Measured with 2D IR and Pump-Probe Experiments. *J. Am. Chem. Soc.* **2017**, *139*, 11222-11232.
166. Whiting, E. E., An Empirical Approximation to the Voigt Profile. *Journal of Quantitative Spectroscopy and Radiative Transfer* **1968**, *8*, 1379-1384.
167. Kwac, K.; Cho, M., Two-Color Pump−Probe Spectroscopies of Two- and Three-Level Systems: 2-Dimensional Line Shapes and Solvation Dynamics. *J. Phys. Chem. A* **2003**, *107*, 5903-5912.
168. Huber, C. J.; Massari, A. M., Characterizing Solvent Dynamics in Nanoscopic Silica Sol-Gel Glass Pores by 2D-IR Spectroscopy of an Intrinsic Vibrational Probe. *J. Phys. Chem. C* **2014**, *118*, 25567-25578.
169. Heilweil, E. J.; Cavanagh, R. R.; Stephenson, J. C., Population Relaxation of CO(V = 1) Vibrations in Solution Phase Metal Carbonyl Complexes. *Chem. Phys. Lett.* **1987**, *134*, 181-188.
170. Barbara, P. F.; Meyer, T. J.; Ratner, M. A., Contemporary Issues in Electron Transfer Research. *J. Phys. Chem.* **1996**, *100*, 13148-13168.
171. Tan, H. S.; Piletic, I. R.; Fayer, M. D., Polarization Selective Spectroscopy Experiments: Methodology and Pitfalls. *J. Opt. Soc. Am. B* **2005**, *22*, 2009-2017.
172. Castner, E. W.; Maroncelli, M., Solvent Dynamics Derived from Optical Kerr Effect, Dielectric Dispersion, and Time-Resolved Stokes Shift Measurements: An Empirical Comparison. *J. Mol. Liq.* **1998**, *77*, 1-36.
173. Joo, T. H.; Jia, Y. W.; Yu, J. Y.; Lang, M. J.; Fleming, G. R., Third-Order Nonlinear Time Domain Probes of Solvation Dynamics. *J. Chem. Phys.* **1996**, *104*, 6089-6108.

174. Kwon, O. H.; Yoo, T. H.; Othona, C. M.; Van Deventer, J. A.; Tirrell, D. A.; Zewail, A. H., Hydration Dynamics at Fluorinated Protein Surfaces. *Proc. Nat. Acad. Soc. USA* **2010**, *107*, 17101-17106.
175. Stratt, R. M.; Maroncelli, M., Nonreactive Dynamics in Solution: The Emerging Molecular View of Solvation Dynamics and Vibrational Relaxation. *J. Phys. Chem.* **1996**, *100*, 12981-12996.
176. Marcus, R. A., Electron-Transfer Reactions in Chemistry - Theory and Experiment. *Rev. Mod. Phys.* **1993**, *65*, 599-610.
177. Gao, J. L., Hybrid Quantum and Molecular Mechanical Simulations: An Alternative Avenue to Solvent Effects in Organic Chemistry. *Acc. Chem. Res.* **1996**, *29*, 298-305.
178. Brunori, M.; Cutruzzola, F.; Savino, C.; Travaglini-Allocatelli, C.; Vallone, B.; Gibson, Q. H., Does Picosecond Protein Dynamics Have Survival Value? *Trends Biochem. Sci.* **1999**, *24*, 253-255.
179. Jackson, T. A.; Lim, M.; Anfinrud, P. A., Complex Nonexponential Relaxation in Myoglobin after Photodissociation of MbCO: Measurement and Analyss from 2 ps to 56 vs. *Chem. Phys.* **1994**, *180*, 131-140.
180. Merchant, K. A.; Noid, W. G.; Akiyama, R.; Finkelstein, I. J.; Goun, A.; McClain, B. L.; Loring, R. F.; Fayer, M. D., Myoglobin-CO Substate Structures and Dynamics: Multidimensional Vibrational Echoes and Molecular Dynamics Simulations. *J. Am. Chem. Soc.* **2003**, *125*, 13804-13818.
181. Ostermann, A.; Waschipky, R.; Parak, F. G.; Nienhaus, G. U., Ligand Binding and Conformational Motions in Myoglobin. *Nature* **2000**, *404*, 205-208.
182. Pu, J. Z.; Gao, J. L.; Truhlar, D. G., Multidimensional Tunneling, Recrossing, and the Transmission Coefficient for Enzymatic Reactions. *Chem. Rev.* **2006**, *106*, 3140-3169.
183. Karplus, M., Aspects of Protein Reaction Dynamics: Deviations from Simple Behavior. *J. Phys. Chem. B* **2000**, *104*, 11-27.
184. Farina, V.; Krishnan, B.; Marshall, D. R.; Roth, G. P., Palladium-Catalyzed Coupling of Arylstannanes with Organic Sulfonates - a Comprehensive Study. *J. Org. Chem.* **1993**, *58*, 5434-5444.
185. Fitzpatrick, P. A.; Klibanov, A. M., How Can the Solvent Affect Enzyme Enantioselectivity. *J. Am. Chem. Soc.* **1991**, *113*, 3166-3171.
186. Riva, R.; Schmeits, S.; Jerome, C.; Jerome, R.; Lecomte, P., Combination of Ring-Opening Polymerization and "Click Chemistry": Toward Functionalization and Grafting of Poly(Epsilon-Caprolactone). *Macromolecules* **2007**, *40*, 796-803.
187. Schutt, T. C.; Bharadwaj, V. S.; Hegde, G. A.; Johns, A. J.; Maupin, C. M., In Silico Insights into the Solvation Characteristics of the Ionic Liquid 1-Methyltriethoxy-3-Ethylimidazolium Acetate for Cellulosic Biomass. *Phys. Chem. Chem. Phys.* **2016**, *18*, 23715-23726.
188. Jones, B. H.; Huber, C. J.; Spector, I. C.; Tabet, A. M.; Butler, R. L.; Hang, Y.; Massari, A. M., Correlating Solvent Dynamics and Chemical Reaction Rates Using Binary Solvent Mixtures and Two-Dimensional Infrared Spectroscopy. *J. Chem. Phys.* **2015**, *142*, 212441.

189. Shirota, H.; Fujisawa, T.; Fukazawa, H.; Nishikawa, K., Ultrafast Dynamics in Aprotic Molecular Liquids: A Femtosecond Raman-Induced Kerr Effect Spectroscopic Study. *Bull. Chem. Soc. Jpn.* **2009**, *82*, 1347-1366.
190. Cho, M. H.; Rosenthal, S. J.; Scherer, N. F.; Ziegler, L. D.; Fleming, G. R., Ultrafast Solvent Dynamics - Connection between Time Resolved Fluorescence and Optical Kerr Measurements. *J. Chem. Phys.* **1992**, *96*, 5033-5038.
191. Cichos, F.; Willert, A.; Rempel, U.; Von Borczyskowski, C., Solvation Dynamics in Mixtures of Polar and Nonpolar Solvents. *J. Phys. Chem. A* **1997**, *101*, 8179-8185.
192. Luther, B.; Kimmel, J.; Levinger, N., Dynamics of Polar Solvation in Acetonitrile–Benzene Binary Mixtures: Role of Dipolar and Quadrupolar Contributions to Solvation. *J. Chem. Phys.* **2002**, *116*, 3370-3377.
193. Maroncelli, M., The Dynamics of Solvation in Polar Liquids. *J. Mol. Liq.* **1993**, *57*, 1-37.
194. Underwood, D. F.; Blank, D. A., Ultrafast Solvation Dynamics: A View from the Solvent's Perspective Using a Novel Resonant-Pump, Nonresonant-Probe Technique. *J. Phys. Chem. A* **2003**, *107*, 956-961.
195. Finkelstein, I. J.; Goj, A.; McClain, B. L.; Massari, A. M.; Merchant, K. A.; Loring, R. F.; Fayer, M. D., Ultrafast Dynamics of Myoglobin without the Distal Histidine: Stimulated Vibrational Echo Experiments and Molecular Dynamics Simulations. *J. Phys. Chem. B* **2005**, *109*, 16959-16966.
196. Merchant, K. A.; Noid, W. G.; Akiyama, R.; Finkelstein, I. J.; Goun, A.; McClain, B. L.; Loring, R. F.; Fayer, M. D., Myoglobin-CO Substate Structures and Dynamics: Multidimensional Vibrational Echoes and Molecular Dynamics Simulations. *J. Am. Chem. Soc.* **2003**, *125*, 13804-13818.
197. Rothschild, W. G., Solvation by Benzene: Molecular Dynamics Simulation of Orientational Motion, Translational Diffusion, and Site-Site Radial Distributions of the Solutes Di- and Trichloromethane (Chloroform). *Mol. Phys.* **2007**, *105*, 1003-1011.
198. Asbury, J. B.; Steinel, T.; Stromberg, C.; Corcelli, S. A.; Lawrence, C. P.; Skinner, J. L.; Fayer, M. D., Water Dynamics: Vibrational Echo Correlation Spectroscopy and Comparison to Molecular Dynamics Simulations. *J. Phys. Chem. A* **2004**, *108*, 1107-1119.
199. Bakulin, A. A.; Liang, C.; Jansen, T. L.; Wiersma, D. A.; Bakker, H. J.; Pshenichnikov, M. S., Hydrophobic Solvation: A 2D IR Spectroscopic Inquest. *Acc. Chem. Res.* **2009**, *42*, 1229-1238.
200. Eaves, J. D.; Loparo, J. J.; Fecko, C. J.; Roberts, S. T.; Tokmakoff, A.; Geissler, P. L., Hydrogen Bonds in Liquid Water Are Broken Only Fleetingly. *Proc. Nat. Acad. Soc. USA* **2005**, *102*, 13019-13022.
201. Ganim, Z.; Chung, H. S.; Smith, A. W.; Deflores, L. P.; Jones, K. C.; Tokmakoff, A., Amide I Two-Dimensional Infrared Spectroscopy of Proteins. *Acc. Chem. Res.* **2008**, *41*, 432-441.
202. Ji, M. B.; Odelius, M.; Gaffney, K. J., Large Angular Jump Mechanism Observed for Hydrogen Bond Exchange in Aqueous Perchlorate Solution. *Science* **2010**, *328*, 1003-1005.
203. Woutersen, S.; Mu, Y.; Stock, G.; Hamm, P., Hydrogen-Bond Lifetime Measured by Time-Resolved 2D-IR Spectroscopy: N-Methylacetamide in Methanol. *Chem. Phys.* **2001**, *266*, 137-147.

204. Jones, B. H.; Huber, C. J.; Massari, A. M., Solvation Dynamics of Vaska's Complex by 2D-IR Spectroscopy. *J. Phys. Chem. C* **2011**, *115*, 24813-24822.
205. Khalil, M.; Demirdoven, N.; Tokmakoff, A., Obtaining Absorptive Line Shapes in Two-Dimensional Infrared Vibrational Correlation Spectra. *Phys. Rev. Lett.* **2003**, *90*, 047401.
206. Faeder, S. M. G.; Jonas, D. M., Two-Dimensional Electronic Correlation and Relaxation Spectra: Theory and Model Calculations. *J. Phys. Chem. A* **1999**, *103*, 10489-10505.
207. Frisch, M. J.; Trucks, G. W.; Schlegel, H. B.; Scuseria, G. E.; Robb, M. A.; Cheeseman, J. R.; Scalmani, G.; Barone, V.; Mennucci, B.; Petersson, G. A.; Nakatsuji, H.; Caricato, M.; Li, X.; Hratchian, H. P.; Izmaylov, A. F.; Bloino, J.; Zheng, G.; Sonnenberg, J. L.; Hada, M.; Ehara, M.; Toyota, K.; Fukuda, R.; Hasegawa, J.; Ishida, M.; Nakajima, T.; Honda, Y.; Kitao, O.; Nakai, H.; Vreven, T.; Montgomery Jr., J. A.; Peralta, J. E.; Ogliaro, F.; Bearpark, M. J.; Heyd, J.; Brothers, E. N.; Kudin, K. N.; Staroverov, V. N.; Kobayashi, R.; Normand, J.; Raghavachari, K.; Rendell, A. P.; Burant, J. C.; Iyengar, S. S.; Tomasi, J.; Cossi, M.; Rega, N.; Millam, N. J.; Klene, M.; Knox, J. E.; Cross, J. B.; Bakken, V.; Adamo, C.; Jaramillo, J.; Gomperts, R.; Stratmann, R. E.; Yazyev, O.; Austin, A. J.; Cammi, R.; Pomelli, C.; Ochterski, J. W.; Martin, R. L.; Morokuma, K.; Zakrzewski, V. G.; Voth, G. A.; Salvador, P.; Dannenberg, J. J.; Dapprich, S.; Daniels, A. D.; Farkas, Ö.; Foresman, J. B.; Ortiz, J. V.; Cioslowski, J.; Fox, D. J. *Gaussian 09 Revision D.01*, Gaussian, Inc.: 2009.
208. Breneman, C. M.; Wiberg, K. B., Determining Atom-Centered Monopoles from Molecular Electrostatic Potentials - the Need for High Sampling Density in Formamide Conformational-Analysis. *J. Comput. Chem.* **1990**, *11*, 361-373.
209. Glendening, E. D.; Landis, C. R.; Weinhold, F., Natural Bond Orbital Methods. *Wiley Interdisciplinary Reviews-Computational Molecular Science* **2012**, *2*, 1-42.
210. Reed, A. E.; Curtiss, L. A.; Weinhold, F., Intermolecular Interactions from a Natural Bond Orbital, Donor-Acceptor Viewpoint. *Chem. Rev.* **1988**, *88*, 899-926.
211. Brooks, B. R.; Brooks, C. L.; Mackerell, A. D.; Nilsson, L.; Petrella, R. J.; Roux, B.; Won, Y.; Archontis, G.; Bartels, C.; Boresch, S.; Caflisch, A.; Caves, L.; Cui, Q.; Dinner, A. R.; Feig, M.; Fischer, S.; Gao, J.; Hodoscek, M.; Im, W.; Kuczera, K.; Lazaridis, T.; Ma, J.; Ovchinnikov, V.; Paci, E.; Pastor, R. W.; Post, C. B.; Pu, J. Z.; Schaefer, M.; Tidor, B.; Venable, R. M.; Woodcock, H. L.; Wu, X.; Yang, W.; York, D. M.; Karplus, M., Charmm: The Biomolecular Simulation Program. *J. Comput. Chem.* **2009**, *30*, 1545-1614.
212. Brooks, B. R.; Bruccoleri, R. E.; Olafson, B. D.; States, D. J.; Swaminathan, S.; Karplus, M., Charmm - a Program for Macromolecular Energy, Minimization, and Dynamics Calculations. *J. Comput. Chem.* **1983**, *4*, 187-217.
213. Ryckaert, J.-P.; Ciccotti, G.; Berendsen, H. J. C., Numberical Integration of the Cartesian Equations of Motion of a System with Constraints: Molecular Dynamics of n-Alkanes. *J. Comput. Phys.* **1977**, *23*, 327-341.
214. Xue, R. J.; Grofe, A.; Yin, H.; Qu, Z. X.; Gao, J. L.; Li, H., Perturbation Approach for Computing Infrared Spectra of the Local Mode of Probe Molecules. *J. Chem. Theory Comput.* **2017**, *13*, 191-201.

215. Colbert, D. T.; Miller, W. H., A Novel Discrete Variable Representation for Quantum-Mechanical Reactive Scattering Via the S-Matrix Kohn Method. *J. Chem. Phys.* **1992**, *96*, 1982-1991.
216. Echave, J.; Clary, D. C., Potential Optimized Discrete Variable Representation. *Chem. Phys. Lett.* **1992**, *190*, 225-230.
217. Light, J. C.; Hamilton, I. P.; Lill, J. V., Generalized Discrete Variable Approximation in Quantum-Mechanics. *J. Chem. Phys.* **1985**, *82*, 1400-1409.
218. Ghysels, A.; Van Neck, D.; Van Speybroeck, V.; Verstraelen, T.; Waroquier, M., Vibrational Modes in Partially Optimized Molecular Systems. *J. Chem. Phys.* **2007**, *126*, 224102.
219. Ghysels, A.; Van Neck, D.; Waroquier, M., Cartesian Formulation of the Mobile Block Hessian Approach to Vibrational Analysis in Partially Optimized Systems. *J. Chem. Phys.* **2007**, *127*, 164108.
220. Arun, K. S.; Huang, T. S.; Blostein, S. D., Least-Squares Fitting of 2 3-D Point Sets. *IEEE Trans. Pattern Anal. Mach. Intell.* **1987**, *9*, 699-700.
221. Kwac, K.; Lee, H.; Cho, M. H., Non-Gaussian Statistics of Amide I Mode Frequency Fluctuation of N-Methylacetamide in Methanol Solution: Linear and Nonlinear Vibrational Spectra. *J. Chem. Phys.* **2004**, *120*, 1477-1490.
222. Gowers, R. J.; Carbone, P., A Multiscale Approach to Model Hydrogen Bonding: The Case of Polyamide. *J. Chem. Phys.* **2015**, *142*, 224907.
223. Rapaport, D. C., Hydrogen-Bonds in Water Network Organization and Lifetimes. *Mol. Phys.* **1983**, *50*, 1151-1162.
224. Michaud-Agrawal, N.; Denning, E. J.; Woolf, T. B.; Beckstein, O., Software News and Updates Mdanalysis: A Toolkit for the Analysis of Molecular Dynamics Simulations. *J. Comput. Chem.* **2011**, *32*, 2319-2327.
225. Marenich, A. V.; Cramer, C. J.; Truhlar, D. G., Universal Solvation Model Based on Solute Electron Density and on a Continuum Model of the Solvent Defined by the Bulk Dielectric Constant and Atomic Surface Tensions. *J. Phys. Chem. B* **2009**, *113*, 6378-6396.
226. Mennucci, B., Polarizable Continuum Model. *Wiley Interdisciplinary Reviews: Computational Molecular Science* **2012**, *2*, 386-404.
227. Fried, S. D.; Boxer, S. G., Measuring Electric Fields and Noncovalent Interactions Using the Vibrational Stark Effect. *Acc. Chem. Res.* **2015**, *48*, 998-1006.
228. Batuev, M. I.; Petrov, A. D.; Ponomarenko, V. A.; Matveeva, A. D., Optical Investigation of the Si-H Bond and Peculiarities in Its Chemical Behavior in Various Compounds. *Bull. Acad. Sci. USSR* **1956**, *5*, 1269-1274.
229. Lucovsky, G., Chemical Effects on the Frequencies of Si-H Vibrations in Amorphous Solids. *Solid State Commun.* **1979**, *29*, 571-576.
230. Lucovsky, G.; Nemanich, R. J.; Knights, J. C., Structural Interpretation of the Vibrational Spectra of a-Si: H Alloys. *Phys. Rev. B* **1979**, *19*, 2064-2073.
231. Smith, A. L.; Angelotti, N. C., Correlation of the SiH Stretching Frequency with Molecular Structure. *Spectrochim. Acta* **1959**, *15*, 412-420.
232. Thompson, H. W., Si-H Vibration Frequency and Inductive Effects. *Spectrochim. Acta* **1960**, *16*, 238-241.

233. Huber, C. J.; Anglin, T. C.; Jones, B. H.; Muthu, N.; Cramer, C. J.; Massari, A. M., Vibrational Solvatochromism in Vaska's Complex Adducts. *J. Phys. Chem. A* **2012**, *116*, 9279-9286.
234. Chuntonov, L.; Pazos, I. M.; Ma, J. Q.; Gai, F., Kinetics of Exchange between Zero-, One-, and Two-Hydrogen-Bonded States of Methyl and Ethyl Acetate in Methanol. *J. Phys. Chem. B* **2015**, *119*, 4512-4520.
235. Laenen, R.; Gale, G. M.; Lascoux, N., IR Spectroscopy of Hydrogen-Bonded Methanol: Vibrational and Structural Relaxation on the Femtosecond Time Scale. *J. Phys. Chem. A* **1999**, *103*, 10708-10712.
236. Moilanen, D. E.; Wong, D.; Rosenfeld, D. E.; Fenn, E. E.; Fayer, M. D., Ion-Water Hydrogen-Bond Switching Observed with 2D IR Vibrational Echo Chemical Exchange Spectroscopy. *Proc. Nat. Acad. Soc. USA* **2009**, *106*, 375-380.
237. Park, S.; Odelius, M.; Gaffney, K. J., Ultrafast Dynamics of Hydrogen Bond Exchange in Aqueous Ionic Solutions. *J. Phys. Chem. B* **2009**, *113*, 7825-7835.
238. Ryckaert, J.-P.; Ciccotti, G.; Berendsen, H. J. C., Numerical Integration of the Cartesian Equations of Motion of a System with Constraints: Molecular Dynamics of N-Alkanes. *Journal of Computational Physics* **1977**, *23*, 327-341.
239. Fung, B. M.; McGaughy, T. W., Molecular Motions in Liquid .1. Rotation of Water and Small Alcohols Studied by Deuteron Relaxation. *J. Chem. Phys.* **1976**, *65*, 2970-2976.
240. Lin, K.; Hu, N. Y.; Zhou, X. G.; Liu, S. L.; Luo, Y., Reorientation Dynamics in Liquid Alcohols from Raman Spectroscopy. *Journal of Raman Spectroscopy* **2012**, *43*, 82-88.
241. Mashimo, S.; Kuwabara, S.; Higasi, K., The Dielectric-Relaxation of Mixtures of Water and Primary Alcohol. *J. Chem. Phys.* **1989**, *90*, 3292-3294.
242. Barthel, J.; Bachhuber, K.; Buchner, R.; Hetzenauer, H., Dielectric Spectra of Some Common Solvents in the Microwave Region - Water and Lower Alcohols. *Chem. Phys. Lett.* **1990**, *165*, 369-373.
243. Tamai, Y.; Tanaka, H.; Nakanishi, K., Molecular Simulation of Permeation of Small Penetrants through Membranes. 1. Diffusion Coefficients. *Macromolecules* **1994**, *27*, 4498-4508.
244. Lim, S. Y.; Tsotsis, T. T.; Sahimi, M., Molecular Simulation of Diffusion and Sorption of Gases in an Amorphous Polymer. *J. Chem. Phys.* **2003**, *119*, 496-504.
245. Kim, B.-Y.; Hong, L.-Y.; Chung, Y.-M.; Kim, D.-P.; Lee, C.-S., Solvent-Resistant PDMS Microfluidic Devices with Hybrid Inorganic/Organic Polymer Coatings. *Adv. Funct. Mater.* **2009**, *19*, 3796-3803.
246. Erman, B.; Flory, P. J., Theory of Elasticity of Polymer Networks. II. The Effect of Geometric Constraints on Junctions. *J. Chem. Phys.* **1978**, *68*, 5363-5369.
247. Arrighi, V.; Ganazzoli, F.; Zhang, C.; Gagliardi, S., New Interpretation of Local Dynamics of Poly(Dimethyl Siloxane) Observed by Quasielastic Neutron Scattering. *Phys. Rev. Lett.* **2003**, *90*, 058301.
248. Flichy, N. M. B.; Kazarian, S. G.; Lawrence, C. J.; Briscoe, B. J., An ATR−IR Study of Poly (Dimethylsiloxane) under High-Pressure Carbon Dioxide: Simultaneous Measurement of Sorption and Swelling. *J. Phys. Chem. B* **2002**, *106*, 754-759.

249. Olson, C. M.; Grofe, A.; Huber, C. J.; Spector, I. C.; Gao, J.; Massari, A. M., Enhanced Vibrational Solvatochromism and Spectral Diffusion by Electron Rich Substituents on Small Molecule Silanes. *J. Chem. Phys.* **2017**, *147*, 124302.
250. Batuev, M. I.; Petrov, A. D.; Ponomarenko, V. A.; Matveeva, A. D., Optical Investigation of the Si-H Bond and Peculiarities in Its Chemical Behavior in Various Compounds. *Bull. Acad. Sci. USSR* **1956**, *5*, 1269-1274.
251. Lucovsky, G.; Nemanich, R. J.; Knights, J. C., Structural Interpretation of the Vibrational Spectra of A-Si:H Alloys. *Phys. Rev. B* **1979**, *19*, 2064-2073.
252. Brennan, D. P.; Dobley, A.; Sideris, P. J.; Oliver, S. R., Swollen Poly(Dimethylsiloxane) (PDMS) as a Template for Inorganic Morphologies. *Langmuir* **2005**, *21*, 11994-11998.
253. Yasunaga, H.; Ando, I., Effect of Cross-Linking on the Molecular Motion of Water in Polymer Gel as Studied by Pulse 1H NMR and PGSE 1H NMR. *Polym. Gels Networks* **1993**, *1*, 267-274.
254. Sotta, P.; Deloche, B., Long-Time Dynamics in Poly(Dimethylsiloxane) Networks Studied by Deuterium Nuclear Magnetic Resonance. *J. Chem. Phys.* **1994**, *100*, 4591-4600.
255. Schmid, H.; Michel, B., Siloxane Polymers for High-Resolution, High-Accuracy Soft Lithography. *Macromolecules* **2000**, *33*, 3042-3049.
256. Eddington, D. T.; Crone, W. C.; Beebe, D. J., Development of Process Protocols to Fine Tune Polydimethylsiloxane Material Properties. In *7th International Conference on Miniaturized Chemical and Biochemical Analysis Systems*, 2003; pp 1089-1092.
257. Fuard, D.; Tzvetkova-Chevolleau, T.; Decossas, S.; Tracqui, P.; Schiavone, P., Optimization of Poly-Di-Methyl-Siloxane (PDMS) Substrates for Studying Cellular Adhesion and Motility. *Microelectron. Eng.* **2008**, *85*, 1289-1293.
258. Johnston, I. D.; McCluskey, D. K.; Tan, C. K. L.; Tracey, M. C., Mechanical Characterization of Bulk Sylgard 184 for Microfluidics and Microengineering. *J. Micromech. Microeng.* **2014**, *24*, 035017.
259. Lamberti, A.; Marasso, S. L.; Cocuzza, M., PDMS Membranes with Tunable Gas Permeability for Microfluidic Applications. *RSC Adv.* **2014**, *4*, 61415-61419.
260. Wang, Z.; Volinsky, A. A.; Gallant, N. D., Crosslinking Effect on Polydimethylsiloxane Elastic Modulus Measured by Custom-Built Compression Instrument. *J. Appl. Polym. Sci.* **2014**, *131*, 41050.
261. Wilder, E. A.; Guo, S.; Lin-Gibson, S.; Fasolka, M. J.; Stafford, C. M., Measuring the Modulus of Soft Polymer Networks Via Buckling-Based Metrology. *Macromolecules* **2006**, *39*, 4138-4143.
262. Seo, J. H.; Sakai, K.; Yui, N., Adsorption State of Fibronectin on Poly(Dimethylsiloxane) Surfaces with Varied Stiffness Can Dominate Adhesion Density of Fibroblasts. *Acta Biomaterialia* **2013**, *9*, 5493-5501.
263. Lötters, J. C.; Olthius, W.; Veltink, P. H.; Bergveld, P., The Mechanical Properties of the Rubber Elastic Polymer Polydimethylsiloxane for Sensor Applications. *J. Micromech. Microeng.* **1997**, *7*, 145-147.
264. Shefer, A.; Gottlieb, M., Effect of Cross-Links on the Glass Transition Temperature of End-Linked Elastomers. *Macromolecules* **1992**, *25*, 4036-4042.

265. Olson, C. M.; Massari, A. M., Influence of Solvent Swelling on Ultrafast Structural Dynamics in Polydimethylsiloxane Thin Films by Two-Dimensional IR Spectroscopy. *J. Phys. Chem. A* **2018**, *122*, 1592-1599.